INFORMATION TO USERS

This manuscript has been reproduced from the microfilm master. UMI films the text directly from the original or copy submitted. Thus, some thesis and dissertation copies are in typewriter face, while others may be from any type of computer printer.

The quality of this reproduction is dependent upon the quality of the copy submitted. Broken or indistinct print, colored or poor quality illustrations and photographs, print bleedthrough, substandard margins, and improper alignment can adversely affect reproduction.

In the unlikely event that the author did not send UMI a complete manuscript and there are missing pages, these will be noted. Also, if unauthorized copyright material had to be removed, a note will indicate the deletion.

Oversize materials (e.g., maps, drawings, charts) are reproduced by sectioning the original, beginning at the upper left-hand corner and continuing from left to right in equal sections with small overlaps. Each original is also photographed in one exposure and is included in reduced form at the back of the book.

Photographs included in the original manuscript have been reproduced xerographically in this copy. Higher quality 6" x 9" black and white photographic prints are available for any photographs or illustrations appearing in this copy for an additional charge. Contact UMI directly to order.

UMI

A Bell & Howell Information Company
300 North Zeeb Road, Ann Arbor MI 48106-1346 USA
313/761-4700 800/521-0600

Observations and Physics of Amplified Subinertial Tidal Currents in Stratification and Mean Shear Flow at a Seamount

by

Daniel L. Codiga

A dissertation submitted in partial fulfillment

of the requirements for the degree of

Doctor of Philosophy

University of Washington

1996

Approved by Charles C. Eriksen
(Chairperson of Supervisory Committee)

Eric Kunze

Program Authorized
to Offer Degree Oceanography

Date 26 April 1996

In presenting this dissertation in partial fulfillment of the requirements for the Doctoral degree at the University of Washington, I agree that the Library shall makes its copies freely available for inspection. I further agree that extensive copying of this dissertation is allowable only for scholarly purposes, consistent with "fair use" as prescribed in the U.S. Copyright Law. Requests for copying of reproduction of this dissertation may be referred to University Microfilms, 1490 Eisenhower Place, P.O. Box 975, Ann Arbor, MI 48106, to whom the author has granted "the right to reproduce and sell (a) copies of the manuscript in microform and/or (b) printed copies of the manuscript from microform."

Signature Dan Codiga.

Date April 26, 1996

University of Washington

Abstract

Observations and Physics of Amplified Subinertial Tidal Currents

in Stratification and Mean Shear Flow at a Seamount

by Daniel L. Codiga

Chairperson of the Supervisory Committee: Professor Charles C. Eriksen

School of Oceanography

Three-dimensional structure of amplified diurnal tidal currents (subinertial, $0.69f$) at Cobb Seamount ($130.8°W, 46.8°N$), collected by ship-mounted Acoustic Doppler Current Profiler, agrees well with a stratified seamount-trapped wave resonant at $0.70f$. The wave solution incorporates measured bathymetry, stratification, and baroclinic mean clockwise current, with parameterized damping of 2-day timescale based on observed dissipation. Physics and observable signatures of damping and mean flow on a wave are explained, including critical surface formation in mean shear.

Observed diurnal currents propagate clockwise with first azimuthal wavenumber. Amplification extends a few km radially and about 100 m vertically from the seamount, reaching 5.3 times open-ocean K_1currents. Characteristics are clockwise rotation in time, in narrow ellipses oriented nearly along isobaths with radial and azimuthal components positively correlated, and anticlockwise turning with depth such that phase propagates downward.

Understanding of stratified seamount-trapped waves is extended in three ways. First, physics are explained using short topographic Rossby waves in stratification, or *stratified slope-Kelvin waves*. An inviscid stratified seamount-trapped wave superposes azimuthally resonant up- and down-going stratified slope-Kelvin waves, causing standing cross-slope (radial and vertical) structure. Second, observable signatures are described, including symmetries in inviscid-wave current patterns inconsistent with the measurements. A forced damped wave transports energy toward the summit where dissipation occurs, breaking cross-slope standing-wave symmetries, and exhibits flow characteristics similar to all those observed at Cobb. Third, because clockwise bottom-intensified mean flow is observed, waves linearized about a representative baroclinic azimuthal current are examined. Mean flow shifts the resonant frequency very weakly, because Doppler shifting is counteracted by the potential vorticity gradient of mean horizontal shear variations, and distorts wave structure weakly also.

Stronger mean flow causes singularities at low (high) subinertial frequencies: *stratified seamount-trapped wave* (*internal wave*) *critical surfaces*. An internal wave critical surface bounds a *superinertial cap*, where subinertial motions are effectively superinertial. Though too weak at Cobb, mean flow at Fieberling Guyot (32.4°N, 127.8°W) forms an internal wave critical surface in diurnal currents ($0.93f$) that is coincident with high turbulence levels.

Table of Contents

List of Figures

List of Tables

Acknowledgments

"C'est doux, c'est dur, c'est la vie."

I thank Charlie Eriksen for his generosity in taking me to sea to collect these unique observations, guiding me through the analysis, and teaching me to think critically in comparing measurements to models. The patience and good humor of Eric Kunze in explaining how to test seamount circulation hypotheses with data, and his tireless editing efforts, were instrumental. I benefited from the breadth of dynamical understanding Peter Rhines shared with me, and found inspiration in doing laboratory experiments with him. Dick Sternberg and Harry Yeh were very constructive committee members.

The help and friendship of fellow (and formerly fellow) students, including Craig Lee, Parker MacCready, Emmanuel Boss, Joanna Muench, Scott Springer, Chris Moore, and others, taught me oceanography but also far more.

I am indebted to Ken Brink for sharing wave expertise and advice on numerical technique; Mitsuhiro Kawase and LuAnne Thompson for graciously fielding wayward theoretical and numerical questions; Steve Riser for his flexibility with me early in the program; Jim Holton for discussing wave-mean interactions; Howard Freeland for sharing current meter data; Brian Dushaw for TOPEX tidal values; Eric Lindahl for inventive lab engineering assistance; Lyn Harris for able and user-friendly programming help; Lin Sylwester for making such pretty cartoons; and finally, Tom Powell for his encouragement to pursue oceanography "way back when."

Friends kept me laughing (you know who you are) throughout. For their patience and unfailing support I thank my parents Richard and Nancy Codiga. I take to heart the grace of Katie Faulkner through the final push here, for wherever we may find ourselves in the years to come.

Funded by an Office of Naval Research fellowship, and ONR grant N00014-89-J-1621.

Chapter 1

Motivation

This dissertation analyzes observations of amplified tidal currents in stratification and mean shear atop Cobb Seamount, and explores physics of tidally-forced stratified seamount-trapped waves as modified by dissipation and mean currents based on measurements. Flow near seamounts exhibits unusually strong currents and vertical displacements at internal-wave, tidal, and lower frequencies, with high turbulent dissipation rates (Roden 1987, Noble et al. 1988, Genin et al. 1989, Eriksen 1991, Mudge 1994, Brink 1995, Kunze and Toole 1996). Interest in these phenomena is motivated by the abundance of seamounts, tens of thousands of which extend more that a kilometer above the surrounding ocean floor in the Pacific ocean alone (Smith and Jordan 1988). An understanding of currents at a seamount is relevant to a number of oceanographic questions.

Circulation at seamounts strongly influences biological processes, causing anomalously high levels of primary productivity (Dower et al. 1992), increased fish abundances (Uchida and Tagami 1984), and bedform modifications controlling benthic communities (Levin et al. 1994). Many seamounts support high water-column biomass with unique trophic structures and species assemblages (Boehlert and Genin 1987). Hypotheses explaining such phenomena involve flow patterns such as isolation of fluid from the surrounding

ocean, or upwelling of nutrient-rich waters, that makes knowledge of the fluid dynamics central. Isolation of recirculating fluid atop Cobb Seamount is not observed during the survey analyzed in Chapter 2.

Tidal currents near a seamount are controlled by the same three influences centrally important to continental shelf processes: the Coriolis effect, density stratification, and steeply sloping bottom topography that occupies a significant fraction of the ocean depth. Stratified seamount-trapped waves (Brink 1989, 1990) are governed by the same dynamics as coastal-trapped waves, oscillations observed along continental margins (Brink 1982) that appear to be important low-frequency signal carriers in basin-scale circulations (Hallberg 1995). Of particular interest is the efficient wave generation of steady currents, as examined in Chapter 3 and demonstrated by recent laboratory experiments (Zhang and Boyer 1993, Codiga 1993), numerical modeling (Haidvogel et al. 1993), and theory (Maas and Zimmerman 1989). Flow at a seamount is thus an example of ocean dynamics with wider applicability, yet occurs on small scales amenable to more complete sampling. The measurements from Cobb Seamount facilitate the most complete comparison of observations to three-dimensional wave structure to date.

Dissipation is a dominant influence on tidal currents at Cobb Seamount. Based on microstructure measurements, average turbulent kinetic energy dissipation levels 10^{-7} W/kg and inferred diffusivities $10 - 500$ cm^2/s extending several kilometers away from the summit are higher, by a factor of

up to 50, than in the bottom boundary layer (Mudge 1994). Left unforced, kinetic energy in ~ 10 cm/s currents over the same region would dissipate in no more than a few days. For these reasons the effect of dissipation on wave physics is examined here using the convenient parameterization of Rayleigh drag with Newtonian cooling and heating with 2-day decay timescale.

A long-standing puzzle in physical oceanography is the disparity between vertical diffusivities inferred indirectly from the structure of the thermocline (Munk 1966) and measured estimates that are an order of magnitude weaker (Gregg 1989, Ledwell et al. 1993). A potential resolution of the paradox presently under dispute (Toole et al. 1994, Lueck and Mudge 1996) is boundary mixing by amplified motions near steeply sloping topography such as seamounts. Critical reflection of internal waves is a source for such amplification (Eriksen 1982, 1985, 1995, Garrett and Gilbert 1988). Critical surfaces of trapped waves in mean flow are another mechanism for elevated turbulence levels at a seamount. As shown in Chapter 4, a critical surface in diurnal currents due to mean flow at Fieberling Guyot coincides with high observed turbulent dissipation rates.

Chapter 5 summarizes the dissertation, with reference to figures and tables, and reviews the conclusions.

Chapter 2

Observations of low-frequency circulation and amplified subinertial tidal currents at Cobb Seamount

2.1. Introduction

Flow near seamounts exhibits high turbulent dissipation rates and unusually strong currents and vertical displacements at internal-wave, tidal, and lower frequencies (Roden 1987, Genin et al. 1989, Eriksen 1991, Mudge 1994, Brink 1995, Kunze and Toole 1996). Seamounts are abundant (Smith and Jordan 1988) and flows near them are of interest because they exert control over anomalously high levels of primary productivity (Dower et al. 1992) and increased fish abundances (Uchida and Tagami 1984), and may be important to the global mixing budget thought necessary to maintain the thermocline (Munk 1966). In addition, flow near a thermocline-depth seamount is an example of the interplay of three fundamental effects on ocean physics: rotation, stratification, and sloping bottom topography. Subinertial waves are supported by and trapped to a sloping bottom in stratification (Rhines 1970) and may be important to basin-scale circulation in the form of coastal-trapped waves (Huthnance 1978) that have been observed along continental margins (Brink 1982). At a seamount, models suggest subinertial tidal currents excite these motions as stratified seamount-trapped waves (Brink 1989, 1990).

We report here current and hydrographic measurements of tidal, near-inertial, and low-frequency flow at Cobb Seamount, and demonstrate that amplified bottom-intensified subinertial diurnal currents occur with characteristics matching a forced damped stratified seamount-trapped wave. Cobb Seamount (Figure 2.1) is located in relatively weak eastward general circulation in the northeastern corner of the North Pacific subtropical gyre (McNally et al. 1983). Its steeply sloping flanks (12° inclination from horizontal) and terrace (2.5° inclination) protrude into the shallowest 300 m where stratification is concentrated. The scale fL/N setting the vertical extent of response to forcing at the boundary of a rotating stratified fluid (Gill 1982) is 50 – 100 m for Coriolis frequency $f = 1.06 \times 10^{-4}$ s^{-1} using seamount terrace length scale $L \approx 4 - 8$km and buoyancy frequency $N \approx 5$cph $= 0.0087$ s^{-1}.

Frequency spectra from the short record of a current meter 50 m off the seamount (Freeland 1994) give an intriguing glimpse at flow characteristics (Figure 2.2). Energy is dominantly near the diurnal and semidiurnal bands, with subinertial diurnal currents amplified more strongly than those at the semidiurnal frequency even though off-seamount tidal currents are dominantly semidiurnal (Egbert et al. 1994). Azimuthal velocities exceed radial, indicating currents are aligned dominantly along seamount isobaths. Stratified seamount-trapped waves are consistent with diurnal motions of this structure and prompt the present analysis, that uses a ship-mounted Acoustic

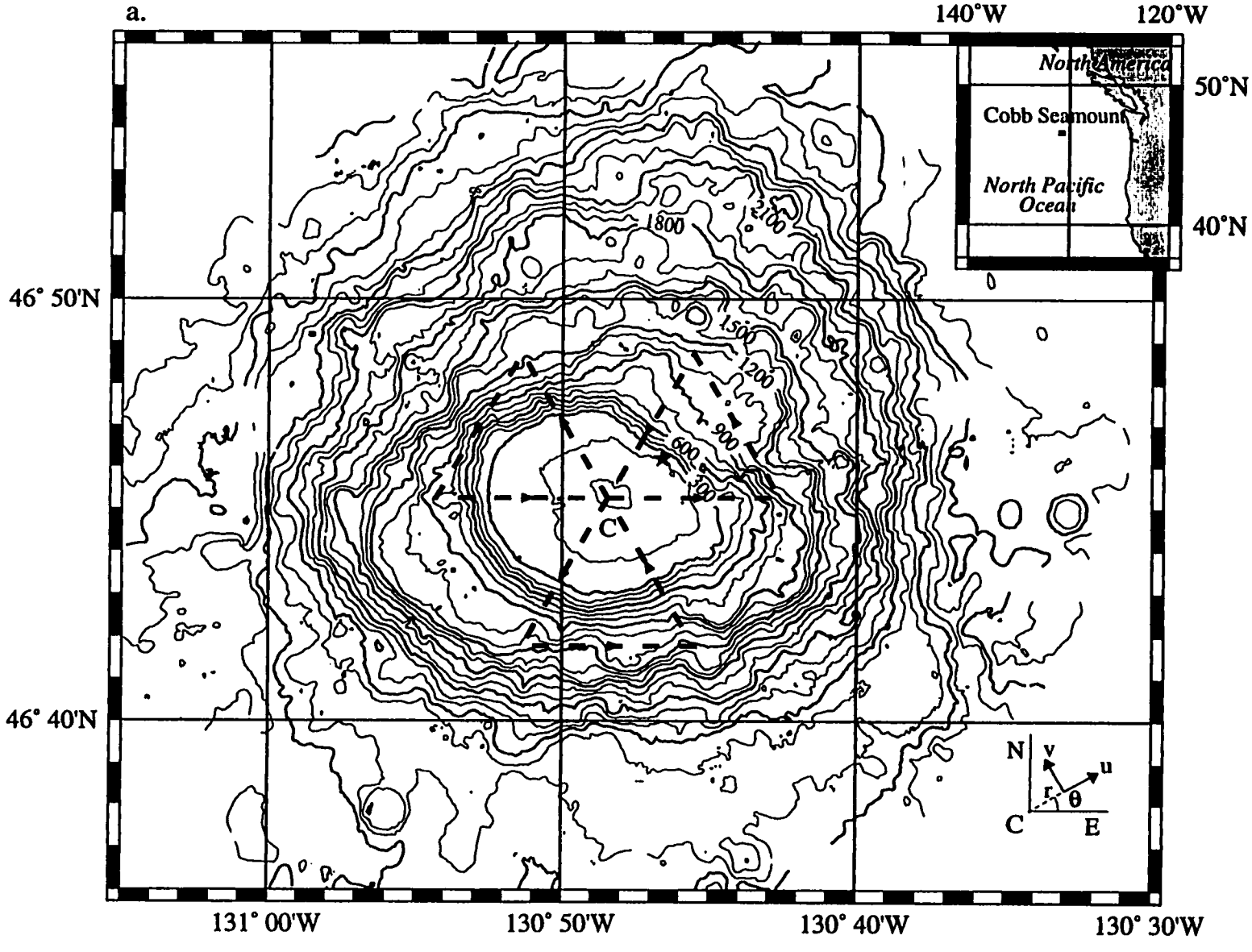
a.
140°W
120°W
North America
Cobb Seamount
North Pacific Ocean
50°N
40°N
46° 50'N
46° 40'N
1800
2100
1500
1200
900
600
300
C
N
v
u
r
θ
C
E
131° 00'W
130° 50'W
130° 40'W
130° 30'W

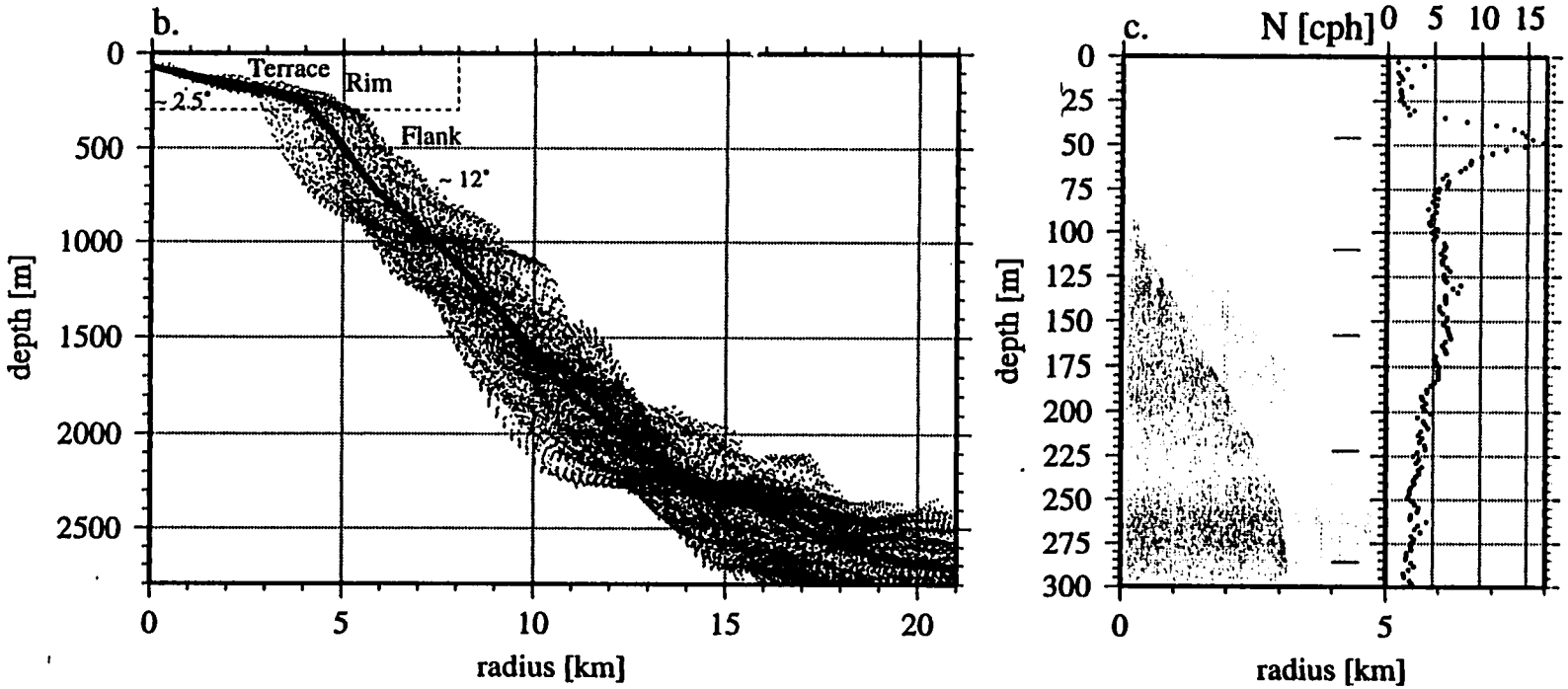

Figure 2.1. (a) Cobb Seamount isobaths, contour interval 100 m, from R/V T. G. Thompson survey with 60-beam Krupp-Atlas Hydrosweep. Dashed line marks ADCP survey pattern. The seamount center (labelled C) is taken at 46°45.21′ N, 130° 48.45′ W with summit considered 70 m deep since the pinnacle (within 25 m of the surface, Budinger and Enbysk 1960) is more narrow than both the 200 m bathymetric data-bin size and the scales of interest. Lower right: cylindrical coordinates, radial and azimuthal velocity convention (u, v) . (b) Bathymetric data in radial-vertical plane, vertical exaggeration 5:1. Azimuthal average profile (solid line) has *terrace* sloping downward at $\cong 2.5°$ from the summit to *rim* $\cong 225$ m deep at radius $\cong 4$km, and *flank* with slope angle reaching $\cong 12°$. (c) Expanded view of region of current and hydrographic sampling (dashed box in (b)), with minimum and maximum bathymetry profiles and ensemble-mean stratification (October 1991 CTD casts, Figure 2.10a).

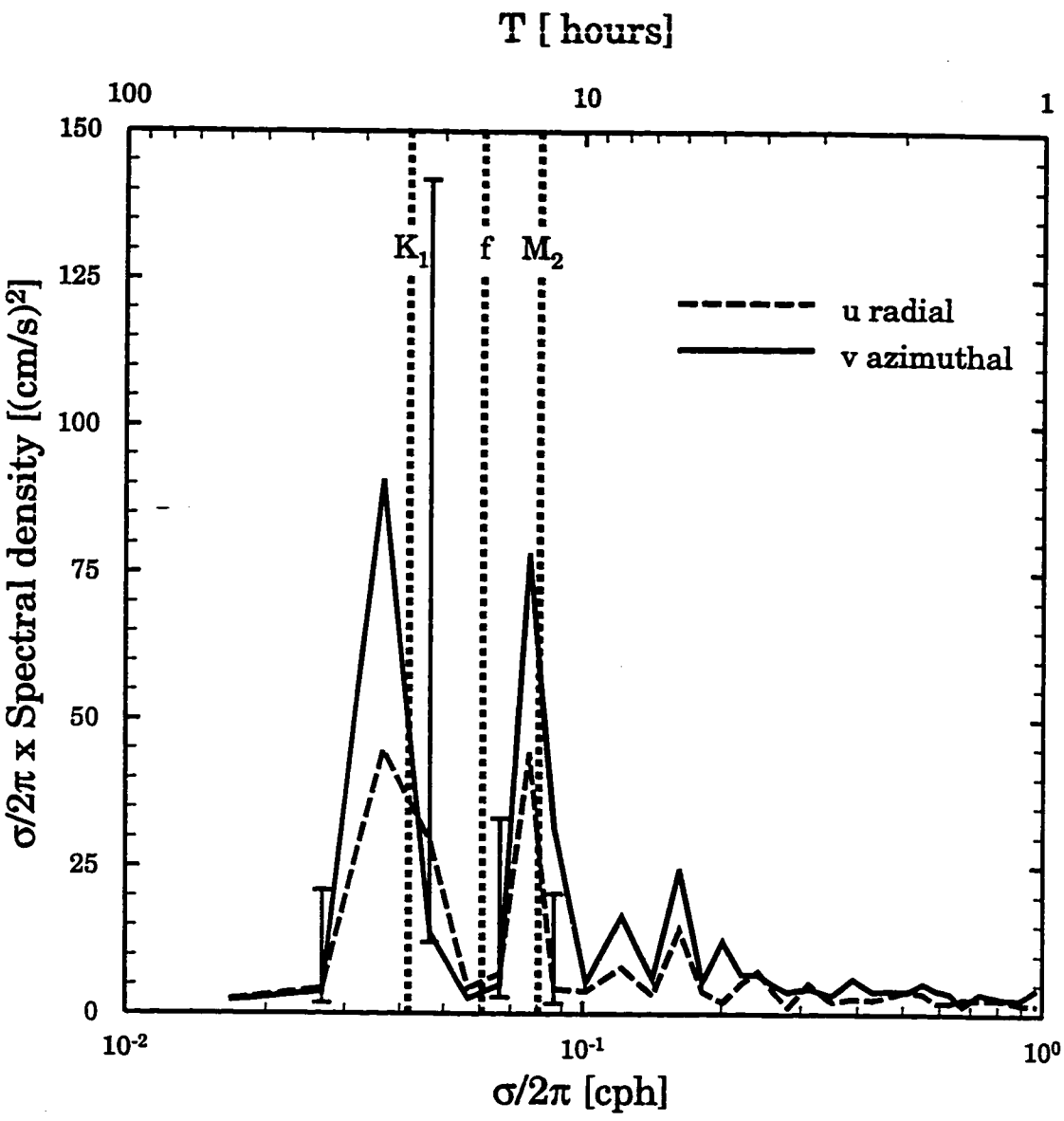

Figure 2.2. Variance-preserving spectra of radial and azimuthal velocities (cylindrical coordinates, Figure 2.1a) from a current meter located 50 m above Cobb Seamount (Freeland 1994) at the star marked in Figure 2.1a. Record length 14 days, sampling interval 2 minutes. Estimates have 3 degrees of freedom and 95% significant confidence intervals shown. The diurnal (semidiurnal) tide K_1 (M_2) is subinertial (superinertial) at frequency $\sigma = 0.69f$ ($1.32f$). Subinertial energy is amplified more strongly than dominantly semidiurnal off-seamount tidal currents. Azimuthal velocities exceed radial.

Doppler Current Profiler (ADCP) survey resolving radial, azimuthal, and vertical structure in direct comparison to three-dimensional wave solutions.

Observed energy in ADCP currents is partitioned into steady and azimuthally propagating harmonics around the seamount at diurnal, inertial, and semidiurnal frequencies in Section 2.2. Steady flow is shown in Section 2.3 to have a component circulating clockwise around the seamount at depth, with an associated positive mean density anomaly based on conductivity-temperature-depth (CTD) data. Section 2.4 describes diurnal currents and compares them to stratified seamount-trapped waves, explaining physics and observational signatures of wave solutions incorporating appropriate bathymetry, stratification, tidal forcing, frictional damping, and azimuthal mean flow. Near-inertial and semidiurnal motions are presented in Section 2.5.

2.2. Energy partition of ADCP currents

We analyze a 3.4-day sequence of absolute horizontal water velocities measured in October 1991 with an RDI instruments ADCP mounted in the hull of the R/V T. G. Thompson. The survey pattern (Figure 2.1) extends to radius 7.4 km over the terrace and upper flanks of the seamount, includes transects crossing the summit at three different headings, and has 1.6 km horizontal resolution. The upper 300 m outside the 40-50 m nearest the bottom is sampled with 16 m vertical resolution nominally once per 4 hours, as explained with data reduction in Appendix A.

East and north velocities are converted to radial and azimuthal velocities (u, v) in cylindrical coordinates (Figure 2.1a), ignoring bathymetric deviations from circular symmetry. Use of a redefined radial coordinate (not shown) that accounts for the difference between the radial position of the topographic boundary and its azimuthal-average value does not alter conclusions.

The radial-vertical plane is divided into 16-m depth intervals and 1.6-km radial regions (for example, Figure 2.4 below), each radial-vertical bin defining an annulus of rectangular cross-section encircling the seamount. A harmonic fit, described below, is applied to the time sequence of measurements from each annulus independently. Radial and azimuthal velocities are fit independently. Lacking vertical velocities, no continuity constraint between adjacent radial-vertical bins is imposed. Conventional Fourier analysis is not applied since data from fixed locations are not equally spaced in time.

2.2.a. Azimuthally propagating harmonics

Radial and azimuthal (u, v) velocity data from each radial-vertical bin are fit by least squares to a sum of harmonics having specified frequencies σ and azimuthal wavenumbers n. Each harmonic has structure

$$\begin{aligned} u &= A^u \cos\left(n\theta - \sigma t + \Phi^u \right) \\ v &= A^v \cos\left(n\theta - \sigma t + \Phi^v \right) \end{aligned} \qquad (2.1)$$

where θ is azimuth (positive counterclockwise from east, Figure 2.1a), t is time, and $\left(A^u, A^v\right) > 0$ and $\left(\Phi^u, \Phi^v\right)$ are constant amplitudes and phases determined by the fit. Positive n indicates anticlockwise propagation (opposite the convention in Brink 1989, 1990). A group of harmonics (Table 2.1) that

Table 2.1. Frequencies and azimuthal wavenumbers included in harmonic fits to ADCP velocities.

Component	Normalized frequency σ/f	Azimuthal wavenumber n
Steady	0	0, -1, -2, -3
Diurnal	0.69	-1
Inertial	1	-1
Semidiurnal	1.32	0, -1, -2

best accounts for measured energy is included, having frequencies and azimuthal wavenumbers justified below by physically reasonable *a priori* information and *a posteriori* knowledge of fit results. Sampling limitations require each frequency to be treated as a narrow-band signal.

Plan view velocity vectors and current ellipses of harmonics for a small group of azimuthal wavenumber n, amplitude $\left(A^u, A^v\right)$, and phase $\left(\Phi^u, \Phi^v\right)$ (2.1) combinations are sufficiently general to interpret the results (Figure 2.3). Each set of ellipses is centered on the seamount with $t = 0$ velocity vectors superposed, in the coordinate system marked in the middle column of (b). Velocity vectors describe completely the zero-frequency harmonics; in nonzero

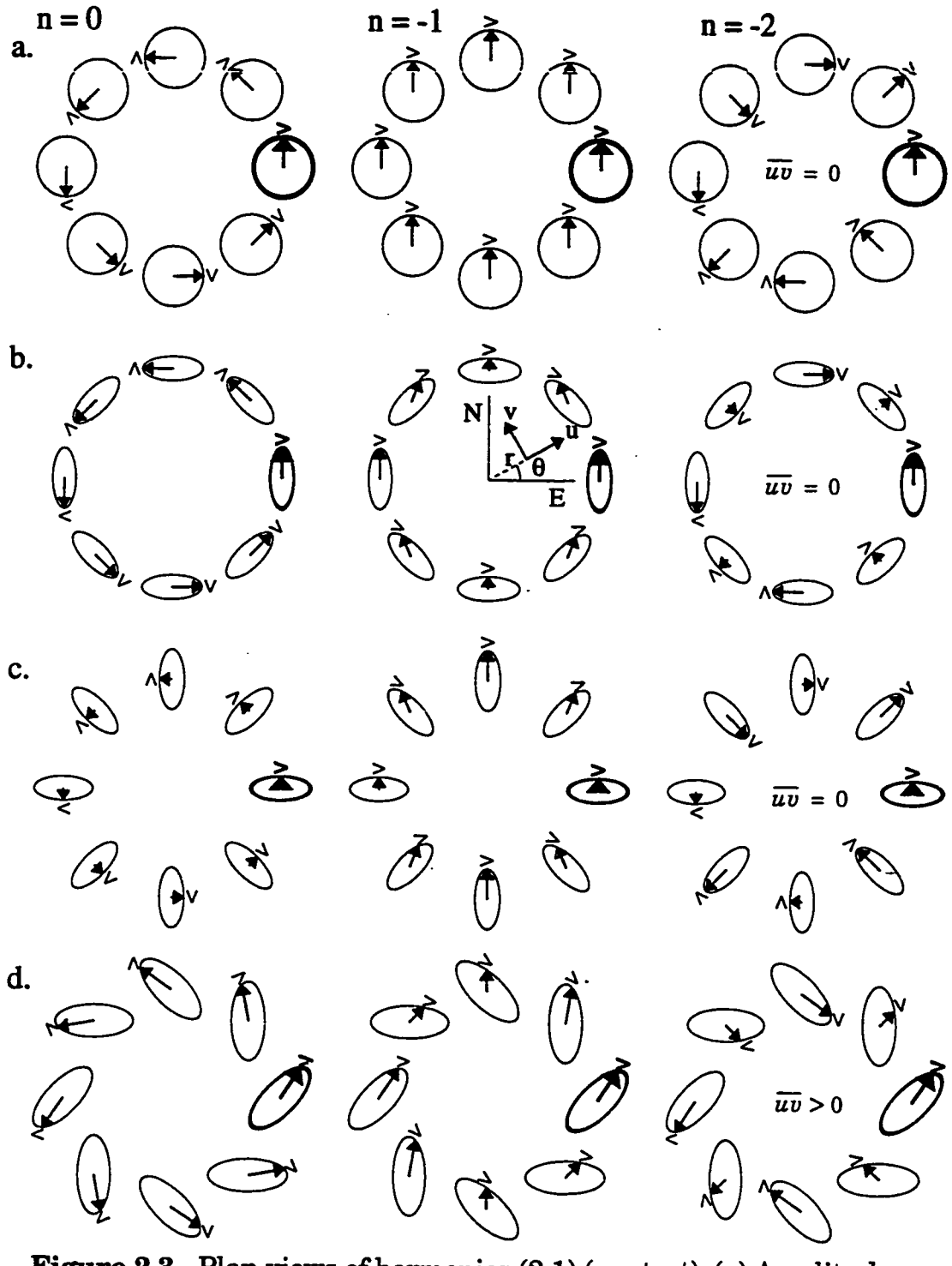

Figure 2.3. Plan views of harmonics (2.1) (see text). (a) Amplitudes A^u=1, A^v=1; phases Φ^u=0°, Φ^v=90°. (b) A^u=0.5, A^v=1; Φ^u=0°, Φ^v=90°. (c) A^u=1, A^v=0.5; Φ^u=0°, Φ^v=90°. (d) A^u=1, A^v=1; Φ^u=0°, Φ^v=45°.

frequency harmonics, velocity vectors sweep out current ellipses as marked by arrows above each vector head. For u and v in quadrature ($\Phi^v - \Phi^u = \pm 90°$), current ellipses have axes parallel or perpendicular to circular seamount isobaths and are elongated across (along) them where radial (azimuthal) amplitude is largest (Figure 2.3a,b,c). Quadrature corresponds to $\overline{uv} = 0$, where $\overline{(\,)}$ indicates an azimuthal average and is equivalent (by (2.1)) to an average over a wave period for an individual harmonic. Current ellipses for phases out of quadrature such that $\overline{uv} > 0$ lie at an angle to isobaths in the sense of Figure 2.3d. Data are presented in later sections using only the current ellipse at $\theta = 0$ (bold in Figure 2.3) to represent azimuthal structures in Figure 2.3.

Frequency content includes four components: low-frequency, diurnal, inertial, and semidiurnal (Table 2.1). The local inertial period is 16.4 hours and the K_1 and M_2 tidal frequencies, with periods 23.9 and 12.4 hours, are used for diurnal and semidiurnal components. In terms of the 3.4-day time sequence of data from a fixed location sampled nominally each 4 hours, the Nyquist period is about 8 hours and frequency resolution ($\sim 0.2f$) is coarse but adequate to resolve diurnal, inertial, and semidiurnal frequencies (0.69, 1.0, and $1.32f$ respectively) from each other. Inclusion of the two tidal bands is justified by current meter spectra (Figure 2.2), and the harmonic with frequency $\sigma = f$ is included because the survey was in autumn after several storms that

are known to excite near-inertial internal waves in the upper few hundred meters (D'Asaro 1984). Lack of energy near the inertial frequency in the spectra of Figure 2.2 reflects both the depth of the mooring and its deployment in summer when winds were not pronounced.

The survey (Figure 2.1a) has three cross-summit transects making it possible to resolve azimuthal wavenumbers $n = -3$ to 3. For steady flow the harmonic fit includes wavenumbers 0 to -3 (Table 2.1), the most general set because positive and negative wavenumber are identical at zero frequency. Total steady flow, the superposition of these four wavenumbers, does not differ significantly from time-mean data and is used in dynamical interpretations (Section 2.3). Wavenumbers included at nonzero frequencies (Table 2.1) have currents in adjacent radial-vertical bins that vary smoothly on a scale of two bins vertically and radially. Wavenumbers not in Table 2.1 comprise residual variance and have been excluded because they lack this spatially coherent structure and are less strongly amplified.

Between 40 and 80%, typically 65-70%, of kinetic energy in data from each radial-vertical bin is captured by the harmonics of Table 2.1 (Figure 2.4). Black, gray, and white represent total energy in harmonics of nonzero frequency, energy in the sum of velocities from all steady harmonics, and residual energy (data less fit) respectively. Residual energy occurs at scales smaller than projects onto the first few azimuthal wavenumbers, is not spatially coherent on a scale of two bins radially and vertically, and/or has frequency

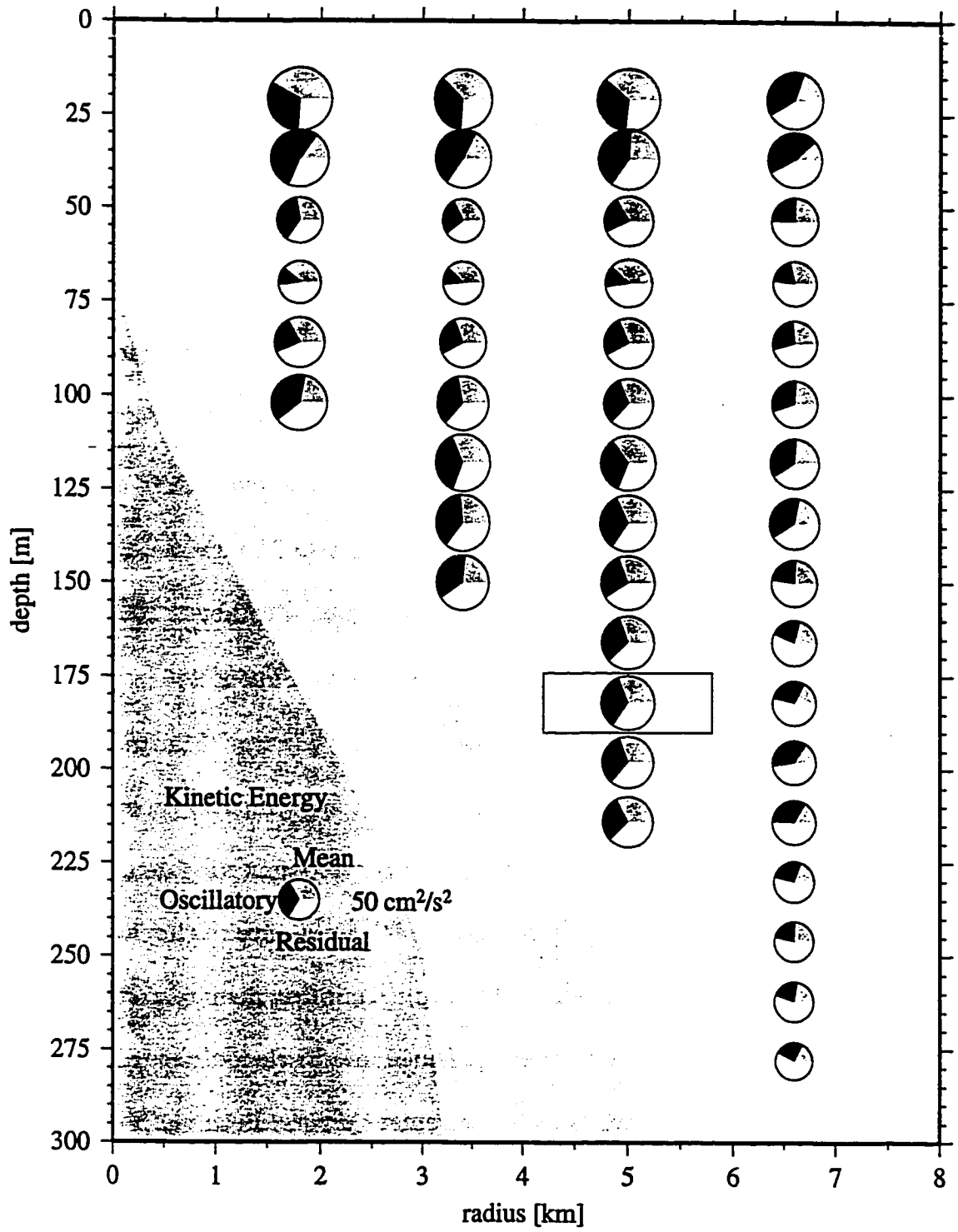

Figure 2.4. Horizontal kinetic energy in ADCP velocities (see text). Minimum and maximum bathymetric profiles shown, in field of view dashed in Figure 2.1b. Box is radial-vertical bin used in Figure 2.5.

higher than resolved. The residual shows no evidence of signals that might be distorted or lost in an azimuthal-harmonic fit, such as short-wavelength motions propagating linearly across the survey region.

2.2.b. Confidence intervals

Results from a representative radial-vertical bin, plotted as timeseries at a fixed azimuthal location (Figure 2.5), demonstrate the harmonic fit and show relative sizes of measurement error and fit confidence intervals. Amplitude and phase for each of the 9 harmonics in Table 2.1, except the $n = 0$ steady harmonic that has only an amplitude, comprise 17 parameters in the fit to each component of velocity. These are constrained by about 100 observations in the inner three radial bins (see Figure 2.4) and about 240 in the outermost radial bin, which includes three additional survey legs (Figure 2.1a).

Confidence intervals calculated using two complementary methods have similar sizes, indicating measurement error and sampling density are comparably important in limiting the statistical confidence in the fit. The bootstrap method (Efron and Gong 1983) tests sampling density and does not depend explicitly on measurement error. The Monte Carlo method (Press et al. 1992) tests sensitivity of results to measurement errors. Both methods were carried out using 50 realizations. Confidence intervals shown in figures to follow indicate the 67% significance level from the bootstrap method.

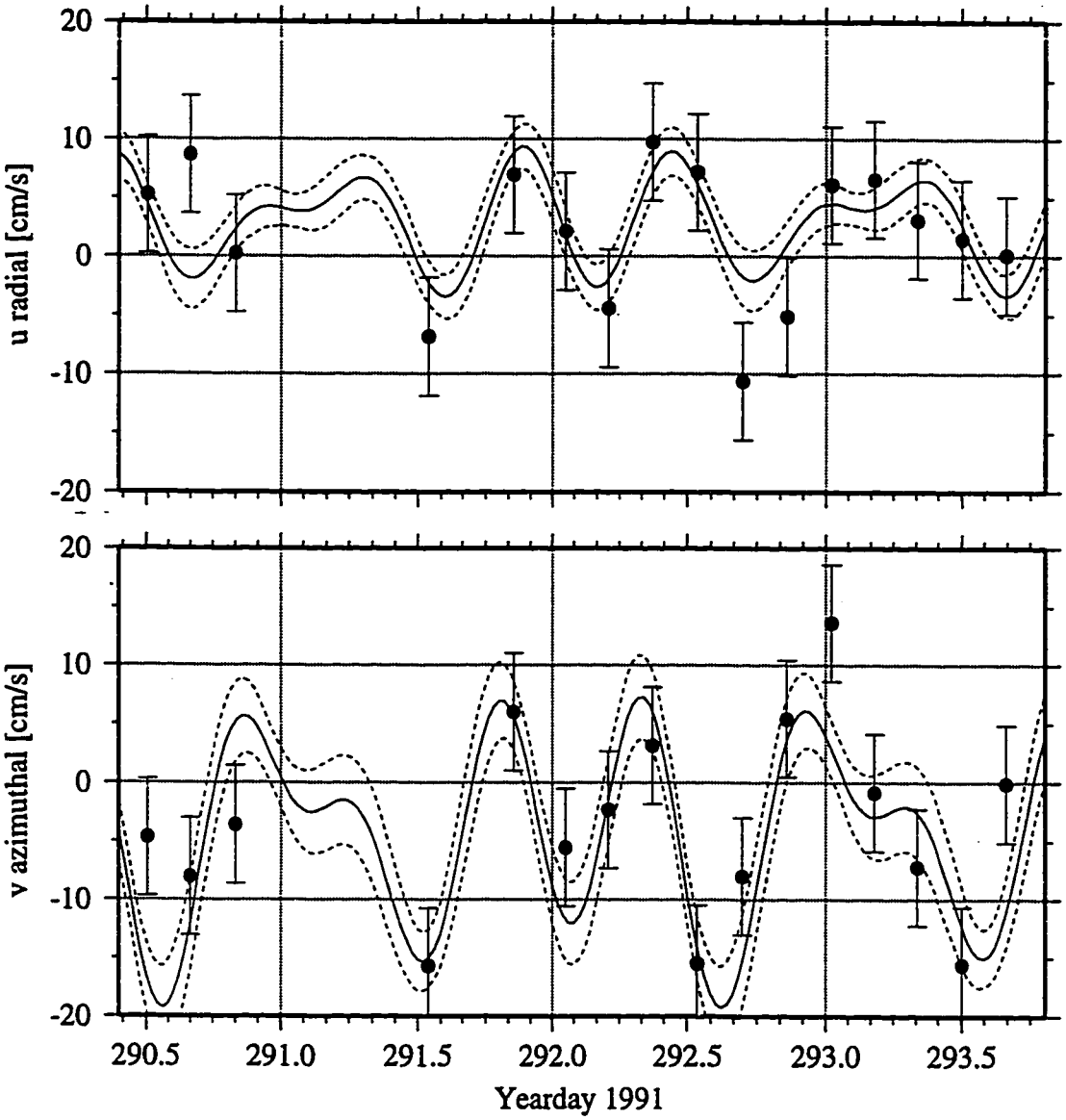

Figure 2.5. Representative fit to harmonics in Table 2.1, shown as a timeseries at a fixed location. Data (circles) are from radial-vertical bin marked in Figure 2.4 on the southeast leg of the survey (Figure 2.1a); they represent about one-sixth the data, from all survey legs, used in this fit. Yearday 291 coverage gap is during CTD survey. Vertical bars are measurement error (Appendix A). Solid curve is the fit, with dashed confidence intervals at the 67% significance level calculated by the bootstrap method.

A number of tests confirm fit results are not sensitive to the combination of harmonics used. In one, additional wavenumbers are included at the three nonzero frequencies; residual variance is decreased slightly but currents in the additional wavenumbers do not vary smoothly between radial-vertical bins and are hence considered noise. In this test, and also when harmonics in Table 2.1 are excluded, currents in the harmonics retained do not change significantly. This indicates sampling resolves each harmonic independently and energy from one does not spread into another.

Aliasing by internal waves amplified through critical reflection at periods shorter the 8-hour nominal Nyquist period is considered minimal. Internal wave critical periods (Eriksen 1982) for typical slopes and stratification at Cobb range from about 1 to 5 hours. Current meter data (Freeland 1994) reveal amplified internal wave energy 10 m off the seamount flanks at these periods, but the internal wave field appears to relax to a background level at 50 m above the bottom (e.g. Figure 2.2) and ADCP coverage does not extend within 40 – 50 m of the seamount due to acoustic backscatter (Appendix A).

2.3. Low frequency flow

2.3.a. Currents

Low-frequency flow consists of a broad current moving over and around the seamount, with a clockwise circulation near the bottom on the terrace. Figure 2.6 shows steady ADCP currents (summed zero-frequency harmonics

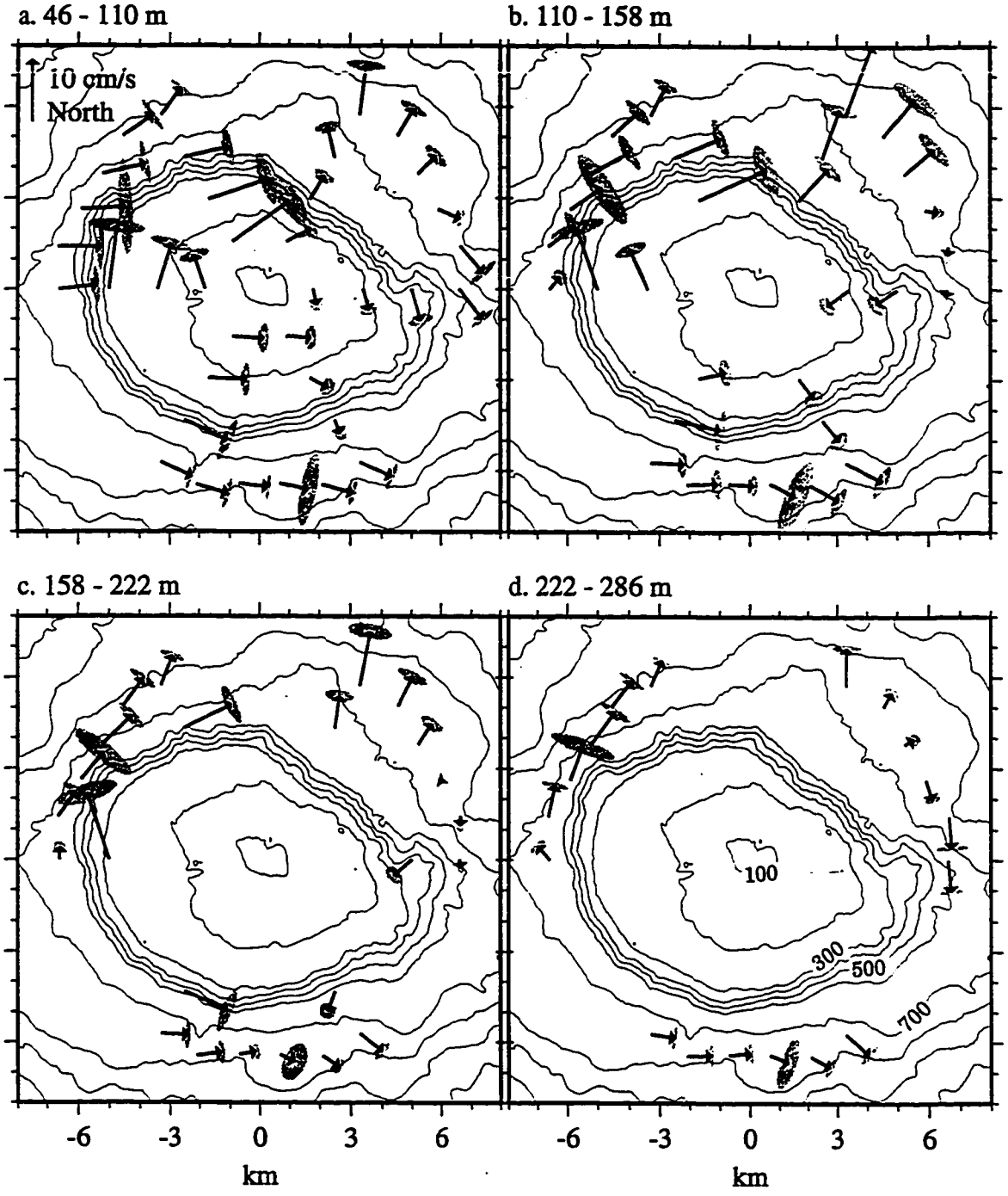

Figure 2.6. Steady ADCP currents, averaged in four depth ranges as labeled (see tick marks in Figures 2.1c and 2.7) with 67% significance level bootstrap confidence intervals. Superposed on 100-m isobaths (labeled in d.). Current incident from the east is strengthened to the northwest side, and there is bottom-intensified clockwise circulation on the terrace (see Figures 2.7 and 2.8).

in least-squares fit, Section 2.2) in four depth ranges below the mixed layer depth (Figure 2.1c). At shallow depths (Figure 2.6a) there is a 7 – 8cm/s incident current directed slightly north of east, with dominantly clockwise flow within a few km of the center. Flow deeper on the terrace (Figure 2.6b) is increased on the northwest side and steered in a direction opposing the incident flow on the southeast side, strengthening the clockwise circulation. Below 158 m (Figure 2.6c,d) currents weaken slightly with depth and northeastward flow splits and moves past the sides of the seamount, strengthened on the northwest side at inner radii. On the northeast segment of the survey there is northward flow to the north and south-southeastward flow to the east.

Clockwise flow at depth at inner radii is revealed clearly by azimuthal-average radial and azimuthal velocities (Figure 2.7). This average removes uniform flow across or symmetrically past the seamount and only net flow directed radially or azimuthally survives. Bottom-intensified clockwise azimuthal flow reaches 4 – 5cm/s on the terrace, falling off with radius over a few kilometers and with height off the seamount over about 100 m. Though not a strong signal, there is weak radially outward flow in the outermost radial bin. Outward flow is seen in current meter data at Cobb (Freeland 1994) and at Fieberling Guyot (Eriksen 1995, Brink 1995), and is qualitatively consistent with Eulerian-mean wave-induced radial-vertical circulation patterns (Figure 3.21, Haidvogel et al. 1993).

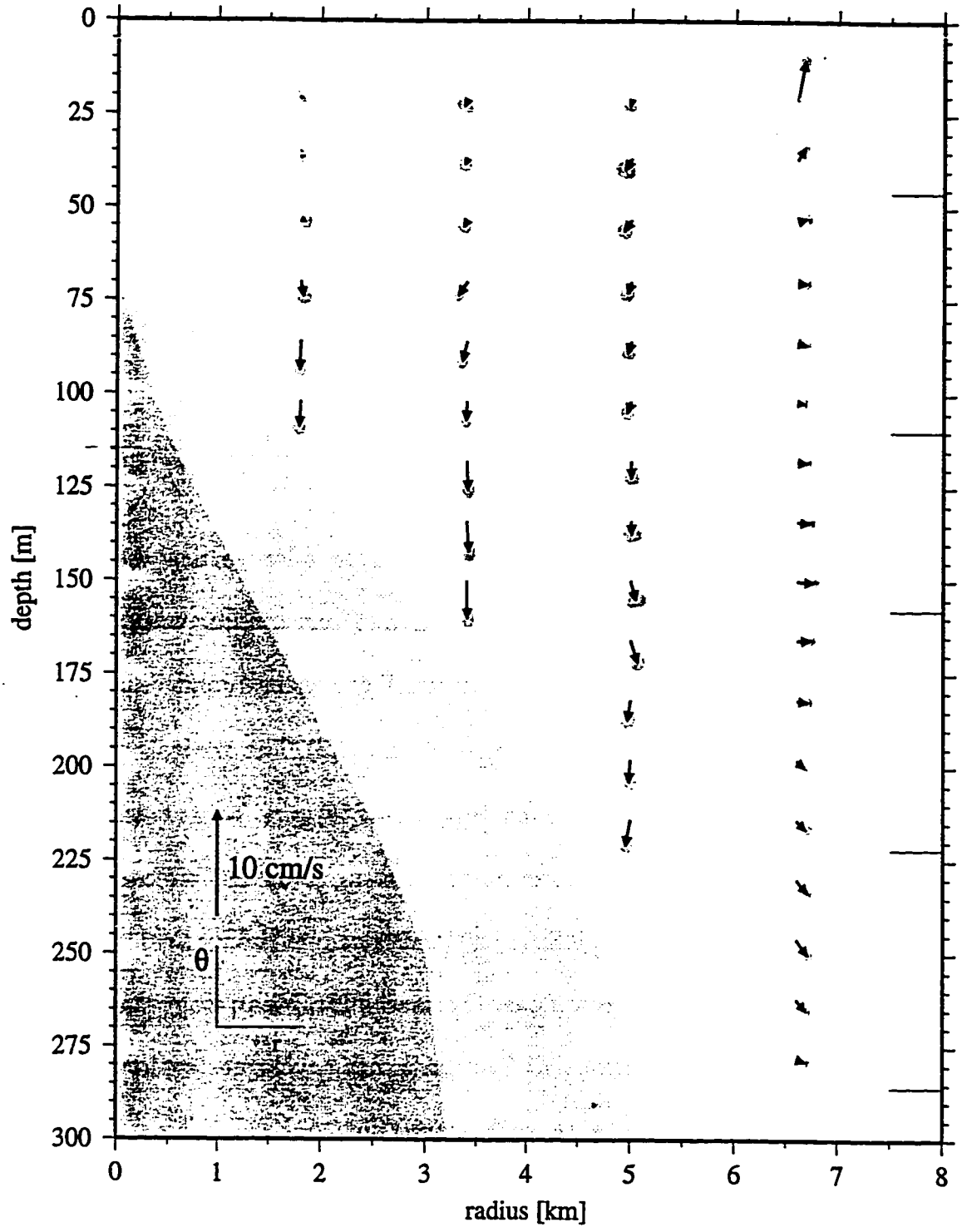

Figure 2.7. Azimuthal-average *radial* and *azimuthal* currents of Figure 2.6 in radial-vertical plane east of seamount center. Clockwise flow (downward vectors) reaches 4 – 5cm/s at depth on the terrace.

The complementary azimuthal average of east and north velocities, that preserves net currents directly across or symmetrically past the seamount, shows east-northeastward flow (Figure 2.8). It is nearly uniform with radius and has magnitude 8cm/s decreasing with depth below about 125 m to 3cm/s at 275 m. Total mean flow (Figure 2.6) can largely be considered a superposition of the clockwise flow of Figure 2.7 on the background current of Figure 2.8 moving over the seamount and past its sides.

2.3.b. Mean density anomaly

In this section, we use CTD data to calculate mean vertical displacement of isopycnals above the seamount relative to surrounding water and test whether the density anomaly is consistent with cyclogeostrophic balance of the measured clockwise mean circulation (Figure 2.7). The analysis presumes the density field associated with background flow (Figure 2.8) is broader than the seamount and is removed in forming an ensemble mean from casts over and away from the seamount. This is justified based on the vertical shear and horizontal scale of mean currents past the seamount. Mean isopycnal uplift, and the associated mean azimuthal flow presuming cyclogeostrophic balance, are both calculated relative to the background flow.

We analyze CTD data from an August 1991 C. S. S. Parizeau survey and an October 1991 R/V T. G. Thompson survey, referred to as AUG and OCT respectively (Figure 2.9). Horizontal spatial resolution of the time-mean den-

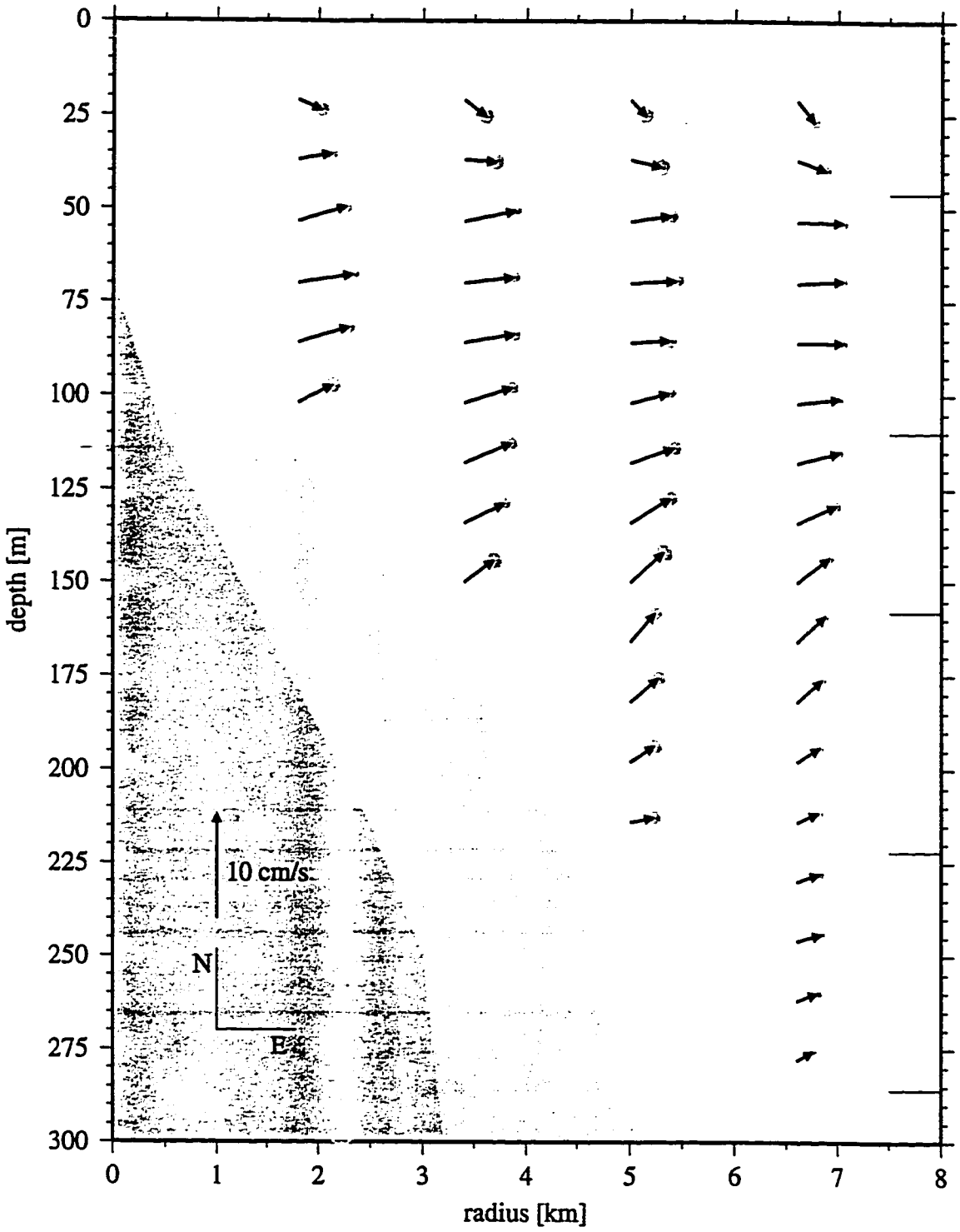

Figure 2.8. Azimuthal-average *east* and *north* currents of Figure 2.6 in the radial-vertical plane east of seamount center. Rightward (upward) vectors represent eastward (northward) flow.

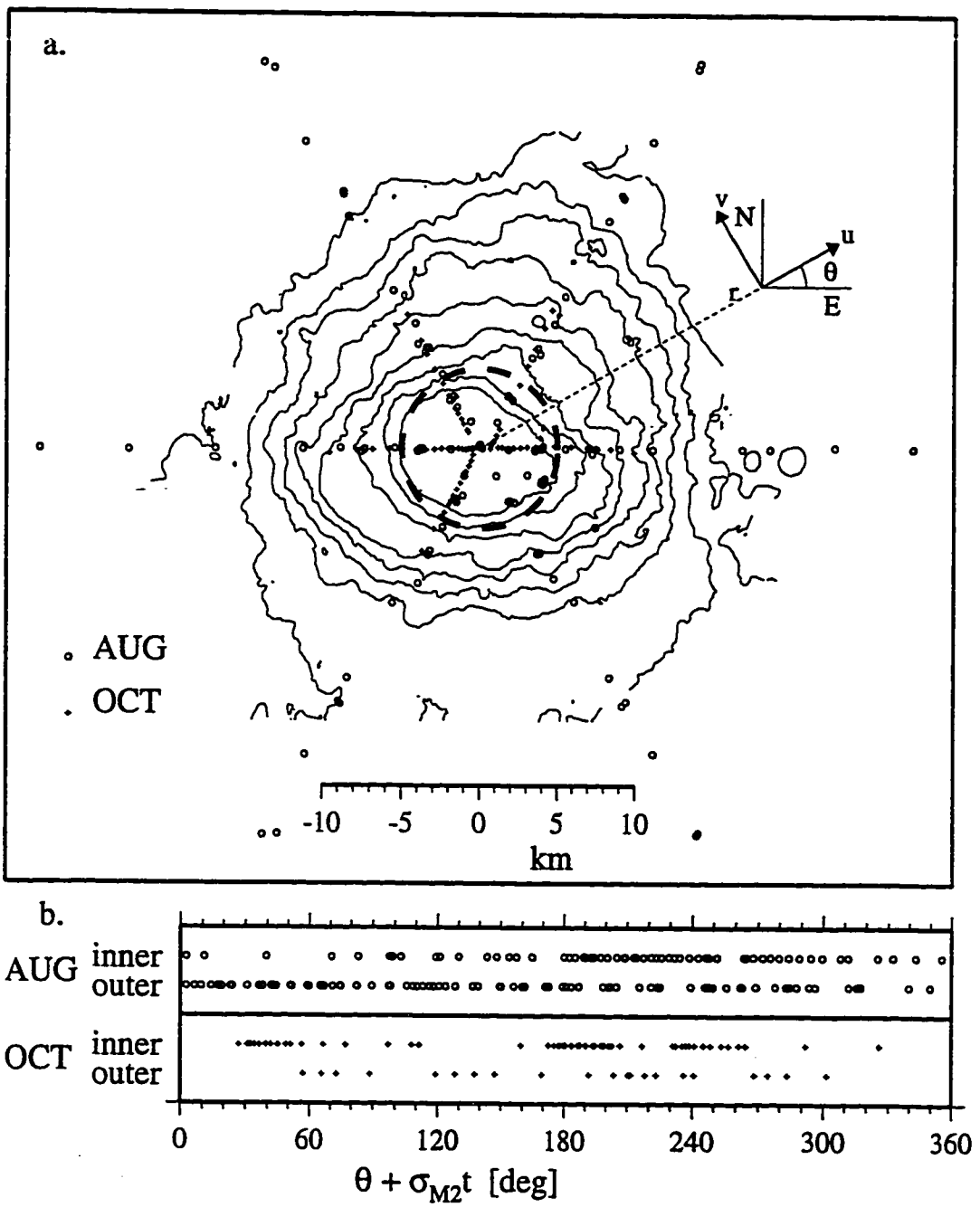

Figure 2.9. CTD data from C.S.S. Parizeau survey (AUG) and R/V Thompson survey (OCT). (a) Spatial sampling: plan view of casts with 5-km boundary between inner and outer radial regions marked. Isobaths 300 to 3000 m by 300 m. (b) Temporal sampling: phases of a first azimuthal wavenumber semidiurnal signal (see text).

sity field is limited to a difference between inner and outer radial regions, due to the dominant amplitude of higher-frequency perturbations and the irregular sampling distribution in time and space. The boundary between inner and outer radii is set arbitrarily at 5km, with conclusions unchanged using 4 or 6km. Semidiurnal tides are expected to dominate time-dependent density perturbations, since both near-inertial motions and subinertial trapped waves that appear to account for diurnal energy (Section 2.4) have weak vertical displacements. Open-ocean tidal currents are broader than the seamount and excite the first azimuthal wavenumber (Chapter 3), that has upward and downward displacements on opposite sides of the seamount. Temporal sampling of the phase of this signal, $\theta + \sigma_{M_2} t$ where σ_{M_2} is M_2 tidal frequency and t time from an arbitrary reference, is adequate to reduce aliasing in forming a time mean (Figure 2.9b). Data analysis is explained in Appendix B.

Ensemble-average potential density $\overline{\sigma_\theta}$ reveals the permanent halocline below about 80 m depth, and seasonal thermocline stratification (mixed layer with stratified base) during the AUG (OCT) survey at shallower depths (Figure 2.10a). At all radii sampled, rms vertical displacements η_{rms} (Appendix B) have magnitude 4-8 m, in reasonable agreement with the Garrett-Munk (GM) internal wave model (Munk 1981) except for increases at terrace depths (Figure 2.10b). Following the reasoning above, enhancement is likely

due to semidiurnal tides that are not included in GM. Limited sampling hinders further conclusions about higher-frequency displacements.

There is $2-4$ m upward survey-mean isopycnal displacement $\Delta Z(z)$ (positive upward) above the seamount relative to the surrounding ocean (Figure 2.10c), where $\Delta Z(z) = \langle Z \rangle_{\text{inner}} - \langle Z \rangle_{\text{outer}}$ for Z the negative vertical coordinate of an isopycnal (Appendix B). This signal is nonzero by one to two standard errors, though smaller than rms time-dependent displacements (Figure 2.10b). Mean potential density anomaly $\Delta\sigma_\theta(z) = \langle \sigma_\theta \rangle_{\text{inner}} - \langle \sigma_\theta \rangle_{\text{outer}}$ (excess density positive) relative to the surrounding ocean is

$$\Delta\sigma_\theta(z) = \frac{\rho_o}{g} N^2(z)\,\Delta Z(z)\,, \tag{2.2}$$

where ρ_o is a constant reference density, g is gravitational acceleration, and $N^2 = \frac{-g}{\rho_o}\frac{d\overline{\sigma_\theta}}{dz}$ (shown in Figure 2.1c for OCT).

The mean density anomaly implies an azimuthal current $V(r,z)$ by cyclogeostrophic balance, the thermal wind relation in cylindrical coordinates

$$\begin{aligned} -\frac{V^2}{r} - fV &= -P_r \\ 0 &= -P_z + B, \end{aligned} \tag{2.3}$$

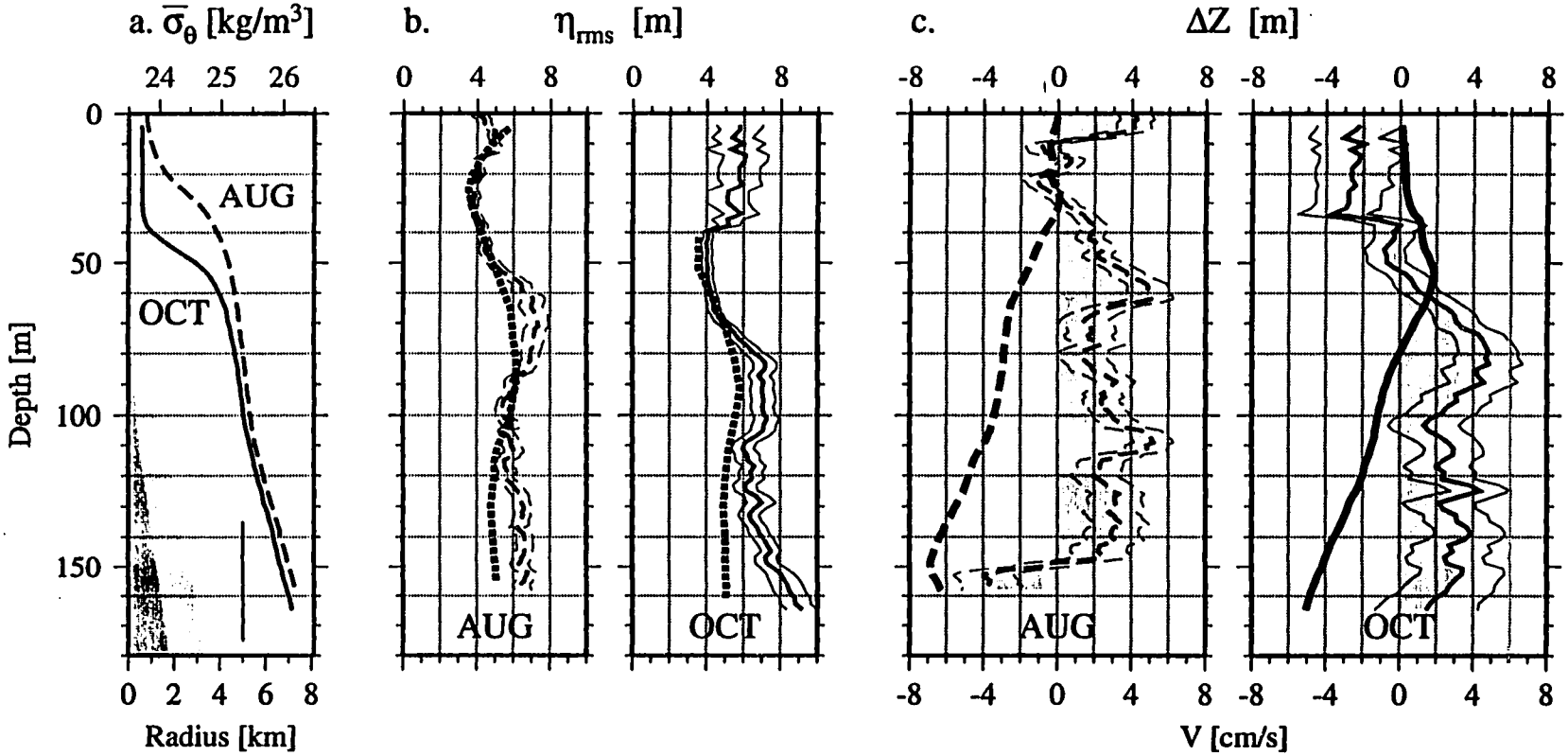

Figure 2.10. (a) Survey-average potential density structure, upper-axis scale. Minimum and maximum bathymetric profiles with vertical line dividing inner and outer regions, lower-axis scale. (b) Rms vertical displacement from casts at all radii, one standard error shown, compared to GM (dotted). (c) Survey-mean isopycnal displacement ΔZ (positive upward) within 5km of seamount center, one standard error shown, upper-axis scale. Azimuthal velocity V relative to surface (bold, lower-axis scale), calculated from ΔZ and N (2.4), is increasingly clockwise with depth.

where $B = -g\sigma_\theta/\rho_o$ is mean buoyancy anomaly and P is mean anomaly of reduced pressure (pressure/ρ_o). Cross-differentiating (2.3) radially and vertically, using (2.2), and neglecting metric term $-V^2/r$ because for $V = 10$cm/s and $r = 5$km its largest fraction $V/(rf)$ of the Coriolis term is 0.25, yields

$$\frac{dV}{dz} = \frac{N^2 \Delta Z}{f \Delta r.} \tag{2.4}$$

This is thermal wind with finite-difference radial derivative. Azimuthal current V relative to the surface is calculated by integrating (2.4) downward using measured ΔZ and N^2 with $\Delta r = 5$km.

Azimuthal current (2.4) implied by thermal wind balance with the mean density anomaly is increasingly clockwise with depth and reaches magnitude 7cm/s and 5cm/s during AUG and OCT respectively (Figure 2.10c). This magnitude agrees with the measured azimuthal current (Figure 2.7) although it is set largely by Δr (2.4), chosen to be 5km as appropriate to first-difference across inner and outer regions divided at $r = 5$km. Regardless of Δr the azimuthal current implied by thermal wind agrees with the ADCP measurements in its clockwise sense and bottom-intensified structure.

Assuming cyclogeostrophic balance (2.3) with an analytic mean azimuthal flow $V(r, z)$ ((4.3), Figure 2.11a) based on the clockwise component of

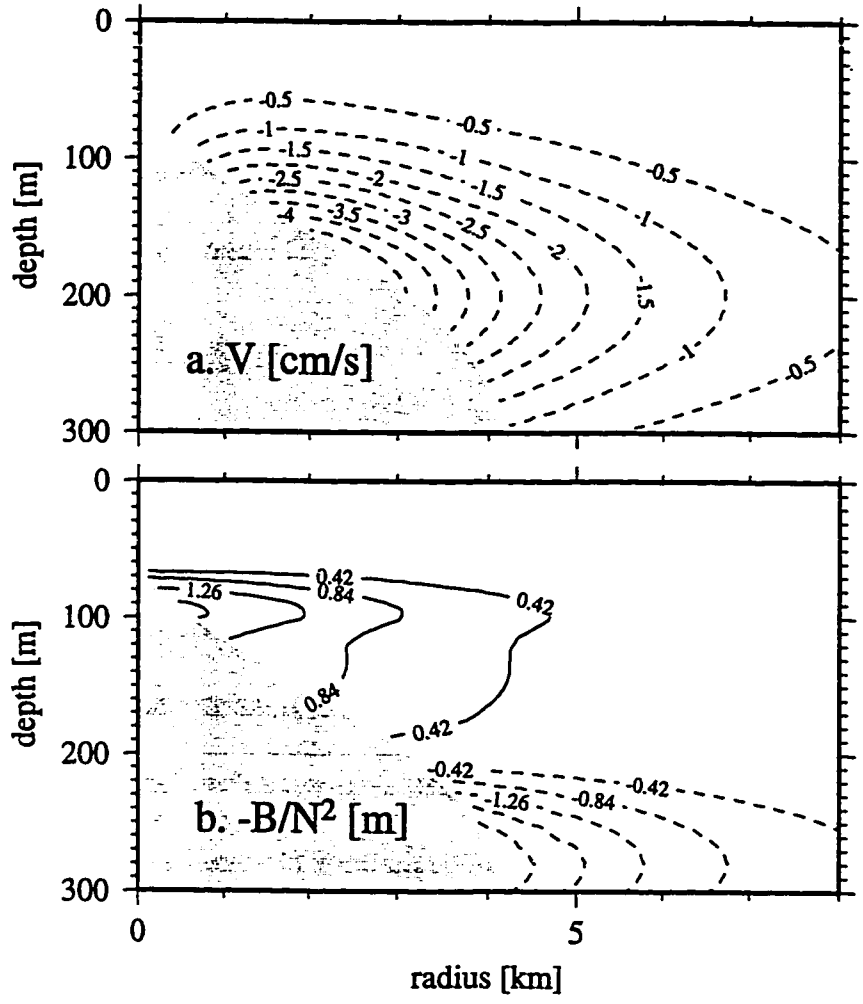

Figure 2.11. (a) Mean azimuthal current V based on clockwise component of ADCP flow (Figure 2.7): analytic form (4.3) for V_i = –5cm/s, R_i = 3km, Z_i = 90 m, and z_i = –200 m. (b) Cyclogeostrophic vertical displacement (2.3) due to (a) for measured $N^2(z)$ of Figure 2.1c.

the measured ADCP velocities (Figure 2.7), the mean vertical displacement $-B(r,z)/N^2(z)$ (Figure 2.11b, positive upward) is consistent with ΔZ of the CTD measurements. Shallower than 200 m $-B/N^2$ is upward within radius 5km, and reaches 1.75 m, within a standard error of the CTD data (Figure

2.10c). Figure 2.11a is an analytic function $V(r,z)$ (4.3) chosen to be qualitatively consistent with the measured mean clockwise current (Figure 2.7), a flow that is concentrated deeper than about 75 m within about 6km radius reaching maximum near radius 3km. Figure 2.11b uses $B_r = (f+2V/r)V_z$ (from (2.3)) integrated radially inward, and measured $N^2(z)$ (Figure 2.1c).

2.3.c. Discussion

ADCP measurements identify a broad mean east-northeastward current across the seamount and clockwise circulation at depth on the terrace (Figures 2.6, 2.7, and 2.8). CTD data reveals a mean density anomaly consistent with cyclogeostrophic balance of the clockwise circulation (Figures 2.10 and 2.11). At the rim depth and below, incident flow splits to move past the seamount. On the northeast (downstream) side currents appear to diverge. This section discusses these features in the context of dynamical models.

Vortex stretching by incident flow (Hogg 1973, Chapman and Haidvogel 1992) and rectification of oscillatory currents (Maas and Zimmerman 1989, Haidvogel et al. 1993) both produce bottom-intensified clockwise currents around a northern hemisphere seamount in a stratified ocean. Limited application of these theories at tall seamounts in strong stratification with strong frictional influence, as characterizes flow at Cobb Seamount, hinders assessment of the mechanism responsible for observed clockwise currents.

The clockwise component of the mean flow measured (Figure 2.6) is marginally strong enough, relative to the broad current across the seamount, to cause a recirculating region of fluid atop the seamount isolated from the incident flow. In inviscid-limit steady solutions for uniform flow past a perturbation-height seamount in a uniformly rotating and uniformly stratified ocean, clockwise circulation occurs atop the seamount in a balance between advection of relative vorticity and anticyclonic vorticity production by topographic vortex stretching (Hogg 1973). This strengthens (weakens) the incident flow on the left (right) side of the seamount viewed from upstream. When this circulation exceeds the incident flow strength a Taylor cap forms, a region of fluid isolated from the incident flow that may be recirculating or stagnant as determined by time-dependent establishment of the flow and its frictional influences (Hogg 1973). A Taylor cap forms for blocking parameter $\delta S^{1/2}/Ro = \delta NH/U$ greater than $O(1)$ (Hogg 1980), where δ is the fraction of depth H the seamount occupies, $S = \left(\frac{NH}{fL}\right)^2$ is the Burger number, and $Ro = U/(fL)$ is the Rossby number of incident flow of strength U. A Taylor cap is broadest at the bottom, extends vertically a fraction of fL/N that increases with blocking parameter (Huppert 1975), and in moderate stratification is nearly centered on the seamount (Chapman and Haidvogel 1992).

Comparison of flow at Cobb to Taylor cap theory is problematic, but blocking parameter estimates exceed 25 so Taylor cap formation cannot be

dismissed. Elevated levels of turbulence at Cobb (Mudge 1994) may make comparisons to inviscid Taylor cap formation inappropriate. Chapman and Haidvogel (1992) model flow at Burger number ≈ 1, showing finite amplitude seamount height to cause Taylor cap formation at slightly higher blocking parameter. Stratification with Burger number significantly exceeding $O(1)$ as characterizes that at Cobb has not been examined. Based on typical values shallower than $H = 300$ m at Cobb of $U = 7$cm/s, $N = 5$cph $= 0.0087$ s^{-1}, and $L = 5$km, or any other appropriate subjectively chosen values, Ro is less than 0.2 and S exceeds 30 so the blocking parameter $\delta S^{1/2}/Ro$ is at least 25. This high blocking parameter suggests inviscid vortex stretching by the current incident on Cobb would cause a Taylor cap. Because its vertical scale would be $fL/N \approx 50 - 100$ m it is possible it exists in the deepest 50 m, outside ADCP coverage. Bathymetric asymmetry causes terrace depth variation $50 - 100$ m azimuthally (e.g. Figure 2.7) and may alter the dynamics in the deepest 50 m.

The clockwise mean flow observed occurs at radii and depths coincident with amplified diurnal tidal currents (Section 2.4), suggesting rectifying oscillations may be an important driving mechanism. Theoretical (Maas and Zimmerman 1989), numerical (Haidvogel et al. 1993), and laboratory (Zhang and Boyer 1993, Codiga 1993) examples of rectified currents are bottom-trapped with flow along isobaths having shallow water on its right. Mean flow arises in response to purely oscillatory forcing, and does not require azimuthal asym-

metry. Waves transfer energy in to mean flow when nonlinearity, friction, or time-dependent amplitudes violate the non-interaction theorem (Andrews et al. 1987). Friction may be most important at Cobb, where estimated kinetic energy decay timescales are a few days based on turbulent dissipation rates (Mudge 1994, Chapter 1). Beyond noting qualitative similarities with the observed flow, conclusions regarding rectification at Cobb are precluded by the short survey length. Rectification depends strongly on frictional influences and, even with better sampling, an improved knowledge of dissipative mechanisms may be necessary to test theories.

To the extent it is cyclogeostrophic, the measured azimuthal current has negative potential vorticity anomaly and therefore may be more consistent with rectifying oscillations than simple parameterizations of friction acting on a Taylor cap. As shown in Chapter 4, the potential vorticity anomaly is $\delta Q_E^V / \left(fN^2 \right) \equiv \left(Q_E^V - fN^2 \right) / \left(fN^2 \right)$ (4.7) (see Figure 4.3), where to a good approximation Ertel potential vorticity is $Q_E^V \approx (f+\zeta)\left(N^2 + B_z \right)$ (4.6), $\zeta = \frac{1}{r}(rV)_r$ is the vertical component of vorticity, and N^2 ($N^2 + B_z$) is the far-field (near-summit) stratification profile. Clockwise circulation excited through inviscid vortex stretching of horizontally uniform incident mean flow conserves potential vorticity (Hogg 1973). Atop the seamount it has no potential vorticity anomaly as a result of compensation between negative ζ and

positive B_z of the bottom-intensified mean buoyancy anomaly. A Taylor cap is a closed circulation excited in this manner that will develop positive (negative) potential vorticity anomaly under dissipative influences if they reduce the vorticity anomaly more strongly (weakly) than the buoyancy anomaly. Cyclogeostrophic mean flow induced by waves (Chapter 3) has negative potential vorticity anomaly, as measurements from Cobb Seamount (Figure 2.11) and Fieberling Guyot (Kunze and Toole 1996) imply.

Deeper than the terrace, observed flow past the sides of the seamount is consistent with currents past an island. Vertical excursions are inhibited by stratification. For parameters appropriate to flow at Cobb the behavior of an inviscid layer model for a steady current past an island (Gordon and Hughes 1981) is near to symmetric potential flow splitting to move around the island.

Flow in the downstream (northeast) section of the survey is northward on the northern side and southward on the eastern side, evidence that streamlines do not straighten to uniform flow as in steady inviscid-limit solutions. Incident-flow models that include time-dependence (Huppert and Bryan 1976) or the effect of Ekman suction (Foster et al. 1990) show flow separation and wake development downstream. In the initial-value problem this is because, in addition to anticyclonic vorticity generated in fluid advected on to the seamount, fluid advected off the seamount gains cyclonic vorticity that can corotate with the anticyclone, remain trapped behind it, or be shed downstream depending on the start-up timescale (Thompson 1990, Schar and Davies

1988). For steady incident flow, laboratory experiments (Boyer et al. 1987) reveal a variety of eddy shedding and wake behaviors controlled strongly by the Reynolds number. Interpretation of downstream flow at Cobb in terms of models is not possible due to poor knowledge of dissipative processes acting on low frequency flow and the limited coverage and short duration of the survey.

2.4. Subinertial energy

2.4.a. Observed diurnal current ellipses

Diurnal ($\sigma = 0.69f$) energy in the harmonic fit to ADCP velocities (Section 2.2) projects on to azimuthal wavenumber $n = -1$ with current ellipse structure shown in Figure 2.12. Each bin of the radial-vertical plane east of the seamount shows the measured horizontal current ellipse corresponding to bold ellipses in the middle column of Figure 2.3 and representing the $n = -1$ harmonic azimuthal structure shown there. Confidence intervals on ellipse axes lengths and ellipse orientation angle, at 67% significance from the bootstrap method (Section 2.2), are shown respectively as dotted lines at the end of each axis and dotted ticks outside the ellipse directed from the ellipse center. Rotation direction is marked at each vector head, bold if significant.

A region of amplified currents extends away from the seamount terrace a few kilometers radially and about 100 m vertically. Rms current-ellipse major and minor axes lengths reach 10.8 cm/s, amplified 5.3 times over that of

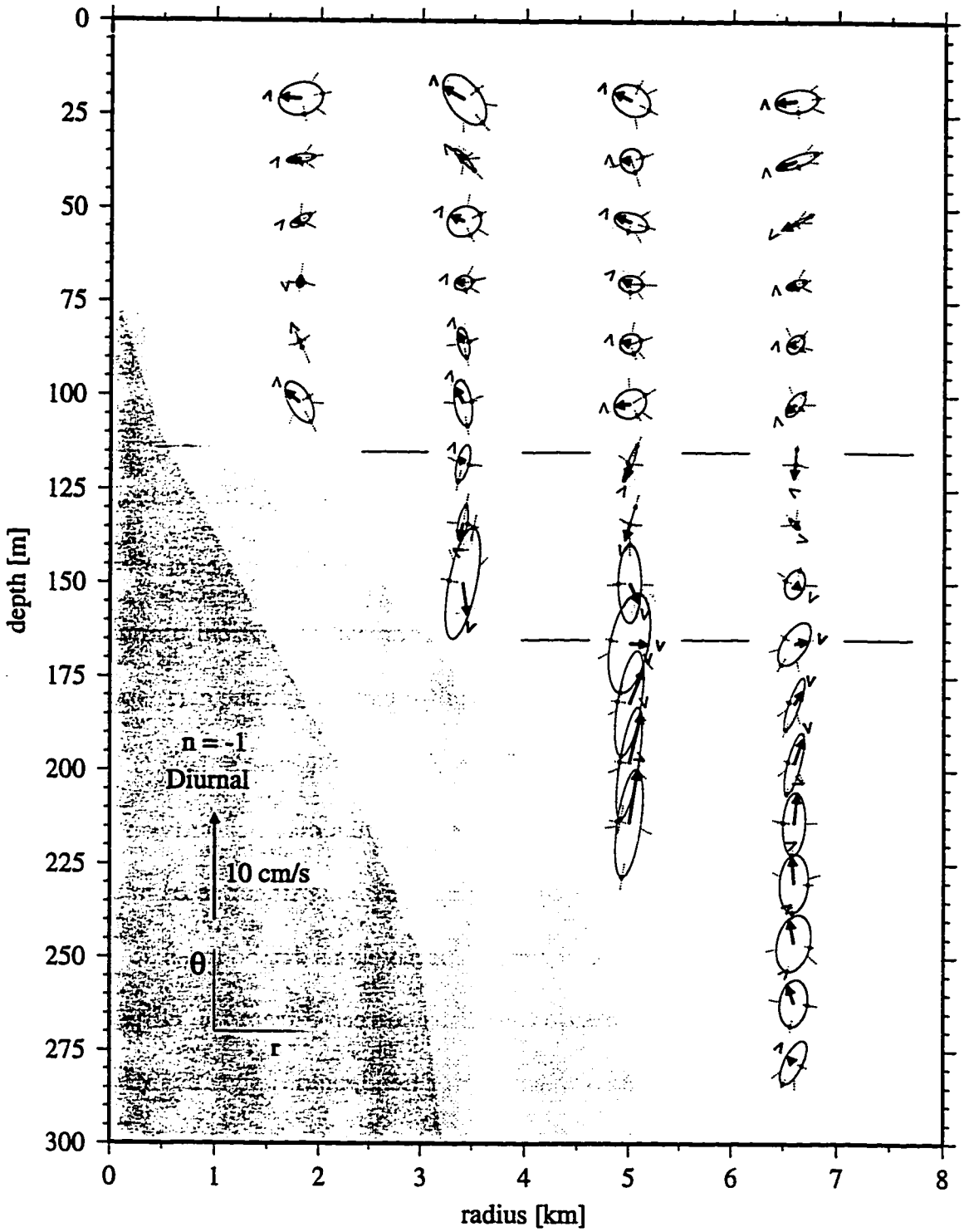

Figure 2.12. (a) Diurnal (σ = 0.69f) n = –1 azimuthal wavenumber (bold ellipses, middle column, Figure 2.3) ADCP current ellipses at yearday 292.0, 1991. Radial (azimuthal) flow rightward (upward).

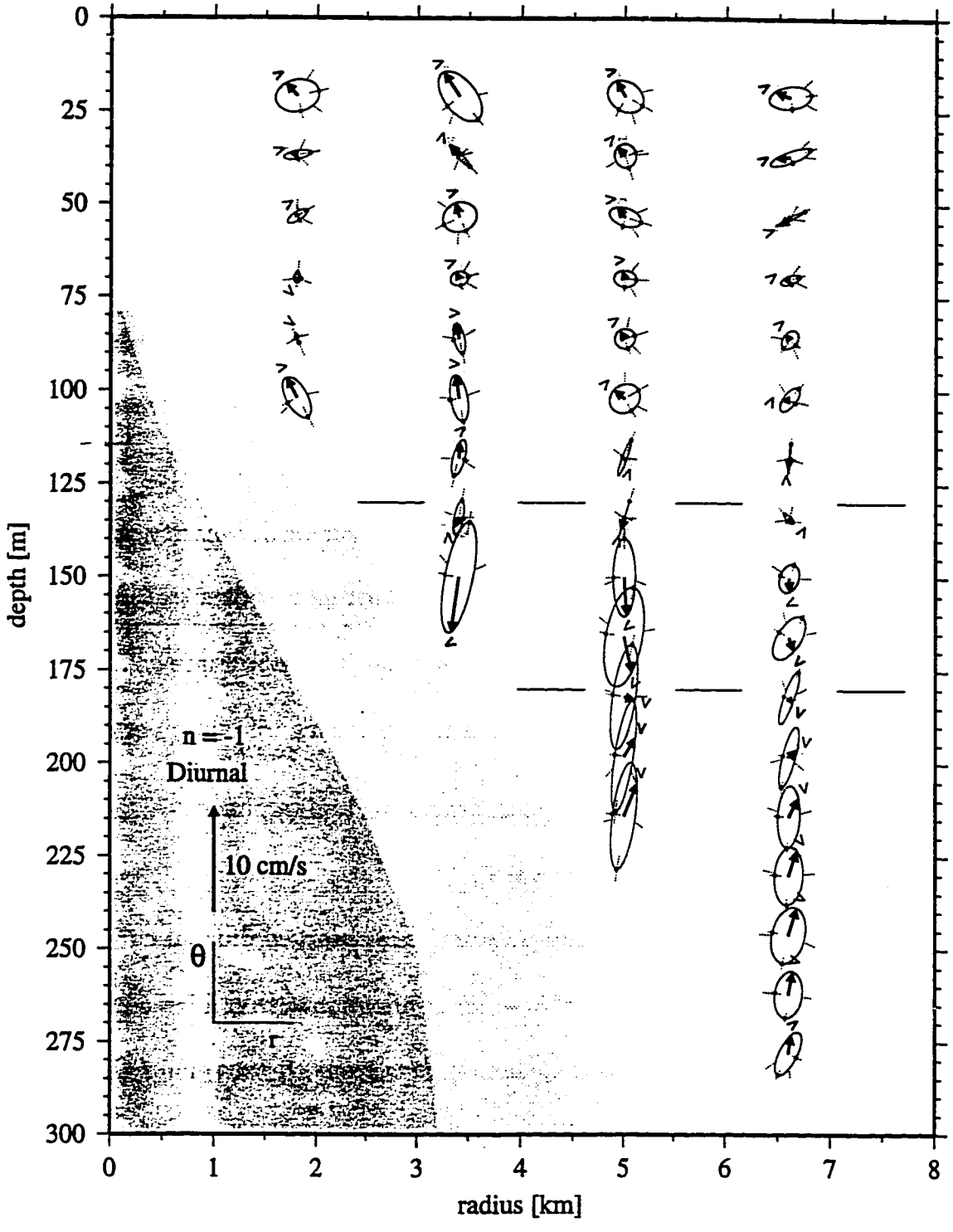

Figure 2.12. (b) Same as (a) one-eighth of a wave period later. Regions of concentrated anticlockwise turning with depth (dashed lines) are 15 m deeper, indicating downward phase propagation.

the K_1 constituent at the location of Cobb Seamount in a 1° resolution empirical-numerical global tide model using TOPEX altimetry (Egbert et al. 1994).

Where amplified most strongly, currents rotate clockwise in time tracing out ellipses elongated azimuthally with axes inclined to radial/azimuthal coordinate axes so radial and azimuthal currents are positively correlated, $\overline{uv} > 0$ (the sense shown in Figure 2.3d). Elongation of current ellipses azimuthally is consistent with moored current meter spectra having azimuthal energy exceeding radial (Figure 2.2).

In the bottom-trapped region of amplified currents, velocity at any instant turns anticlockwise with depth. This turning is concentrated near 115 m and 165 m deep (dashed lines) at the time shown in Figure 2.12a. Downward phase propagation is evident in the downward motion of depth intervals of concentrated turning (Figure 2.12b), and in phases Φ^u and Φ^v (2.1) (not shown) that increase upward.

In summary, dominant characteristics of observed diurnal currents are energy in azimuthal harmonic $n = -1$; amplification within a few km radially and about 100 m vertically of the seamount; current ellipses elongated azimuthally; clockwise rotation in time; radial and azimuthal velocities positively correlated, $\overline{uv} > 0$; anticlockwise turning with depth at any instant; and downward phase propagation. The next section demonstrates that a forced damped stratified seamount-trapped wave exhibits all of these features.

2.4.b. Stratified seamount-trapped waves

Both the subinertial frequency and bottom-intensification of amplified diurnal tidal currents (Figure 2.12) suggest they obey trapped-wave dynamics. This section demonstrates strong similarity of the measurements to a forced damped stratified seamount-trapped wave in mean flow (Chapter 3, Chapter 4), using wave solutions for measured topographic and stratification profiles (Figure 2.1b,c). Reference is made to the physics of stratified seamount-trapped waves, and modifications due to friction and mean flow, that are explained in detail in Chapter 3 and Chapter 4.

Diurnal energy observed dominantly in azimuthal wavenumber $n = -1$ is consistent with excitation by broad open-ocean tidal currents interacting with the seamount. Tidal currents broader than the seamount project on to $n = \pm 1$, and response to clockwise-rotating far-field currents ($n = -1$) is preferentially amplified because free waves only propagate clockwise ($n < 0$) (Chapman 1989, Brink 1989, 1990, Chapter 3). Excitation of $n = \pm 1$ by broad currents is understood by recognizing these are the only wavenumbers with flow in the same direction on opposite sides of the seamount.

Measured currents are compared to a stationary (steady amplitude in time) forced damped stratified seamount-trapped wave in the presence of a mean azimuthal current, because (i) tidal forcing is periodic, (ii) elevated levels of kinetic energy dissipation (Mudge 1994) imply decay times as short as a

few days, and (iii) mean flow strength (Section 2.3) is similar to amplified tidal currents. Damping is parameterized as Rayleigh drag and Newtonian cooling/ heating with 2-day timescales. This is not intended to accurately represent turbulence, but is chosen for its convenience and physically interpretable signature. Though it causes qualitatively similar flow signatures, for simplicity bottom friction is not included; dissipation levels outside the bottom boundary layer exceed those within it (Mudge 1994), suggesting Rayleigh damping is more appropriate. Only the azimuthal component of the mean flow observed (Figure 2.11, based on Figure 2.7) is included in determining the wave solution. Mean flow across the seamount (Figure 2.8) may importantly influence waves, though solutions without it compare well to observed flow.

Forced damped stratified seamount-trapped waves linearized about mean azimuthal flow in a uniformly rotating ocean obey hydrostatic and Boussinesq momentum, buoyancy and continuity equations in cylindrical coordinates (r, θ, z)

$$
\begin{aligned}
u_t + \frac{V}{r}u_\theta - \left(f + \frac{2V}{r}\right)v &= -p_r + F^u - Ru && (a)\\
v_t + \frac{V}{r}v_\theta + wV_z + \left(f + \frac{1}{r}(rV)_r\right)u &= -\frac{1}{r}p_\theta + F^v - Rv && (b)\\
0 &= -p_z + b && (c)\\
b_t + \frac{V}{r}b_\theta + B_r u + \left(N^2 + B_z\right)w &= F^b - Rb && (d)\\
\frac{1}{r}(ru)_r + \frac{1}{r}v_\theta + w_z &= 0\ , && (e)
\end{aligned}
\qquad (2.5)
$$

where (p, u, v, w, b) are reduced pressure, radial, azimuthal, and vertical velocity, and buoyancy perturbations linearized about cyclogeostrophic (2.3) mean components V, B, and P. Boundary conditions

$$\begin{aligned} (p, u, v, w, b) &= (0, u_F, v_F, 0, 0) \quad \text{as} \quad r \to \infty && (a) \\ (p, u, v, w, b) &\quad \text{bounded at} \quad r = 0 && (b) \\ w + h_r u &= 0 \quad \text{at} \quad z = -h && (c) \\ w &= 0 \quad \text{at} \quad z = 0\,. && (d) \end{aligned} \tag{2.6}$$

require wave decay to far-field flow (u_F, v_F) at large radius, disallow singularities at the origin, incorporate the kinematic condition of no flow across the topographic boundary, and impose a rigid lid at the surface. Waves are excited through the condition (2.6)(c) of no flow perpendicular to the sloping bottom, in response to horizontally and vertically uniform clockwise-rotating tidal currents (u_F, v_F) that are horizontal as maintained by body forces $\left(F^{u,v,b}\right)$ (2.5). Damping is Rayleigh drag (2.5)(a),(b) and Newtonian cooling/heating (2.5)(d) of timescale R^{-1}. Azimuthal wavenumber $n = -1$ waves have (p, u, v, w, b), using u as an example, of form

$$\begin{aligned} u(r, \theta, z, t) &= |\tilde{u}(r, z)| \cos\left[-\theta - \sigma t + \Phi^u(r, z)\right] \\ &= \Re\left\{\tilde{u}(r, z) \exp\left[i(-\theta - \sigma t)\right]\right\} \end{aligned} \tag{2.7}$$

where $\tilde{u}(r,z)$ is the modal structure function (complex if $R \neq 0$) and $\Phi^u(r,z)$ is phase (see (2.1)). Appendix C explains the solution technique.

Wave solutions are calculated for a circularly symmetric seamount with azimuthal-average Cobb Seamount bathymetric profile (Figure 2.1b), and depth-varying stratification from ensemble-mean October 1991 CTD casts (Figure 2.1c). Conclusions drawn are unchanged by (i) off-seamount depth differing from 2750 m (Figure 2.1b) by up to 200 m, since energy is concentrated at shallow depths with significant stratification, or (ii) bathymetric profile narrower or broader within minimum and maximum profiles defined by azimuthal asymmetry of the seamount (Figure 2.1b). Stratification in the upper 50 m has almost no effect on the bottom-intensified waves, so N at the mixed layer base is used within the mixed layer to reduce the numerical resolution required. Deeper than 300 m, N^2 values are taken to decay exponentially through that measured 1500 m deep by Levine et al. (1986).

2.4.b.i.Inviscid wave, no mean flow

For measured bathymetry (Figure 2.1b) and stratification (Figure 2.1c) at Cobb Seamount, inviscid $n = -1$ stratified seamount-trapped waves without mean flow occur at resonant frequencies $\sigma/f = 0.92, 0.86, 0.70, 0.61, 0.53$, ..., each a higher radial-vertical mode. These are solutions to (3.1) and (3.2), the inviscid ($R = 0$) and unforced ($F^{u,v,b} = 0$) subset of (2.5) and (2.6) linear-

ized without mean flow ($V = 0$), as Section 3.2 discusses. The highest-frequency, "gravest" subinertial mode has simplest radial-vertical structure and higher modes have decreasing frequencies and spatial scales (Brink 1989).

Diurnal ($\sigma_{K_1}/f = 0.69$) currents are within $0.01f$ of the resonant frequency $\sigma/f = 0.70$ for the 3rd-gravest $n = -1$ radial-vertical mode, so it is expected to dominate the response and is compared to observed currents. Wave solutions have amplified response to forcing in a frequency range about $0.05f$ wide near resonances (see Figure 3.12). This width is set by forced, inviscid behavior. Friction reduces the peak height but has minimal effect on its width (Section 3.4.b). The frequency shift by mean azimuthal flow of Figure 2.11 is less than $0.01f$, as will be discussed in Section 2.4.b.iii.

In the inviscid wave with no mean flow, amplified current ellipses elongated in the azimuthal direction occur within a few km radially and about 100 m vertically of the seamount terrace (Figure 2.13). Current ellipses are shown at arbitrary amplitude and phase to facilitate comparison to the measurements. Relatively stronger (weaker) currents outside (within) narrow depth intervals at about 75, 100, and 160 m deep rotate clockwise (anticlockwise) in time, as characterizes standing-wave radial and vertical structure in free waves (Section 3.2). Clockwise rotation in time occurs in relatively larger regions because of stratification (see Figures 3.2 and 3.6). Stratification limits vertical displacements $-b/N^2$ to at most 2 m (not shown). Continuous turn-

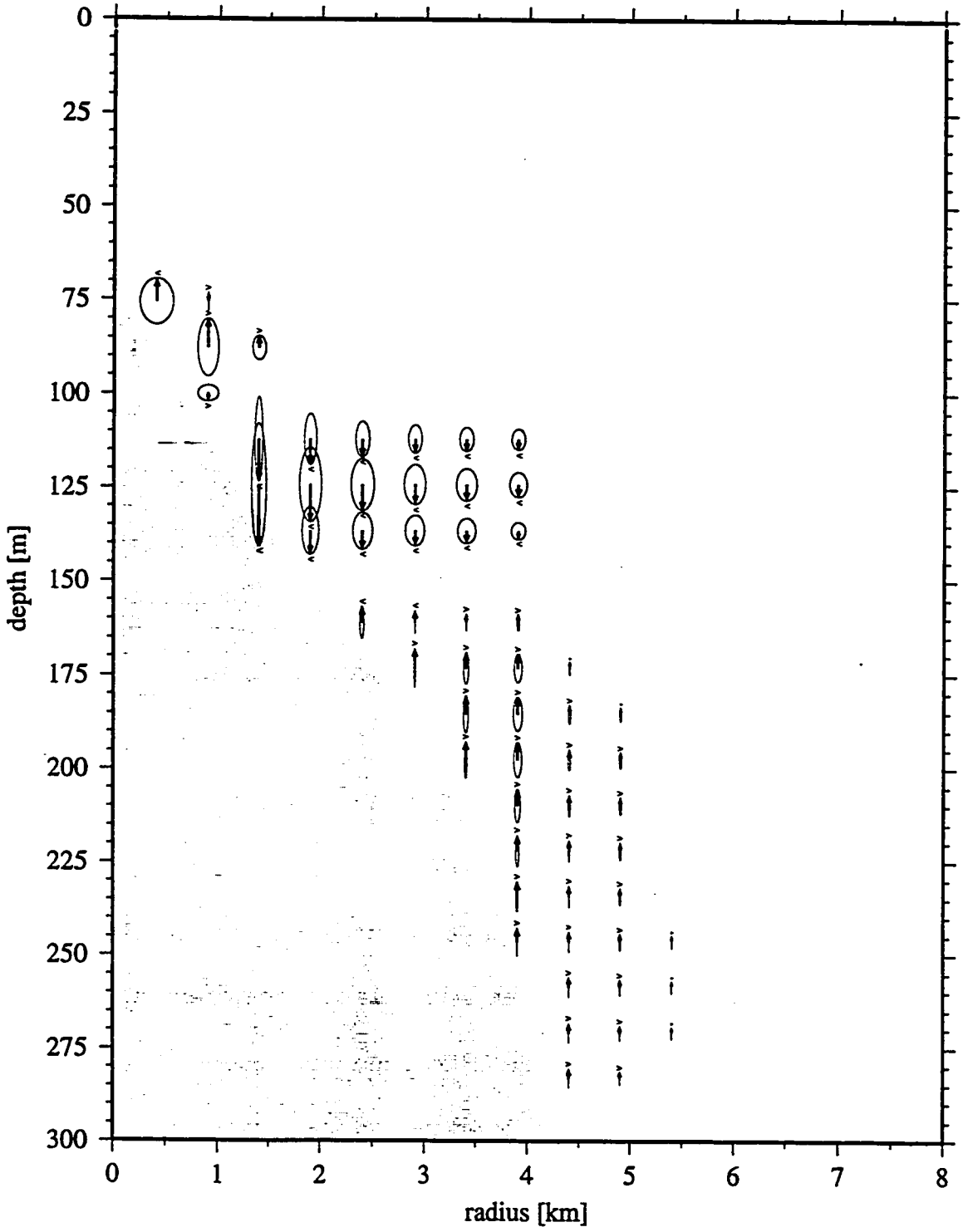

Figure 2.13. Azimuthal wavenumber $n = -1$ inviscid 3rd-gravest stratified seamount-trapped wave ($\sigma = 0.70f$) for Cobb Seamount bathymetry and stratification, no mean flow. As Figure 2.12; see text.

ing with depth of the horizontal velocity vector does not occur at the time shown in Figure 2.13, but anticlockwise and clockwise turning occurs alternately in successive quarters of a wave period (see Figure 3.5), an attribute of the standing-wave vertical structure. Section 3.3 discusses these physics in terms of superposed upgoing and downgoing stratified slope-Kelvin waves.

2.4.b.ii.Forced damped wave, no mean flow

For the same wave maintained at constant amplitude in a forced and damped state (Figure 2.14), amplified currents rotate clockwise in time everywhere on the terrace (except within 0.5km of the summit) in ellipses with axes oriented at an angle to circular seamount isobaths such that $\overline{uv} > 0$. Turning of the horizontal velocity vector with depth at any instant is anticlockwise and concentrated at certain depths, for example near 105 and 170 m deep in Figure 2.14. Phase propagation is radially outward and vertically downward (Section 3.4.d.ii, Figure 3.17), causing regions of concentrated anticlockwise turning to move outward and downward in time. Figure 2.14 is a solution at $\sigma = 0.70f$ with $R^{-1} = 2$days to (3.35) and (3.36), the subset of (2.5) and (2.6) without mean flow ($V = 0$) as described in Section 3.4. Nearness to resonance does not change wave structure strongly, though it significantly modifies amplification and phase relative to forcing velocities (Section 3.4, Figure 3.12);

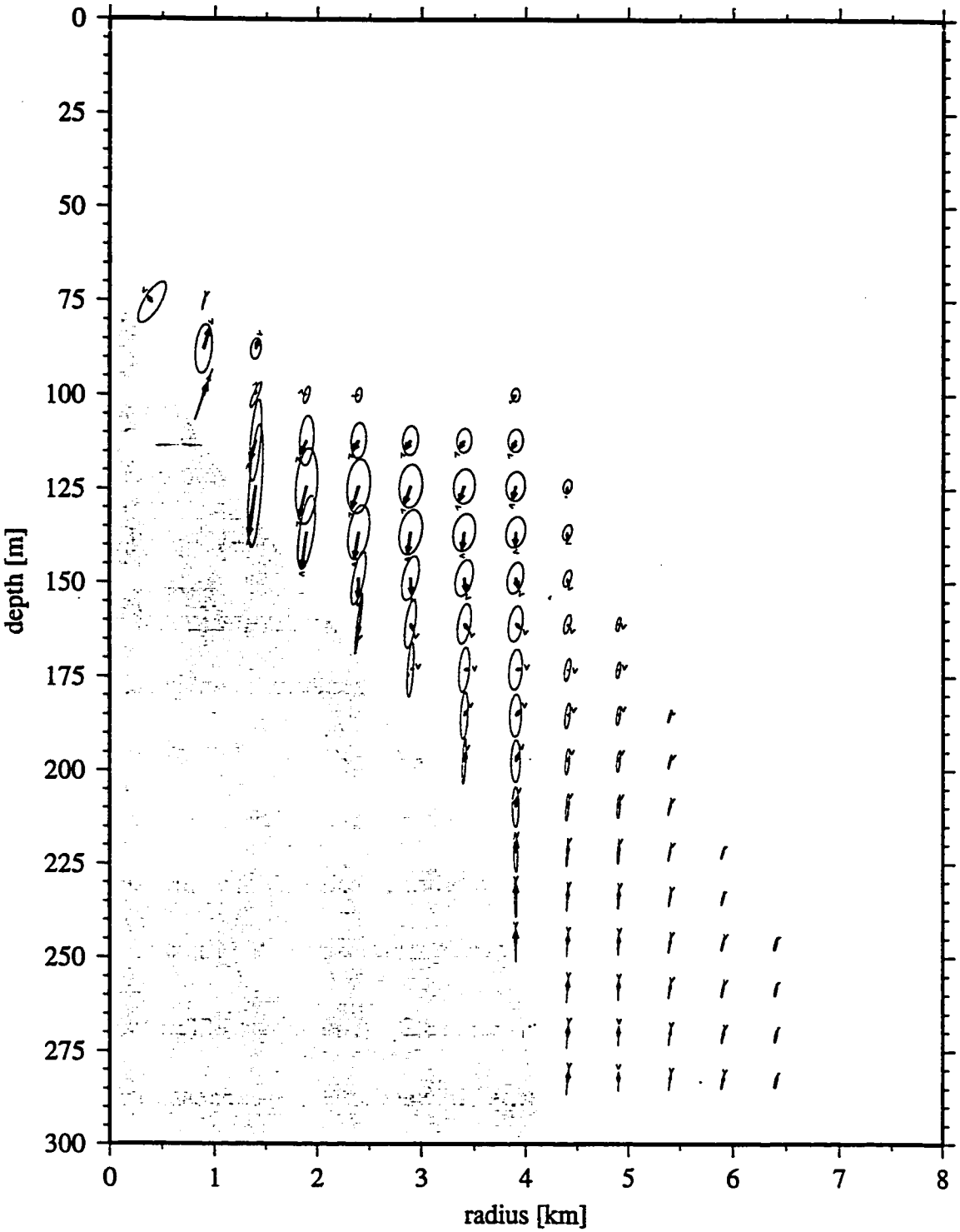

Figure 2.14. As Figure 2.13 but forced damped wave with 2-day frictional timescale. Compare to Figure 2.12. Table 2.2 shows asymmetries due to damping, including anticlockwise turning with depth.

Figure 2.14 is shown at arbitrary amplitude with phase chosen to facilitate comparison of current ellipse diagnostics to measured flow (Figure 2.12).

Asymmetries in the forced damped wave (Figure 2.14) indicate the standing-wave structure of the inviscid wave (Figure 2.13) is disrupted such that energy is transported radially inward and vertically upward to a region at depth near the summit where it is dissipated, as in the example of Section 3.4.d (Figure 3.18). On the terrace, diagnostic signatures of the forced damped wave are downward and outward phase propagation, positive $\overline{uv}$, clockwise rotation in time and anticlockwise turning with depth throughout the wave period (Table 2.2).

2.4.b.iii.Forced damped wave in mean azimuthal current

Chapter 4 discusses how mean currents modify frequency and structure of linear wave perturbations, and can cause critical surfaces for both stratified

Table 2.2. Diagnostic features on terrace in the forced damped wave (Figure 2.14) compared to the inviscid wave (Figure 2.13).

Diagnostic	Inviscid wave	Forced damped wave
phase propagation	azimuthally clockwise only	azimuthally clockwise, radially outward, vertically downward
current ellipse axes	parallel/perpendicular to isobaths, $\overline{uv} = 0$	across isobaths such that $\overline{uv} > 0$
current rotation in time	CW and ACW in alternating regions	CW only
turning with depth of velocity at fixed time	CW and ACW in successive quarter-periods	ACW throughout wave cycle

seamount-trapped waves and internal waves depending on the strength and geometry of the current and the wave frequency. Mean azimuthal current and associated cyclogeostrophic buoyancy (Figure 2.11) based on measured mean flow (Figure 2.7) is not sufficiently strong to cause either type of critical surface at the diurnal frequency at Cobb Seamount (Figure 2.15).

An inviscid wave linearized about azimuthal flow based on mean observed current (Figure 2.11) has resonant frequency increased by $0.003f$, from $\sigma = 0.700f$ to $\sigma = 0.703f$, over the wave with no mean flow. An estimate of the Doppler shift $-V/r$, the azimuthal wavenumber $1/r$ (2.7) dotted with the mean flow, suggests the frequency would increase by a much larger magnitude, at least $0.1f$ for $r < 4\text{km}$. The mean flow potential vorticity gradient acts in opposition to the Doppler shift and is responsible for the weak frequency change, as discussed in Chapter 4.

The effect of the mean flow of Figure 2.11 on the structure of the forced damped wave of Figure 2.14 on the terrace is a nearly undetectable distortion of its spatial scales (Figure 2.16), consistent with the results of Chapter 4 (Figure 4.6). Mean flow changes wave currents far less significantly than damping. Measured diurnal currents are comparable to the mean flow and exceed the linearization about the mean flow required to determine wave solutions. Current ellipses in Figure 2.16 are shown at arbitrary amplitude with phase chosen to facilitate comparison to measured currents (Figure 2.12).

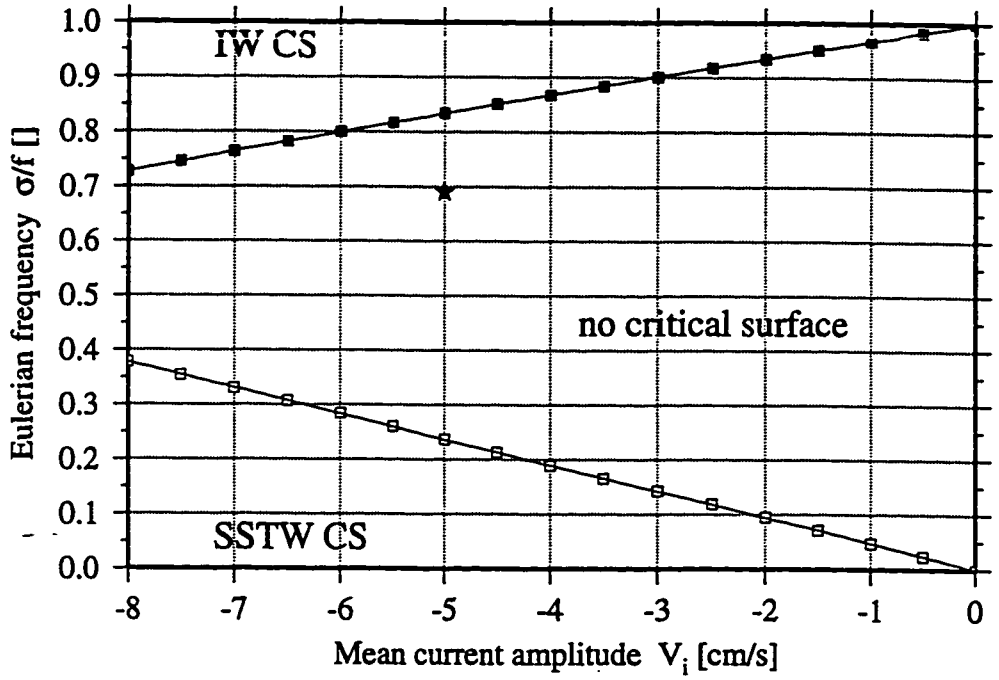

- $\sigma_d = f_{eff}$ Internal wave critical surface forms
- $\sigma_d = 0$ Stratified seamount-trapped wave critical surface forms

Figure 2.15. Critical surface formation in waves on cyclogeostrophic mean current of *shape* in Figure 2.11 at a range of clockwise mean flow *amplitudes* ($V_i < 0$), for Cobb Seamount bathymetry and stratification (Figure 2.1b,c). Section 4.4 defines intrinsic frequency σ_d and f_{eff} explains stratified seamount-trapped wave (SSTW CS) and internal wave (IW CS) critical surfaces. No critical surfaces form (star) for measured mean flow amplitude at the diurnal frequency.

2.4.c. Discussion

Currents at the diurnal frequency $\sigma = 0.69f$ (Figure 2.12) are nearly resonant (within $0.013f$) with the 3rd-gravest wavenumber $n = -1$ subinertial stratified seamount-trapped wave for measured bathymetry, stratification, and azimuthal mean flow at Cobb Seamount (Figure 2.16). Diurnal

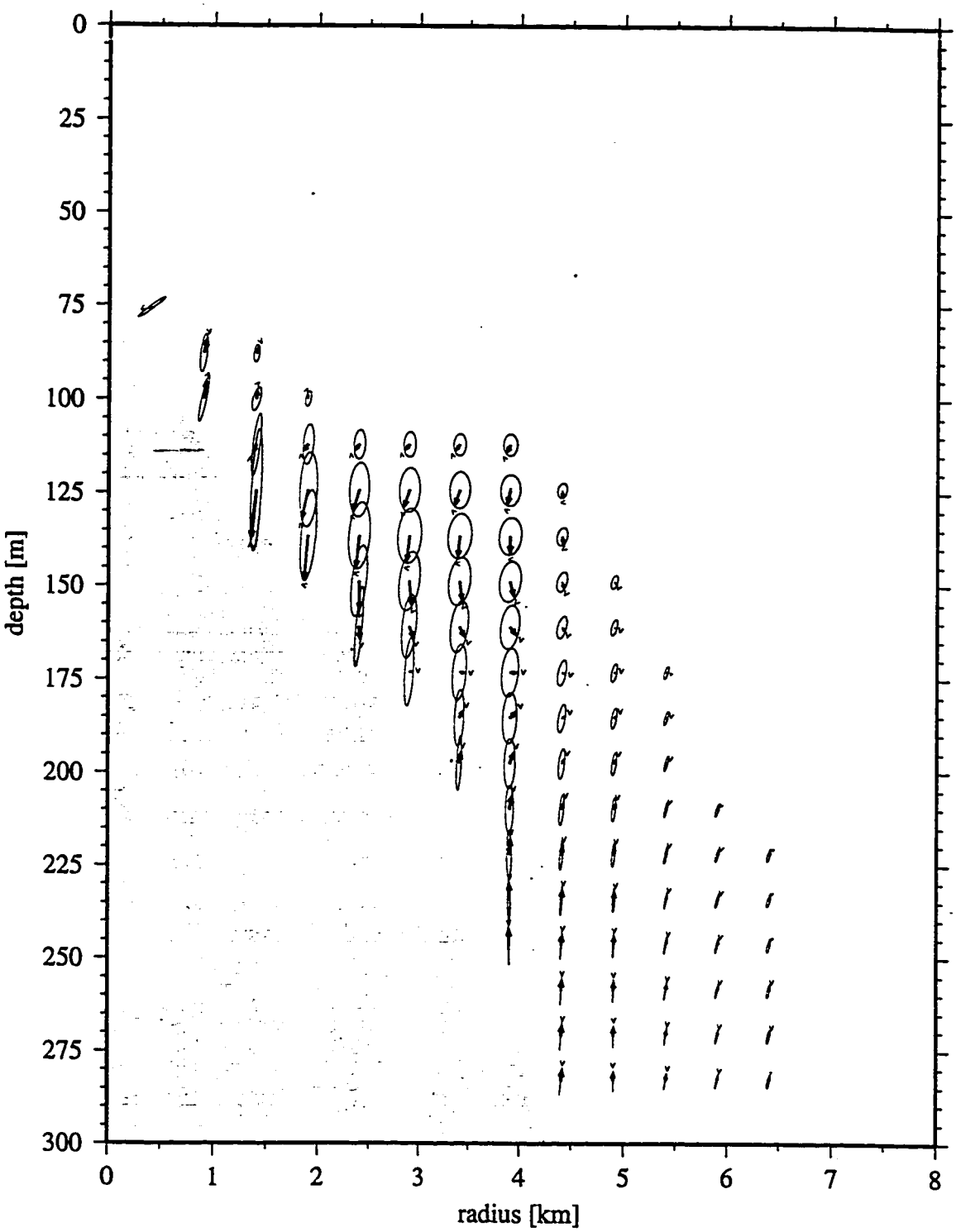

Figure 2.16. Same as Figure 2.15 but in the presence of mean azimuthal current and cyclogeostrophic mean buoyancy of Figure 2.11. Wave structure is changed very little by mean flow.

energy is dominantly in the first azimuthal wavenumber, that most efficiently excited by interaction of open-ocean tidal currents more broad than the seamount with its sloping sides (Section 3.4). Observed currents are amplified within a few km radially and about 100 m vertically of the seamount (Figure 2.12). Observations are best compared to a forced damped wave, because measured dissipation rates (Mudge 1994) give estimated decay timescales of a few days. All current diagnostics agree well with those of the forced damped stratified seamount-trapped wave in mean azimuthal flow (Figure 2.16).

Because several measured current diagnostics do not compare well with the standing-wave radial and vertical structure of an inviscid wave (Figure 2.13), but agree with waves damped on 2-day timescale (Figure 2.14), we conclude dissipation exerts a dominant influence on the response. In forced damped waves incorporating Rayleigh drag with Newtonian cooling and heating, energy is transported radially inward and azimuthally upward toward the summit where it is dissipated (see Figure 3.18). Though the Rayleigh damping is a crude representation of the effects of turbulent dissipation, bottom stress parameterizations have qualitatively similar effects (Brink 1990). It is thus consistent, based on agreement between measurements and wave solutions, to attribute observed diagnostics to dissipative influences.

Azimuthal mean flow present during the October 1991 survey is not strong enough (Figure 2.15) to cause critical surfaces (Section 4.4), and its effect on the wave is much weaker than that of damping (compare Figures

2.16 and 2.14 to Figure 2.13). Mean vorticity (Figure 2.11) consistent with that measured (Figure 2.7) reaches $-0.32f$, yet the influence on subinertial trapped waves is minimal. However, vorticities reported from a different survey to Cobb Seamount reach $-0.5f$ (Freeland 1994), nearly strong enough to cause an internal wave critical surface at the diurnal frequency (Figure 2.15). This suggests a superinertial cap and internal wave critical surface (Section 4.4.b) may form intermittently for diurnal tides at Cobb Seamount.

2.5. Higher frequency motions

This section describes energetic inertial and semidiurnal ($\sigma_{M_2} = 1.32f$) ADCP currents. At these frequencies waves trapped to the sloping bottom (Section 2.4, Chapter 3) occur, since the high-frequency limit $N\sin\left(\tan^{-1}h_r\right)$ (Rhines 1970) based on typical slopes and stratification (Figure 2.1b,c) is $(3-15f) > (f, \sigma_{M_2})$. However, in contrast to subinertial motions (Section 2.4), response to superinertial ($\sigma > f$) forcing need not be trapped to the seamount since internal waves propagate freely in the surrounding ocean. Formation of "leaky modes" (Hendershott 1981) may be expected, with energy partitioned between waves trapped and not trapped to the seamount; distinguishing these is difficult since even a wave that is not trapped, if excited at the seamount, falls off in energy with increasing radius in cylindrical geometry.

Internal waves are excited at near-inertial frequencies ($\sigma = 1.0 - 1.05f$) in the upper few hundred meters by wind stress (D'Asaro 1984), and at the semidiurnal frequency through internal tide generation (Baines 1982) in response to tidal currents incident on the sloping bottom. Because typical slope angles of the seamount terrace and flanks ($> 2°$) are steeper than inertial and semidiurnal internal wave rays ($<0.3°$ and $0.3 - 1.5°$ from horizontal respectively) in measured stratification at Cobb, critical reflection (Eriksen 1982) will not be important at these frequencies unless small, locally flat regions of seamount bathymetry strongly control the flow field. Critical reflection is not required to generate internal tides (Baines 1982).

Description of measured currents is followed by brief discussion of qualitative features, as is appropriate given the limited duration and radial extent of the survey and the known intermittence and nonstationarity of near-inertial waves (Kunze 1985) and internal tides (Wunsch 1975). No comparison to wave solutions, as in Section 2.4, is made because the numerical solution technique for trapped waves is not valid for $\sigma > 0.95f$ (Section 3.2.a).

2.5.a. Near-inertial

Near-inertial energy in ADCP currents occurs in the clockwise-propagating first azimuthal wavenumber ($n = -1$) harmonic (2.1) with nearly horizontally uniform structure (Figure 2.17). This is consistent with the

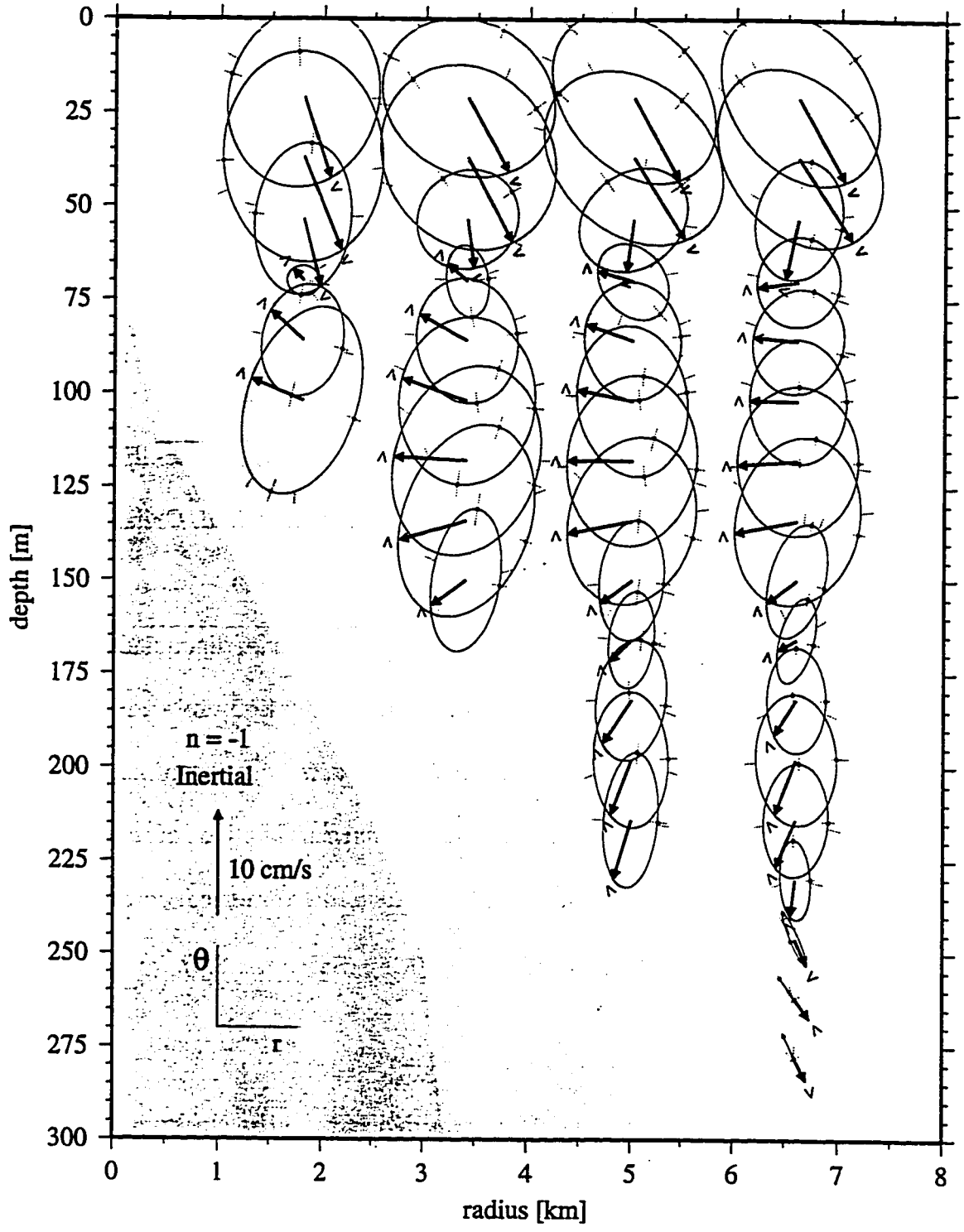

Figure 2.17. Inertial ($\sigma = f$) $n = -1$ azimuthal wavenumber (bold ellipses, middle column, Figure 2.3) ADCP current ellipses at year-day 292.0, 1991. Radial (azimuthal) flow rightward (upward).

horizontally uniform clockwise-rotating flow of a near-inertial internal wave of horizontal wavelength significantly greater than the survey coverage.

Rms current-ellipse major and minor axes lengths reach 25cm/s at the surface, are weaker in a narrow depth interval about 70 m deep (below the mixed layer base, Figure 2.1c), and decay deeper than about 175 m. Amplitude variation with depth is significantly reduced (not shown) when stratification variations of Figure 2.1c are accounted for under WKB scaling of velocities by $\sqrt{N/N_o}$ (Gill 1982) relative to constant buoyancy frequency N_o.

Velocities rotate clockwise in time in current ellipses that are roughly circular near the surface and become elongated azimuthally with increasing depth. Turning with depth of velocity at the time shown in Figure 2.17 is representative, though it changes throughout a wave period because current ellipse shapes vary with depth (see Section 3.2.b.ii). Turning is clockwise (anticlockwise) at depths shallower (deeper) than about 70 m, the depth of the seamount summit. Interpreted as a single propagating plane wave, this sense of turning implies that above (below) the summit, energy is carried downward (upward) and phase propagates upward (downward). Downward phase propagation is also evidenced below the summit by phases (Φ^u, Φ^v (2.1)) increasing upward (not shown).

Inertial flow shallower than the seamount summit is similar to that observed away from the seamount (D'Asaro 1984). Near-inertial internal

waves with horizontal wavelengths of at least 50km are excited by surface wind stress and carry energy downward. Though more complex patterns result when interactions with mesoscale currents are important (Lee 1995), dominantly clockwise turning with depth of currents is a signature of waves carrying energy downward.

Deeper than the summit, near-inertial currents at the seamount differ from open-ocean measurements by azimuthal elongation of current ellipses and anticlockwise turning with depth of the velocity. As demonstrated in Section 2.4, these features are more consistent with a forced damped seamount-trapped wave: superposed upgoing and downgoing waves trapped to the sloping bottom, with net energy transport upward because of a region of strong dissipation just above the summit (see Figure 3.18). However, it is not clear what source of energy would support trapped waves carrying energy upward from the flanks of the seamount at near-inertial frequencies. Bottom-reflected energy must originate on the surrounding seafloor or a nearby seamount, because Cobb is too steep on scales of hundreds of meters (Figure 2.1b) to reflect downgoing near-inertial rays upward.

There is a more speculative resolution to the apparent puzzle of upward energy transport below the summit depth. The mechanism by which broad barotropic tidal currents incident on the sloping seamount generate forced damped trapped waves carrying energy upward may also be active for incident wind-driven near-inertial currents. Excitation through the kinematic

bottom boundary condition of both upgoing and downgoing trapped waves, with dissipation concentrated near the summit, breaks the symmetry and causes net energy transport upward (see Figure 3.18). Testing this supposition would require better sampling, improved knowledge of dissipation, and a model that handles steep topography and superinertial currents.

2.5.b. Semidiurnal

Semidiurnal ADCP currents are energetic in harmonics (2.1) of azimuthal wavenumbers $n = 0, -1$, and -2. These lack common patterns of energy amplification in the radial-vertical plane (Figure 2.18). A consistent interpretation is that internal tides, excited by barotropic open-ocean tides (Baines 1982), carry energy away on ray paths selected by the irregular seamount geometry. The only diagnostic shared throughout the radial-vertical plane in each harmonic is clockwise rotation of horizontal currents in time.

The $n = -1$ wavenumber (Figure 2.18b) is strongest, with rms current ellipse axes lengths reaching 15.2cm/s, an amplification of 4.1 times over that of the M_2 constituent at the location of Cobb Seamount in a $1°$ resolution empirical-numerical global tide model using TOPEX altimetry (Egbert et al. 1994). This wavenumber is amplified both in the mixed layer (shallower than 50 m) and in a bottom-intensified region within about 100 m vertically and a few km radially of the seamount, where current ellipse axes are oriented

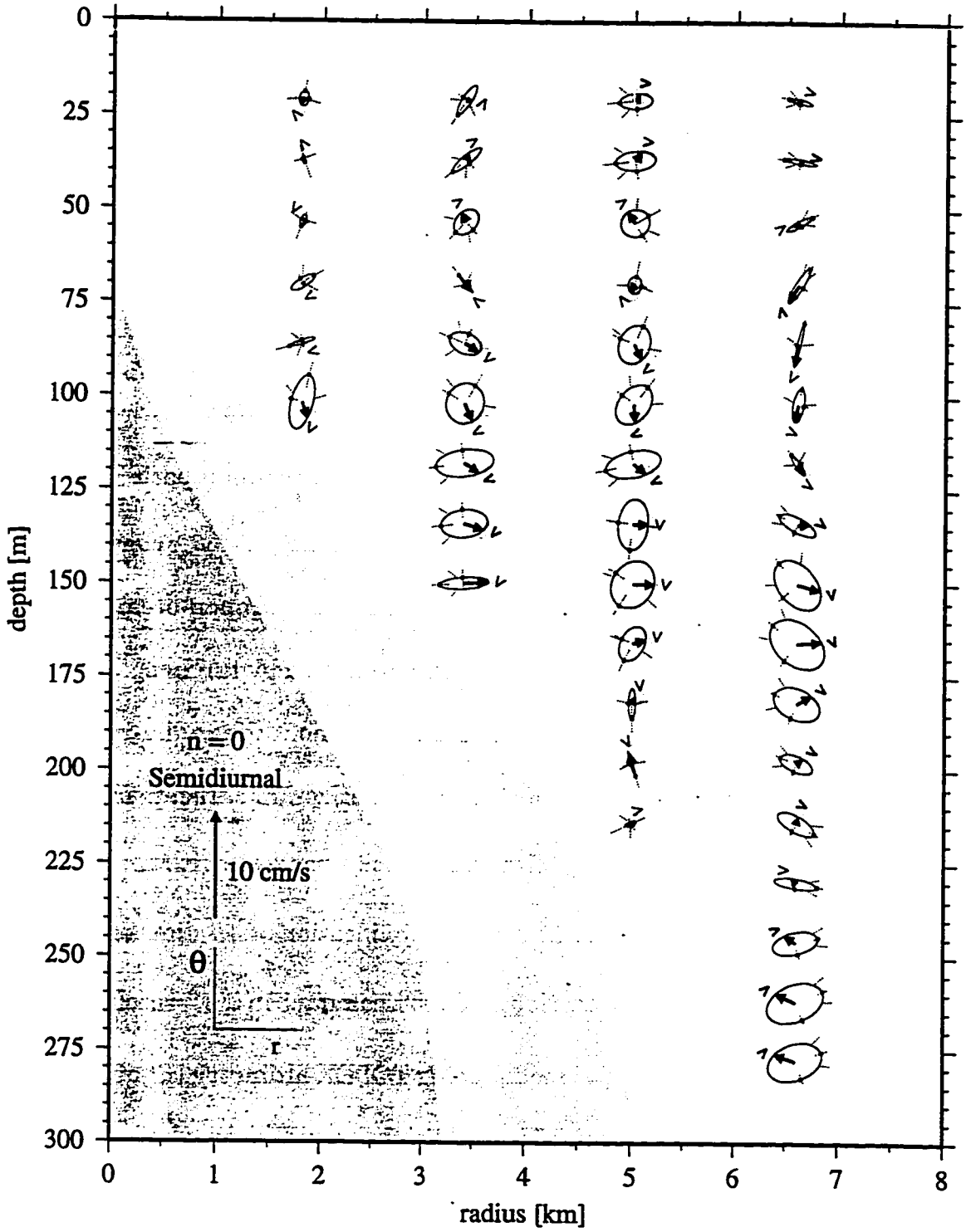

Figure 2.18. (a)Semidiurnal ($\sigma = 1.32f$) $n = 0$ azimuthal wavenumber (bold ellipses, left column, Figure 2.3) ADCP current ellipses at yearday 292.0, 1991. Radial (azimuthal) flow rightward (upward).

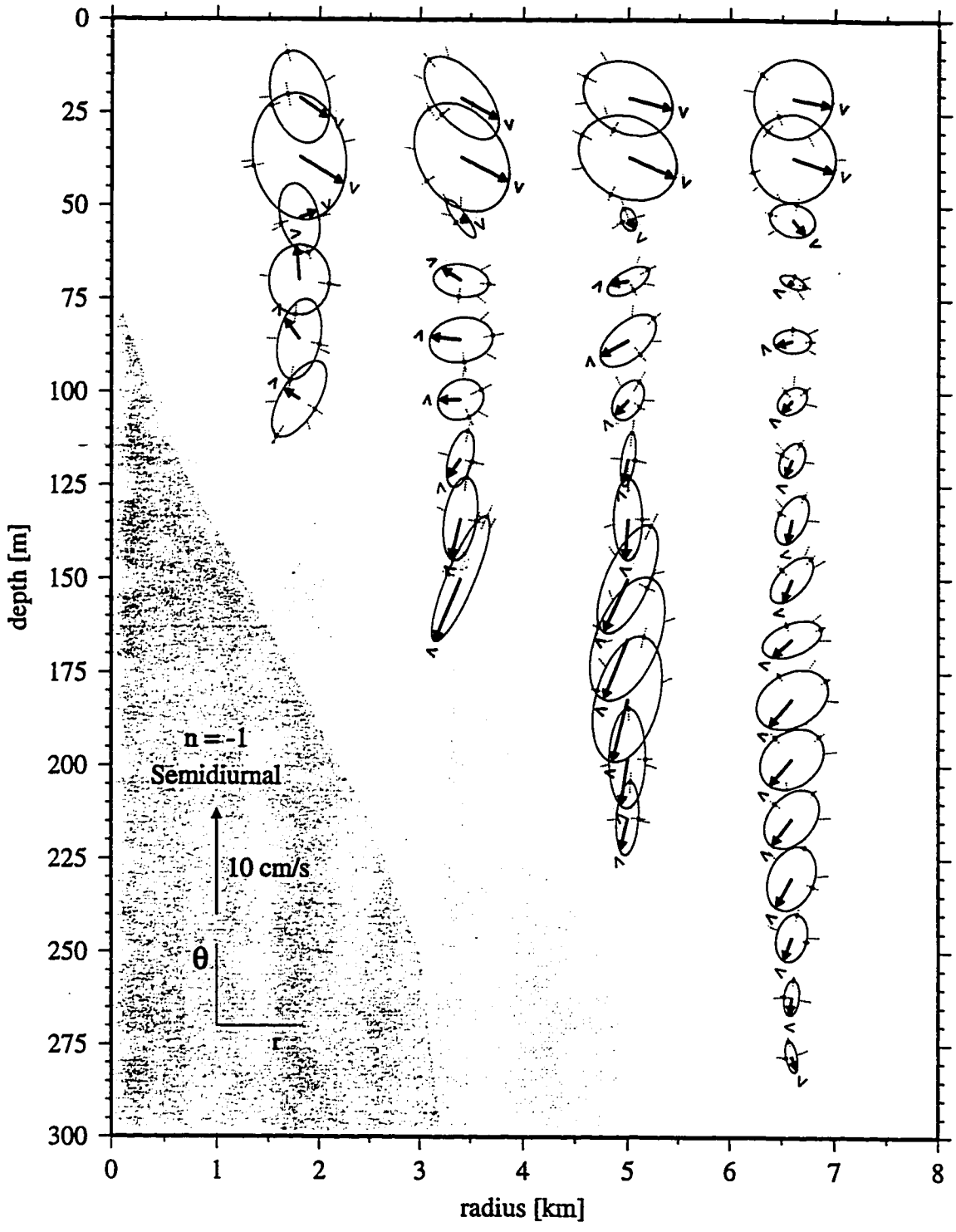

Figure 2.18. (b) Same as (a) except $n = -1$ azimuthal wavenumber (bold ellipses, middle column, Figure 2.3).

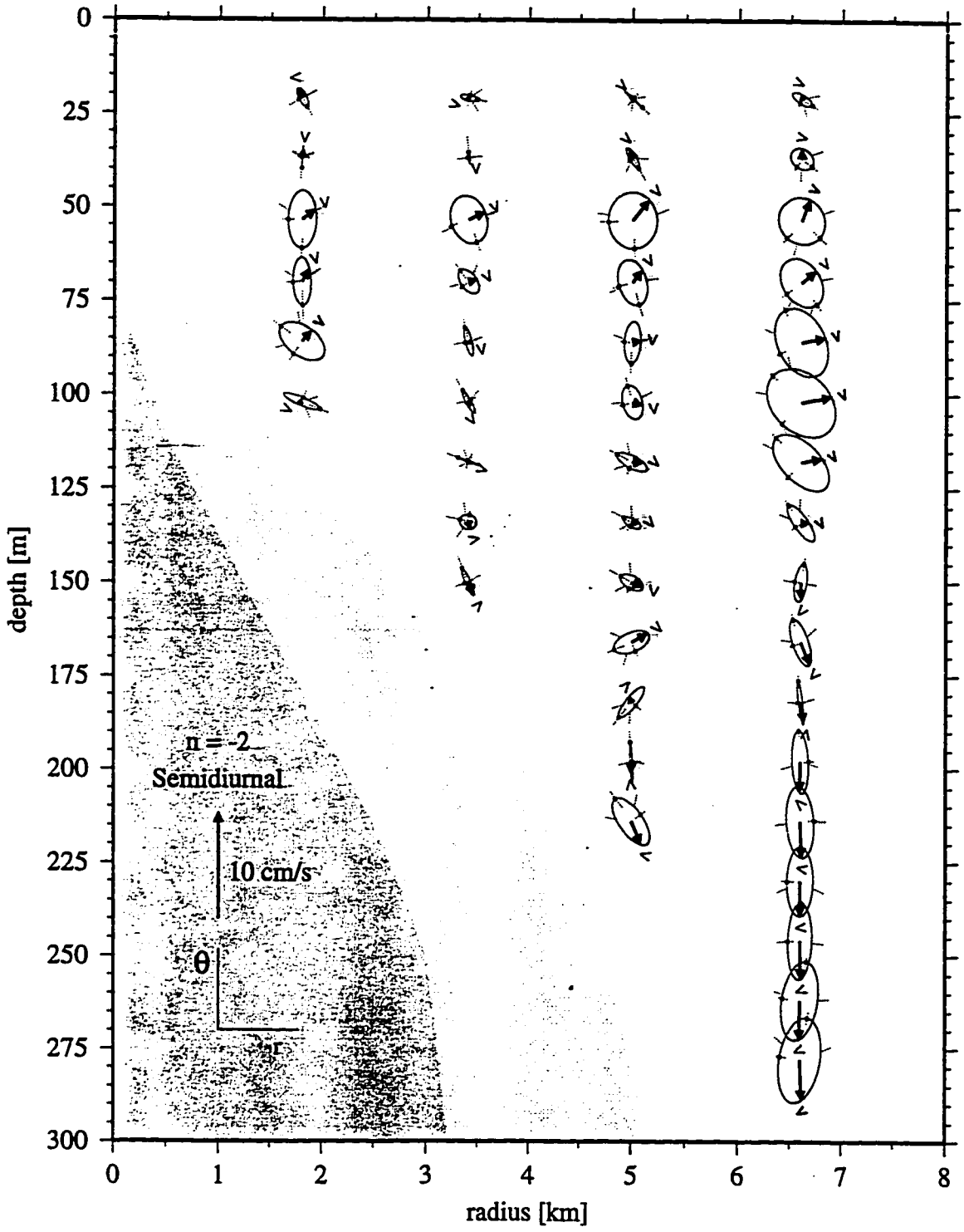

Figure 2.18. (c) Same as (a) except $n = -2$ azimuthal wavenumber (bold ellipses, right column, Figure 2.3).

across radial and azimuthal coordinate axes with $\overline{uv} > 0$ (see Figure 2.3d). Flow near the bottom thus has some characteristics of the forced damped trapped wave described in Section 2.4 and is consistent with the expectation of partial trapping of semidiurnal energy.

The $n = 0$ and $n = -2$ wavenumber harmonics (Figure 2.18a,c respectively) are less energetic than $n = -1$ and appear to concentrate in complementary regions of the radial-vertical plane. Energy in the $n = 0$ harmonic is distributed across the radial-vertical plane deeper than the summit, while energy in the $n = -2$ harmonic is strongest in the outer radial bin. A speculative interpretation of the dominance of $n = -1$ over $n = 0$ and $n = -2$ is that $n = -1$ is most strongly excited by broad open-ocean tidal currents (see Section 3.4), and its imperfect trapping at the asymmetric seamount causes the energy in other harmonics. Concentration of $n = 0$ and $n = -2$ in differing radial-vertical regions is consistent with this view.

2.5.c. Discussion

To the extent allowed by the limited coverage and duration of the survey, inertial (Figure 2.17) and semidiurnal (Figure 2.18) currents are in reasonable agreement with previous observations of wind-forced near-inertial waves (D'Asaro 1984) and internal tides (Wunsch 1975). At these frequencies, both trapped waves and internal waves not trapped to the seamount may be

excited. Some flow characteristics at both frequencies resemble the forced damped trapped wave described in Section 2.4 and may be a signature of partial trapping of energy.

Inertial currents at the seamount project on to the $n = -1$ harmonic, are nearly uniform across the horizontal extent of the survey, and rotate clockwise in time reaching 12.5cm/s (Figure 2.17). Shallower than the summit, velocities at a fixed time appear to turn clockwise with depth. These features agree well with nearby open-ocean observations (D'Asaro 1984) of near-inertial waves having horizontal wavelengths much greater than the survey breadth. The primary difference from open-ocean currents occurs deeper than the summit, where current ellipses are elongated azimuthally and turning with depth at a fixed time is anticlockwise. These features resemble a forced damped trapped wave carrying energy upward toward the summit where it is dissipated (Section 2.4). The source of the upward energy flux implied by anticlockwise turning with depth is a puzzle, since the seamount is too steep to reflect near-inertial waves upward. A speculative explanation is that the upward energy flux arises in the same manner as in forced damped trapped waves excited by broad open-ocean tidal currents. Specifically, near-inertial currents incident on the seamount excite upgoing and downgoing trapped waves and dissipation near the summit breaks the symmetry to cause upward and inward energy flux (see Figure 3.18).

Semidiurnal currents are amplified in azimuthal wavenumbers $n = 0$, -1, and -2, each with different structure in the radial-vertical plane (Figure 2.18). The $n = -1$ harmonic is most energetic, as expected in response to tidal currents broader than the seamount (Brink 1990). The $n = 0$ and $n = -2$ harmonics concentrate in complementary regions of the radial-vertical plane, as might be expected for incomplete trapping of the $n = -1$ energy around the irregular seamount bathymetry. In the most energetic ($n = -1$) harmonic, velocities are amplified in a bottom-intensified region within about 100 m vertically and a few km horizontally of the seamount where current ellipses are oriented with $\overline{uv} > 0$. These characteristics match those of the forced damped trapped wave described in Section 2.4, suggesting this energy comprises the portion of the semidiurnal flow trapped to the seamount.

2.6. Conclusions

An ADCP survey resolving radial, azimuthal, and vertical structure of steady, diurnal, inertial, and semidiurnal currents in thermocline stratification atop Cobb Seamount (Figure 2.1) is analyzed. A set (Table 2.1) of azimuthally propagating harmonics ((2.1), Figure 2.3) fit by least squares to the data (Figure 2.5) accounts for 65-70% of the kinetic energy (Figure 2.4).

Mean currents (Figure 2.6) consist of a clockwise circulation near the bottom on the terrace (Figure 2.7), superposed on east-northeastward flow

across the seamount and past its sides (Figure 2.8). CTD data portray a mean density anomaly (2.2) with 2-4 m vertical displacement (Figure 2.10), consistent with cyclogeostrophy (2.3) of the clockwise flow (Figure 2.11). The clockwise current is not strong enough to isolate fluid from the background flow, as in a Taylor cap (Hogg 1973), unless this occurs in the deepest 50 m (outside ADCP coverage). Both steady incident mean flow (Chapman and Haidvogel 1992) and rectifying oscillations (Section 3.5, Maas and Zimmerman 1989, Codiga 1993) cause bottom-intensified clockwise flow similar to that observed.

Diurnal currents (subinertial, $\sigma_{K_1} = 0.69f$, Figure 2.12) are amplified by up to 5.3 times K_1 tidal currents (Egbert et al., 1994) of the surrounding ocean. Energy is in the first azimuthal wavenumber (middle column, Figure 2.3) and amplification is trapped within a few km radially and about 100 m vertically of the seamount. Currents rotate clockwise in time in ellipses elongated azimuthally and oriented at an angle to isobaths such that $\overline{uv} > 0$ (Figure 2.3d). Velocity turns anticlockwise with depth at any instant, and phase propagates downward (Figure 2.12b).

Each diagnostic of the measured diurnal currents is present in a forced damped stratified seamount-trapped wave ((2.5) and (2.6), Figure 2.16) calculated using Cobb Seamount bathymetry and stratification (Figure 2.1) with mean clockwise current (Figure 2.11) based on that measured (Figure 2.7). The resonant frequency of the 3rd-gravest radial-vertical mode of first azi-

muthal wavenumber is $0.70f$. Currents of an inviscid free wave without mean flow (Figure 2.13) exhibit symmetries (regions of clockwise and anticlockwise rotation in time, clockwise and anticlockwise turning with depth during successive quarter-cycles (see Figure 3.5), and quadrature $\overline{uv} = 0$) not seen in measured diurnal currents. However, a wave (Figure 2.14) maintained against 2-day Rayleigh damping, as is appropriate based on measured dissipation rates (Mudge 1994, Chapter 1), has diagnostics matching the observations. It transports energy upslope and inward toward the summit (see Figure 3.18), breaking the symmetries in the inviscid wave as in the measurements: all currents rotate clockwise in time, $\overline{uv} > 0$, velocity turns anticlockwise with depth throughout the wave period, and phase propagates downward. Mean clockwise flow based on the measurements (Figure 2.11) is not strong enough to cause critical surfaces (Figure 2.15, Section 4.4) and modifies the frequency and structure of a wave very weakly (Figure 2.16).

Near-inertial (Figure 2.17) and semidiurnal (Figure 2.18) currents generally agree with other observations of wind-forced near-inertial waves (D'Asaro 1984) and internal tides (Wunsch 1975), though survey coverage is limited relative to horizontal scales of these motions.

Chapter 3

Physics and Observational Signatures of Free, Forced, and Frictional Stratified Seamount-trapped Waves

3.1. Introduction

Measurements reveal amplified subinertial currents over isolated topography at numerous sites (Hunkins 1986). At Cobb Seamount, observed diurnal currents (Chapter 2) have characteristics of stratified seamount-trapped waves (Brink 1989, 1990). Microstructure observations at seamounts (Mudge 1994, Kunze and Toole 1996) frequently reveal high dissipation rates implying kinetic energy decay timescales of a few days (Chapter 1). Observational signatures of forced stratified seamount-trapped waves maintained against dissipation of this magnitude need to be explained. In addition, most measurements near seamounts indicate clockwise low-frequency flow (in the Northern hemisphere). This is in some instances linked to subinertial motions (Brink 1995), though the mechanism is not well understood.

This chapter explores the physics and observational signatures for free, forced, and frictional stratified seamount-trapped waves, and associated wave-induced mean flow, using parameters appropriate to oceanic currents at a typical seamount. A "free wave" is inviscid and propagates freely in azimuth, though it is *trapped* to the seamount in the radial and vertical directions. To isolate robust observational signatures, simple dissipative

parameterizations are imposed on waves at an axisymmetric Gaussian seamount in constant continuous stratification. Effects of asymmetry, bottom roughness, and incident mean flow are not included.

Wave solutions are found numerically (following Brink 1989, 1990), with the advantage that realistic bathymetric and stratification profiles may be included, but the disadvantage that physical intuition is obscured even for simple topographic shape and constant stratification. A more physical understanding is developed by interpreting a stratified seamount-trapped wave as a cross-slope (radial and vertical) mode of short bottom-trapped topographic Rossby waves (Rhines 1970), here called *stratified slope-Kelvin waves*. When friction breaks the standing-wave cross-slope structure of an inviscid wave, flow diagnostics include downward propagation as is prominent in measured flow at Cobb Seamount (Chapter 2) and Fieberling Guyot (Eriksen 1995).

Response at a seamount to incident open-ocean tidal currents, under strong dissipation, is controlled by the forms of forcing and of friction. Solutions are excited here by far-field flow with features typical of the most energetic tidal currents: barotropic vertical structure, horizontal variations unimportant on the scale of a seamount, and combined anticlockwise- and clockwise-rotating components. As a first step toward understanding observed fortnightly amplitude variations, nonstationary (time-varying amplitude) waves excited by exponentially growing or decaying forcing amplitude are also examined. Because the source of observed turbulence is not fully understood

crude parameterizations are employed, Rayleigh drag with Newtonian cooling and heating (called *Rayleigh damping* hereafter) or Ekman suction, to seek physical understanding and observational signatures. Ekman suction requires effective bottom boundary layer diffusivities orders of magnitude higher than measured to achieve a decay time as short as that observed. In addition, at Cobb Seamount, measured diffusivities outside the boundary layer exceed those within it (Mudge 1994). Thus Rayleigh friction appears a more suitable representation. Its simplicity yields physically interpretable phase behavior and an understanding of energy flow through the system that may be representative of other frictional forms.

An idealized example is used to demonstrate nonlinear rectification of waves in exciting a mean azimuthal current through azimuthal-mean cross-slope buoyancy and momentum flux divergences. The mechanism accelerates mean clockwise azimuthal flow, as seen in laboratory data (Zhang and Boyer 1993, Codiga 1993) and numerical models (e.g. Haidvogel et al. 1993).

In Section 3.2, currents of a free wave are described in detail. The underlying physics are illustrated in Section 3.3 using stratified slope-Kelvin waves. Section 3.4 demonstrates resonance behavior of forced and frictional waves and their associated current signatures, and Section 3.5 explains mean-flow induction.

3.2. Free stratified seamount-trapped waves

3.2.a. Governing equations

Consider a cylindrical coordinate system (r, θ, z) with origin at the sea surface above the seamount summit and θ the anticlockwise angle from eastward. Radial, azimuthal, and vertical velocity components (u, v, w) are positive outward, counterclockwise, and upward. The seamount is of Gaussian shape with horizontal scale L, summit depth h_0, and far-field depth H, so the ocean bottom lies at $z = -h(r)$ where

$$h(r) = H - (H - h_0)\exp\left[-(r/L)^2\right].$$

An incompressible Boussinesq ocean, rotating uniformly with Coriolis frequency f and continuously stratified with constant buoyancy frequency N, surrounds the seamount. The Burger number $S = \left(\frac{NH}{fL}\right)^2$ is the squared ratio of the first baroclinic Rossby radius to the horizontal scale of the topography. Parameters are chosen (Table 3.1) to represent a typical midlatitude northern hemisphere seamount extending into the main thermocline.

To most simply demonstrate wave physics the central example (Table 3.1, $S = 12$) has stratification somewhat weaker than that observed near thermocline-depth seamount summits, and effects of higher stratification are illustrated for doubled N^2 ($S = 48$) where important (Section 3.2.b.iii). Oceanic stratification varies with depth. This changes wave geometry but not the

Table 3.1. Parameters representative of a typical northern hemisphere midlatitude seamount extending into the main thermocline.

horizontal scale	L	12 km
far-field depth	H	3000 m
summit depth	h_0	300 m
maximum bottom slope	$\max\left(\tan^{-1} h_r\right)$	11°
buoyancy frequency	N	$1.4\times10^{-3}\left[2.8\times10^{-3}\right]$ s^{-1}
Coriolis frequency	f	10^{-4} s^{-1}
Burger number	$S = (NH/fL)^2$	12 [48]

physics discussed here. A way to estimate the vertically uniform buoyancy frequency best representing a depth-varying profile is to use stratification near the summit, where wave energy concentrates. At Fieberling Guyot, $S \approx 70$ estimated in this manner (Codiga 1993). Alternately, the Burger number may be chosen to match the squared ratio between the Rossby radius c_p/f, based on the first baroclinic mode phase speed c_p in the stratification profile of the surrounding ocean, and the horizontal scale of the seamount near its summit. Stratification (Figure 2.1c) near Cobb Seamount has c_p/f= 30km and the terrace is $\approx$ 5km wide, giving Burger number 36. In these two examples, constant $S = 48$ stratification appears to be more appropriate than $S = 12$.

The inviscid, unforced, linearized hydrostatic momentum, buoyancy, and continuity equations for reduced pressure p (pressure/ρ_o where ρ_o is a

constant reference density), velocities (u, v, w), and buoyancy b as functions of (r, θ, z, t) are

$$\begin{aligned} u_t - fv &= -p_r && (a) \\ v_t + fu &= -\frac{1}{r} p_\theta && (b) \\ 0 &= -p_z + b && (c) \\ b_t + N^2 w &= 0 && (d) \\ \frac{1}{r}(ru)_r + \frac{1}{r} v_\theta + w_z &= 0 \ . && (e) \end{aligned} \tag{3.1}$$

Boundary conditions require flow to be trapped to the topography, remain bounded at the center, obey the kinematic condition of no flow perpendicular to the bottom and the rigid lid condition at the surface:

$$\begin{aligned} (p, u, v, w, b) &\to 0 \quad \text{as} \quad r \to \infty && (a) \\ (p, u, v, w, b) &\quad \text{bounded at} \quad r = 0 && (b) \\ w + h_r u &= 0 \quad \text{at} \quad z = -h && (c) \\ w &= 0 \quad \text{at} \quad z = 0 \, . && (d) \end{aligned} \tag{3.2}$$

Free stratified seamount-trapped waves are eigensolutions of the system ((3.1), (3.2)) at subinertial frequencies (Brink 1989). Conceptually, they are coastal-trapped waves (Huthnance 1978) resonant in the re-entrant waveguide formed by a submerged periodic coastline. The potential vorticity gradient provided by the sloping bottom supports the waves and eigensolu-

tions may be considered radial-vertical normal modes of short bottom-trapped topographic Rossby waves in stratification (Rhines 1970), or *stratified slope-Kelvin* waves (Section 3.3).

Wave physics will be illustrated using the "gravest" radial-vertical mode, that with the highest subinertial frequency and simplest spatial structure, of the first azimuthal wavenumber. This is motivated by frequencies, for example, of diurnal tides at latitudes (35°, 45°, 55°) at σ/f= (0.87, 0.71, 0.61), and the fact that tidal currents more broad than the seamount excite the first azimuthal wavenumber (Chapman 1989, Brink 1990). For a given azimuthal wavenumber a countably infinite number of resonances exists at increasingly lower frequencies, corresponding to higher radial-vertical modes of increasingly smaller scales (Brink 1989).

For $\sigma > f$ trapped waves may occur, but because internal waves not trapped to the seamount also exist, response to forcing need not concentrate as strongly in trapped waves as it does at subinertial frequencies. The upper frequency limit for a trapped wave is $N\sin\left(\tan^{-1}h_r\right)$ (Rhines 1970), well above the inertial frequency for slopes and stratification at a typical seamount (Table 3.1). Resonant frequencies of seamount-trapped waves may reach and exceed f because the seamount circumference fixes the effective wavelength, and phase speed increases with topographic slope and stratification. At superinertial frequencies, both trapped waves and superposed pairs of inci-

dent and reflected internal waves not trapped to the seamount can satisfy the bottom boundary condition. The numerical technique used to find trapped-waves (Appendix C) is contaminated at frequencies above about $0.95f$ by quantization and amplification of internal waves due to the finite domain.

3.2.b. Currents

Free waves have standing-wave cross-slope (radial and vertical) structure with purely azimuthal phase propagation, energy flux, and buoyancy flux. Azimuthal wavenumber one variables $\{p, u, v, w, b\}$ are of form, using u as an example,

$$\begin{aligned} u(r,\theta,z,t) &= |\tilde{u}(r,z)| \cos\left[-\theta - \sigma t + \Phi^u(r,z)\right] \\ &= \Re\{\tilde{u}(r,z) \exp[i(-\theta - \sigma t)]\} \end{aligned} \tag{3.3}$$

where $\tilde{u}(r,z)$ is the *modal structure function*, phase Φ^u is defined

$$\begin{aligned} \Phi^u(r,z) &= \tan^{-1}\{\Im[\tilde{u}(r,z)], \Re[\tilde{u}(r,z)]\} \\ &[\text{from } \tan\Phi^u = \pm\Im(\tilde{u})/\Re(\tilde{u})] \end{aligned} \tag{3.4}$$

for *4-quadrant* inverse tangent, $\Re$ ($\Im$) indicates the real (imaginary) part, and σ is frequency. Free waves exist at discrete resonant frequencies and propagate phase clockwise purely azimuthally because modal structure functions are real ($\tilde{u}$ and $\tilde{w}$) or imaginary ($\tilde{p}$, $\tilde{v}$, and $\tilde{b}$), not complex.

For the $S = 12$ system in Table 3.1, the gravest mode of azimuthal wavenumber one is resonant at $\sigma = 0.657f$. Modal structure functions are bottom-intensified and dominated by horizontal velocities (Figure 3.1, Figure 3.2). The amplitude of a free wave may be characterized by its wave steepness, the ratio between current speed and phase speed, or equivalently the ratio of particle orbit scale to wavelength. Nominal particle orbit size is $u_A T$ where

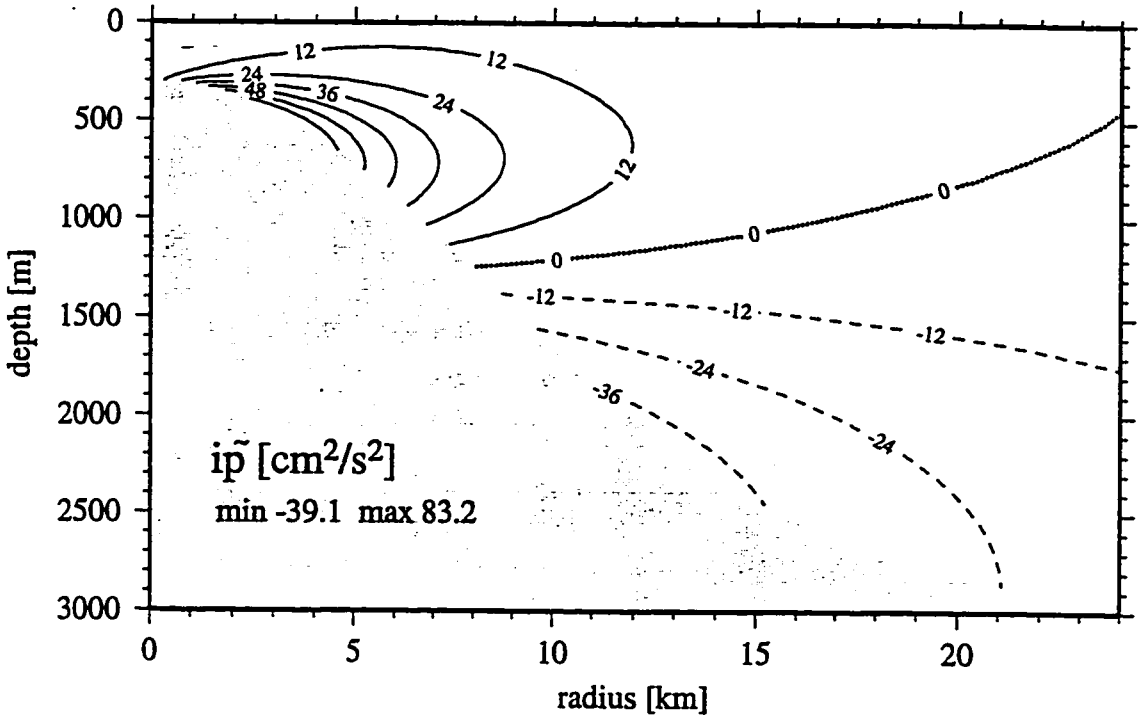

Figure 3.1. Modal structure function of reduced pressure of gravest free wave eigensolution ($\sigma/f = 0.657$, see Figure 3.12) for parameters in Table 3.1, at amplitude $\varepsilon = 0.15$. The plotting convention here and for all figures to follow is dotted zero contours and solid (dashed) contours indicating positive (negative) values.

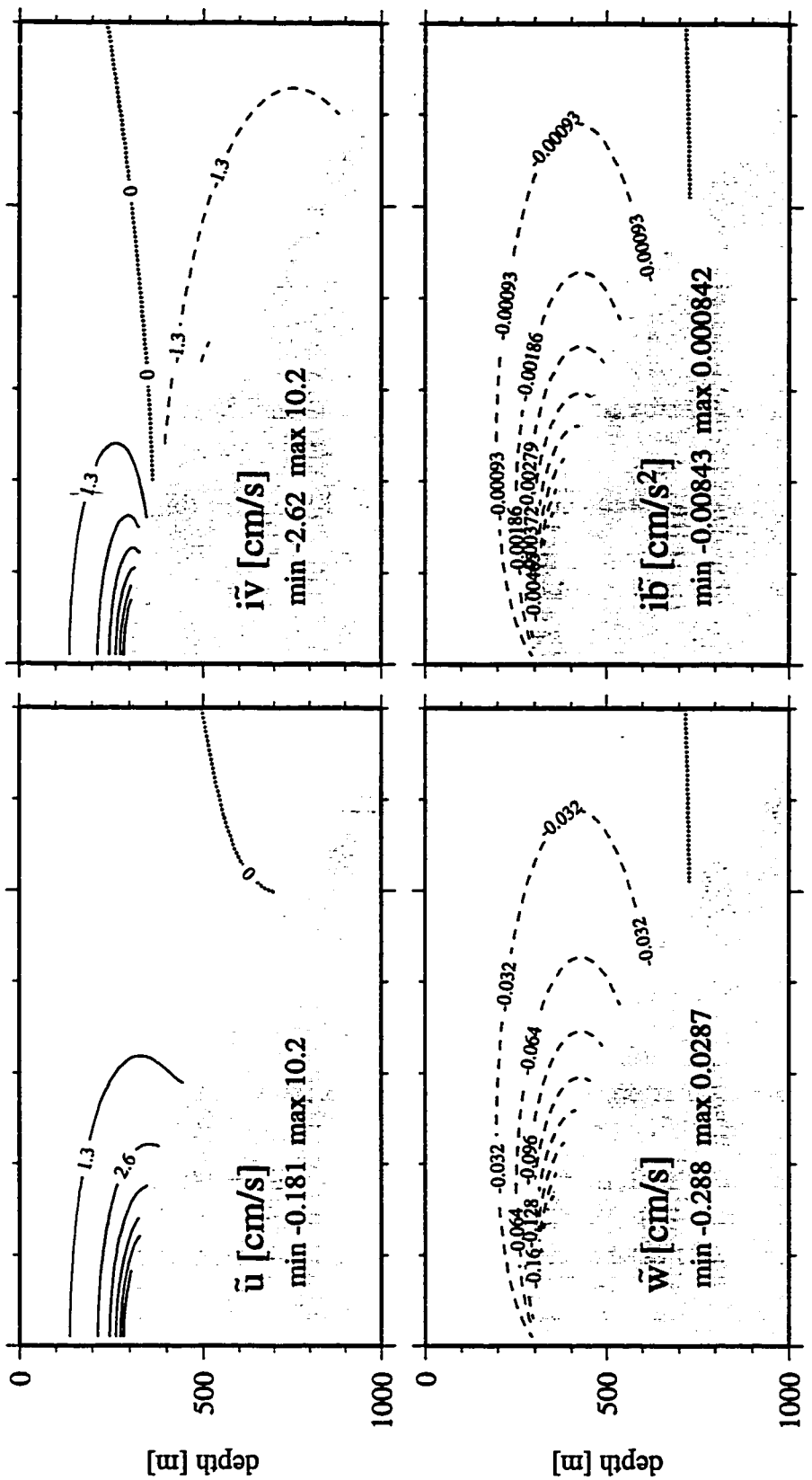

Figure 3.2. Modal structure functions of radial, azimuthal, and vertical velocities, and buoyancy, for free wave of Figure 3.1. Field of view is a subset of that in Figure 3.1 because the signal is concentrated near the summit. Zero contours are *nodal lines*.

u_A is the maximum wave velocity and $T = 2\pi/\sigma$ the period. The nominal wavelength of the first azimuthal mode is $2\pi L$, so wave steepness is defined

$$\varepsilon = \frac{u_A T}{2\pi L} = \frac{Ro}{\sigma/f} = \frac{u_A}{\sigma L} \tag{3.5}$$

where $Ro = \frac{u_A}{fL}$ is the Rossby number. As appropriate for observed velocities reaching $u_A \approx 15$ cm/s, eigensolutions are examined here at amplitude corresponding to wave steepness $\varepsilon = 0.15$.

Phase of each dynamical variable (3.4) takes values differing by 180° in alternating regions of the radial-vertical plane bounded by *nodal lines*, zero contours in its modal structure function. Stated differently,

$$\frac{\partial \Phi}{\partial r} = \frac{\partial \Phi}{\partial z} = 0 \tag{3.6}$$

except at nodal lines. For example, by (3.4), where $\tilde{u} > 0$ ($\tilde{u} < 0$), $\Phi^u = 0°$ ($\Phi^u = 180°$) because $\tilde{u}$ is real, and where $\tilde{v} > 0$ ($\tilde{v} < 0$), $\Phi^v = 90°$ ($\Phi^v = -90°$) because $\tilde{v}$ is imaginary. Phases of u and w are such that correlations with v, b, and p are zero,

$$\overline{uv} = \overline{ub} = \overline{up} = \overline{wv} = \overline{wb} = \overline{wp} = 0, \tag{3.7}$$

where $\overline{(\ )}$ indicates an average over wave period and equivalently an azimuthal average because of the harmonic dependence in (3.3). Energy flux $\overline{\tilde{u}\tilde{p}}$ and buoyancy flux $\overline{\tilde{u}\tilde{b}}$ are thus purely azimuthal and free waves cannot redistribute energy or buoyancy radially or vertically.

Plan-view currents at a fixed depth tend toward one of two forms: a jet across the seamount center or incident flow splitting to pass its sides (Figure 3.3a,b, and d), or currents of one sense on two opposite flanks with counterflow in the other two quadrants (Figure 3.3c). These two patterns may be identified with circulation in the familiar first-azimuthal wavenumber dipole, in regions of inner and outer radii respectively. Stratification and sloping bottom topography combine to stack them effectively vertically in the baroclinic wave.

3.2.b.i.Rotation in time

Currents shallower than the summit rotate clockwise in time in nearly circular current ellipses, while below the summit in alternating depth ranges currents rotate clockwise or anticlockwise in time to trace out narrow current ellipses elongated in the radial or azimuthal directions (Figure 3.4). As shown in Figure 3.4a, the region of currents rotating anticlockwise in time is bounded below (above) by the nodal line in radial (azimuthal) velocity, the zero contour in Figure 3.2a(b). Force balances are mainly inertial (two left-hand terms in (3.1)(a), (b)) where current ellipses are nearly circular, with the pressure gradient important in narrower ellipses (Codiga 1993).

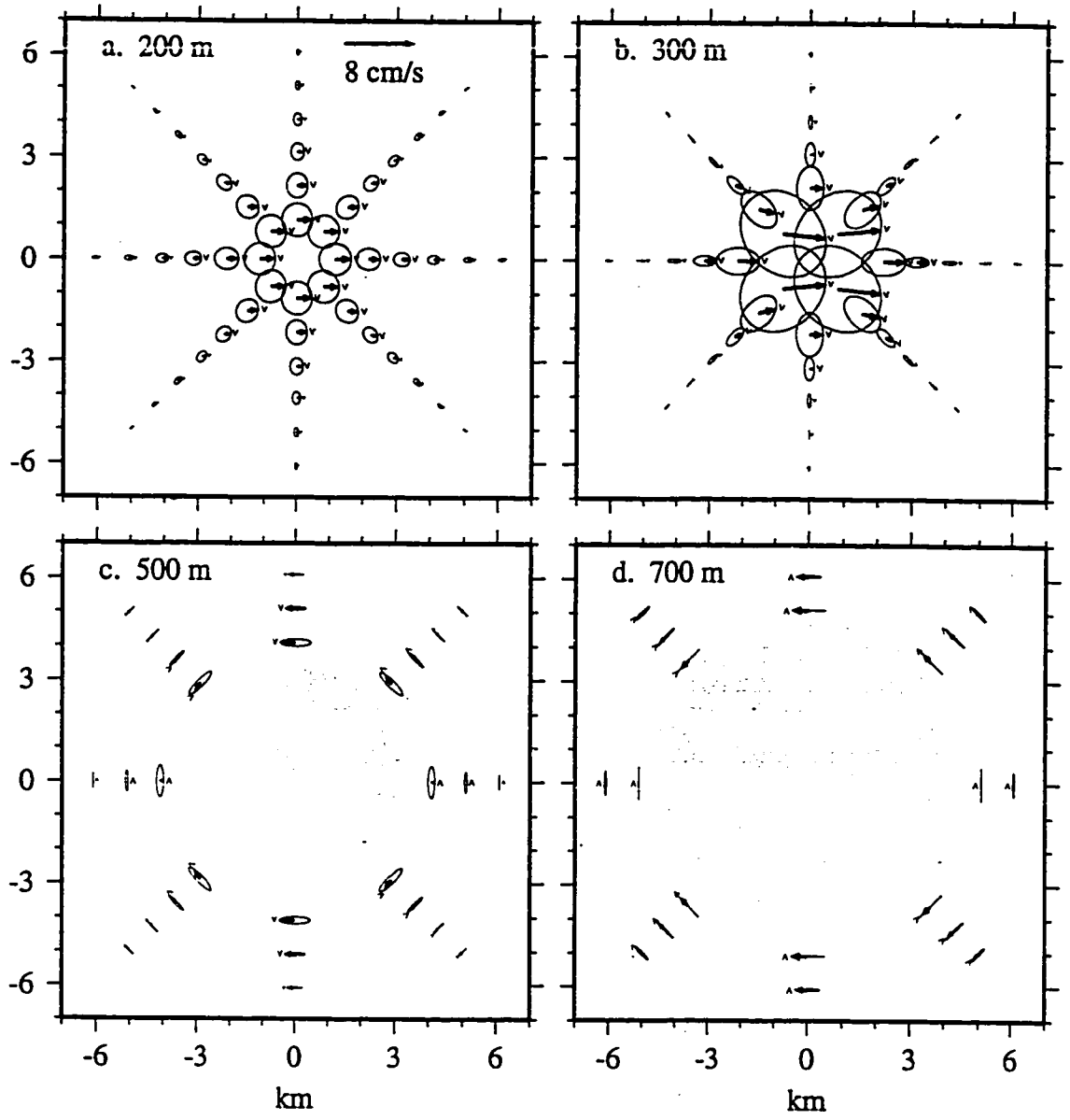

Figure 3.3. Plan-view instantaneous $t = 0$ horizontal velocities and current ellipses of free wave (Figure 3.2) at four depths, as labelled. Scale vector in first frame. With time each velocity vector rotates in the direction marked near its head to trace out its ellipse.

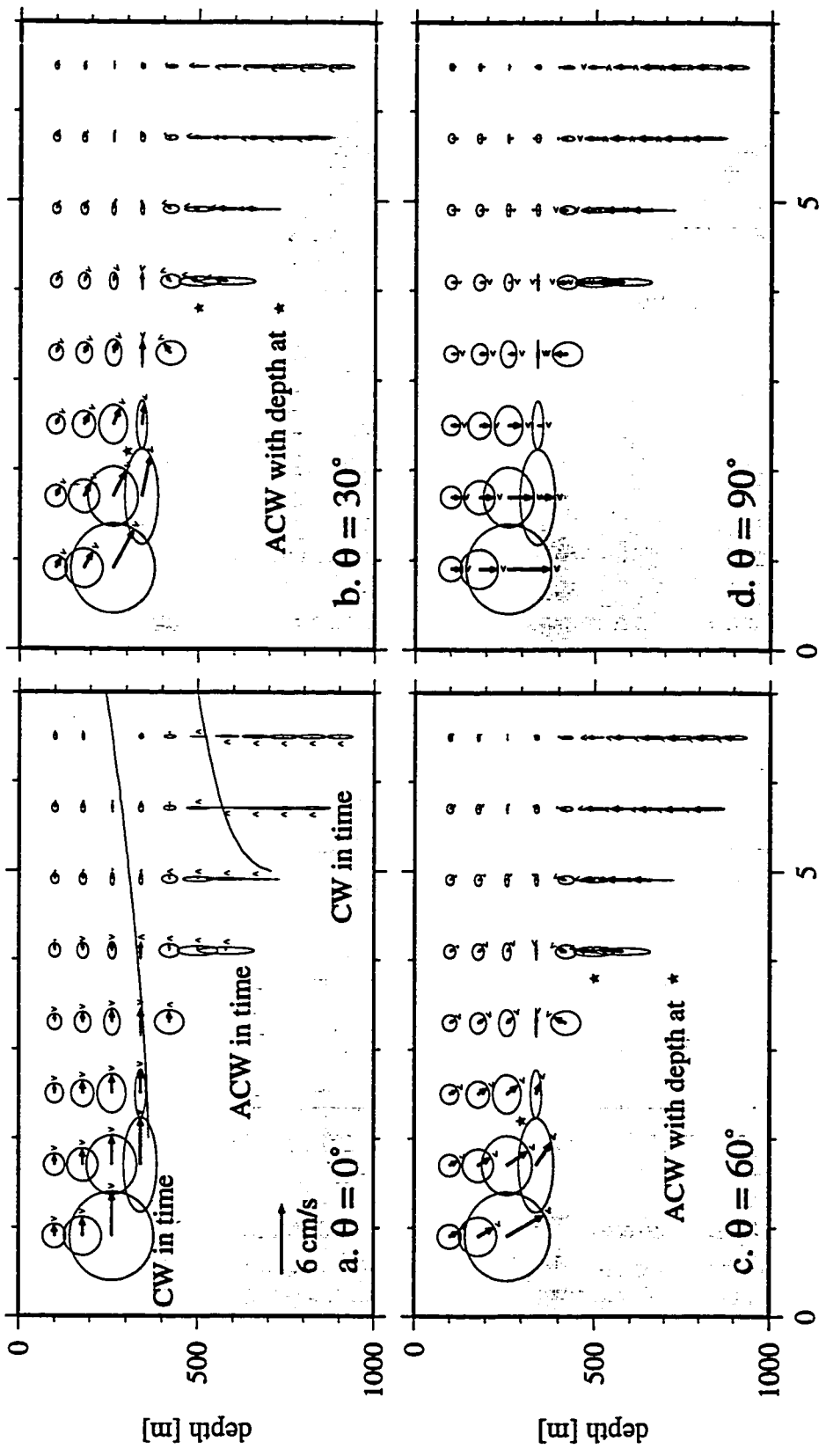

Figure 3.4. Free wave (Figure 3.3) horizontal velocity (radial rightward, azimuthal upward) current ellipses in radial-vertical planes at labelled azimuths in the northeast quadrant ($0 < \theta < 90°$) at $t = 0$. Equivalent to flow in the eastward radial-vertical plane $\theta = 0$ at $t = (0, T/12, T/6, T/4)$.

3.2.b.ii.Turning with depth

At a fixed location, turning with depth of horizontal velocity is alternately anticlockwise and clockwise during successive quarter-periods (Figure 3.5). For east $u^x = u\cos\theta - v\sin\theta$ and north $u^y = u\sin\theta + v\cos\theta$ currents, the horizontal velocity azimuth is

$$\Theta(r, \theta, z, t) = \tan^{-1}\left(u^y, u^x\right) \tag{3.8}$$

for 4-quadrant inverse tangent, and velocity turns at rate $d\Theta/dz < 0$ (> 0) anticlockwise (clockwise) with increasing depth. East of the seamount center at the beginning of a wave period (Figure 3.4a) Θ is everywhere either 0 (shallow) or 180 (deeper) and there is no continuous turning with depth, only

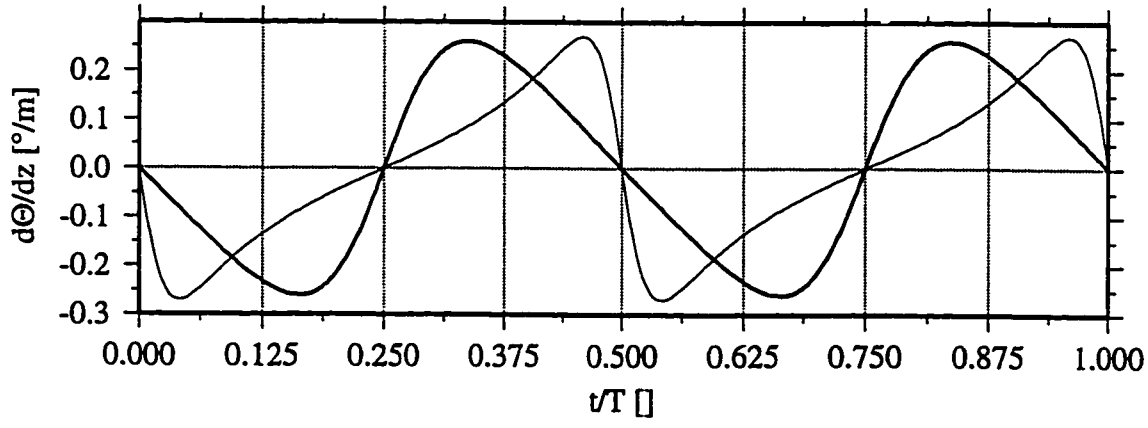

Figure 3.5. Horizontal velocity turning with depth during one wave period, at shallow (bold) and deep stars in Figure 3.4b,c for $\theta = 0$. Standing-wave structure exhibits alternately anticlockwise and clockwise turning with depth ($d\Theta/dz < 0$ and > 0, (3.8)) during successive quarter-periods.

a reversal at the nodal line in radial velocity. One quarter-cycle later (Figure 3.4d) these orientation angles are –90 and 90 respectively and there is also no continuous turning with depth. Between these two times, at radii and depths marked by stars in Figure 3.4b,c, the velocity turns anticlockwise ($d\Theta/dz < 0$) continuously with increasing depth. In the next quarter-cycle there is similar turning but in the opposite (clockwise) sense, as characterizes standing-wave vertical structure (Figure 3.5). Turning at depths sufficiently shallower and deeper than those marked by stars in Figure 3.4b,c is of sense opposite that shown in Figure 3.5, because standing-wave structure consists at any instant of alternating nearly horizontal depth regions with turning of opposite senses. Variation of turning rate with radius, depth, and time (Figure 3.5) is controlled by depth variations of current ellipse shapes.

3.2.b.iii.Higher radial-vertical modes in stronger stratification

Higher radial-vertical modes have smaller horizontal and vertical scales, weaker vertical displacements, and currents rotating dominantly clockwise in time. As N doubles to increase S from 12 to 48 for parameters of Table 3.1, the gravest (second-gravest) radial-vertical mode of azimuthal wavenumber one increases in frequency from σ = 0.66 (0.47) to 0.92f (0.75f). The second-gravest S = 48 mode is thus similar in frequency to the gravest S = 12 mode described above, though it has reduced vertical and horizontal

scales (Figure 3.6a,b), and vertical displacement amplitude $\max\left(-b/N^2\right)$ reduced from 40 m (Figure 3.2d) to 10 m (not shown). In higher modes, radial-vertical regions where currents rotate anticlockwise in time are reduced in size relative to those rotating clockwise in time (Figure 3.6c).

3.3. Physics of stratified slope-Kelvin wave rays

In this section, the free seamount-trapped wave is explained using topographic Rossby wave rays in a continuously stratified and uniformly rotating ocean, the "edge," or short, bottom-trapped, limit of Rhines (1970). These are called *stratified slope-Kelvin waves* here to avoid confusion with surface gravity waves refractively trapped by a sloping beach, commonly known as edge waves. Quasigeostrophic scaling simplifies the dynamics to give physical intuition. A seamount-trapped wave is a superposition of upgoing and downgoing stratified slope-Kelvin waves refracted and trapped in the cross-slope direction by changing bottom slope, with radially concentrated energy and azimuthally quantized structure due to cylindrical geometry.

Quasigeostrophic scaling of flow with horizontal velocity magnitude U that varies on horizontal and temporal scales L and T requires that $\frac{U}{fL}$ and $\frac{1}{fT}$ are of order the small expansion parameter Ro, buoyancy fluctuations have vertical gradient of order RoN^2, and motions are horizontally nondiver-

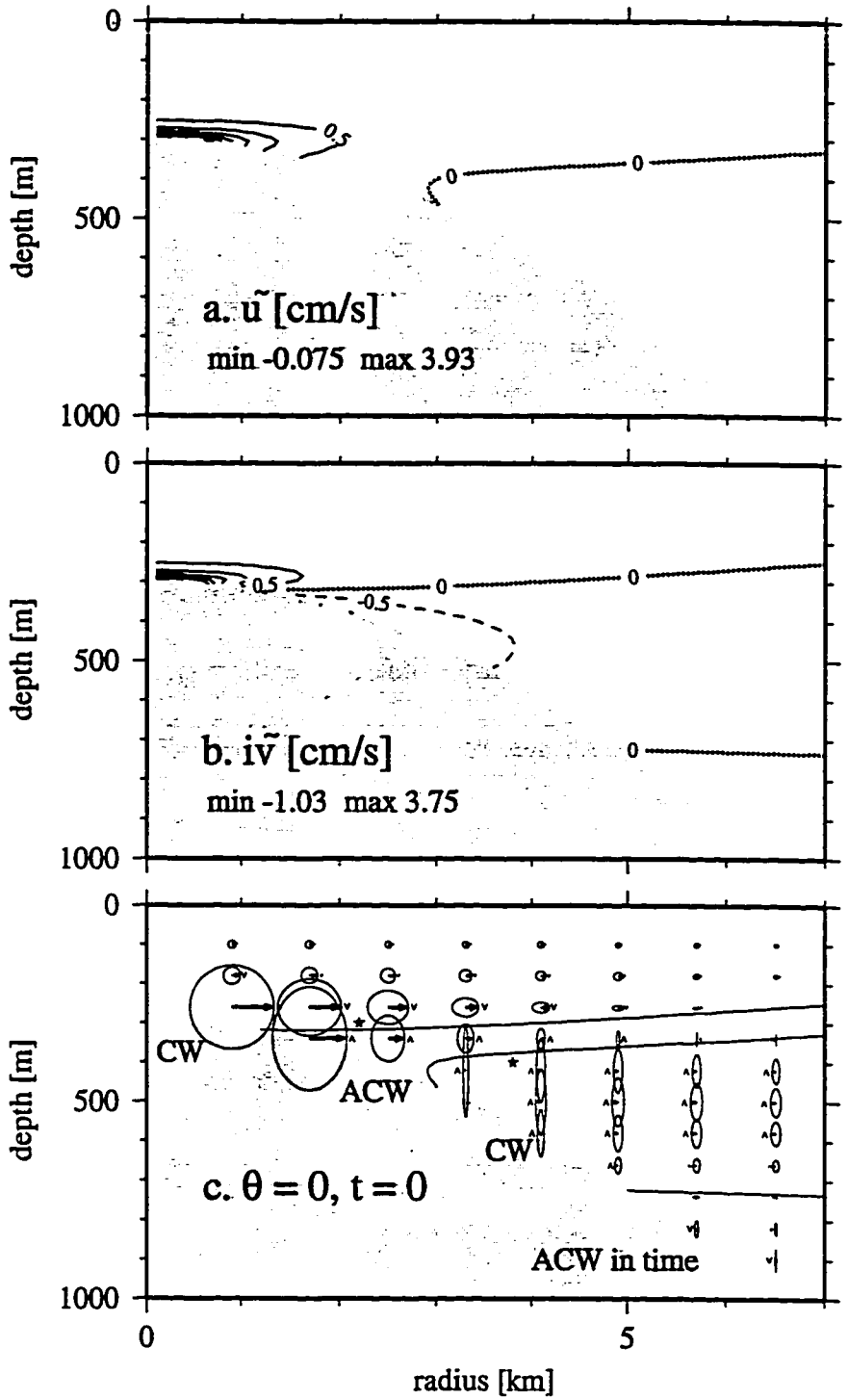

Figure 3.6. Higher-stratification (S = 48) 2nd-gravest radial-vertical mode, $\sigma = 0.75f$. (a), (b) Radial, azimuthal velocity modal structure functions, see Figure 3.2a,b. (c) Current ellipses, as Figure 3.4a.

gent to lowest order (Gill 1982). Governing equations for velocities (u, v, w) in *Cartesian coordinates* (x, y, z) are to first order

$$\begin{aligned} u_t + uu_x + vu_y - fv &= -p_x \qquad (a) \\ v_t + uv_x + vv_y + fu &= -p_y \qquad (b) \\ 0 &= -p_z + b \qquad (c) \\ b_t + ub_x + vb_y + wN^2 &= 0 \qquad (d) \\ u_x + v_y + w_z &= 0, \qquad (e) \end{aligned} \tag{3.9}$$

where nonlinear terms are retained to facilitate inclusion of mean flow in Chapter 4. Lowest-order flow is geostrophic and in thermal wind balance, with variables related to the quasigeostrophic streamfunction ψ as

$$p = f\psi \qquad u = -\psi_y \qquad v = \psi_x \qquad b = f\psi_z. \tag{3.10}$$

Conservation of Ertel potential vorticity captures the dynamics of (3.9) in a single equation for streamfunction, and can be written

$$\begin{aligned} &\frac{\partial}{\partial t} q + J(\psi, q) = 0 \\ &q = \nabla_H^2 \psi + \frac{f^2}{N^2} \psi_{zz} \end{aligned} \tag{3.11}$$

where q is the quasigeostrophic potential vorticity, $J(A,B) = A_x B_y - A_y B_x$, and $\nabla_H^2 \psi = \Psi_{xx} + \Psi_{yy}$. Quasigeostrophic potential vorticity q is related to Ertel potential vorticity by

$$q_{ertel} = (f+q)N^2. \tag{3.12}$$

The ocean bottom is at $z = -h(x)$ where to lowest order $h(x) = h_o$ is constant, and the topographic slope h_x is in the x direction only, and of order $Ro\frac{f}{N}$ to maintain quasigeostrophic scaling. Linearized potential vorticity conservation (3.11) is

$$\nabla_H^2 \psi_t + \frac{f^2}{N^2}\psi_{zzt} = 0. \tag{3.13}$$

The kinematic bottom boundary condition $w = -h_x u$ applied in the linearized buoyancy equation (3.9)(d) at the bottom gives

$$f\psi_{zt} + h_x N^2 \psi_y = 0 \text{ at } z = -h_o. \tag{3.14}$$

Plane wave solutions to (3.13) and (3.14) trapped to the bottom with vertical scale Z much smaller than h_o have form (Rhines 1970)

$$\psi(x,y,z,t) = \psi_b \exp(-(z+h_o)/Z) \exp(i(kx+ly-\sigma t)), \qquad (3.15)$$

where ψ_b is the amplitude at the bottom, and k and l are across- and along-slope wavenumbers. By (3.13), the vertical trapping scale is proportional to the horizontal scale,

$$Z = \frac{f}{N\kappa}, \qquad (3.16)$$

where $\kappa = \left(k^2 + l^2\right)^{1/2}$ is the total horizontal wavenumber. Energy density is

$$\frac{1}{2}\left(u^2 + v^2 + b^2/N^2\right) = \kappa^2 \psi_b^2 \exp\left(\frac{-(z+h_o)}{Z/2}\right), \qquad (3.17)$$

and vertically integrated energy per unit horizontal area averaged over a wave period is

$$E^z = \frac{1}{4} Z \kappa^2 \psi_b^2 = \frac{f}{4N} \kappa \psi_b^2. \qquad (3.18)$$

The dispersion relation follows from (3.14),

$$\sigma = -N h_x \frac{l}{\kappa}, \qquad (3.19)$$

and the group velocity

$$c_g^x = \frac{Nh_x kl}{\kappa^3} \qquad c_g^y = \frac{-Nh_x k^2}{\kappa^3} \qquad c_g^z = 0 \tag{3.20}$$

is purely horizontal due to the trapped vertical structure.

Because the influence of topographic slope does not appear in q (3.11), the potential vorticity gradient is zero in the interior of the fluid and nonzero only at the bottom boundary. Taking its influence to extend $Z/2$ away from the boundary based on (3.17), its strength is (Pedlosky 1987)

$$Q_x^h = -\frac{fh_x}{Z/2} = -2Nh_x\kappa. \tag{3.21}$$

Thus the topographic potential vorticity gradient Q_x^h supporting the wave is directed upslope (for example $Q_x^h < 0$ for $h_x > 0$) and is inversely proportional to the horizontal scale κ^{-1} and, by (3.16), vertical scale Z of the wave. Dispersion relation (3.19) may be written

$$\sigma = Q_x^h \frac{l}{2\kappa^2}, \tag{3.22}$$

a form found useful in Section 4.3 when an additional "interior" potential vorticity gradient due to mean flow variations is considered.

3.3.a. Uniform slope

Consider a uniform slope with $h_x > 0$ so the downslope direction is along the positive x axis (Figure 3.7). Alongslope wavenumber and alongslope group velocity are negative,

$$l < 0 \qquad c_g^y < 0,$$

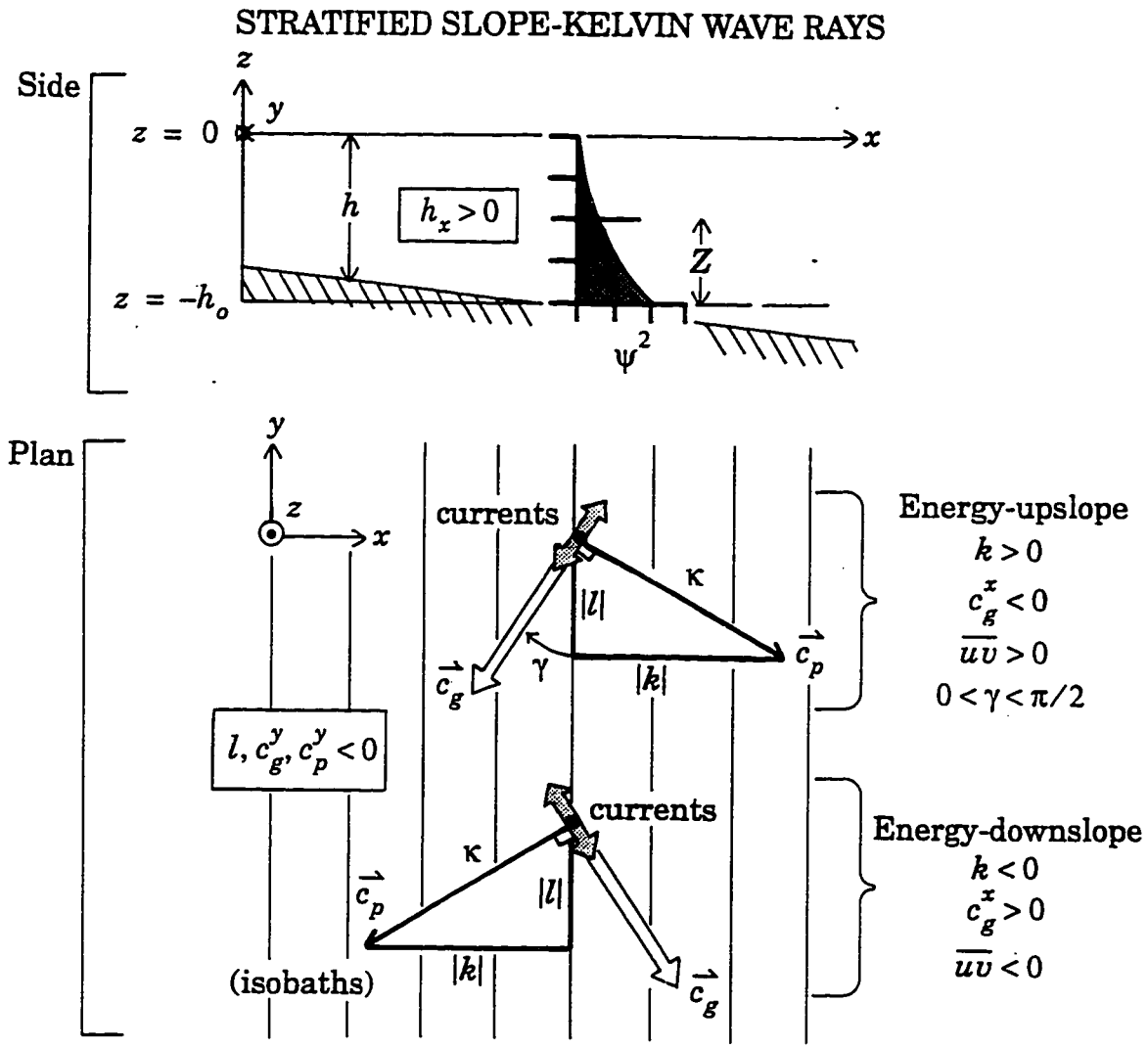

Figure 3.7. Schematic stratified slope-Kelvin wave, as discussed in text. Bold axes (upper panel) showing vertical structure of quasigeostrophic streamfunction ψ appear as insets in figures to follow.

by dispersion relation (3.19) and group velocity (3.20), so alongslope phase propagation and energy flux occur with shallow water on the right. For given l two cross-slope wavenumbers $\pm k$ correspond to downslope phase propagation with upslope energy flux ($k > 0$), and upslope phase propagation with downslope energy flux ($k < 0$). Surfaces of constant phase are vertical planes at an angle to isobaths (Figure 3.7).

Currents of an individual wave are linearly polarized and oriented along the group velocity, so superpositions of equal-amplitude upgoing and downgoing waves form cross-slope modes with open current ellipses that propagate phase and carry energy purely along isobaths. An individual wave carrying energy upslope (downslope) has positive (negative) correlation between across- and along-slope velocity components, $\overline{uv} > 0$ ($\overline{uv} < 0$). Cross-slope modes are superposed upgoing and downgoing waves of equal amplitude with standing-wave cross-slope structure: alternating bands of clockwise- and anticlockwise-rotating currents separated by vertical surfaces parallel to isobaths, and current ellipse axes parallel and perpendicular to isobaths so $\overline{uv} = 0$.

3.3.b. Refraction by changing bottom slope

For an energy-upslope wave ($k > 0$) define γ

$$\cos\gamma = k/\kappa \qquad \sin\gamma = -l/\kappa \qquad \tan\gamma = -l/k \tag{3.23}$$

as the angle the group velocity makes with the direction of alongslope propagation along the $-y$ axis (Figure 3.7). The dispersion relation (3.19) is

$$\sigma = Nh_x \sin\gamma, \tag{3.24}$$

and the group velocity (3.20) is

$$c_g^x = \frac{\sigma}{l}\cos\gamma\sin\gamma \qquad c_g^y = \frac{\sigma}{l}\cos^2\gamma \qquad \left|\vec{c_g}\right| = \left|\frac{\sigma}{l}\cos\gamma\right|. \tag{3.25}$$

A ray path $y^{ray}(x)$ is oriented at an angle to isobaths such that

$$\frac{dy}{dx}^{ray} = c_g^y / c_g^x = -k/l = \cot\gamma. \tag{3.26}$$

Expressions using γ apply only to upslope-energy rays, $0 < \gamma < \pi/2$.

Consider an upslope-energy ray crossing a region of increased bottom slope that changes steepness over a lengthscale much longer than the wavelength so WKB ray theory (Lighthill 1978) applies (Figure 3.8). Along the ray, frequency σ and alongslope wavenumber l remain constant. From (3.24), as the ray encounters steeper (gentler) slope, it is refracted toward (away from) the along-slope direction as its cross-slope wavenumber k increases (decreases). The vertical trapping scale Z, by (3.16), thus decreases (increases) over steeper (gentler) slope.

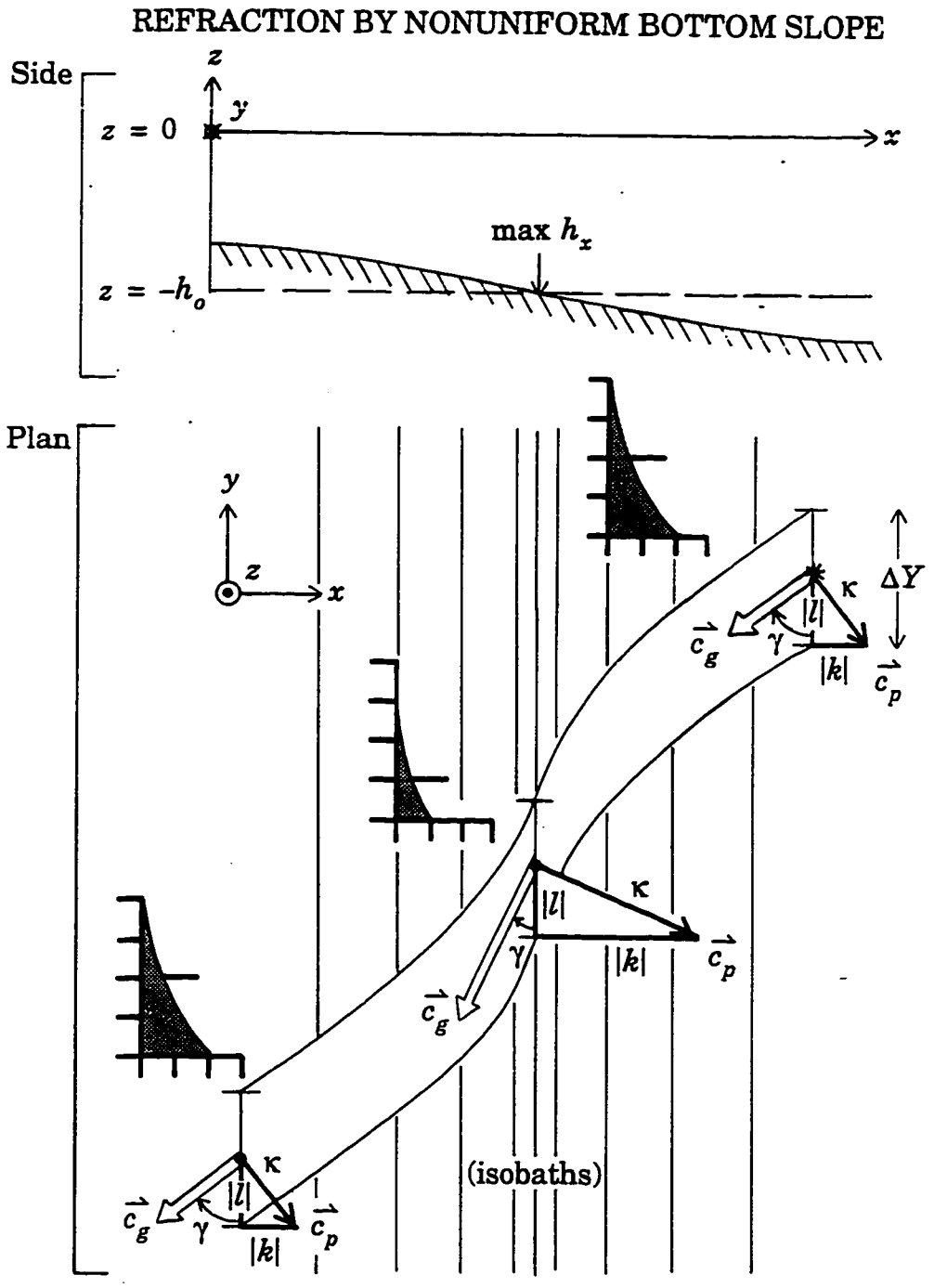

Figure 3.8. Refraction of upslope-energy ray by nonuniform slope. Insets show vertical structure variation (see Figure 3.7) of ray started at asterisk with $\gamma_* < \pi/4$ (schematic only). See text for discussion.

As a ray moving primarily along isobaths ($\gamma < 45°$) encounters a local maximum in slope, there is a local maximum in energy E^z (3.18) and a local minimum in streamfunction amplitude ψ_b (3.15). (Though not quasigeostrophic, rays on the flanks of a typical seamount with slope angle 10° and stratification at least $N = 10f$ (see Table 3.1) have $\gamma < 45°$ by (3.24).) A ray started with E^z_*, ψ_{b*}, $\vec{c}_{g*}$, γ_*, and alongslope cross-section ΔY_* has cross-slope energy transport $T^x_* = E^z_* c^x_{g*} \Delta Y_*$. Energy conservation requires constant cross-slope energy transport T^x along the ray,

$$T^x = E^z c^x_g \Delta Y = T^x_*$$

and by ray geometry $\Delta Y = \Delta Y_*$, so energy variation along the ray is

$$\frac{E^z}{E^z_*} = \frac{c^x_{g*}}{c^x_g} = \frac{\cos\gamma_* \sin\gamma_*}{\cos\gamma \sin\gamma} \tag{3.27}$$

by (3.25). As a ray initially oriented with $\gamma_* < 45°$ ($\gamma_* > 45°$) reaches steeper slope, its energy E^z increases (decreases). Rays with $\gamma < 45°$ therefore have a local maximum in energy at a local maximum in slope. Using (3.18) and (3.25) in (3.27), streamfunction amplitude varies as

$$\frac{\Psi_b^2}{\Psi_{b*}^2} = \frac{\cos\gamma_*}{\cos\gamma} \tag{3.28}$$

so as the ray reaches steeper (gentler) slope the streamfunction amplitude decreases (increases) as shown in Figure 3.8.

3.3.c. Turning points, refractive trapping, cross-slope modes

A ray reaches a turning point where the slope has value (from (3.24))

$$h_x = \sigma/N, \tag{3.29}$$

so a sloping region bounded on both sides by weaker slopes than (3.29) refractively traps rays and forms a waveguide (Figure 3.9). Refractive trapping of stratified slope-Kelvin wave rays and formation of cross-slope modes by changing bottom slope is analogous to formation of baroclinic vertical modes by internal gravity waves trapped to a thermocline above and below which the buoyancy frequency decreases. As a ray approaches bottom slope of (3.29), cross-slope wavenumber k tends toward zero. A turning point is reached, where k passes through zero and the cross-slope sense of travel reverses. Near the turning point WKB assumptions are invalid and the amplitude has Airy function structure (Lighthill 1978). Rays do not propagate where the slope is weak so are trapped in a waveguide centered on the maximum slope.

WAVEGUIDE: TURNING POINTS AND REFRACTIVE TRAPPING

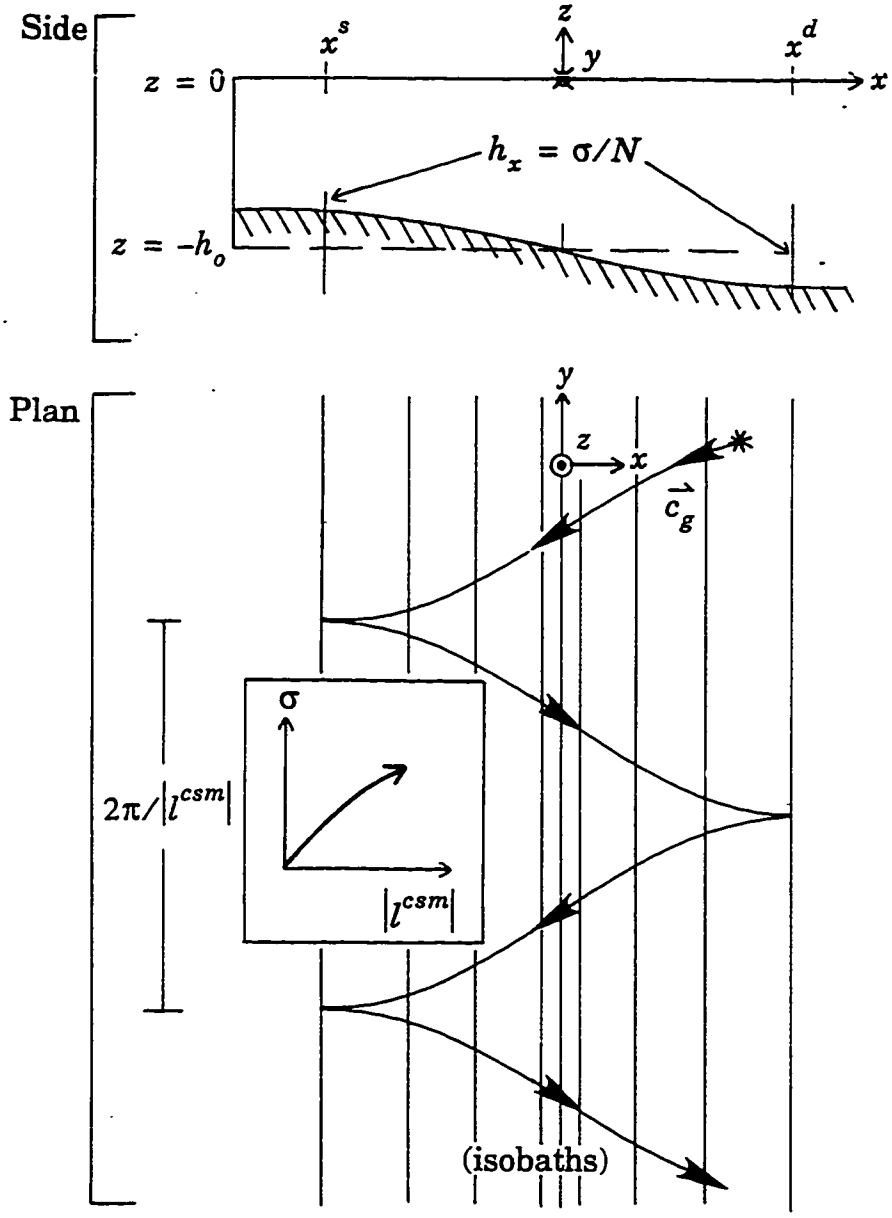

Figure 3.9. Idealized ray path with turning points, showing refractive trapping and waveguide formation. Inset: schematic dispersion relation of resulting cross-slope modes. See text for discussion.

The distance between successive turning points on one side of the waveguide sets an alongslope lengthscale that determines the wavenumber l^{csm} of a *cross-slope mode* (Figure 3.9). A cross-slope mode forms from constructive interference of rays having alongslope wavenumber l such that l^{csm}/l is an integer. Cross-slope modes propagate phase purely alongslope with shallow water on the right ($l^{csm} < 0$) and have standing-wave cross-isobath structure. Ray behavior helps to conceptualize the formation of the lowest cross-slope mode ($l = l^{csm}$) though WKB ray theory does not strictly apply. Cross-slope modes may be identified with coastal-trapped waves (Huthnance 1978) in strong stratification away from the influence of the coastal boundary.

The bathymetric shape $h(x)$ sets the dispersion relation (inset, Figure 3.9) between cross-slope mode frequency σ and wavenumber magnitude $|l^{csm}|$

$$\sigma = D\left(|l^{csm}|\right), \tag{3.30}$$

where the monotonically increasing function D represents the relation

$$\int_{x^s(h_x = \sigma/N)}^{x^d(h_x = \sigma/N)} \left|\frac{dy}{dx}^{ray}\right| dx = \frac{\pi}{|l^{csm}|} \tag{3.31}$$

involving the integral of ray orientation $\frac{dy}{dx}^{\text{ray}}$ (3.26) between turning points on the shallow x^s and deep x^d sides of the waveguide. For the first cross-slope mode ($l^{\text{csm}} = l$), (3.26) and (3.19) may be used in (3.31) to obtain

$$\int_{x^s(h_x=\sigma/N)}^{x^d(h_x=\sigma/N)} \sqrt{(Nh_x(x)/\sigma)^2 - 1}\; dx = \frac{\pi}{|l^{\text{csm}}|}. \tag{3.32}$$

The monotonic increase of D is clear from (3.32): for a given $h(x)$ and N, an increase in σ decreases both the wave ray orientation $\frac{dy}{dx}^{\text{ray}}$ (integrand) and the distance between turning points determining the waveguide width (region of integration), hence $|l^{\text{csm}}|$ must increase. For a cross-slope mode the dispersion relation (3.30) is a one-to-one relation between frequency and alongshore wavenumber magnitude $|l^{\text{csm}}|$, in contrast to the dispersion relation for an individual ray (3.24) in which frequency is a function only of wavevector *orientation* (the ratio l/k) and not its *magnitude* (l and k magnitudes).

3.3.d. Phase behavior on steep slopes

Unlike the vertical phase planes of quasigeostrophic stratified slope-Kelvin rays (3.15), for realistic topographic slopes and frequencies higher than

allowed by quasigeostrophic scaling ($h_x > Ro\frac{f}{N}$, $\sigma/f > Ro$) phase planes of individual energy-upslope (-downslope) rays are inclined such that they disappear into (are emitted from) a uniformly sloping boundary (Rhines 1970). To illustrate this consider the coordinate frame (x', y, z') rotated about the y-axis from (x, y, z) above such that x' is downslope across bathymetric contours *parallel to the boundary*, and z' increases from zero with *perpendicular* distance from the boundary. Dynamical variables in terms of wavenumbers (k', l, m') are proportional to

$$\exp(-z'/Z)\exp(i(k'x' + ly + m'_{\text{real}}z' - \sigma t)), \tag{3.33}$$

where the total wavenumber perpendicular to the boundary

$$m' = i/Z + m'_{\text{real}}$$

is *complex*, comprised of a real component m'_{real} in addition to the imaginary part $1/Z$ that causes trapping perpendicular to the boundary as in quasigeostrophic waves (3.15). The sign of m'_{real} is the same as that of k' (Rhines 1970) so phase propagates into (out of) the boundary in waves propagating downslope (upslope), that carry energy upslope (downslope) as in Figure 3.7.

For non-quasigeostrophic stratified slope-Kelvin rays the dispersion relation dependence on wavenumber components (k', l) *in the plane of the boundary* is identical to that of (k, l) for quasi-geostrophic rays (3.19). Group

velocity is parallel to the boundary. The additional phase structure associated with complex wavenumber perpendicular to the slope does not change ray behavior. Ray refraction by nonuniform slope as described above applies unmodified to non-quasigeostrophic rays moving in the plane of a steep boundary having WKB variations in slope.

Refractively-trapped cross-slope modes formed from non-quasigeostrophic rays propagate phase purely alongslope, not into or out of the boundary, unlike the individual rays. Superposition of upslope and downslope rays of equal amplitude offsets equal and opposite real wavenumber components perpendicular to the slope, causing the resulting cross-slope mode to have purely imaginary wavenumber perpendicular to the boundary. Surfaces of constant phase of the cross-slope mode are thus vertical even though this is not true of the individual rays superposed to comprise them.

3.3.e. Effects of cylindrical geometry

A ray on the uniformly sloping side of a cone spirals inward and is geometrically compressed, causing energy and streamfunction amplitude to be inversely proportional to radius (Figure 3.10). Many wavelengths away from the center, the behavior may be understood by converting locally to cylindrical coordinates (r, θ, z) . The dispersion relation (3.24) becomes

$$\sigma = Nh_r \sin\gamma,$$

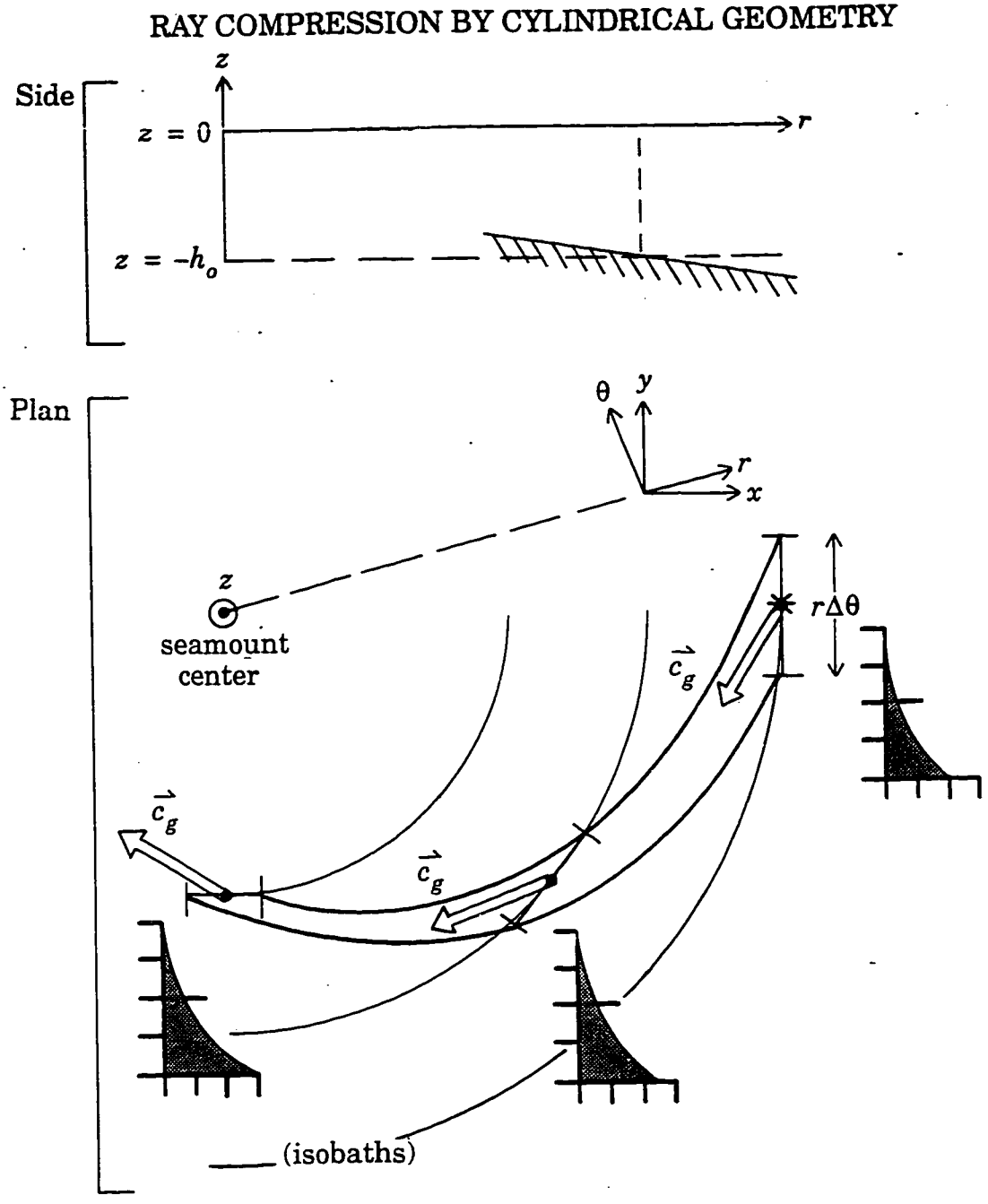

Figure 3.10. Compression of wave ray due to cylindrical geometry on the uniformly sloping side of a cone in the southeast quadrant. Schematic as in Figure 3.7 and Figure 3.8. See text for discussion.

where h_r is the uniform slope along a radius and γ is the angle the ray makes with the circular isobath. To preserve γ, rays spiral inward, geometrically compressing ray tubes. Energy transport in the radial direction is preserved,

$$T^r = E^z c_g^r r \Delta\theta = T_*^r.$$

Ray geometry has $\Delta\theta = \Delta\theta_*$, and for constant bottom slope $c_g^r = c_{g*}^r$, so

$$\frac{E^z}{E_*^z} = \frac{\psi_b^2}{\psi_{b*}^2} = \frac{r_*}{r}. \tag{3.34}$$

Hankel functions near the origin (Rhines 1969) give the same result. Constant-phase surfaces of upslope- (downslope-) energy quasigeostrophic rays are vertical sheets spiralling from the origin clockwise (anticlockwise).

A seamount has sloping flanks bounded by flat regions at inner and outer radii, so forming a waveguide in the azimuthal direction that is re-entrant and hence has resonance frequencies for cross-slope modes: seamount-trapped waves. The resonance frequency for a first azimuthal mode is that for which a ray, on encountering turning points at an inner radius and an outer radius that are separated by π in azimuth, reaches its original position to interfere constructively with itself (Figure 3.11). In terms of the rectilinear example above (Figure 3.9) the re-entrant nature of the waveguide in cylindrical coordinates is equivalent to fixing the alongslope wavelength of the cross-

FIRST AZIMUTHAL WAVENUMBER RESONANCE

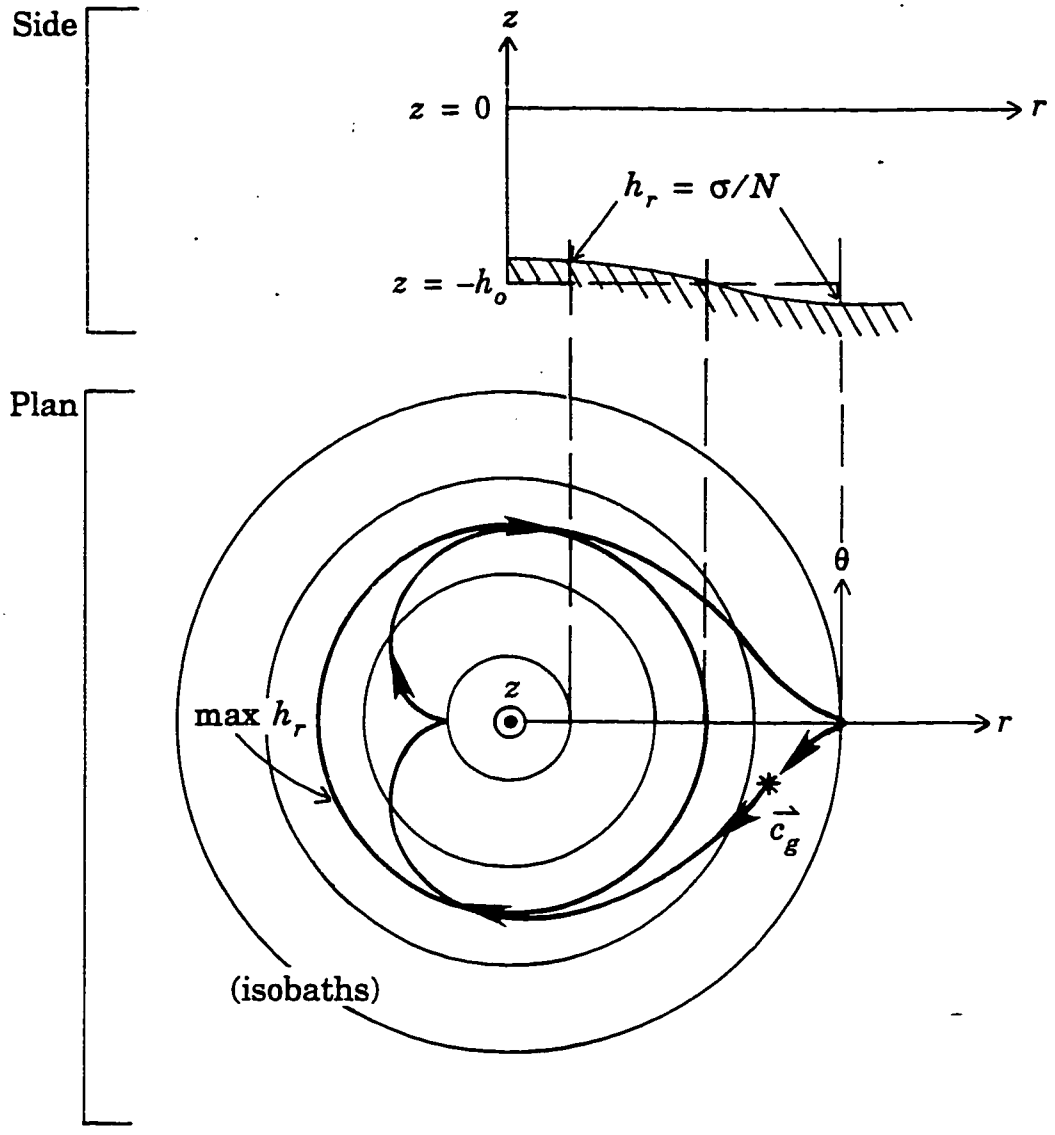

Figure 3.11. Schematic ray path, from asterisk, for first azimuthal wavenumber resonance. As Figure 3.8. See text for discussion.

slope mode to a value set by the effective seamount circumference $l^{csm} = l_{smt}$ and hence allowing one resonant frequency $\sigma = D(|l_{smt}|)$ (3.30).

Associated with the increase in seamount-trapped wave resonant frequency for increased bottom slopes (Rhines 1970, Brink 1989) is a reduction of

$\left|\frac{dy}{dx}^{\text{ray}}\right|$, corresponding to wave rays that form the mode oriented more strongly across isobaths (3.26). As is physically intuitive, increased bottom slope strengthens the potential vorticity gradient supporting the wave and increases the resonant frequency because the wavelength is fixed by the seamount circumference. This may be understood using (3.32) for fixed $l^{\text{csm}} = l_{\text{smt}}$ but increasing the slope everywhere $h_x \to c h_x$ by a factor c: the frequency increases $\sigma \to c\sigma$. Chapter 4 explains mean flow changes to resonant frequencies in terms of in terms of how $\left|\frac{dy}{dx}^{\text{ray}}\right|$ is modified.

3.3.f. Summary: formation of stratified seamount-trapped wave

The free seamount-trapped wave described in Section 3.2.b is a cross-slope (radial and vertical) mode propagating azimuthally clockwise with azimuthal wavenumber one at the resonant frequency. It can be considered a superposition of equal-amplitude upslope- and downslope-energy non-quasi-geostrophic stratified slope-Kelvin rays started with constant phase from points along a radius. Cross-slope variations of amplitude and vertical trapping scale are determined by the combined influence on the rays of (i) refraction by changing bottom slope, (ii) Airy-function behavior near turning points, and (iii) geometric compression by cylindrical geometry. Individual upslope- and downslope-energy rays propagate phase equally and oppositely in the ver-

tical and radial, so the superposition propagates phase in the azimuthal direction only and not radially or vertically.

3.4. Forcing and frictional influences

It is appropriate to investigate the influence of forcing and friction in this idealized setting, since periodically forced and strongly dissipated observed currents are best compared to a stationary (steady amplitude in time) forced and damped response. Forcing by far-field currents with both anticlockwise- and clockwise-rotating components excites distinct current ellipse patterns. Free wave symmetry is broken by friction or nonstationarity, which cause superposed upgoing and downgoing rays to have different amplitudes and net cross-slope fluxes of momentum and buoyancy, absent in the free wave, to be nonzero. Mean azimuthal circulation and buoyancy anomaly, as seen in observations (Chapter 2, Brink 1995) and models (Haidvogel et al. 1993, Codiga 1993) can be excited by such cross-slope flux divergences (Section 3.5). This section explains observational signatures of forced and damped waves, relating them to ray behavior of Section 3.3.

3.4.a. Governing equations

Forcing and friction are incorporated in the system of equations and boundary conditions (3.1) and (3.2) in the following way:

$$
\begin{aligned}
u_t - fv &= -p_r + F^u - Ru && (a)\\
v_t + fu &= -\frac{1}{r}p_\theta + F^v - Rv && (b)\\
0 &= -p_z + b && (c)\\
b_t + N^2 w &= -Rb && (d)\\
\frac{1}{r}(ru)_r + \frac{1}{r}v_\theta + w_z &= 0 && (e)
\end{aligned}
\qquad (3.35)
$$

$$
\begin{aligned}
&(p, u, v, w, b) = (0, u_F, v_F, 0, 0) \quad \text{as} \quad r \to \infty && (a)\\
&(p, u, v, w, b) \quad \text{bounded at} \quad r = 0 && (b)\\
&w + h_r u = w_E(u, v) \quad \text{at} \quad z = -h && (c)\\
&w = 0 \quad \text{at} \quad z = 0\,. && (d)
\end{aligned}
\qquad (3.36)
$$

As described in the following two subsections, waves are excited through (3.36)(c) in response to spatially uniform oscillating far-field tidal currents (u_F, v_F) maintained by body forces $\left(F^u, F^v\right)$; R is a constant coefficient of Rayleigh drag with Newtonian cooling and heating; and w_E is pumping due to bottom-stress parameterization of a time-dependent bottom Ekman layer.

3.4.a.i.Excitation by tidal currents

To represent barotropic open-ocean tidal currents with horizontal scale much greater than the seamount, waves are forced by oscillatory horizontal flow without horizontal or vertical shear. This far-field flow is maintained by the body forces to have arbitrary current-ellipse shape and rotation direction.

It is a superposition of components rotating anticlockwise and clockwise in time. East and north far-field velocities $\left(u_F^x, u_F^y\right)$ in *Cartesian* coordinates are

$$u_F^x(r,\theta,z,t) = u_F^x(t) = \exp\left(\frac{t}{T_{td}}\right)\Re\left[\left(u_F^{ACW}+u_F^{CW}\right)\exp\left(-i\sigma t\right)\right]$$
$$u_F^y(r,\theta,z,t) = u_F^y(t) = \exp\left(\frac{t}{T_{td}}\right)\Re\left[i\left(u_F^{ACW}-u_F^{CW}\right)\exp\left(-i\sigma t\right)\right]$$

where $\Re$ indicates the real part, and complex constants u_F^{ACW} and u_F^{CW} (real part eastward current, imaginary part northward current) give magnitude and phase of anticlockwise- and clockwise-rotating components respectively. Exponential growth of tidal amplitude on timescale T_{td} (subscript *td* for "time-dependence") longer than the wave period may be included, for example, as a simple representation of a short portion of a fortnightly cycle.

Equivalent radial and azimuthal velocities in cylindrical coordinates,

$$u = u^x\cos\theta + u^y\sin\theta$$
$$v = -u^x\sin\theta + u^y\cos\theta,$$

propagate azimuthally anticlockwise and clockwise:

$$u_F(r,\theta,z,t) = u_F(\theta,t) = u_F^+(\theta,t) + u_F^-(\theta,t) = \exp\left(\frac{t}{T_{td}}\right)\Re\left[\tilde{u}_F^+\exp\left(i\varphi^+\right)+\tilde{u}_F^-\exp\left(i\varphi^-\right)\right] \qquad (a)$$
$$v_F(r,\theta,z,t) = v_F(\theta,t) = v_F^+(\theta,t) + v_F^-(\theta,t) = \exp\left(\frac{t}{T_{td}}\right)\Re\left[\tilde{v}_F^+\exp\left(i\varphi^+\right)+\tilde{v}_F^-\exp\left(i\varphi^-\right)\right] \qquad (b) \qquad (3.37)$$

where

$$\varphi^{+} = +\theta - \sigma t; \quad \text{anticlockwise propagation}$$
$$\varphi^{-} = -\theta - \sigma t; \quad \text{clockwise propagation}$$

and the complex constants are defined

$$\tilde{u}_F^{+} = u_F^{ACW} \qquad \tilde{u}_F^{-} = u_F^{CW}$$
$$\tilde{v}_F^{+} = iu_F^{ACW} \qquad \tilde{v}_F^{-} = -iu_F^{CW}.$$

In summary, far-field flow in (3.36)(a) is specified using (3.37) with real constants (σ, T_{td}^{-}) and complex constants $\left(u_F^{ACW}, u_F^{CW}\right)$.

3.4.a.ii.Friction

To examine modifications to waves by frictional damping, two artificial parameterizations may be included. The first is Rayleigh drag with Newtonian heating and cooling, terms in (3.35)(a), (b), and (d) proportional to the constant R (dimensions [1/time]), that are together referred to as *Rayleigh damping*. This is not intended to represent accurately the poorly understood mechanism of oceanic dissipation. It is applied to allow strong frictional influence throughout the water column, as seems appropriate based on turbulence measurements from Cobb Seamount (Mudge 1994) and Fieberling Guyot (Kunze and Toole 1996), with an analytically convenient form. Unforced waves decay exponentially with timescale R^{-1}.

The second form of damping is a pumping velocity w_E deviation from the kinematic bottom condition (3.36)(c), representing the integrated effect of an oscillatory bottom Ekman layer (Brink 1989). Reduced bottom stress (stress/ρ_o) is parameterized in terms of the velocity at the top of the bottom boundary layer,

$$\left[\tau^r, \tau^\theta\right]\Big|_{z=-(h+\delta_E)} = \kappa_E \left[u, v\right]\Big|_{z=-h} , \tag{3.38}$$

where δ_E is boundary layer thickness and κ_E is a constant resistance parameter (dimensions [length/time]). No buoyancy effects are included and the derivation of $w_E(u, v)$ is in the limit $\delta_E \to 0$ (Appendix C), so the boundary layer is not resolved and secondary circulation effects of the type considered by MacCready and Rhines (1991) in the steady case are not accounted for. Comparison with steady flat-bottom Ekman theory yields eddy viscosity in the boundary layer $\upsilon_E \approx 2\kappa_E^2/f$ and boundary layer thickness $\delta_E \approx 2\kappa_E/f$. Using vertical scale fL/N of rotating stratified flow (Gill 1982), the spin-down timescale $\frac{\text{vertical scale}}{f\delta_E}$ (Greenspan 1960) is $\frac{fL}{N\kappa_E}$, in agreement with spin-down timescales from a perturbation method using specific wave structures (Brink 1989).

3.4.b. Resonance behavior

Comparing summit response to far-field flow provides two diagnostics, the amplification

$$A = u_A / \sqrt{u_F^2 + v_F^2}$$

and relative velocity orientation angle

$$\Delta = \tan^{-1}\left(u^y, u^x\right)\Big|_{\text{summit}} - \tan^{-1}\left(u_F^y, u_F^x\right).$$

Summit velocity is rotated counterclockwise by Δ from the far-field velocity.

Frequency response (Figure 3.12) of the $S = 12$ system in Table 3.1 is dominated by resonances of free waves described in Section 3.2. Consider frictionless response to clockwise-rotating far-field currents (circles, Figure 3.12). There are 2 resonances for $0.4 \le \sigma/f \le 0.95$, each an eigensolution for which $A \to \infty$. As frequency passes through resonance Δ changes by $180°$, the signature of a summit velocity reversal analogous to behavior of a forced pendulum.

For clockwise-rotating far-field currents A is at least 50, far exceeding observed amplifications, even at frequencies away from resonance and when damping occurs on a timescale as short as a few days. This is associated with the circular symmetry of the seamount (Beckmann, 1995). Solutions are examined here for amplitudes corresponding to wave steepness $\varepsilon = 0.15$ in order that near-summit flow is consistent with observed levels $u_A \approx 15$ cm/s, with the result that exaggerated amplification is de-emphasized.

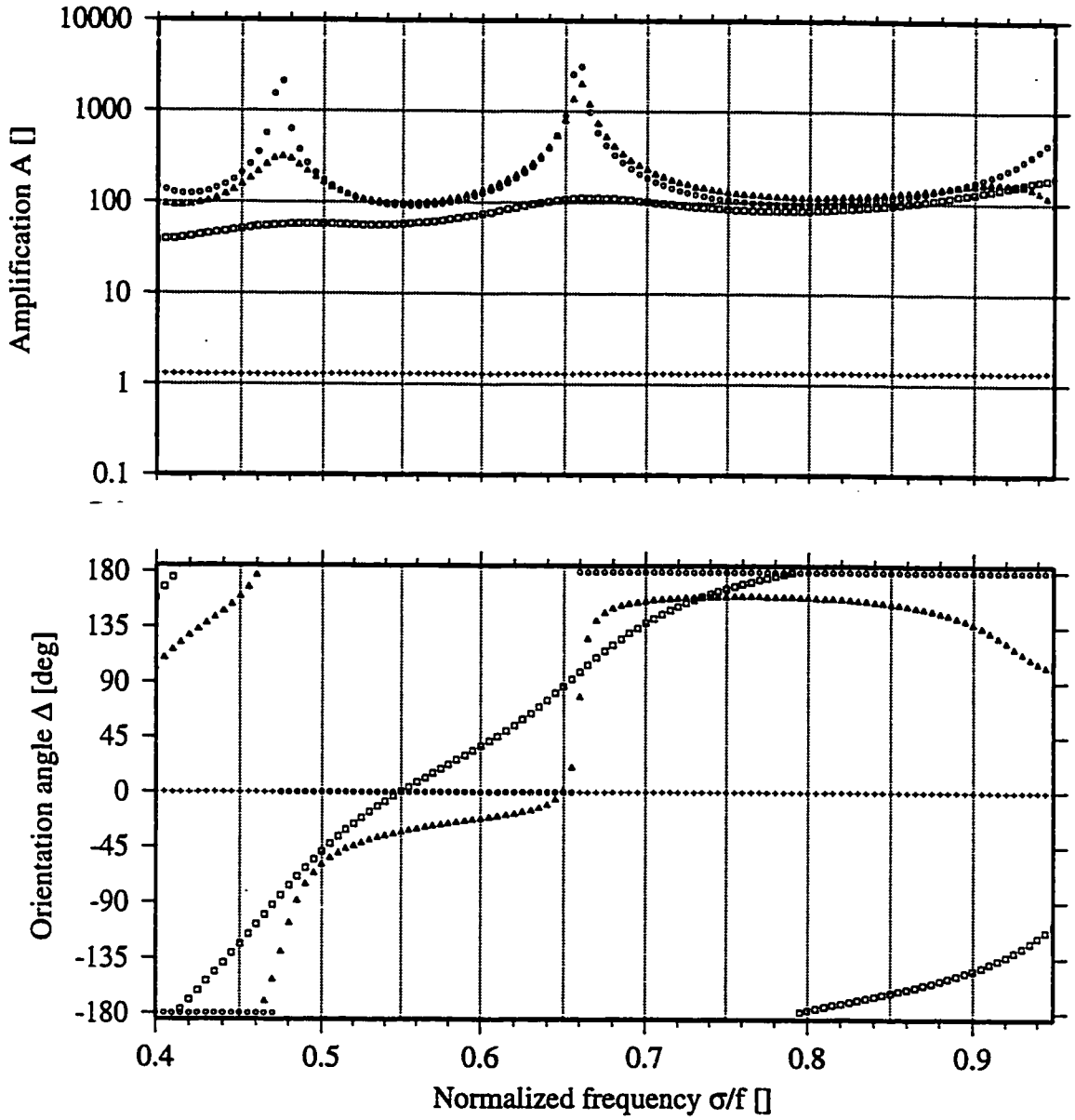

Figure 3.12. Amplification (upper panel) and counterclockwise rotation angle (lower panel) of summit response velocity relative to far-field flow. Circles (crosses): inviscid solutions with clockwise- (anti-clockwise-) rotating far-field currents. Squares [triangles] are solutions with clockwise-rotating far-field currents, damped by: Rayleigh friction ($\kappa_E = 0$) of timescale $R^{-1} = 2$ days [Ekman pumping ($R = 0$) for $\kappa_E = 0.05$ cm/s, that corresponds to spin-down timescale 18 days and 10 m-thick boundary layer with eddy viscosity 50 cm^2/s].

Friction gives finite amplification at eigensolution frequencies, preferentially damps modes other than the gravest, and causes the relative summit velocity orientation angle Δ to change continuously as frequency passes through a resonance (squares and triangles, Figure 3.12). The variation of Δ with frequency is a strong function of the strength and parameterization of friction. For 2-day decay timescale appropriate to measured levels of turbulence (Mudge 1994), friction parameterized as Rayleigh drag with Newtonian cooling and heating effectively replaces reversals of summit velocity above and below resonances with nearly linear frequency variation of Δ.

3.4.c. Off-resonant and anticlockwise-rotating forcing

Amplification weakens at frequencies away from resonance, though remaining significantly enhanced over the minimum off-resonant amplification in a frequency range about $0.05f$ wide (circles, Figure 3.12). Peak width is set by inviscid behavior of the system. Friction reduces amplification levels near resonance, but changes only slightly the frequency of maximum response from the inviscid case ($< 0.01f$ in Figure 3.12) and the peak width. Strong response may thus be expected even at seamounts where tidal forcing is not closely tuned to the resonant frequency (Chapman 1989, Brink 1990).

Frictionless off-resonant solutions for clockwise-rotating far-field flow (not shown) exhibit the same standing cross-slope behavior, and very similar current-ellipse patterns, as free waves. They are a forced response formed

from forced stratified slope-Kelvin waves, denoted *evanescent* waves by Eriksen (1995), in the same way free seamount-trapped waves are related to free stratified slope-Kelvin wave rays (Section 3.3).

Anticlockwise-rotating far-field currents excite no resonances (crosses, Figure 3.12), because no anticlockwise-propagating free waves are allowed (Brink 1989). The response is not amplified ($A \approx 1$), has summit velocity oriented parallel to forced velocity ($\Delta = 0$) if inviscid, and is nearly barotropic with current ellipses (not shown) modified from the far-field flow only to accommodate the presence of the topography.

Response to mixed anticlockwise- and clockwise-rotating tidal currents has current ellipses at certain azimuths oriented at an angle to bathymetric contours (Figure 3.13), but azimuthal-mean cross-slope fluxes remain zero. Typical oceanic tidal currents are a superposition of clockwise- and anticlockwise-rotating components. Responses to the two may be of comparable magnitude at off-resonant frequencies if, as is caused by asymmetric seamount shape (Beckmann 1995), the response to clockwise-rotating forcing is less exaggerated than in the present circular geometry. In this case, at certain azimuths current ellipses have axes oriented at an angle to isobaths (for example Figure 3.13a, at $\theta = 45°$). Time-mean correlations between dynamical variables that are in quadrature in the free-wave eigensolutions, for example u and v (3.7), may therefore be nonzero at these locations. However, because

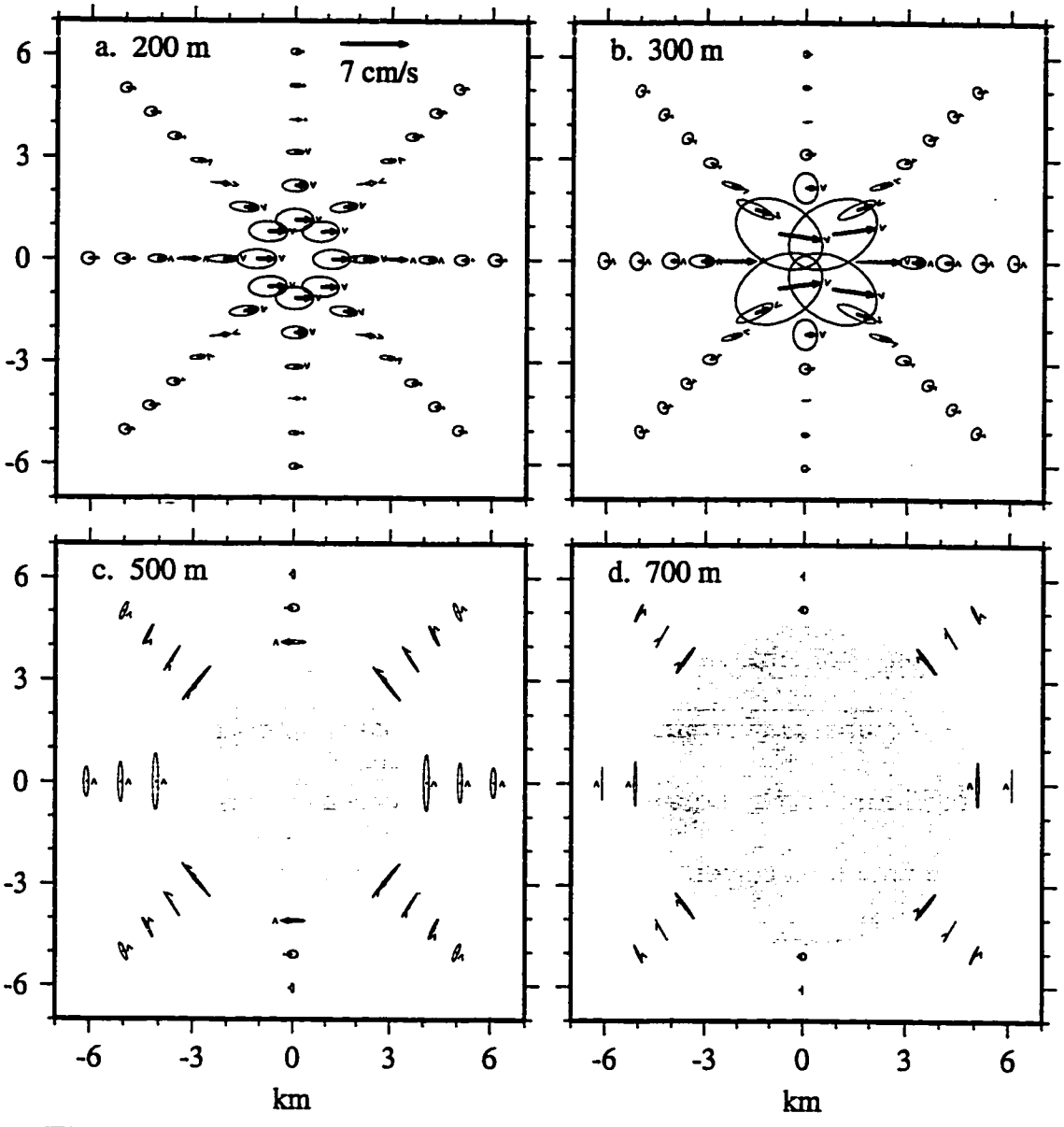

Figure 3.13. Current ellipses away from resonance (σ/f = 0.55, Figure 3.12) for mixed clockwise- and anticlockwise-rotating far-field components in relative proportion 1:50 such that responses to the two are comparably strong. Shown as the free wave in Figure 3.3. In contrast to the free wave, current ellipses lie at an angle to seamount contours at certain azimuths (compare θ = 45° in a. to Figure 3.3a).

this superposes clockwise- and anticlockwise-rotating components, an average over a wave period is not the same as an azimuthal average. By symmetry the correlations do not survive the azimuthal average and azimuthal-average cross-slope buoyancy and energy fluxes remain zero as in the free wave.

Current ellipses with major axes aligned dominantly east-west at all azimuths (Figure 3.13) are seen in laboratory response (Zhang and Boyer 1993) forced by large-amplitude east-west currents, a mixture of clockwise- and anticlockwise-rotating components. Large-amplitude forcing reduces the relative amplification of the clockwise-rotating component. For weaker forcing amplitudes, response to clockwise-rotating forcing dominates (Codiga 1993).

3.4.d. Forced damped and nonstationary waves

In a nonstationary wave forced by time-dependent far-field flow and in a frictionally damped wave, contrasting a free wave, radial and vertical phase propagation occurs and azimuthal-average cross-slope buoyancy and energy fluxes are nonzero because of phase shifts between dynamical variables. This subsection examines such modifications. Only clockwise-rotating tidal currents are treated ($u^{ACW} = 0$), so in calculating cross-slope fluxes an average over a wave period and an azimuthal average $\overline{(\,)}$ are equivalent. For analytical convenience, and because it is more appropriate based on measured turbulence (Mudge 1994, Chapter 1), only Rayleigh friction is included ($w_E = 0$). Phase shifts caused by friction are qualitatively similar when parameterized

using Rayleigh friction and Ekman pumping from bottom stresses, suggesting it is appropriate to compare the results to observed flow even though its frictional mechanisms are not well understood.

Three types of waves have identical structure: a *stationary forced and damped* wave maintained against Rayleigh friction R by body forces; an *unforced damped wave* decaying under Rayleigh friction R after forcing has been discontinued; and an *undamped nonstationary wave* excited by time-dependent forcing that grows on timescale $T_{td} = R^{-1}$. Though instantaneous $t = 0$ structures are identical, amplitudes are constant, decaying, and increasing in time respectively for these three types of wave.

Nonstationary or frictional waves have nonzero azimuthal-mean correlations between dynamical variables $\overline{uv}$, $\overline{ub}$, $\overline{up}$, $\overline{wv}$, $\overline{wb}$, and $\overline{wp}$, in contrast to free waves (3.7). To solve (3.35), (3.36), and (3.37), velocities (u, v) are divided into components (u_S, v_S) trapped to the seamount and spatially uniform far-field components (u_F, v_F). By (3.37) with $u^{ACW} = 0$,

$$\begin{aligned} u_F &= \exp\left(\frac{t}{T_{td}}\right)\Re\{\tilde{u}_F \exp[i(-\theta - \sigma t)]\} \\ v_F &= \exp\left(\frac{t}{T_{td}}\right)\Re\{\tilde{v}_F \exp[i(-\theta - \sigma t)]\}, \end{aligned} \tag{3.39}$$

where superscripts "-" have been dropped. The trapped portion of the solution (p, u_S, v_S, w, b) has form, using p as an example, matching the harmonic azimuthal structure of the far-field flow but varying in radius and depth,

$$p(r,\theta,z,t) = \exp\left(\frac{t}{T_{td}}\right)\Re\{\tilde{p}(r,z)\exp[i(-\theta-\sigma t)]\}. \tag{3.40}$$

Using (3.35) less the governing equations of the far-field flow,

$$\begin{aligned} u_{Ft} - fv_F &= F^u - Ru_F \\ v_{Ft} + fu_F &= F^v - Rv_F, \end{aligned} \tag{3.41}$$

the modal structure functions for each dynamical variable in terms of the pressure modal structure function $\tilde{p}$ are

$$\begin{aligned} \tilde{u}_S &= \left(f^2 - \sigma'^2\right)^{-1}\left(i\sigma'\tilde{p}_r + \frac{if}{r}\tilde{p}\right) & \tilde{w} &= \frac{i\sigma'}{N^2}\tilde{p}_z \\ \tilde{v}_S &= \left(f^2 - \sigma'^2\right)^{-1}\left(f\tilde{p}_r + \frac{\sigma'}{r}\tilde{p}\right) & \tilde{b} &= \tilde{p}_z. \end{aligned} \tag{3.42}$$

where $\sigma' \equiv \sigma + iR + iT_{td}^{-1}$. Nonstationarity and/or friction cause complex σ', introducing phase shifts such that u and w are no longer in quadrature with p, v, and b. This causes azimuthal-mean cross-slope fluxes described below.

A stationary forced and damped wave is described here for parameters of Table 3.1 at $S = 12$, forced at the resonance frequency $0.657f$ of the gravest free wave described in Section 3.2.b. Rayleigh damping of timescale $R^{-1} =$ 2 days is included, as appropriate to dissipation observed at Cobb Seamount (Mudge 1994, Chapter 1) and Fieberling Guyot (Kunze and Toole 1996).

3.4.d.i.Currents

Three current signatures of a stationary forced and damped wave indicate the standing-wave radial and vertical structure of the free wave is broken such that energy propagates inward and upward. First, the stationary forced and damped wave is distinct from a free wave in that horizontal current ellipse axes are oriented at an angle, at all azimuths, to bathymetric contours such that $\overline{uv} > 0$ (Figures 3.14 and 3.15). In terms of superposed stratified slope-Kelvin wave rays, positive $\overline{uv}$ corresponds to upslope-energy ray amplitude exceeding that of the downslope-energy ray (Figure 3.7). Wave energy transport plays an important role in the energy budget (Section 3.4.d.iii).

Second, for higher radial-vertical modes that have free-wave structure with relatively narrower depth intervals where currents rotate anticlockwise in time (Figure 3.6), the stationary forced and damped wave may have currents rotating clockwise in time everywhere. Friction spreads features in modal structures over larger scales, so narrow depth intervals where currents

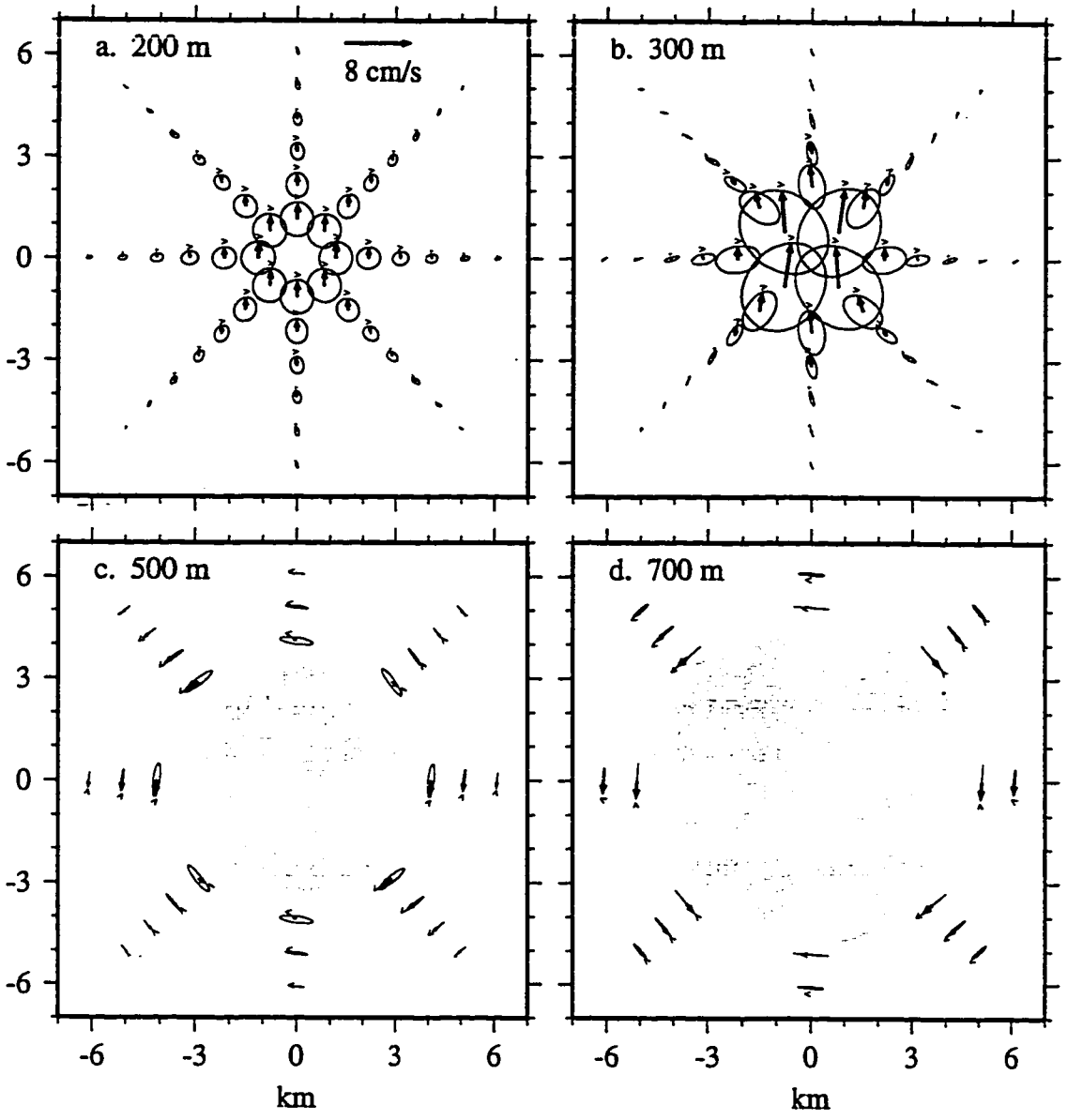

Figure 3.14. Current ellipses for the wave of Figure 3.3 damped by 2-day Rayleigh friction. Current ellipses at all azimuths have axes oriented across seamount contours (compare c. to Figure 3.3c) such that $\overline{uv} > 0$ (see also Figure 2.3d).

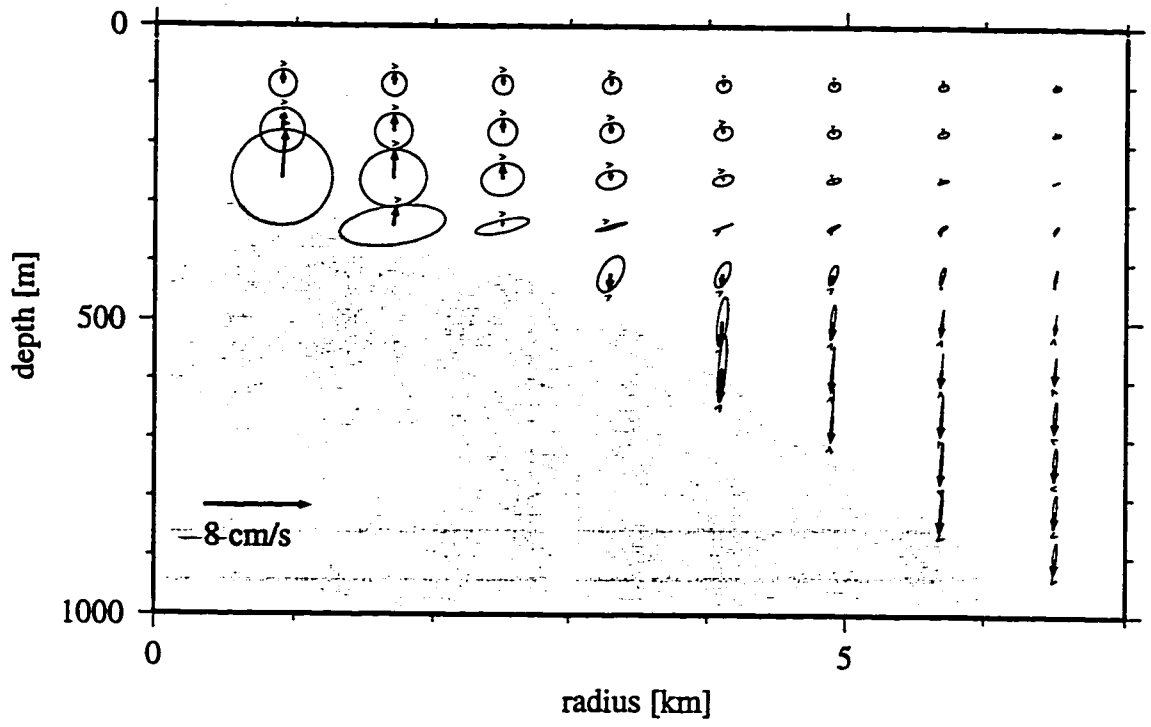

Figure 3.15. Current ellipses of the wave in Figure 3.14, shown as in Figure 3.4a. There is systematic asymmetry with $\overline{uv} > 0$.

rotate anticlockwise in time can be overcome by adjacent regions rotating clockwise in time.

Finally, the forced and damped wave exhibits dominantly anticlockwise turning with depth of horizontal velocity, breaking the symmetry of alternately anticlockwise- and clockwise- turning during a period in a free wave. This effect is strongest in higher radial-vertical modes due to their smaller vertical scales. Figure 3.16 demonstrates the asymmetry at two locations in the 2nd-gravest $S = 48$ mode of Figure 3.6. In higher radial-vertical modes (not shown) turning with depth becomes anticlockwise throughout the period.

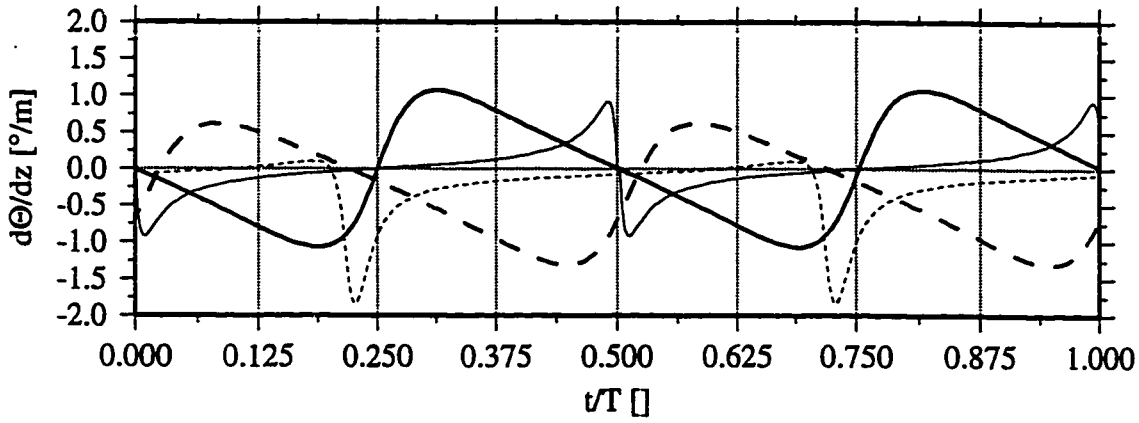

Figure 3.16. Horizontal velocity turning with depth during a wave period, as Figure 3.5, in the free (solid) and forced-damped (dashed) 2nd-gravest radial-vertical mode for $S = 48$; the bold (thin) curve is from the shallow (deep) star in Figure 3.6c. The forced-damped wave is phase shifted and anticlockwise turning with increasing depth ($d\Theta/dz < 0$) dominates, breaking free-wave symmetry.

In summary, signatures of a forced and damped higher radial-vertical mode that contrast with the corresponding free wave are (i) regions where currents rotate anticlockwise in time can be eliminated, (ii) turning with depth at a fixed time becomes dominantly anticlockwise, and (iii) phase propagates downward and outward in addition to clockwise (next subsection).

3.4.d.ii.Phase behavior

In a nonstationary or frictional wave, phase propagates in three dimensions and constant-phase surfaces do not lie in vertical planes as for free waves (3.6). By the governing equation (C.9), $\tilde{p}$ is complex (not real or imaginary) for complex σ' (Appendix C). The result is that all dynamical variables have complex modal structure functions and phase (3.4) propagates radially

and vertically in addition azimuthally. In terms of non-quasigeostrophic stratified slope-Kelvin waves (Section 3.3.d), superposed upgoing and downgoing rays have different amplitudes hence the superposition propagates phase across bathymetric contours and into or out of the boundary, as for a single non-quasigeostrophic ray on a steep slope.

The phase signature of a stationary forced and damped wave is dominated by propagation outward radially and downward vertically, in addition to azimuthally clockwise (Figure 3.17). With respect to the superposed non-quasigeostrophic wave rays of Section 3.3.d, the upslope-energy wave has larger amplitude so phase propagates downslope and into the boundary. Phase in a radial-vertical plane at a fixed time therefore increases radially inward and vertically upward. The effect of friction is to spread over a finite depth range the abrupt 180° change in phase that occurs at nodal lines in modal structure functions of the free wave (Figure 3.2, Section 3.2.b). Different phase behavior can occur, for example at the summit in Figure 3.17c, at radii smaller than the turning-point $h_r = \sigma/N$ waveguide boundary (Section 3.3.c) at $r = 1.25$ km.

3.4.d.iii.Energy balance

The budget for azimuthal-mean energy density consists of local rate of change balanced by dissipation, work done by body forces, and convergence of

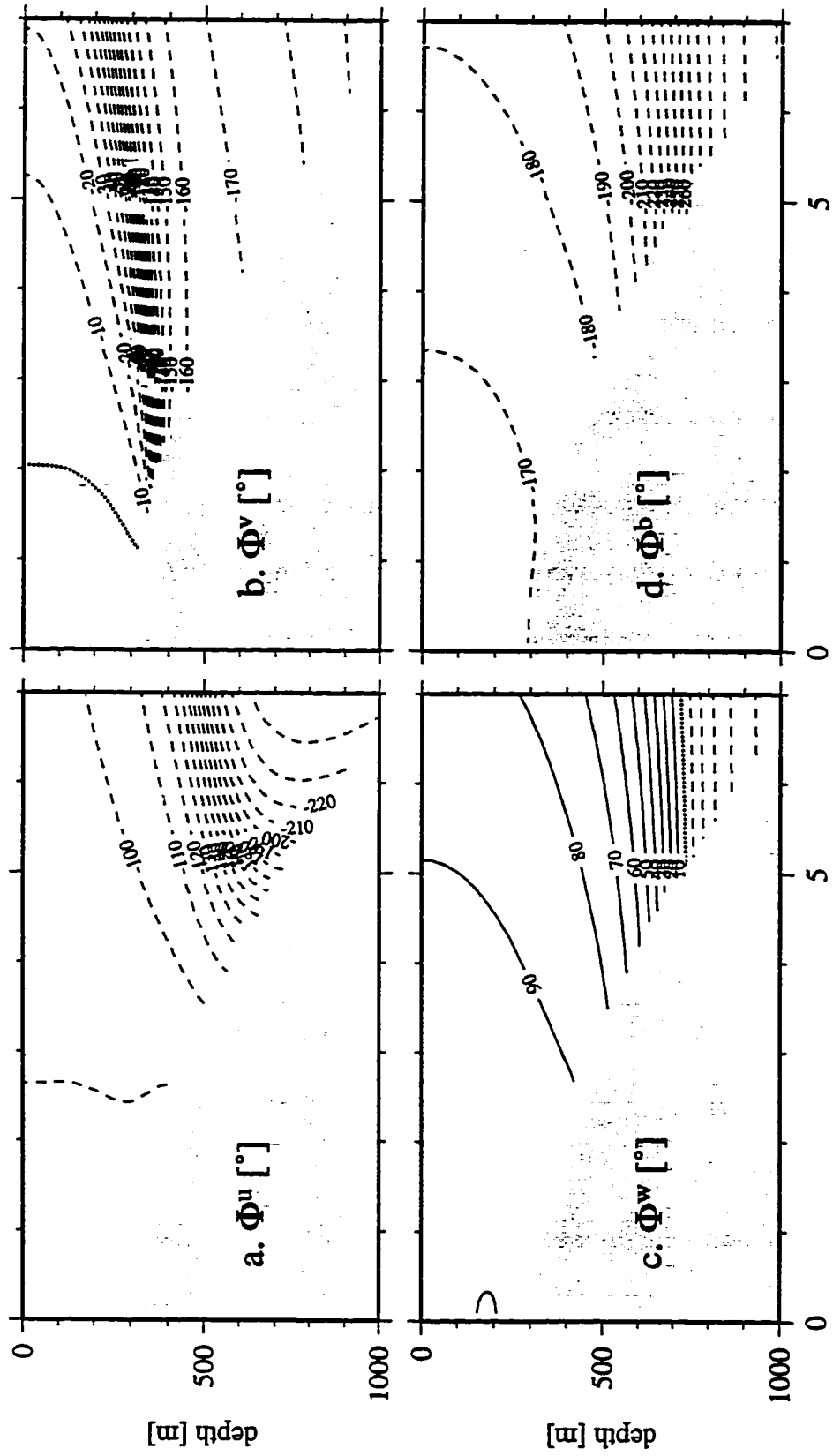

Figure 3.17. Phase (3.4) of radial, azimuthal, and vertical velocities and buoyancy ($t = 0$, $\theta = 0$) for the wave of Figure 3.14. More positive phases lead. Phase increases inward and upward across regions nodal lines (modal structure function zero contours) in a free wave (Figure 3.2).

wave energy flux. The sum of $\hat{u}$ dotted into (3.35)(a), (b) and (c) and b times (3.35)(d), after manipulation, yields

$$\bar{E}_t = -\overline{\nabla\bullet(p\hat{u})} - 2R\bar{E} + \bar{W}, \tag{3.43}$$

where each term is a function of radius and depth. The left side is local rate of change of azimuthal-mean energy density $\bar{E} = \frac{1}{2}\left(\overline{u^2} + \overline{v^2} + \overline{b^2}/N^2\right)$, where $\overline{(\,)}$ is an azimuthal average or equivalently an average over a wave period. For a stationary forced and damped wave this term is zero. The first term on the right of (3.43) is convergence of wave energy flux. The second term on the right is dissipation due to Rayleigh friction, proportional to wave energy and hence concentrated atop the summit at inner radii. The last term is work by body forces, $\bar{W} = \overline{F^u u} + \overline{F^v v}$, where from (3.39) and (3.41) with $T_{td}^{-1} = 0$,

$$\begin{aligned} F^u &= \Re\{\tilde{F}^u \exp[-i(\theta+\sigma t)]\} \\ F^v &= \Re\{\tilde{F}^v \exp[-i(\theta+\sigma t)]\} \end{aligned} \quad \text{where} \quad \begin{aligned} \tilde{F}^u &= i(f-\sigma-iR)\,\tilde{u}_F \\ \tilde{F}^v &= i(-f-\sigma-iR)\,\tilde{v}_F. \end{aligned} \tag{3.44}$$

Friction ($R \neq 0$) introduces a phase shift between body forces and velocities that are otherwise in quadrature, causing nonzero correlations ($\overline{F^u u}$, $\overline{F^v v}$) and work to be done by the body forces.

In the stationary forced and damped wave, wave energy flux is radially inward ($\overline{pu} < 0$) and upward ($\overline{pw} > 0$) and flux convergence is positive near the summit (Figure 3.18). Each term in the wave energy flux convergence

$$\overline{\nabla \bullet (\vec{u}p)} = (\overline{up})_r + \frac{\overline{up}}{r} + (\overline{wp})_z$$

makes an important contribution (not shown). Dissipation proportional to wave energy and hence concentrated near the summit necessitates inward and upward wave energy transport. The primary balance in (3.43) is between convergence of wave energy flux and dissipation, each with structure as in Figure 3.18c. Body force work is everywhere less than a tenth as large.

3.5. *Acceleration of mean flow by waves*

This section examines nonlinear rectification of stratified seamount-trapped waves at a typical midlatitude seamount, illustrating the azimuthal-mean cross-slope momentum transport responsible for induced mean flow. The results should be compared to previous studies of tidal rectification on linear banks in an unstratified system (Loder 1980) and in stratification over a perturbation-height topography (Maas and Zimmerman 1989). The azimuthal-average hydrostatic nonlinear form of governing equations (3.35) after each variable (p, u, v, w, b), for example p, is Reynolds decomposed $p \rightarrow \bar{p} + p$ into an azimuthal-mean component $\bar{p}(r, z)$ and a wave component $p(r, \theta, z, t)$, is

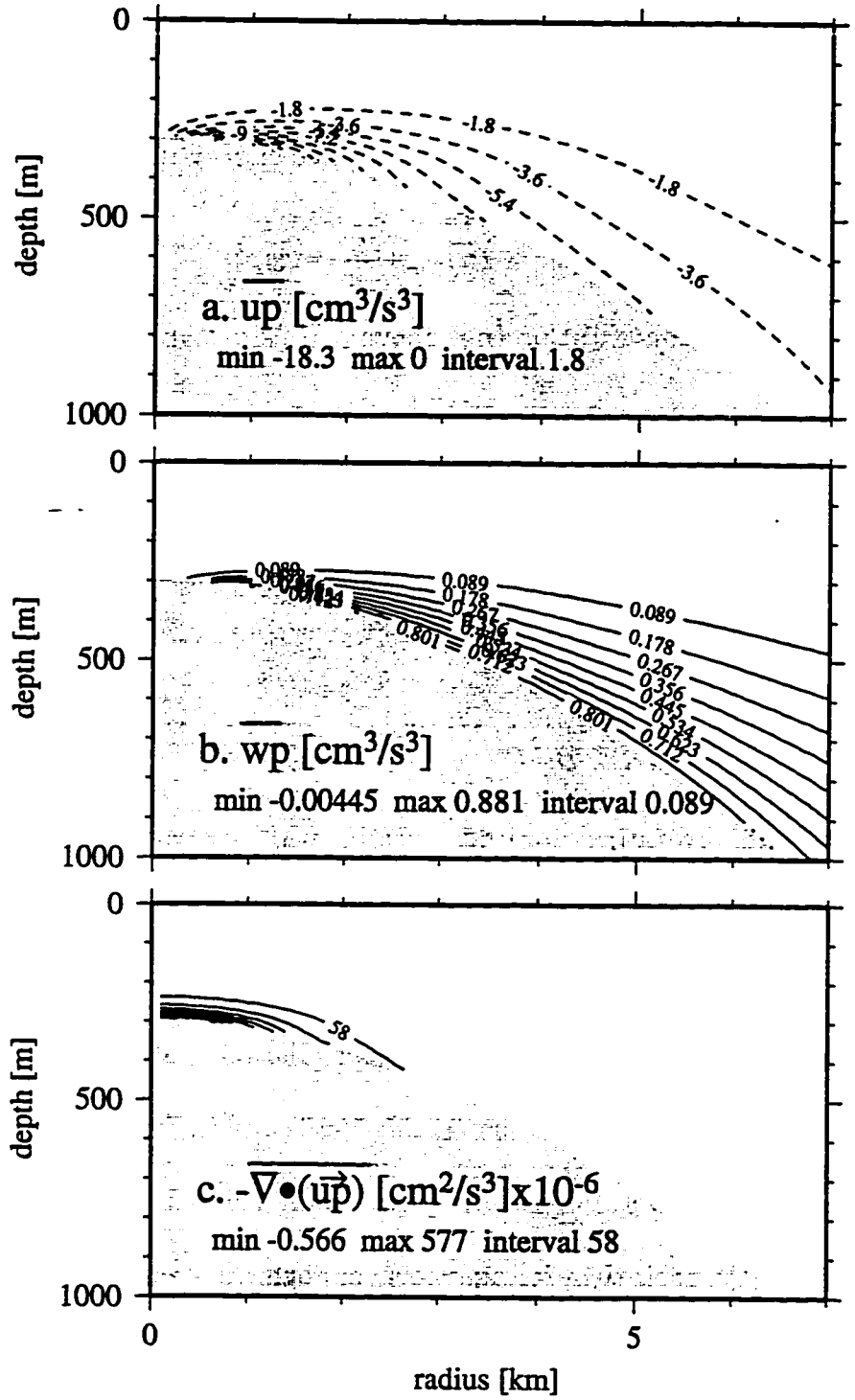

Figure 3.18. Azimuthal-mean flux of energy in the radial (a) and vertical (b) by the wave in Figure 3.14. Flux convergence (c) is positive at depth near the summit, where the wave deposits energy.

$$
\begin{aligned}
&\bar{u}_t + \bar{u}\bar{u}_r - \frac{\bar{v}^2}{r} + \bar{w}\bar{u}_z - f\bar{v} = -\bar{p}_r - \overline{\nabla\bullet(\vec{u}u)} + \frac{\overline{v^2}}{r} - R\bar{u} && \text{(a)}\\
&\bar{v}_t + \bar{u}\bar{v}_r + \frac{\bar{u}\bar{v}}{r} + \bar{w}\bar{v}_z + f\bar{u} = -\overline{\nabla\bullet(\vec{u}v)} - \frac{\overline{uv}}{r} - R\bar{v} && \text{(b)}\\
&0 = -\bar{p}_z + \bar{b} && \text{(c)}\\
&\bar{b}_t + \bar{u}\bar{b}_r + \bar{w}\bar{b}_z + N^2\bar{w} = -\overline{\nabla\bullet(\vec{u}b)} - R\bar{b} && \text{(d)}\\
&\frac{1}{r}(r\bar{u})_r + \bar{w}_z = 0\,, && \text{(e)}
\end{aligned}
\qquad (3.45)
$$

where $\left(\bar{u}_t, \bar{v}_t, \bar{b}_t\right)$ vary on timescales longer than the wave period. Diagnosis of observed currents at seamounts appears to require an understanding of the nonlinear frictional equilibration of this set for large-amplitude fluctuations, as is being developed with numerical models (Haidvogel et al. 1993). Here, mean flow acceleration under much simpler conditions is described. Only clockwise-rotating tidal forcing is considered ($u^{ACW} = 0$) so an azimuthal average is equivalent to a time average (see (3.37)).

We examine a nonstationary small-amplitude inviscid wave excited by tidal currents growing on a timescale longer than the wave period, as motivated by previous mean-flow induction studies (McIntyre 1980). A wave growing exponentially on timescale T_{td} (3.37) has the same phase shifts between variables (3.42) and current structure as a stationary forced damped wave maintained against Rayleigh friction of timescale $R = T_{td}^{-1}$ (Section 3.4.d). These features are described in Section 3.4.d and shown in Figures 3.14, 3.15,

3.16 and 3.17. Cross-slope flux divergences shown here for a nonstationary wave are thus also present in a stationary forced damped wave.

Consider mean flow $\bar{v}$ weak compared to an inviscid ($R = 0$) wave of small wave steepness ($\varepsilon \ll 1$ (3.5)), such that the radial momentum balance (3.45)(a) obeys geostrophy. For maximum wave velocity u_A this holds when $u_A \gg \bar{v} \gg \left(-\overline{\nabla\bullet(\tilde{u}\tilde{u})} + \overline{v}^2/r \right)/f$. To lowest order in mean quantities, (3.45) is

$$
\begin{aligned}
-f\bar{v} &= -\bar{p}_r && \text{(a)} \\
\bar{v}_t &= F^{\mathcal{D}} - f\bar{u} && \text{(b)} \\
0 &= -\bar{p}_z + \bar{b} && \text{(c)} \\
\bar{b}_t + N^2\bar{w} &= F^{\mathcal{b}} && \text{(d)} \\
\frac{1}{r}(r\bar{u})_r + \bar{w}_z &= 0 && \text{(e)}
\end{aligned}
\qquad (3.46)
$$

where 'direct' azimuthal momentum forcing $F^{\mathcal{D}}$ consists of both azimuthal-mean convergence of azimuthal momentum flux $-\overline{\nabla\bullet(\tilde{u}\tilde{v})}$ and the term $-\overline{uv}/r$, and buoyancy forcing $F^{\mathcal{b}}$ is buoyancy flux convergence $-\overline{\nabla\bullet(\tilde{u}\tilde{b})}$:

$$
\begin{aligned}
F^{\mathcal{D}} &= -\overline{\nabla\bullet(\tilde{u}\tilde{v})} - \frac{\overline{uv}}{r} = -(\overline{uv})_r - \frac{2\overline{uv}}{r} - (\overline{vw})_z && \text{(a)} \\
F^{\mathcal{b}} &= -\overline{\nabla\bullet(\tilde{u}\tilde{b})} = -(\overline{ub})_r - \frac{\overline{ub}}{r} - (\overline{wb})_z . && \text{(b)}
\end{aligned}
\qquad (3.47)
$$

The set (3.46) governs an Eulerian-mean circulation of accelerating azimuthal flow $\bar{v}_t$, growing buoyancy anomaly $\bar{b}_t$ in thermal wind balance, and non-divergent radial-vertical circulation $(\bar{u}, \bar{w})$. Note that a *stationary* inviscid wave, with $\overline{uv} = \overline{vw} = \overline{ub} = \overline{wb} = 0$ (3.7) so $F^u = F^b = 0$, is an example of non-acceleration conditions (Andrews et al. 1987).

The example here is a nonstationary inviscid wave in the $S = 12$ system of Table 3.1 for wave steepness $\varepsilon = 0.01$, with maximum wave velocity $u_A = 1\text{cm/s}$. It is excited at the resonant free wave frequency $\sigma = 0.657f$ by tidal currents growing in amplitude (3.37) on timescale $T_{td} = 10$ wave periods. For $\bar{v}/u_A \approx 0.1$, approximations in forming (3.46) from (3.45) are valid.

Acceleration of mean azimuthal flow $\bar{v}_t$ (3.46)(b) is dominated by direct forcing F^v, with that due to mean radial flow $f\bar{u}$ weaker (see below). Azimuthal mean flow acceleration $\bar{v}_t \approx F^v$ due to direct forcing (3.47)(a) is clockwise and concentrated in a bottom-intensified region near the summit, due to inward azimuthal-mean wave transport of negative azimuthal momentum (Figure 3.19). Each of the three terms on the right of (3.47)(a) contributes significantly, including the term $\overline{uv}/r$ (equal to half of Figure 3.19c). Acceleration strength is such that in 10days the mean current $|\bar{v}|$ increases by $0.016u_A$, a significant fraction of its own magnitude.

Azimuthal-mean cross-slope buoyancy flux convergence $\bar{F}^b$ (Figure 3.20) induces a positive density anomaly to maintain geostrophy (3.46)(a) of the bottom-intensified clockwise azimuthal current accelerated. Buoyancy flux is directed radially outward and downward away from the seamount summit ($\overline{ub} > 0$, $\overline{wb} < 0$) with negative flux convergence ($\bar{F}^b < 0$) near the summit. The flux convergence has significant contributions from each of the three terms on the right of (3.47)(b) (not shown individually).

Acceleration $f\bar{u}$ (3.46)(b) due to radial mean flow is relatively unimportant. Using streamfunction χ for non-divergent (3.46)(e) azimuthal-mean radial-vertical circulation, defined $\bar{u} = -\chi_z$ and $\bar{w} = \frac{1}{r}(r\chi)_r$, (3.46) becomes

$$\chi_{rr} + \frac{f^2}{N^2}\chi_{zz} + \frac{1}{r}\chi_r - \frac{1}{r^2}\chi = \frac{1}{N^2}\left(\bar{F}^b_r - f\bar{F}^u_z\right). \tag{3.48}$$

An appropriate boundary condition is that Eulerian-mean radial-vertical circulation cannot cross the ocean surface or seamount boundary, so

$$\chi = 0 \text{ on } r = 0, \text{ as } r \to \infty, \text{ on } z = 0 \text{ and on } z = -h(r). \tag{3.49}$$

The set (3.48) and (3.49) is solved numerically as is (C.9) (Appendix C). There is an Eulerian-mean circulation cell with flow downward above the summit and radially outward at depth (Figure 3.21). Though it is not appropriate to

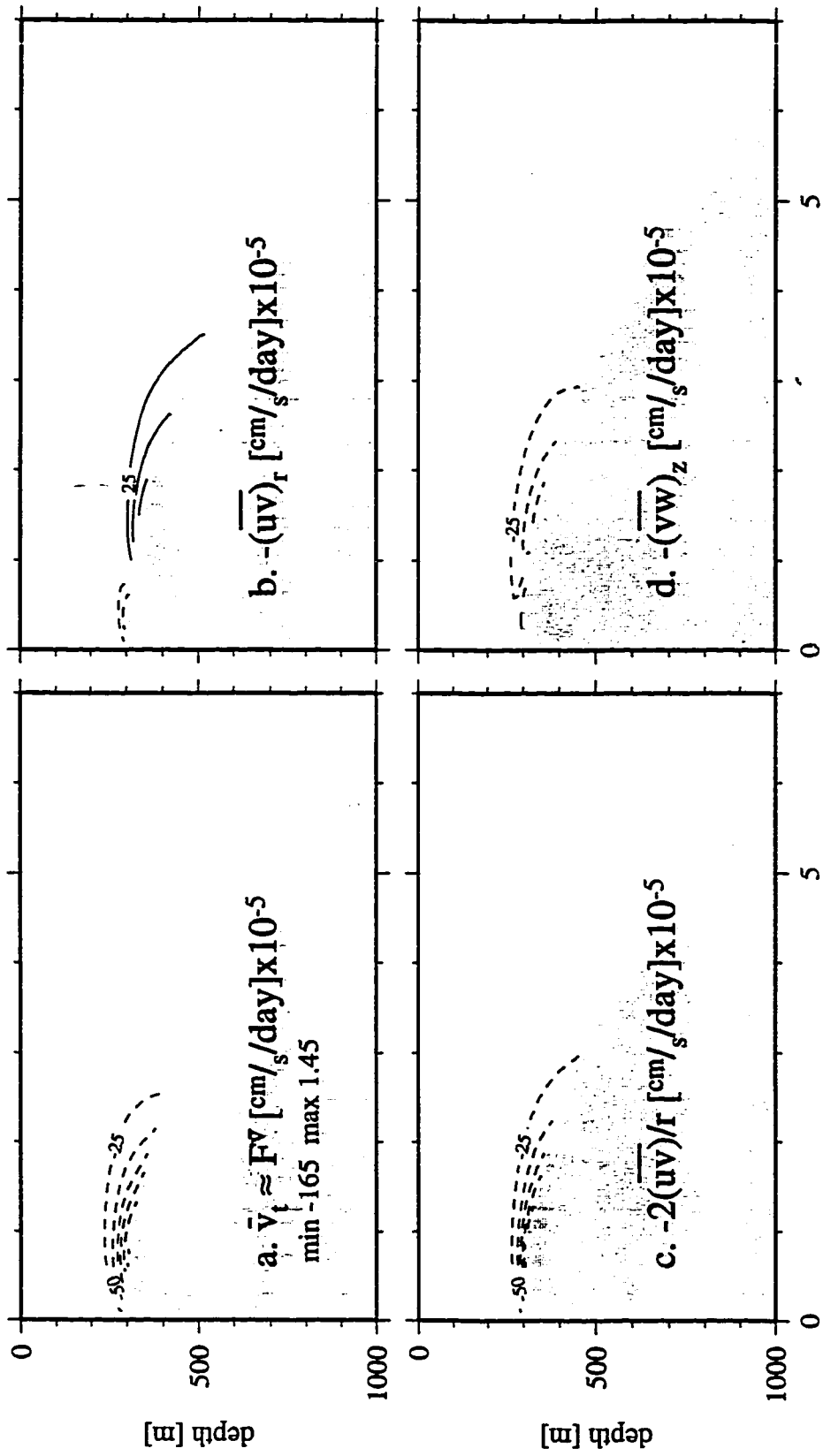

Figure 3.19. Mean azimuthal current acceleration $\bar{v}_t \equiv F^D$ (3.46)(b) by nonstationary inviscid wave discussed in text. (a) =(b)+(c)+(d) are $F^D = -(\overline{uv})_r - 2\overline{uv}/r - (\overline{vw})_z$ (3.47)(a), contour intervals same.

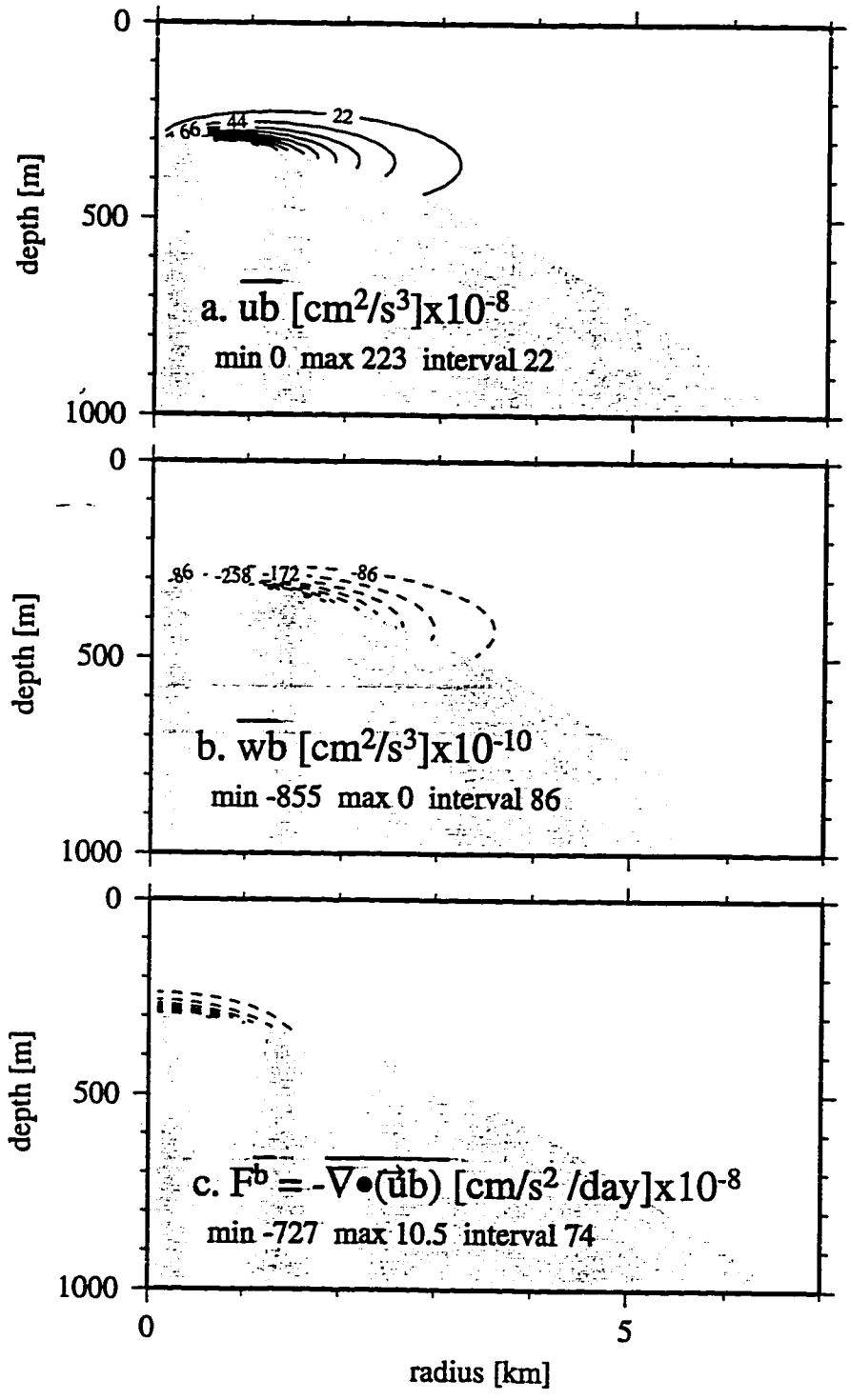

Figure 3.20. Azimuthal-mean buoyancy fluxes radially (a) and vertically (b) for the nonstationary inviscid wave discussed in text. Azimuthal-mean flux convergence (c) is negative near the summit.

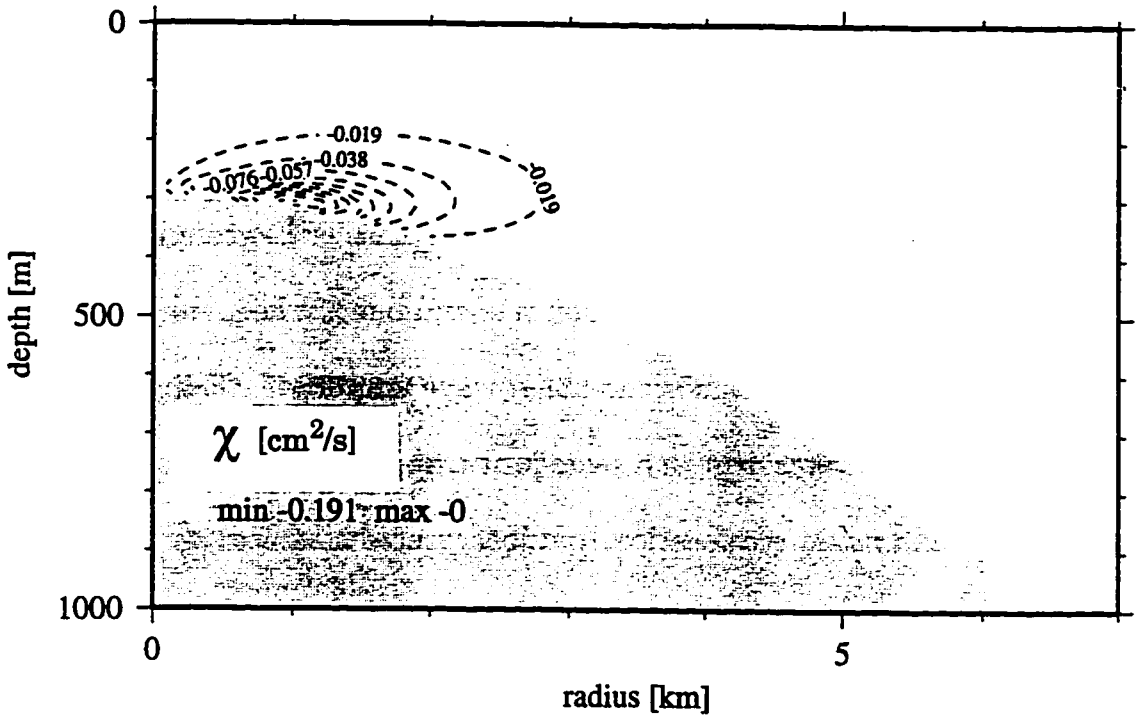

Figure 3.21. Streamfunction χ (3.48) for azimuthal-average Eulerian mean radial-vertical circulation $(\bar{u}, \bar{w})$ of nonstationary inviscid wave discussed in text. Maximum $|\bar{u}|$ ($|\bar{w}|$) is $7 \times 10^{-5}\left(6 \times 10^{-6}\right)$cm/s so this circulation is unimportant to azimuthal mean flow acceleration. Flow is outward (downward) at depth (on the summit). Though not apparent due to the plotting technique, the seamount boundary is a streamline (χ = 0 (3.49)) not intersected by other streamlines.

compare its amplitude to observations, the sense agrees with Eulerian-mean measured flow at Cobb Seamount (Chapter 2) and at Fieberling Guyot (Eriksen 1995, Brink 1995). We caution this is an Eulerian-mean circulation associated with an azimuthal mean current accelerated by small-amplitude waves. An Eulerian mean does not describe particle motion and in terms of oceanic measurements, even for conditions when (3.46) might be valid, Figure 3.21 does not imply fluid would be downwelled over the summit. Here, we empha-

size only that radial mean flow is unimportant relative to direct forcing in accelerating mean azimuthal flow (3.46)(b).

Rectification accelerates a clockwise Eulerian-mean azimuthal current (Figure 3.19a), but the direction of mean particle drift, or Lagrangian mean flow, requires knowledge of Stokes transports and has not been addressed. Stokes drift depends on spatial gradients of wave amplitude. Codiga (1993) showed horizontal Stokes drift in a seamount-trapped wave is anticlockwise, opposite Eulerian mean acceleration, and interpreted a laboratory data with clockwise particle drift as Eulerian mean flow exceeding the Stokes drift. More generally the Stokes drift may overcome mean Eulerian flow, as in the barotropic Rossby wave example of Charney and Flierl (1981). Application of theory involving particle displacements (Rhines 1977, Andrews et al. 1987) in the present context would improve understanding of Lagrangian mean flow.

Though rectification illustrated here (3.46) under simplifying assumptions is somewhat removed from oceanic currents governed by more complex equations (3.35), speculative remarks regarding observed flows may be made. To the extent induced negative relative vorticity dominates potential vorticity (4.6), rectification causes a negative potential vorticity anomaly (4.7). This suggests the negative potential vorticity anomaly observed at Fieberling Guyot (Kunze and Toole 1996) can be explained as mean flow due to rectification of tidal currents. Mean flow strength at Fieberling Guyot also modulates on a fortnightly basis (Eriksen 1991, Brink 1995). By (3.42), growth on times-

cale T_{td} and Rayleigh friction of timescale $R^{-1} = T_{td}$ cause equivalent cross-slope fluxes. Recall the turbulent damping timescale is 2 – 3days at Fieberling (Kunze and Toole 1996), and consider growth/decay over a week ($T_{td} = \pm 1$ week) to model portions of the fortnightly cycle in tidal current amplitude. A consistent interpretation of observed mean fluctuations follows: cross-slope fluxes due to friction drive the main clockwise current, while those due to fortnightly tidal current variations cause slightly weaker mean flow modulations.

3.6. Conclusions

Observational signatures of stratified seamount-trapped waves (Brink 1989, 1990) of first azimuthal wavenumber at a typical midlatitude seamount (Table 3.1) are explored and signatures of forcing and frictional influences demonstrated. A *free* wave (eigensolution to (3.1) and (3.2) of form (3.3)) is radially and vertically trapped to the seamount but propagates freely azimuthally clockwise. Flow characteristics exhibit symmetries due to standing-wave radial and vertical structure. Phase (3.4) of each variable takes values differing by 180° in regions of the radial-vertical plane bounded by nodal lines, zero contours in modal structure functions (Figures 3.1 and 3.2). Current ellipse axes are parallel or perpendicular to isobaths, with ellipses shallower (deeper) than the summit nearly circular (elongated in the radial or azimuthal directions in alternating depth ranges) as shown in Figures 3.3 and

3.4. Rotation of currents in time is clockwise/anticlockwise in alternating, nearly horizontal depth regions. At a fixed location, turning of velocity with depth is alternately clockwise and anticlockwise during successive quarter-periods (Figure 3.5). In stronger stratification, higher radial-vertical modes occur with reduced spatial scales, weaker vertical displacements, and relatively smaller regions of anticlockwise rotation in time (Figure 3.6).

To provide physical intuition for frictional modifications, stratified seamount-trapped waves are explained in terms of *stratified slope-Kelvin waves* (Figure 3.7), short bottom-trapped topographic Rossby waves in stratification (Rhines 1970). A free stratified seamount-trapped wave is a resonant cross-slope (radial and vertical) mode formed from superposed equal-amplitude upgoing and downgoing stratified slope-Kelvin rays in the re-entrant waveguide formed by the sloping seamount sides (Figure 3.11). Cross-slope structure is set by control on rays by (i) refraction due to varying bottom slope (Figure 3.8), (ii) Airy-function behavior near turning points (Figure 3.9), and (iii) geometric compression in cylindrical geometry (Figure 3.10).

In a stationary forced damped stratified seamount-trapped wave (Section 3.4.d) friction is strongest near the summit, because it is proportional to wave amplitude, and breaks the cross-slope standing-wave structure such that the ray carrying energy upslope dominates. This causes current ellipses oriented at an angle to isobaths such that $\overline{uv} > 0$ (Figures 3.14 and 3.15),

phase propagation downward and outward (Figure 3.17), reduced regions of anticlockwise rotation in time, and dominantly anticlockwise turning with depth of horizontal velocity at a fixed time (Figure 3.16). The energy budget is dominated by wave transport of energy toward the region where dissipation occurs near the summit (Figure 3.18). A nonstationary inviscid wave growing in time has the same phase shifts between dynamical variables (3.42) as a stationary forced damped wave. This causes azimuthal-mean cross-slope flux divergence (3.47)(a) of azimuthal momentum that drives rectified azimuthal mean flow clockwise in a bottom-trapped region (Figure 3.19).

Chapter 4

Trapped wave modification and critical surface formation by mean horizontal and vertical shear at a seamount

4.1. Introduction

Most observations of amplified tidal currents at seamounts are accompanied by low frequency azimuthal flow of amplitude at least a significant fraction of the oscillations and often of similar or greater strength (Chapter 2, Meincke 1971, Genin et al. 1989, Eriksen 1991, Freeland 1994, Brink 1995, Kunze and Toole 1996). The effect of mean flow on the frequency and currents of stratified seamount-trapped waves excited by tidal forcing has not been examined. On the summit plain of Fieberling Guyot, dissipation levels and diurnal (slightly subinertial) tidal current amplitudes are maximal at depths above the bottom, and extend several km laterally away from the seamount (Eriksen 1991, Brink 1995, Kunze and Toole 1996). This is not characteristic of high-frequency internal wave critical reflection processes (Eriksen 1982, 1985) nor of seamount-trapped waves (Brink 1989, 1990). A critical surface due to mean flow that occurs at these locations is a plausible mechanism.

This chapter describes how a moderately strong horizontally and vertically sheared azimuthal mean current at a seamount causes (i) stratified seamount-trapped wave (Brink 1989, Chapter 3) frequency and structure modifications, (ii) critical surfaces in stratified seamount-trapped waves, and

(iii) a "superinertial cap," or region trapped to the seamount in which a subinertial tidal frequency becomes effectively superinertial, bounded by an internal wave critical surface.

Mean azimuthal currents at a seamount may result from numerous dynamical mechanisms, including nonlinear rectification of oscillations (Chapter 3, Loder 1980, Maas and Zimmerman 1989), Taylor cap formation by vortex stretching due to incident flow (Hogg 1973, Chapman and Haidvogel 1992), and topographic form drag associated with azimuthal asymmetry or bottom roughness (Holloway 1987, Pratte and Hart 1991). Most observed low-frequency currents at seamounts are intensified near the bottom and predominantly along isobaths in the clockwise sense in the northern hemisphere, as is consistent with these theories. To isolate and illustrate physics we *impose* moderate-amplitude bottom-intensified azimuthal mean flow without reference to its dynamical origin, and consider its effect on waves at a circular Gaussian seamount in constant stratification.

The frequency and structure of stratified seamount-trapped waves in mean flow are compared to those without mean flow in Section 4.2, and results are given dynamical justification in Section 4.3 through examination of stratified slope-Kelvin waves in idealized mean flows. In Section 4.4 mean flow is demonstrated to cause two types of critical surfaces at subinertial frequencies, those of stratified seamount-trapped waves and those of internal waves propagating in an effectively superinertial region above the seamount summit. Sec-

tion 4.5 is a demonstration of internal wave critical surfaces that form for mean flow and stratification measured at Fieberling Guyot.

4.2. Stratified seamount-trapped waves in mean shear flow

4.2.a. Mean current

This section describes the bottom-intensified azimuthal mean flow, together with its vorticity and potential vorticity structures, used to illustrate how mean flow changes wave physics. The setting is the northern hemisphere midlatitude seamount of Section 3.2.a (Table 3.1, $S = 12$) in cylindrical coordinates with origin at the sea surface centered on the seamount axis and (r, θ, z) increasing outward, anticlockwise from east, and upward respectively. The seamount is azimuthally symmetric, of Gaussian profile with lengthscale L, and surrounded by a Boussinesq ocean rotating uniformly at $f/2$ with constant buoyancy frequency N. Mean flow $\vec{U} = (U, V, W)$ is an azimuthal current $V(r,z)$ $(U = W = 0)$ in cyclogeostrophic and hydrostatic balance with reduced pressure $P(r,z)$ and buoyancy $B(r,z)$ anomalies,

$$\begin{aligned} -\frac{V^2}{r} - fV &= -P_r \\ 0 &= -P_z + B. \end{aligned} \tag{4.1}$$

In practice, $V(r,z)$ is specified and $B(r,z)$ calculated by integrating

$$B_r = (f + 2V/r)\, V_z \tag{4.2}$$

inward from some large radius where $B = 0$. Associated with buoyancy B is mean vertical displacement $-B/N^2$ (positive upward). Mean flow is *imposed*, without reference to forcing or frictional influences maintaining it, in order to assess its impact on waves. None of the effects of mean flow described is contingent on the presumption of cyclogeostrophy.

The mean current (Figure 4.1) is bottom-intensified and concentrated near the summit similarly to currents of the seamount-trapped wave without mean flow (Figure 3.2). This is motivated by measured flow at Cobb Seamount (Figure 2.7) and by tidal rectification dynamics in which mean flow strength generally parallels that of the driving oscillations (Section 3.5, Maas and Zimmerman 1989). The analytic form is

$$V = V_i G(r, z) \tag{4.3}$$

where V_i is amplitude (positive anticlockwise) and the shape function

$$G(r, z) = G_i \frac{(r/R_i)\exp(-r/R_i)}{1 + (r/R_i)^2} \exp\left(-\left(\frac{z + z_i}{Z_i}\right)^2\right) \tag{4.4}$$

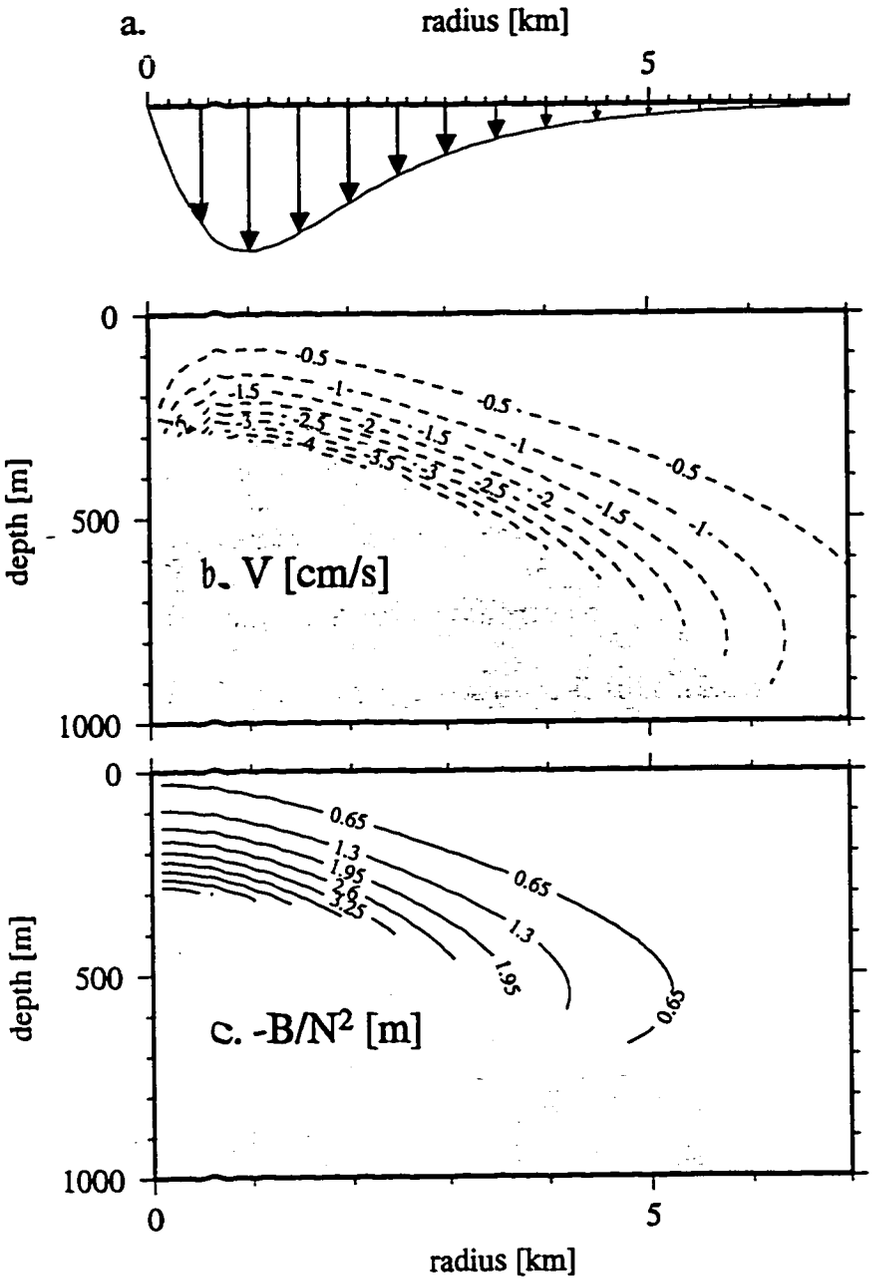

Figure 4.1. Baroclinic mean azimuthal current at a seamount in an ocean with parameters as in Table 3.1 for $S = 12$. (a) Plan view of clockwise current $V_i < 0$, at fixed depth. (b) $V(r,z)$ for $V_i = -5$cm/s, showing shape function $G(r,z)$ (4.4) for $R_i = 1.8$km, $Z_i = 350$ m, and $z_i = -800$ m. (c) Vertical displacement $-B/N^2$ in cyclogeostrophic balance (4.1). Isopycnal uplift reaches 6.5 m at the bottom.

has radial scale R_i, decays on vertical scale Z_i with distance from depth z_i, and is unit-normalized over $z > -h(r)$ by the positive constant G_i.

Anticlockwise (clockwise) mean flow has positive (negative) vertical component of vorticity ζ

$$\zeta = \nabla \times \vec{U}\big|_z = \frac{1}{r}(rV)_r = V_r + \frac{V}{r} \tag{4.5}$$

near the summit (Figure 4.2). At small radii V_r, V/r, and hence ζ have the same sign as V_i. At large radii V_r has sign opposite to V/r so the sign of ζ is the same as (opposite to) V_i if the shape function $G(r,z)$ decays with radius slower (faster) than $1/r$. Because a mean flow of uniform sign may have regions of both anticyclonic ($\zeta < 0$) and cyclonic ($\zeta > 0$) vertical vorticity as determined by the radial dependence of $G(r,z)$, currents are described here as anticlockwise or clockwise, instead of in terms of anticyclonic or cyclonic vorticity. The dominant vorticity signal of anticlockwise (clockwise) mean flow of structure shown in Figure 4.1 is a dome of positive (negative) vorticity near the summit. Due to the small horizontal scale of the seamount, even weak mean flow has vorticity magnitude reaching $0.5f$ (Figure 4.2).

The Ertel potential vorticity anomaly, controlled mainly by the vertical component of vorticity, is positive (negative) near the summit for an anticlock-

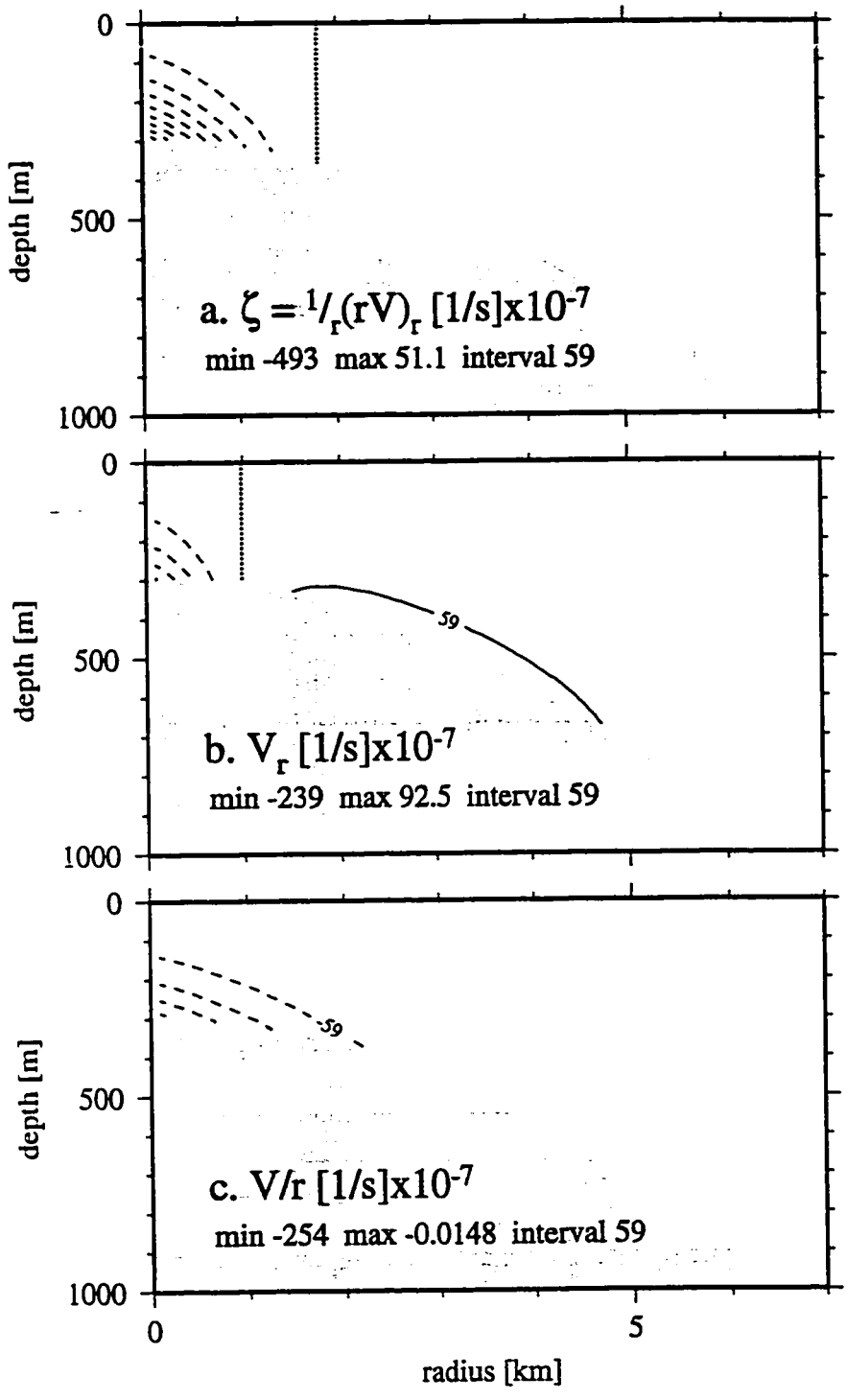

Figure 4.2. Vertical component of vorticity (4.5) (a) = (b) + (c), for clockwise current V_i = −1.5cm/s of shape as in Figure 4.1. Negative vorticity reaches $-0.5f$ even at this weak amplitude.

wise (clockwise) current (Figure 4.3). In a continuously stratified and uniformly rotating Boussinesq ocean, Ertel potential vorticity is (Muller 1995)

$$Q_E^V = (f\hat{z} + \nabla\times\vec{U}) \bullet \nabla\left(-\frac{\rho_o}{g}\rho_s(z) + B(r,z)\right), \tag{4.6}$$

where $\hat{z}$ is the vertical unit vector, $\nabla\times\vec{U} = \left(-V_z, 0, \frac{1}{r}(rV)_r\right)$ is vorticity, $N^2 = -\frac{g}{\rho_o}\frac{d}{dz}\rho_s(z)$ is stratification of background density profile $\rho_s(z)$ in the absence of mean flow (subscript s for "stationary"), B is buoyancy due to cyclo-

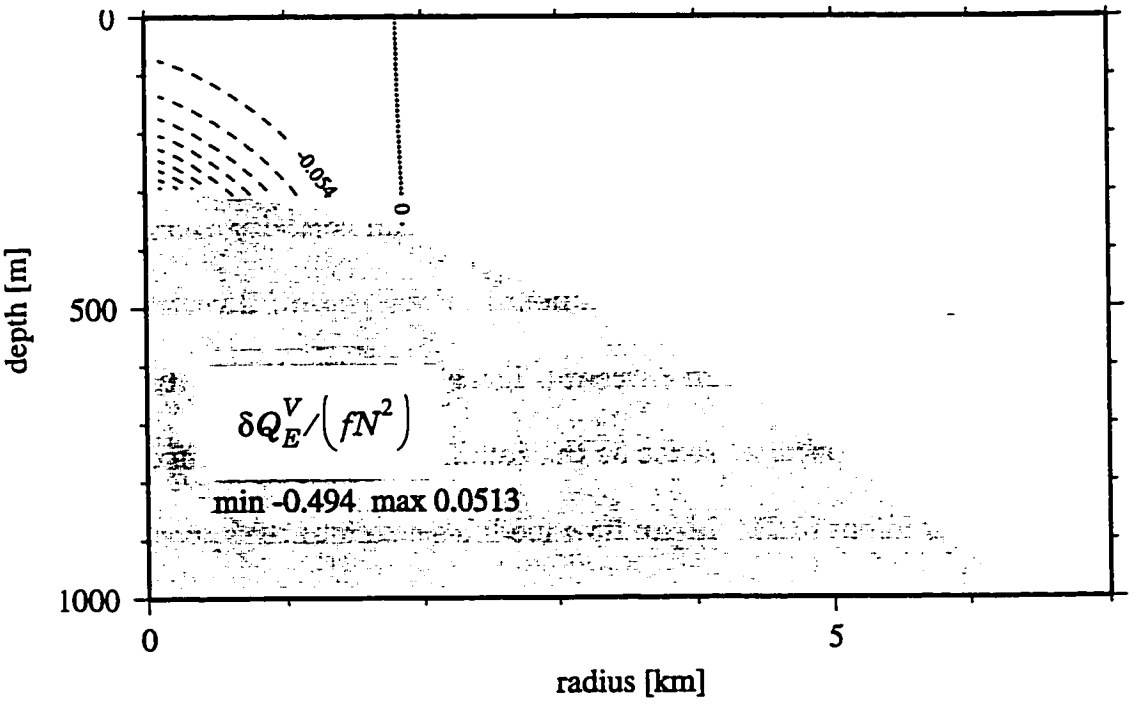

Figure 4.3. Ertel potential vorticity anomaly for clockwise current $V_i = -1.5$cm/s of shape as in Figure 4.1. The vertical component of vorticity (Figure 4.2) dominates terms in (4.7) (Figure 4.4). Near the summit the anomaly is negative and thus the radial gradient is outward (positive) and opposite to that of the topographic slope (3.21).

geostrophic balance of mean flow (4.1), ρ_o is constant background density, and g is gravitational acceleration constant. Rest-state potential vorticity is fN^2 and the fractional anomaly $\delta Q_E^V/\left(fN^2\right) = \left(Q_E^V - fN^2\right)/\left(fN^2\right)$ is

$$\delta Q_E^V/\left(fN^2\right) = \left[\frac{f+\zeta}{f}\right]\left[\frac{N^2+B_z}{N^2}\right] + \left[\frac{f+2V/r}{f}\right]\left[\frac{(V_z)^2}{N^2}\right] - 1 \qquad (4.7)$$

using (4.2) in (4.6). Because $\left(N^2+B_z\right)/N^2 \approx 1$ and $(V_z)^2/N^2 \ll 1$, the fractional anomaly is dominated by the vertical component of vorticity, $\delta Q_E^V/\left(fN^2\right) \approx \zeta/f$, as shown by the four square-bracketed terms (Figure 4.4) in (4.7) for mean flow of Figure 4.1. Measurements at Fieberling Guyot (Kunze and Toole 1996) indicate a similar negative potential vorticity anomaly.

Near the summit the radial gradient in Ertel potential vorticity of an anticlockwise (clockwise) mean current (Figure 4.3) is inward (outward) and hence of the same (opposite) sense as the radially inward topographic potential vorticity gradient (3.21). Mean flow modifies seamount-trapped waves, supported by the gradient in potential vorticity (Section 3.3), by this means and additionally by advection as explained in Section 4.3. The necessary condition for baroclinic instability of the mean current, a potential vorticity gradient of reversing sign (Gill 1982), may be met where the gradient in Ertel potential vorticity opposes the inward topographic potential vorticity gradient

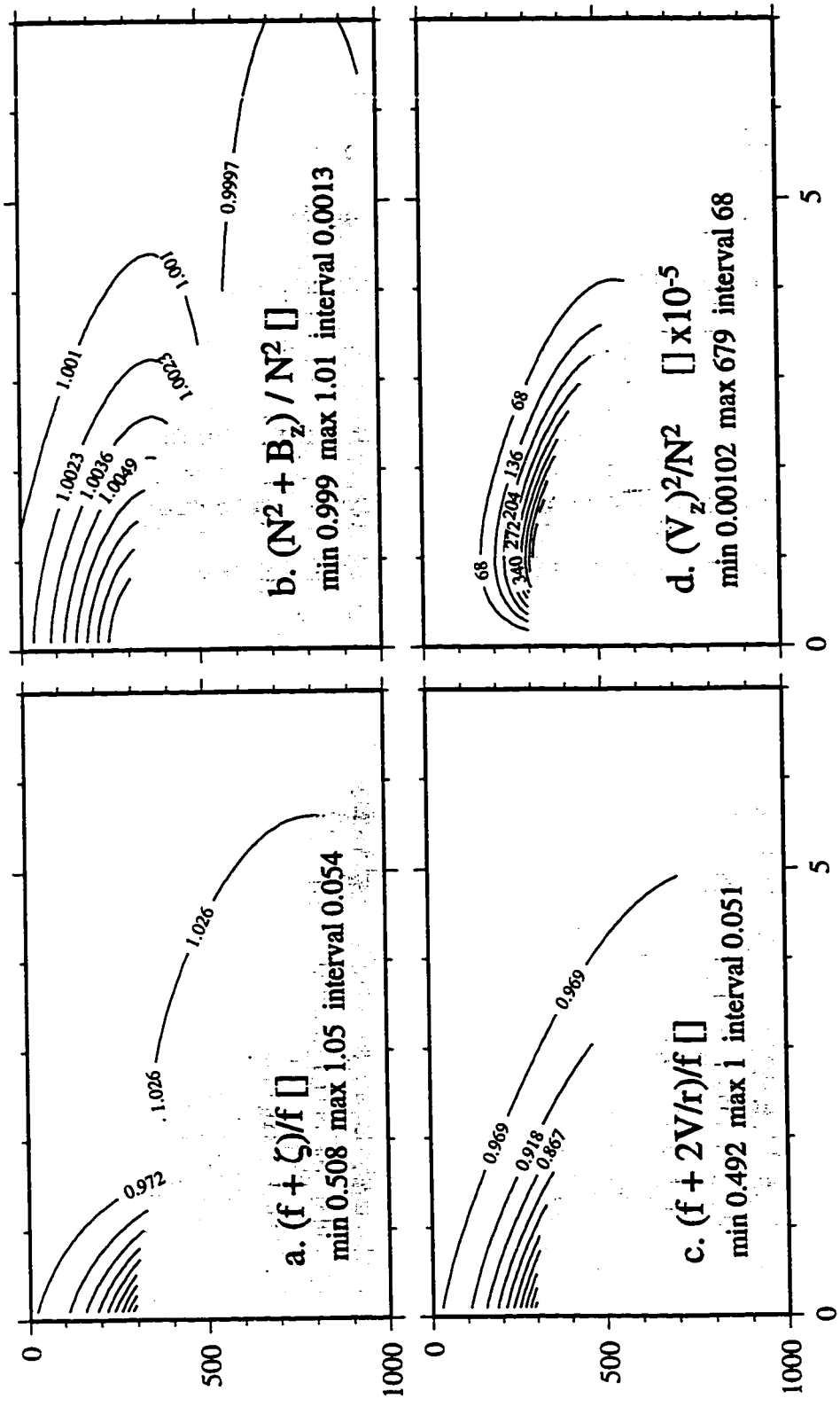

Figure 4.4. Ratios controlling fractional Ertel potential vorticity anomaly $\delta Q_E^V / \left(fN^2 \right)$. Four square-bracketed terms in (4.7) are shown for clockwise current V_i = −1.5cm/s of shape as in Figure 4.1.

(3.21) and reaches its magnitude. Wave solutions in mean flow (at weaker amplitude than causes critical surfaces in waves, Section 4.4) are examined here despite the fact that the necessary condition for baroclinic instability of the current is met. Fastest-growing instabilities have the scale of the baroclinic deformation radius (Gill 1982). Based on the relatively small ratio between the scale of the seamount and the first baroclinic deformation radius, $L/(NH/f) = 1/S^{1/2} = 0.29$ (Table 3.1), the growth rate of baroclinic instabilities is likely to be small. Resonances found may be considered neutrally stable modes and are well-behaved with no signs of instability.

4.2.b. Wave modifications

Stratified seamount-trapped waves in mean flow are perturbations (p, u, v, w, b), functions of (r, θ, z, t), that obey inviscid and unforced hydrostatic momentum, buoyancy, and continuity equations linearized about mean flow variables (V, P, B) (4.1):

$$
\begin{aligned}
u_t + \frac{V}{r}u_\theta - \left(f + \frac{2V}{r}\right)v &= -p_r && (a)\\
v_t + \frac{V}{r}v_\theta + wV_z + \left(f + \frac{1}{r}(rV)_r\right)u &= -\frac{1}{r}p_\theta && (b)\\
0 &= -p_z + b && (c)\\
b_t + \frac{V}{r}b_\theta + B_r u + \left(N^2 + B_z\right)w &= 0 && (d)\\
\frac{1}{r}(ru)_r + \frac{1}{r}v_\theta + w_z &= 0\ . && (e)
\end{aligned}
\qquad (4.8)
$$

Boundary conditions require motions to be trapped to the seamount, remain bounded at the center, and obey the rigid lid condition at the surface and the kinematic condition at the bottom,

$$\begin{aligned} (p,u,v,w,b) &\to 0 \quad \text{as} \quad r \to \infty && (a) \\ (p,u,v,w,b) &\quad \text{bounded at} \quad r = 0 && (b) \\ w + h_r u &= 0 \quad \text{at} \quad z = -h && (c) \\ w &= 0 \quad \text{at} \quad z = 0\,. && (d) \end{aligned} \tag{4.9}$$

This chapter treats mean flow effects on free waves, unforced and inviscid subinertial eigensolutions to (4.8) and (4.9), found as shown in Appendix C. Chapter 3 treated effects of forcing and friction on waves without mean flow.

Two effects of mean flow on free waves are shifts in the resonance frequency and distortion of current structure. Free wave variables $\{p,u,v,w,b\}$ have form, using u as an example,

$$\begin{aligned} u(r,\theta,z,t) &= |\tilde{u}(r,z)|\cos\left[-\theta-\sigma t+\Phi^u(r,z)\right] \\ &= \Re\{\tilde{u}(r,z)\exp[i(-\theta-\sigma t)]\}\,, \end{aligned} \tag{4.10}$$

where $\tilde{u}(r,z)$ is the modal structure function, σ is the resonant frequency, and Φ^u is phase. Waves propagate azimuthally clockwise. Modal structure functions $\tilde{p}$, $\tilde{v}$, and $\tilde{b}$ are imaginary, and $\tilde{u}$ and $\tilde{w}$ are real, as explained in

Section 3.2.b. A free wave without mean flow has modal structure functions as in Figures 3.1 and 3.2 and current ellipse patterns as in Figures 3.3 and 3.4.

Changes to frequency and structure of waves are examined for mean flow of vorticity $\zeta/f = \pm 0.5$. Because of the small horizontal scale of the seamount, this corresponds to weak mean flow amplitude 1.5cm/s (Figure 4.2). At this amplitude, critical surfaces (Section 4.4, Figure 4.9) do not form near the frequency ($0.657f$) of the gravest radial-vertical mode examined here.

Anticlockwise (clockwise) mean flow decreases (increases) the resonant frequency by just $0.001f$ from its value $\sigma = 0.657f$ without mean flow (Figure 4.5). This is somewhat unexpected. Because the azimuthal wavenumber is effectively fixed at $-1/r$ (4.10) by the seamount circumference, the resonance frequency would be expected to be Doppler-shifted by $-V/r$. Estimates of $|V/r|$ using $V_i = 1.5$cm/s are about $0.05f$, much larger than the shifts in Fig-

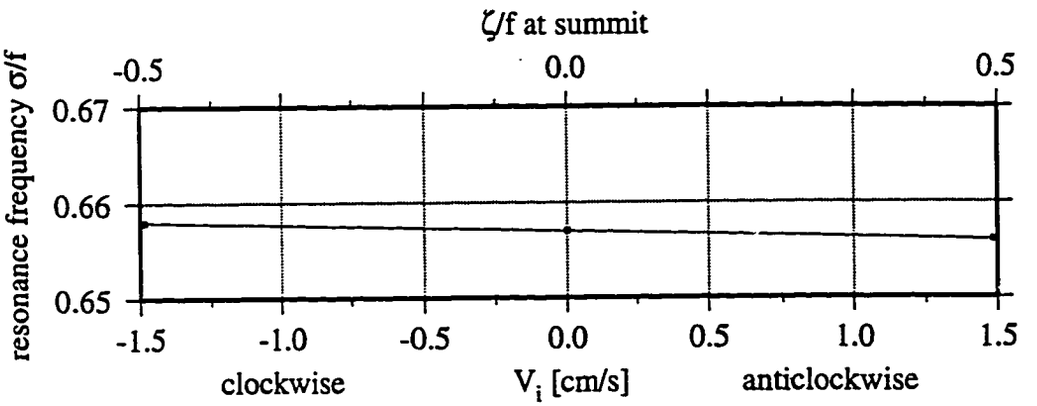

Figure 4.5. Increase (decrease) to resonant frequency of gravest stratified seamount-trapped wave of Section 3.2 by clockwise (anticlockwise) mean flow of radial-vertical structure shown in Figure 4.1.

ure 4.5. Brink (1995) shows that an anticlockwise (clockwise) barotropic mean current increases (decreases) the frequency of a barotropic seamount-trapped wave, a result also contrary to the expected Doppler shift. In Section 4.3 the frequency shift due to the mean flow potential vorticity gradient is shown to oppose the Doppler shift.

Spatial scales of waves are weakly increased (decreased) by anticlockwise (clockwise) mean flow of the shape shown in Figure 4.1 with vorticity reaching $\zeta/f = +0.5$ (-0.5), as demonstrated in Figure 4.6. In the azimuthal velocity modal structure function $\tilde{v}$ (4.10) at $r = 1\text{km}$, the vertical scale for decay to half the bottom value increases (decreases) from 100 m in the wave without mean flow to 120 m (80 m) for anticlockwise (clockwise) mean current. This is representative of the compression or expansion of spatial scales that occurs (not shown) in all modal structure functions $(\tilde{p}, \tilde{u}, \tilde{v}, \tilde{w}, \tilde{b})$. Considering that these mean flows have vorticities reaching $|\zeta/f| = 0.5$, the change to modal structure seems relatively small. Senses of these changes are consistent with mean flow potential vorticity gradient effects in Section 4.3.

Mean flow horizontal shear, not vertical shear or mean buoyancy anomaly, are dominantly responsible for the changes to frequency and modal structure. Solutions identical to those discussed but for barotropic mean flow ($Z_i \to \infty$ in (4.3), not shown) are not materially different.

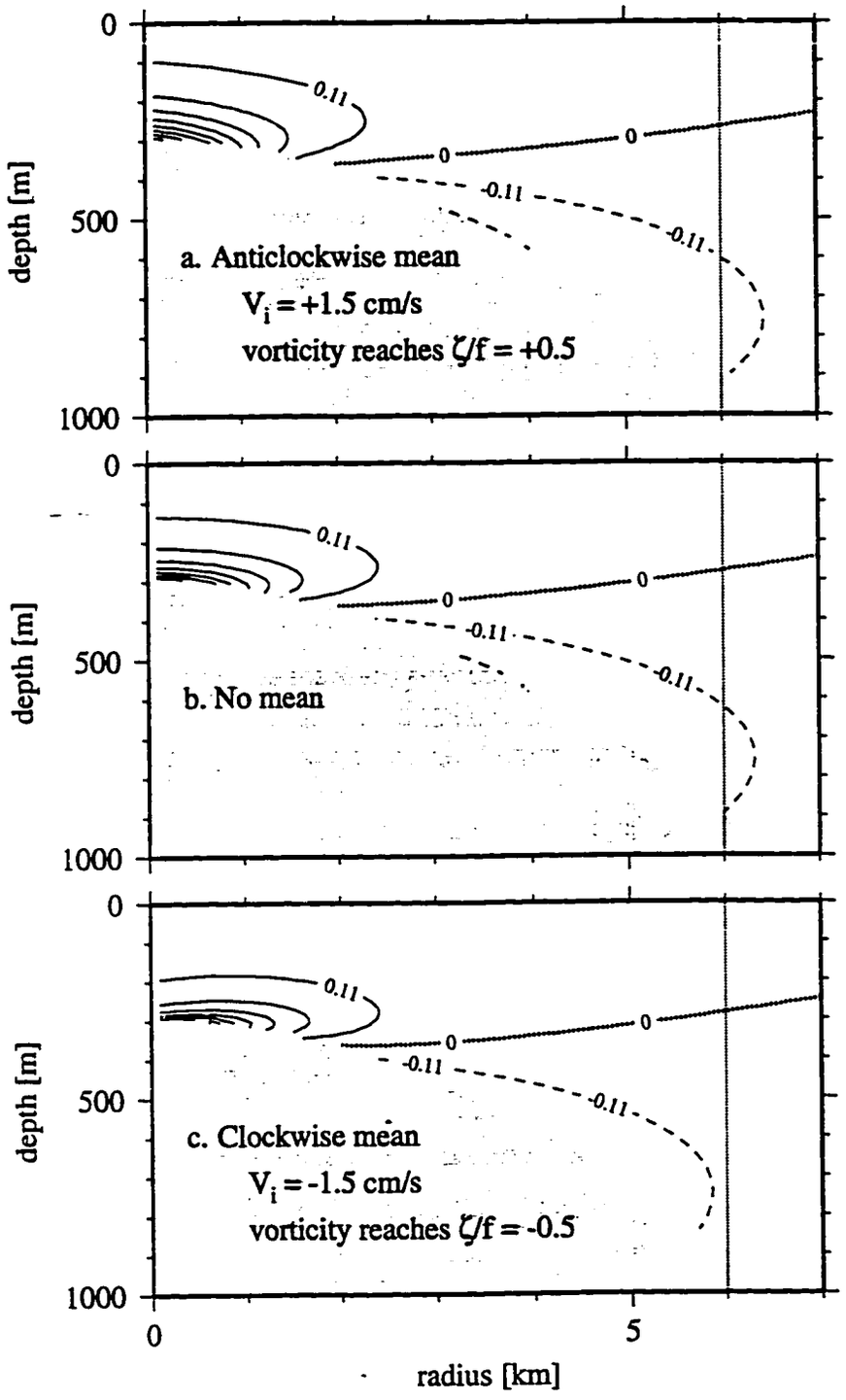

Figure 4.6. Normalized azimuthal velocity modal structure $i\tilde{v}/\max|i\tilde{v}|$ (4.10) of wave in (a) anticlockwise (b) zero (upper right of Figure 3.2) and (c) clockwise mean current of shape in Figure 4.1.

4.3. Physics of stratified slope-Kelvin waves in mean shear

To understand mean flow modifications to stratified seamount-trapped waves we examine the influence of mean flow on their underlying stratified slope-Kelvin waves (Section 3.3). Following the analysis of Section 3.3 for a resting background state and making use of the same waveguide in Cartesian coordinates (Figure 3.9), this section analyses quasigeostrophic wave perturbations linearized about a quasigeostrophic along-isobath mean current. Changes to cross-slope mode frequency and vertical trapping scale caused by mean flow advection, refraction, and potential vorticity gradients are explained for idealized mean flow configurations, and finally applied to mean flow at a seamount.

4.3.a. Advection and potential vorticity gradients of mean flow

Seamount-trapped wave behavior is analogous to that of a cross-slope mode of fixed alongslope wavenumber that is formed by rays trapped in a *Cartesian* waveguide (Section 3.3, Figures 3.9 and 3.11). Consider a uniformly rotating and uniformly stratified quasigeostrophic system in Cartesian coordinates (x, y, z). Bottom depth $h(x)$ increases in the x direction as a weak deviation from its constant lowest order value h_o, so $h_x < Ro\frac{f}{N}$ for Rossby number $Ro \ll 1$. A waveguide is formed by WKB-varying (Lighthill 1978) bot-

tom slope $h_x(x) > 0$ having a local maximum bounded on both shallower and deeper sides by flat regions (Figure 3.9).

Quasigeostrophic mean flow $V(x,z)$ along isobaths in hydrostatic and geostrophic balance with mean buoyancy anomaly $B(x,z)$ is imposed,

$$\begin{aligned} -fV &= -P_x \qquad \text{(a)} \\ 0 &= -P_z + B. \qquad \text{(b)} \end{aligned} \tag{4.11}$$

Thermal wind balance of vertical shear causes a horizontal buoyancy gradient

$$B_x = fV_z. \tag{4.12}$$

Quasigeostrophic perturbations obey (3.9) linearized about the mean flow,

$$\begin{aligned} u_t + Vu_y - fv &= -p_x \qquad (a) \\ v_t + Vv_y + (f+V_x)u &= -p_y \qquad (b) \\ 0 &= -p_z + b \qquad (c) \\ b_t + uB_x + Vb_y + wN^2 &= 0 \qquad (d) \\ u_x + v_y + w_z &= 0. \qquad (e) \end{aligned} \tag{4.13}$$

This set reduces to the quasigeostrophic potential vorticity equation (3.11)

$$\left(\frac{\partial}{\partial t}+V\frac{\partial}{\partial y}\right)\left(\nabla_H{}^2\psi+\frac{f^2}{N^2}\psi_{zz}\right)-Q_x^V\psi_y=0$$
$$Q^V=V_x+\frac{f}{N^2}B_z, \tag{4.14}$$

where ψ is streamfunction related to p, u, v, and b as in (3.10), and Q^V is the quasigeostrophic potential vorticity of the mean flow, related to Ertel potential vorticity as in (3.12). The bottom boundary condition $w = -h_x u$ applied in (4.13)(d) yields

$$f\left(\frac{\partial}{\partial t}+V\frac{\partial}{\partial y}\right)\psi_z+\left(N^2h_x-B_x\right)\psi_y=0 \text{ at } z=-h_o. \tag{4.15}$$

There exist plane wave solutions to (4.14) and (4.15) trapped to the bottom on vertical scale Z much smaller than h_o having form as in (3.15),

$$\psi(x,y,z,t) = \psi_b \exp\left(-(z+h_o)/Z\right)\exp\left(i\left(kx+ly-\sigma t\right)\right), \tag{4.16}$$

where ψ_b is streamfunction amplitude at the bottom and k and l are wavenumber components. Vertically integrated energy per unit horizontal area averaged over a wave period is (3.18)

$$E^z = \frac{1}{4}Z\kappa^2\psi_b^2, \tag{4.17}$$

where $\kappa = \left(k^2 + l^2\right)^{1/2}$ is total horizontal wavenumber.

Advection and changes to the potential vorticity gradient are the two effects of mean flow, as seen on comparing (4.14) and (4.15) to (3.13) and (3.14). To an observer advected at the speed of the mean flow, the wave oscillates with *intrinsic* or *Doppler-shifted* (subscript d) frequency

$$\sigma_d = \sigma - lV. \tag{4.18}$$

The intrinsic frequency is the fixed Eulerian frequency σ Doppler-shifted by $-lV$ due to advection terms ($V\frac{\partial}{\partial y}$) in (4.14) and (4.15), and varies along a ray in varying mean flow. Throughout this analysis subscript d is used to denote intrinsic wave properties, such as group velocity, seen by an observer moving at the mean flow speed or equivalently calculated relative to the mean flow.

Waves are supported by a total potential vorticity gradient comprised of the topographic potential vorticity gradient $Q_x^h = -2Nh_x\kappa$ (3.21) that is present without mean flow, and two components associated with mean flow: Q_x^V due to variations in mean flow shear, and Q_x^B due to thermal wind buoyancy at the bottom due to mean flow vertical shear. The potential vorticity gradient Q_x^V due to mean flow shear variations is, using (4.12) in (4.14),

$$Q_x^V = V_{xx} + \frac{f^2}{N^2} V_{zz}. \tag{4.19}$$

The potential vorticity gradient Q_x^B of thermal-wind buoyancy at the bottom due to vertically sheared mean flow, as identified using (4.15) together with the form of the topographic potential vorticity gradient (3.21), has strength

$$Q_x^B = \frac{2\kappa}{N} B_{bx} = \frac{2\kappa f V_{bz}}{N} \tag{4.20}$$

where subscript b indicates the value at the bottom, $B_{bx} = B_x(z = -h_o)$. The potential vorticity gradient due to mean flow shear variations Q_x^V (4.19) exists within the fluid away from the bottom boundary and is independent of the wavenumber; in contrast, potential vorticity gradients due to topography Q_x^h and mean-flow buoyancy Q_x^B exist only at the bottom boundary, have influence $Z/2$ away from the boundary (3.21), and are inversely proportional to the horizontal scale $1/\kappa$ of the wave. The magnitude of Q_x^h is proportional to the angle rest-state isopycnals make with the bottom, or equivalently the bottom slope angle, and Q_x^B has magnitude proportional to the angle of isopycnals at the bottom relative to horizontal, due to mean flow vertical shear in thermal-wind balance (4.12).

4.3.b. Review of cross-slope modes and rays without mean flow

To aid description of mean flow effects below, we review a cross-slope mode with no mean flow ($V = Q_x^V = Q_x^B = 0$, Section 3.3) and introduce subscript-*o* variables to indicate the no mean flow case. A cross-slope mode has standing-wave across-slope structure, phase propagation purely alongslope with shallow water on its right side (along the $-y$ axis), and frequency σ_o with variables proportional to

$$\exp\left(i\left(l_{\text{smt}}y - \sigma_o t\right)\right) . \tag{4.21}$$

The negative wavenumber is denoted l_{smt} because in the analogous cylindrical system its value is effectively fixed by the seamount circumference. A *cross-slope mode* is a superposition of equal amplitude up- and downslope *rays* of form (3.15) that constructively interfere after reaching turning points (3.29) at the sides of the waveguide (Figure 3.9). In a cross-slope mode streamfunction amplitude at the bottom $\psi_{bo}(x)$, vertical trapping scale $Z_o(x)$, and vertically integrated energy per unit horizontal area $E_o^z(x)$ vary in the across-slope direction (x) as controlled by refraction of individual rays by varying bottom slope (Section 3.3.b, Figure 3.8).

Unlike cross-slope modes, individual rays propagate phase across the slope with wavenumber $k_o(x)$, in addition to alongslope with wavenumber

l_{smt} . The dispersion relation for rays (3.19) determines $k_o(x)$ as a function of $h_x(x)$ for given l_{smt} and corresponding σ_o. Rays move with group velocity components c_{go}^x and c_{go}^y (3.20) along paths $y_o^{\text{ray}}(x)$ (Figure 3.9) that are oriented across isobaths with (3.26)

$$\frac{dy_o^{\text{ray}}}{dx} = c_{go}^y / c_{go}^x = -k_o(x)/l_{smt} = \cot(\gamma_o(x)), \tag{4.22}$$

where an upslope energy ray makes angle γ (3.23) with isobaths (Figure 3.7).

The resonant frequency σ_o of the cross-slope mode is related to the orientation of individual rays from which it is formed, following (3.31), as

$$\int_{x^s(h_x=\sigma_o/N)}^{x^d(h_x=\sigma_o/N)} \left| \frac{dy_o^{\text{ray}}}{dx} \right| dx = \frac{\pi}{|l_{\text{smt}}|} \tag{4.23}$$

where ray orientation (4.22) is integrated between turning points ($h_x = \sigma_o/N$ (3.29)) on the shallow x^s and deep x^d sides of the waveguide (Figure 3.9). This expresses the resonance condition at a seamount that a ray constructively interfere with itself on reaching its original position after encountering turning points at inner and outer radii separated by π in azimuth (Figure 3.11).

4.3.c. Dispersion relation for rays in mean flow

Consider mean flow having potential vorticity gradient components that are weak perturbations about the topographic gradient, so

$$Q_x^V / Q_x^h \ll 1 \quad \text{and} \quad Q_x^B / Q_x^h \ll 1 . \tag{4.24}$$

The dispersion relation

$$\begin{aligned} \sigma &= \frac{l}{2\kappa^2} Q_x^h + lV + \frac{l}{2\kappa^2} Q_x^V + \frac{l}{2\kappa^2} Q_x^B \\ &= -Nh_x \frac{l}{\kappa} + lV + \frac{l}{2\kappa^2}\left(V_{xx} + \frac{f^2}{N^2} V_{zz} \right) + \frac{l}{\kappa} \frac{B_{bx}}{N} \\ &\qquad\qquad \text{(i)} \qquad\qquad \text{(ii)} \qquad\qquad \text{(iii)} \end{aligned} \tag{4.25}$$

applies to a wave ray in mean flow with WKB horizontal and vertical variations on lengthscales large compared to the wavelength and vertical trapping scale respectively. The first term on the right is the dispersion relation without mean flow (3.22), in which rays are refracted by changing bottom slope. Rays are also refracted by (i) advection of sheared mean flow, (ii) the potential vorticity gradient due to mean flow shear variations (4.19), and (iii) the potential vorticity gradient due to mean flow buoyancy at the bottom (4.20). Dispersion relation (4.25) follows from (4.24) in the equation using (4.16) in (4.14) and (4.15) for WKB-varying mean flow shears V_x and V_z,

$$\sigma_{\hat{a}}^{\,2} - \frac{l}{\kappa^2} Q_x^V \sigma_{\hat{a}} - \left(\frac{l}{2\kappa^2} \left(Q_x^h + Q_x^B \right) \right)^2 = 0. \tag{4.26}$$

This equation applies for weak Doppler shift changes to the frequency $|lV| \ll \sigma$ and weak shear variations $|V_{xx}| \ll l\sigma$ occurring on scales much greater than the wavelength $\left|\frac{V_{xx}}{V}\right| \ll l^2, \frac{f^2}{N^2}\left|\frac{V_{zz}}{V}\right| \ll l^2$. Terms (ii) and (iii) in dispersion relation (4.25) are smaller than (i) by the ratio of wavelength to the scale of shear variations. The vertical trapping scale obtained from the dispersion relation (4.25) used in (4.14), (4.15), and (4.16) is to lowest order in Q_x^V/Q_x^h and Q_x^B/Q_x^h

$$Z = \frac{f}{N\kappa}\left(1 + \frac{Q_x^V + Q_x^B}{Q_x^h} \right). \tag{4.27}$$

Ray behavior is used to determine mean flow effects on cross-slope modes. The group velocity of a ray is, using (4.25),

$$\begin{aligned} c_g^x &= \frac{N h_x k l}{\kappa^3}\left(1 + \frac{2Q_x^V}{Q_x^h} + \frac{Q_x^B}{Q_x^h} \right) \\ c_g^y &= V - \frac{N h_x k^2}{\kappa^3}\left(1 + \left(1 - \frac{l^2}{k^2} \right)\frac{Q_x^V}{Q_x^h} + \frac{Q_x^B}{Q_x^h} \right) \end{aligned} \tag{4.28}$$

and a ray moves on a path $y^{ray}(x)$ oriented such that

$$\frac{dy}{dx}^{ray} = c_g^y / c_g^x. \tag{4.29}$$

The group velocity relative to the mean flow (subscript d) is

$$\begin{aligned} c_{gd}^x &= c_g^x \\ c_{gd}^y &= c_g^y - V \end{aligned} \tag{4.30}$$

and to lowest order in Q_x^V/Q_x^h and Q_x^B/Q_x^h, intrinsic ray orientation is

$$\frac{dy_d}{dx}^{ray} = \frac{c_{gd}^y}{c_{gd}^x} = -\frac{k}{l}\left(1 - \left(1 + \frac{l^2}{k^2}\right)\frac{Q_x^V}{Q_x^h} + \frac{Q_x^B}{Q_x^h}\right) = \cot\gamma\left(1 - \left(1 + \tan^2\gamma\right)\frac{Q_x^V}{Q_x^h} + \frac{Q_x^B}{Q_x^h}\right) \tag{4.31}$$

where γ (3.23) is the angle a ray makes with isobaths *relative to the mean flow.*

By (4.31), mean flow controls intrinsic ray orientation $\frac{dy_d}{dx}^{ray}$ both through its potential vorticity gradients and through k/l; even for $Q_x^V = Q_x^B = 0$ intrinsic ray orientation may be changed by mean flow shear through advective refraction of rays (4.25)(i).

4.3.d. Resonance frequencies of cross-slope modes

For seamount-trapped waves in azimuthal mean flow, the azimuthal wavenumber is effectively fixed by the seamount circumference and resonance corresponds to an *intrinsic* ray constructively interfering with itself on reaching its original position (shown without mean flow in Figure 3.11). For the analogous cross-slope mode in the Cartesian waveguide with mean flow this relationship forms the dispersion relation, following (4.23), as

$$\int_{x^s(h_x=\sigma_d/N)}^{x^d(h_x=\sigma_d/N)} \left| \frac{dy_d^{\text{ray}}}{dx} \right| dx = \frac{\pi}{|l_{\text{smt}}|}. \tag{4.32}$$

Intrinsic ray orientation $\frac{dy_d^{\text{ray}}}{dx}$, that seen by an observer moving with the mean flow, is integrated between turning points on the shallow x^s and deep x^d sides of the waveguide. Turning points ($k = 0$) occur at slopes

$$h_x = \sigma_d/N. \tag{4.33}$$

For uniform mean flow or uniform horizontal shear, $Q_x^V = Q_x^B = 0$ and (4.33) is exact; deviation from (4.33) at turning points in more general cases is neglected based on the assumed smallness of Q_x^V/Q_x^h and Q_x^B/Q_x^h.

By (4.32) mean flow changes cross-slope mode frequency through its net effect integrated across the waveguide on the intrinsic orientation of rays, as controlled (4.31) both by potential vorticity gradients Q_x^V and Q_x^B and by advective ray refraction (4.25)(i). Mean flow potential vorticity gradients of the same (opposite) sense as the topographic potential vorticity gradient supporting the waves act to increase (decrease) the frequency. Varying mean flow can change intrinsic ray orientation in different senses in different portions of the waveguide. The integrated effect (4.32) determines the resonant frequency. The sense and magnitude of frequency shifts of cross-slope modes therefore depend on the geometry of the waveguide and mean flow. Further analysis uses simple geometries (next three subsections) to illustrate the physics, finally allowing application to more realistic flow at a seamount.

4.3.e. Uniform mean flow

This subsection and the following two demonstrate senses of changes to frequency and vertical trapping scale of a cross-slope mode by (i) uniform mean flow, (ii) mean flow with uniform horizontal shear (no potential vorticity gradient due to mean flow), and (iii) uniformly varying horizontal shear with corresponding potential vorticity gradient (Figure 4.7). Effects of vertical shear and associated thermal wind buoyancy are insignificant in the examples of Section 4.2.b and not included here. The setting is a symmetric waveguide $h_x(-x) = h_x(x)$ of width $2X$ centered on $x = 0$ with shallow and deep turn-

MEAN FLOW CHANGES TO
CROSS-SLOPE MODE FREQUENCY AND VERTICAL TRAPPING SCALE

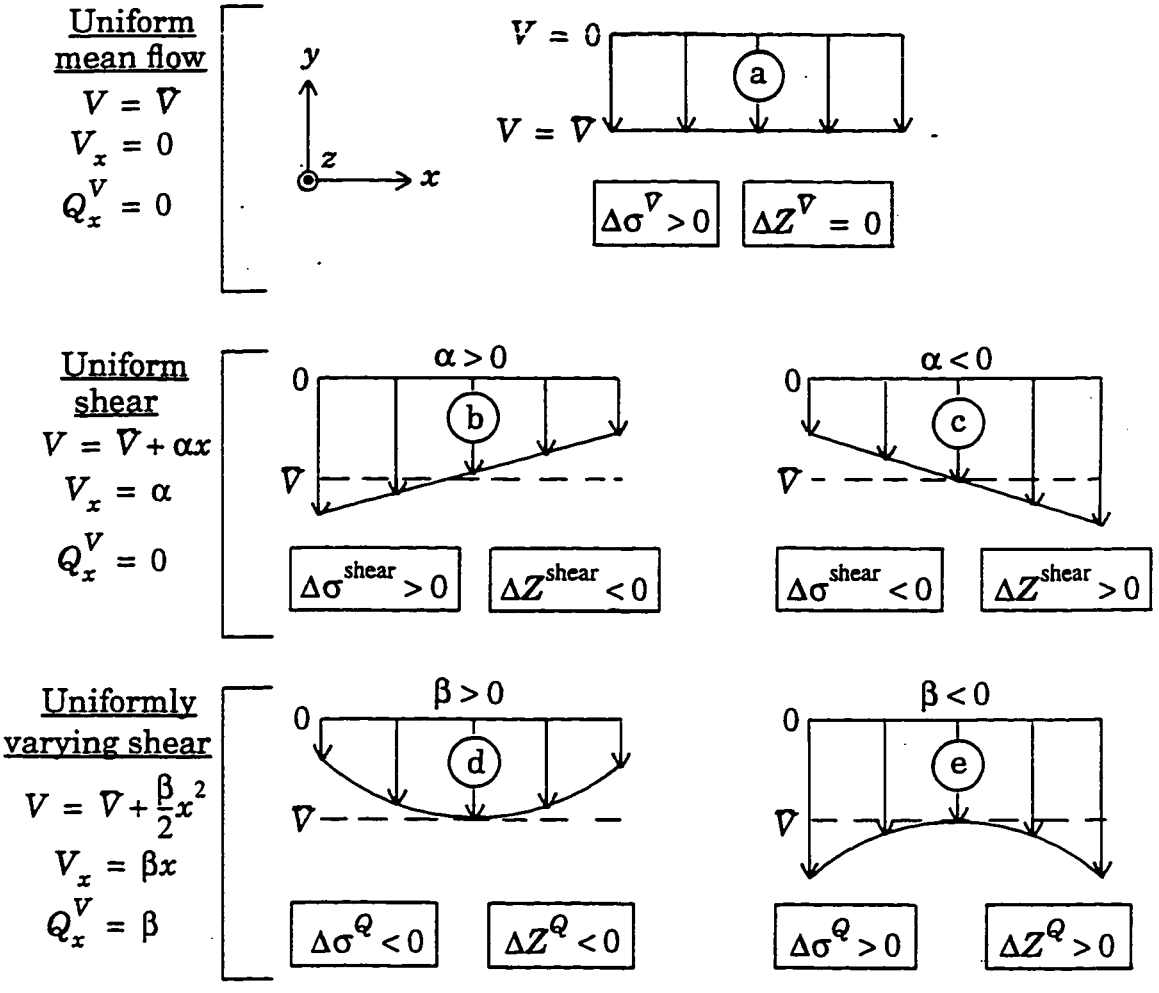

Figure 4.7. Senses of changes to cross-slope mode frequency (4.35) and vertical trapping scale (4.36) caused by mean flow (4.34) in the waveguide of Figure 3.9 for fixed alongslope wavenumber l_{smt}.

ing points at x^s and x^d where $x^d = -x^s = X > 0$ (Figure 3.9). Mean flow is vertically uniform and of the form

$$V = \bar{V} + \alpha x + \frac{\beta}{2} x^2, \tag{4.34}$$

where $\bar{V}$, α and β are constants obeying $|\alpha X|/|\bar{V}| \ll 1$ and $|\beta X^2|/|\bar{V}| \ll 1$ such that mean flow variations are weak and their change to turning point locations (4.33) is neglected. To exclude critical layer behavior (Section 4.4) from these examples, V is more positive than σ/l_{smt} so σ_d (4.18) remains positive.

Mean flows and results for the senses of the changes with $\bar{V} < 0$ are shown schematically in Figure 4.7. Changes by mean flow to the fixed Eulerian frequency σ and vertical trapping scale $Z(x)$ of a cross-slope mode, relative to values without mean flow (σ_o and $Z_o(x)$ in Section 4.3.b), are

$$\sigma - \sigma_o = \Delta\sigma^{\bar{V}} + \Delta\sigma^{shear} + \Delta\sigma^{Q}, \text{ and} \tag{4.35}$$

$$Z(x) - Z_o(x) = \Delta Z^{\bar{V}}(x) + \Delta Z^{shear}(x) + \Delta Z^{Q}(x). \tag{4.36}$$

First, $\Delta\sigma^{\bar{V}}$ and $\Delta Z^{\bar{V}}(x)$ for uniform mean flow $V = \bar{V}$ ($\alpha = \beta = 0$) are treated (this section). Next, uniform shear $V_x = \alpha$ ($\beta = 0$) is included in Sec-

tion 4.3.f to examine $\Delta\sigma^{shear}$ and $\Delta Z^{shear}(x)$. Finally, $\Delta\sigma^{Q}$ and $\Delta Z^{Q}(x)$ for uniformly varying shear $V = \bar{V} + \frac{\beta}{2}x^2$ ($\alpha = 0$) with mean flow potential vorticity gradient $Q_x^V = V_{xx} = \beta$ are considered in Section 4.3.g.

The only effect a uniform mean flow $\bar{V}$ ($V_x = V_z = Q_x^V = Q_x^B = \alpha = \beta = 0$, Figure 4.7a) has on a cross-slope mode is to Doppler shift the frequency by

$$\Delta\sigma^{\bar{V}} = l_{smt}\bar{V} \tag{4.37}$$

$$\text{to} \qquad \sigma^{\bar{V}} = \sigma_o + l_{smt}\bar{V}. \tag{4.38}$$

Mean flow $\bar{V} < 0$ ($\bar{V} > 0$) in the same (opposite) sense as the propagation of the mode, with shallow water on the right $l_{smt} < 0$ (4.21), acts to increase (decrease) the frequency. This behavior (4.37) results from the fixed wavenumber, as seen comparing resonance conditions (4.32) and (4.23) and using (4.31).

Uniform mean flow does not change the structure of a cross-slope mode, $\Delta Z^{\bar{V}} = 0$ (4.36). The intrinsic frequency $\sigma_d = \sigma^{\bar{V}} - l_{smt}\bar{V} = \sigma_o$ (4.38) is spatially uniform so by the dispersion relation (4.25) all ray properties *relative to the mean flow* are the same as in the case without mean flow,

$$\left\{ \begin{array}{ll} k(x) = k_o(x) & \overrightarrow{c_{gd}}(x) = \overrightarrow{c_{go}}(x) \\ \gamma(x) = \gamma_o(x) & \frac{d}{dx} y_d^{\text{ray}}(x) = \frac{d}{dx} y_o^{\text{ray}}(x) \end{array} \right\} \quad \text{for } V = \bar{V}. \qquad (4.39)$$

Structure of a cross-slope mode, controlled by the underlying rays, is thus also the same as the case without mean flow, $Z(x) = Z_o(x)$, so $\Delta Z^{\bar{V}} = 0$ (4.36).

4.3.f. Uniform horizontal shear

Mean flow with uniform horizontal shear $V_x = \alpha$ (4.34) ($V_z = Q_x^V = Q_x^B = \beta = 0$, Figure 4.7b,c) causes no potential vorticity gradient, but by advectively refracting rays (4.25)(i) changes both the frequency and structure of a cross-slope mode. This section explains how uniform shear with $\alpha > 0$ ($\alpha < 0$) causes positive (negative) change $\Delta\sigma^{\text{shear}}$ (4.35) to cross-slope mode frequency and negative (positive) change $\Delta Z^{\text{shear}}(x)$ (4.36) to vertical trapping scale.

Refraction of rays by mean flow shear is analogous to that by changing bottom slope described in Section 3.3.b and shown in Figure 3.8. Consider a ray on a uniformly sloping bottom in horizontally sheared mean flow (4.34) with $\bar{V} < 0$ and $\alpha > 0$ positive (Figure 4.8 shows a ray relative to the mean flow). An upslope-energy ray with alongslope cross-section ΔY_* is started at x_* with intrinsic frequency σ_{d*}, wavenumbers l_{smt} and k_*, energy E_*^z (4.17),

REFRACTION BY MEAN SHEAR AND CRITICAL LAYER FORMATION

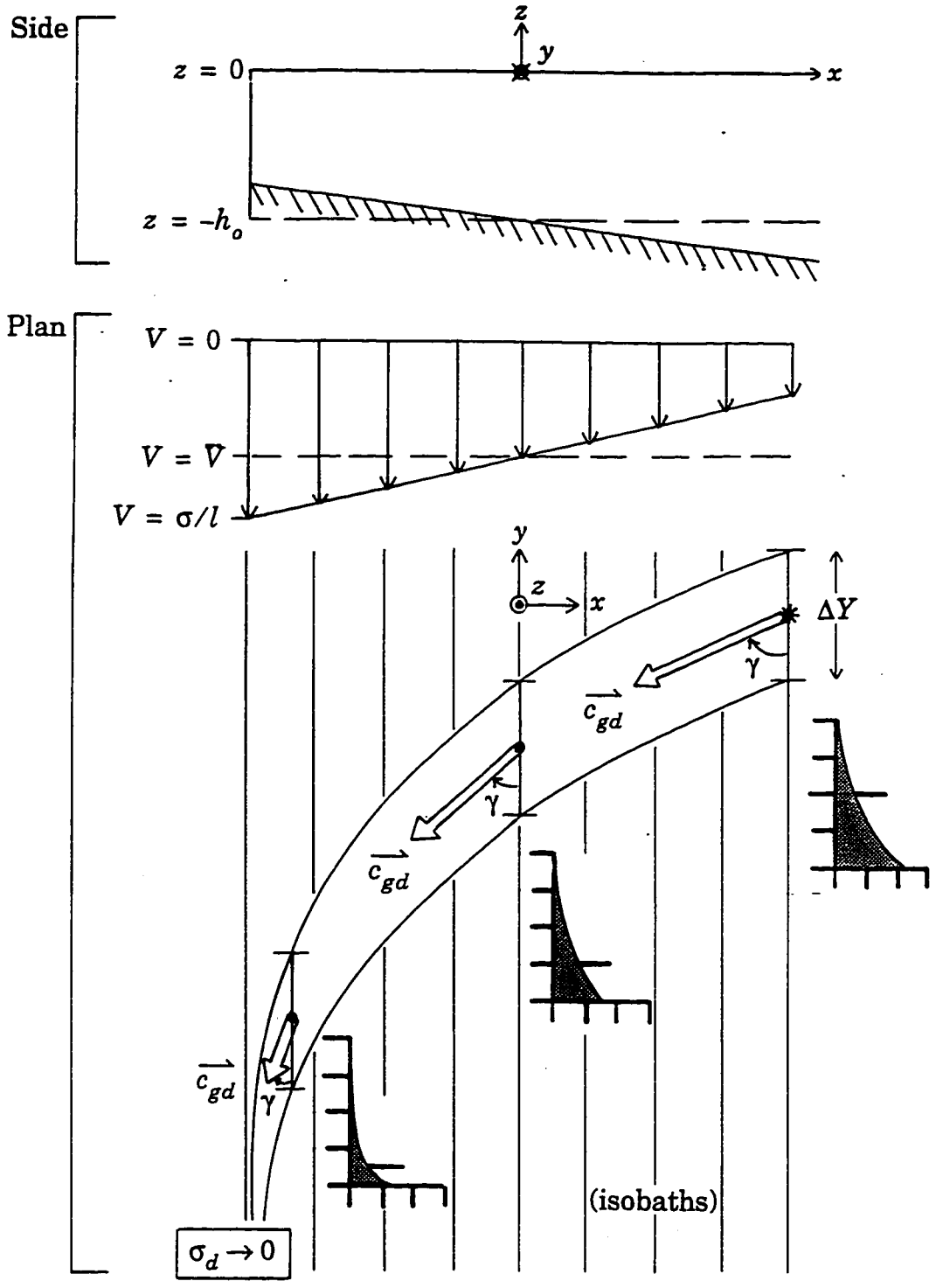

Figure 4.8. Schematic refraction of stratified slope-Kelvin wave ray by horizontally sheared mean flow, and formation of critical layer. Insets: vertical structure (see Figure 3.7). See text for discussion.

streamfunction ψ_{b*} (4.14), group velocity $\overrightarrow{c_{gd*}}$, and orientation angle γ_* (3.23) relative to mean flow. The dispersion relation ((4.25) using (3.23)) is

$$\sigma = Nh_x \sin(\gamma(x)) + l_{smt}(\bar{V} + \alpha x), \text{ or}$$

$$Nh_x \sin(\gamma(x)) = \left(\sigma - l_{smt}\bar{V}\right) - l_{smt}\alpha x. \tag{4.40}$$

Along the ray σ and h_x are constant (both positive) and l_{smt} and α are constant (both negative). The first term on the right side of (4.40) is constant, positive and larger in magnitude than the second. Therefore as the ray moves upslope and x becomes more negative, γ must be reduced so $\frac{dy_d^{ray}}{dx}$ increases (4.31) and the ray becomes oriented less strongly across isobaths. This corresponds to increased k, increased κ, and hence decreased vertical trapping scale $Z = \frac{f}{N\kappa}$ (4.27).

By conservation of wave action density E^z/σ_d (Lighthill 1978), as the ray moves upslope interaction with the mean flow causes the streamfunction amplitude ψ_b to decrease and energy E^z to increase (decrease) for a ray with $\gamma < 45°$ ($\gamma < 45°$) oriented dominantly along (across) isobaths relative to the mean flow. Cross-slope transport of wave action is preserved at its initial

value $\overline{T}_*^x = \dfrac{E_*^z}{\sigma_{d*}} c_{g*}^x \Delta Y_*$. Because ΔY is invariant by geometry and

$\dfrac{c_g^x}{\sigma_d} = \dfrac{1}{l_{\text{smt}}} \cos\gamma \sin\gamma$ by (4.25) and (4.40), energy varies as

$$\frac{E^z}{E_*^z} = \frac{\cos\gamma_* \sin\gamma_*}{\cos\gamma \sin\gamma}. \tag{4.41}$$

A ray with $\gamma_* < 45°$ ($\gamma_* > 45°$) increases (decreases) in energy as it travels upslope. By (4.17) and (4.27) in (4.41) then, streamfunction amplitude varies as

$$\frac{\psi_b^2}{\psi_{b*}^2} = \frac{\cos\gamma_*}{\cos\gamma}. \tag{4.42}$$

Should the mean flow approach strength $V \to \sigma / l_{\text{smt}}$ a critical layer forms; slope-Kelvin wave critical layers in stratified seamount-trapped waves are the subject of Section 4.4.a.

The frequency change $\Delta\sigma^{\text{shear}}$ (4.35) of a cross-slope mode is positive (negative) for horizontal shear (4.34) with $\alpha > 0$ ($\alpha < 0$), the result of advective ray refraction (4.25)(i) increases (decreases) to intrinsic ray orientation $\left| \dfrac{dy}{dx}_d^{\text{ray}} \right|$

(4.31) relative to the constant mean flow case $\left|\frac{dy_o^{ray}}{dx}\right|$ (4.39). By the resonance condition (4.32),

Uniform horizontal shear: Uniform mean flow:

$$\int_{x^s(h_x=(\sigma-l_{smt}\nabla)/N)}^{x^d(h_x=(\sigma-l_{smt}\nabla)/N)} \left|\frac{dy_d^{ray}}{dx}\right| dx = \int_{x^s\left(h_x=\left(\sigma^\nabla-l_{smt}\nabla\right)/N\right)}^{x^d\left(h_x=\left(\sigma^\nabla-l_{smt}\nabla\right)/N\right)} \left|\frac{dy_o^{ray}}{dx}\right| dx, \qquad (4.43)$$

where the effect of shear on turning point locations (limits of left-hand integral) have been ignored based on the assumed smallness of α (4.34). By (4.31) and (3.26), the integrand on the left (right) of (4.43) is larger for $\alpha > 0$ ($\alpha < 0$) because ray refraction causes intrinsic ray orientation less (more) strongly across isobaths as compared to the case with constant mean flow (Section 4.3.e, Figure 4.8). By (4.43) turning points for shear having $\alpha > 0$ ($\alpha < 0$) must therefore be closer together (farther apart) than without shear, hence occur at higher (lower) h_x corresponding to steeper (gentler) slopes, and require $\sigma > \sigma^\nabla$ ($\sigma < \sigma^\nabla$). The frequency shift due to the shear, by (4.35)

$$\Delta\sigma^{shear} = \sigma - \left(\sigma_o + l_{smt}\nabla\right) = \sigma - \sigma^\nabla,$$

is thus positive (negative) for shear with $\alpha > 0$ ($\alpha < 0$).

4.3.g. Uniformly varying horizontal shear

Mean flow $V = \bar{V} + \frac{\beta}{2}x^2$ ($\alpha = 0$ in (4.34), Figure 4.7d,e) of uniformly *varying* horizontal shear with $\beta > 0$ ($\beta < 0$) causes positive (negative) potential vorticity gradient $Q_x^B = V_{xx} = \beta$ opposing (reinforcing) the negative topographic potential vorticity gradient Q_x^h (3.21). Because shear variations necessitate inclusion of shear, rays are refracted by both the advection (previous section) and potential vorticity gradient terms in the dispersion relation ((4.25)(i) and (ii)). Under WKB scaling the effect (ii) is small compared to (i). Modifications to cross-slope mode frequency $\Delta\sigma^Q$ (4.35) and to vertical trapping scale $\Delta Z^Q(x)$ (4.36) are due to the potential vorticity gradient only.

Shear variations with $\beta > 0$ ($\beta < 0$) cause negative (positive) change $\Delta\sigma^Q$ (4.35) to cross-slope mode frequency (Figure 4.7d,e), in accord with intuition regarding a mean flow potential vorticity gradient opposing (reinforcing) that of the bottom slope. This is evident by the reasoning of the previous section using (4.31) in (4.32) for positive (negative) Q_x^V and recalling that $Q_x^h < 0$ (3.22). Shear variations with $\beta > 0$ ($\beta < 0$) cause negative (positive) change to vertical trapping scale $\Delta Z^Q(x)$ (4.36), from positive (negative) Q_x^V in (4.27).

4.3.h. Summary and application to seamount

Figure 4.7 displays the sense of frequency changes $\left(\Delta\sigma^{\nabla}, \Delta\sigma^{\text{shear}}, \Delta\sigma^{Q}\right)$ (4.35) and changes in vertical trapping scale $\left(\Delta Z^{\nabla}(x), \Delta Z^{\text{shear}}(x), \Delta Z^{Q}(x)\right)$ (4.36) to a cross-slope mode in the Cartesian waveguide of Figure 3.9 that result from constant mean flow, uniform shear, and mean flow with uniformly varying shear respectively. Even for these simple flow configurations, centered on a symmetric waveguide, the three influences can cause modifications of opposing senses. More general waveguide and mean flow geometries may have net frequency shift $\sigma - \sigma_o$ (4.35) and net change to vertical trapping scale $Z(x) - Z_o(x)$ (4.36) of either sense, and net changes to vertical trapping scale may be of different senses and magnitudes at different cross-slope locations.

Comparison of results of Section 4.2.b for mean flow in a realistic seamount setting to physics of idealized mean flow in the symmetric Cartesian waveguide is problematic. The simplest mean current at a seamount, $V = V_i r$ in solid-body rotation, is not a Galilean transformation as constant V is in the rectilinear waveguide; quasigeostrophic scaling is inappropriate at a tall seamount; WKB scaling of variations of mean flow and bottom slope is violated; and the neglect of changes to turning point locations due to mean flow variations may not be valid. Nonetheless, a consistent interpretation of results from the realistic case in terms of idealized mean flow behavior is as follows.

Section 4.2.b demonstrated two effects of the clockwise mean flow in Figure 4.1 on the stratified seamount-trapped wave of Section 3.2: the resonance frequency increases by just $0.001f$ (Figure 4.5), and spatial scales are weakly reduced (Figure 4.6). Estimates of the Doppler shift $-V/r$ imply much larger increases to resonant frequency, so a process acting in opposition to the Doppler shift is implicated. The current of Figure 4.1a is most similar to the $V<0$ and $Q_x^V>0$ idealized mean flow case (Figure 4.7d). The effect of $Q_x^V>0$ is to cause $\Delta\sigma^Q<0$, in opposition to $\Delta\sigma^V>0$, and to reduce the vertical trapping scale ($\Delta Z^Q<0$). Thus a consistent interpretation of the realistic case is that the mean flow potential vorticity gradient is responsible for the weak resonance frequency change and reduced spatial scales of the wave.

4.4. Critical surfaces

Governing equations for stratified seamount-trapped waves in a mean azimuthal current ((4.8) and (4.10)) reduce to a single second-order partial differential equation ((C.9), Appendix C) for the pressure modal structure as a function of radius and depth. For moderate mean flow $V\cong 5$cm/s the equation is singular where the wave equation discriminant vanishes due to either of two conditions. This section identifies these singularities as a *stratified seamount-trapped wave critical surface* in one case and an *internal wave critical surface* in the other, shows that the internal wave critical surface bounds a

superinertial cap or region where the governing equation is hyperbolic, and demonstrates critical surface shapes for mean flow of Figure 4.1.

In azimuthal mean flow V the intrinsic or Doppler-shifted (subscript d) frequency σ_d of a first-azimuthal mode seamount-trapped wave, for which the azimuthal wavenumber is $-1/r$ by (4.10), is

$$\sigma_d(r,z) = \sigma + V(r,z)/r. \tag{4.44}$$

It is a function of radius and depth, and is greater (less) than the constant Eulerian frequency σ in anticlockwise (clockwise) mean flow. Physically it is the frequency of the wave relative to the mean flow, or equivalently the frequency seen by an observer moving locally with the mean current.

The discriminant of wave equation (C.9) for waves (4.10) linearized about mean azimuthal flow (4.8) is

$$\frac{4\sigma_d^2\left(\sigma_d^2 - f_{eff}^2\right)^3}{\left(N^2 + B_z\right)}, \tag{4.45}$$

where the "effective" Coriolis frequency f_{eff} is defined

$$f_{eff}^2(r,z) = \left(f + \frac{2V}{r}\right)\left(f + \frac{1}{r}(rV)_r - \frac{(V_z)^2}{\left(N^2 + B_z\right)}\left(f + \frac{2V}{r}\right)\right). \tag{4.46}$$

Discriminant (4.45) is a function of radius and depth. Where it vanishes the wave equation becomes singular. If this occurs because

$$\sigma_d(r,z) = 0,$$

a *stratified seamount-trapped wave critical surface* forms as described in Section 4.4.a. In Section 4.4.b, the dynamical role of f_{eff} is explained and a vanishing discriminant where

$$\sigma_d(r,z) = f_{eff}(r,z)$$

is identified as an *internal wave critical surface.*

Frequencies and mean flow amplitudes at which the two types of critical surfaces form are shown in Figure 4.9 for mean flow of radial-vertical structure shown in Figure 4.1. As clockwise mean current increases in magnitude, for low (high) subinertial frequencies a stratified seamount-trapped wave critical surface (internal wave critical surface) forms.

4.4.a. Stratified seamount-trapped wave critical surfaces $\sigma_d = 0$

A stratified seamount-trapped wave critical surface occurs where

$$\sigma_d = \sigma + V/r = 0, \tag{4.47}$$

corresponding physically to wave phase speed $\vec{c_p} = \frac{\sigma}{-1/r}\hat{\theta} = -r\sigma\hat{\theta}$ overcome by mean flow, and thus forms only for clockwise current $V<0$. This section

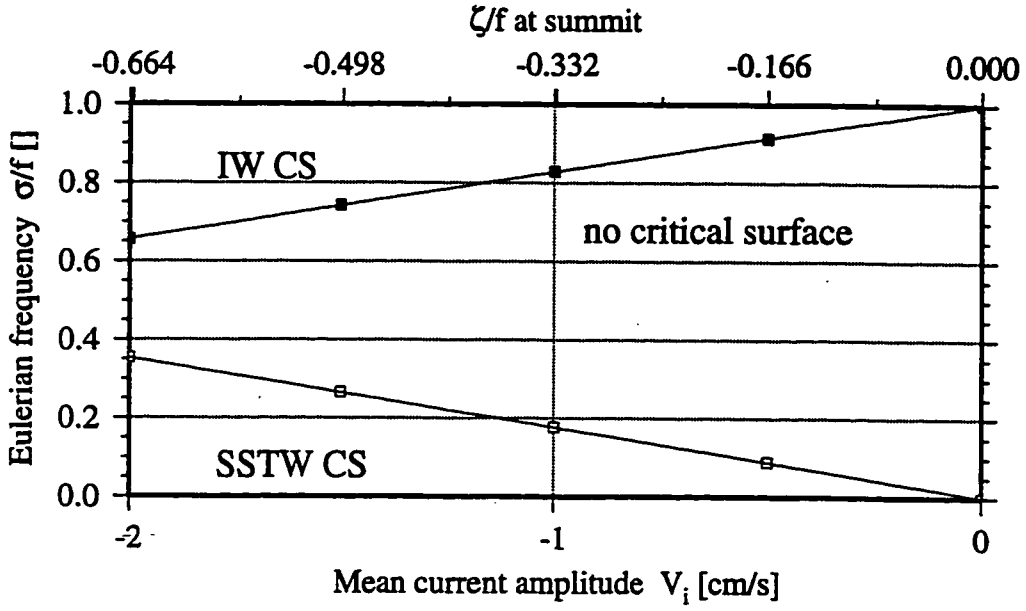

- ■ $\sigma_d = f_{eff}$ Internal wave critical surface forms
- □ $\sigma_d = 0$ Stratified seamount-trapped wave critical surface forms

Figure 4.9. Formation of stratified seamount-trapped wave critical surface (SSTW CS, shown in Figure 4.10) and internal wave critical surface (IW CS, shown in Figure 4.12) as a function of wave frequency and amplitude of clockwise mean flow of shape in Figure 4.1.

demonstrates that near a critical surface horizontal and vertical scales of the wave diminish to infinitesimal magnitude.

A stratified seamount-trapped wave critical surface may be understood by considering the effect of sheared mean flow on stratified slope-Kelvin waves (Section 4.3), the plane-wave elements from which a stratified seamount-trapped wave is formed (Section 3.3). Critical layer formation is shown in Figure 4.8 for a stratified slope-Kelvin wave ray moving upslope across horizontally sheared alongslope mean flow in a Cartesian coordinate system with a planar ocean bottom. As the critical layer is approached (Section 4.3.f) the

ray becomes oriented along isobaths, the across-slope wavenumber $k \to \infty$ becomes infinite, the intrinsic frequency falls to zero $\sigma_d \to 0$, the group speed relative to the mean flow vanishes $\overrightarrow{c_{gd}} \to 0$, and energy of the wave is partitioned between mean flow and turbulence (Muench 1995). This behavior is identical to that of a plane, vertically propagating, non-rotating internal wave ray in vertically sheared mean flow as analyzed by Lighthill (1978). In a stratified slope-Kelvin wave, the vertical trapping scale Z decreases as the horizontal wavelength does (4.27), so as a critical layer is approached *both* become arbitrarily small and vertical as well as horizontal shear becomes large.

Stratified seamount-trapped wave critical surfaces formed by clockwise mean flow with structure shown in Figure 4.1 curve upward and inward from the point where they intersect the seamount (Figure 4.10). At a given mean flow amplitude, the critical surface expands as wave frequency decreases (Figure 4.10a). At a fixed frequency, for increased mean flow strength the critical surface expands (Figure 4.10b).

Because seamount-trapped wave critical surfaces form in relatively weak mean currents they may be important in maintaining clockwise mean flow that is frequently observed at seamounts. For Kelvin waves in the equatorial waveguide, analogous to stratified slope-Kelvin waves, transfer of wave energy to mean flow is most efficient at critical layers and accelerates currents in the direction of wave propagation (McPhaden et al. 1986).

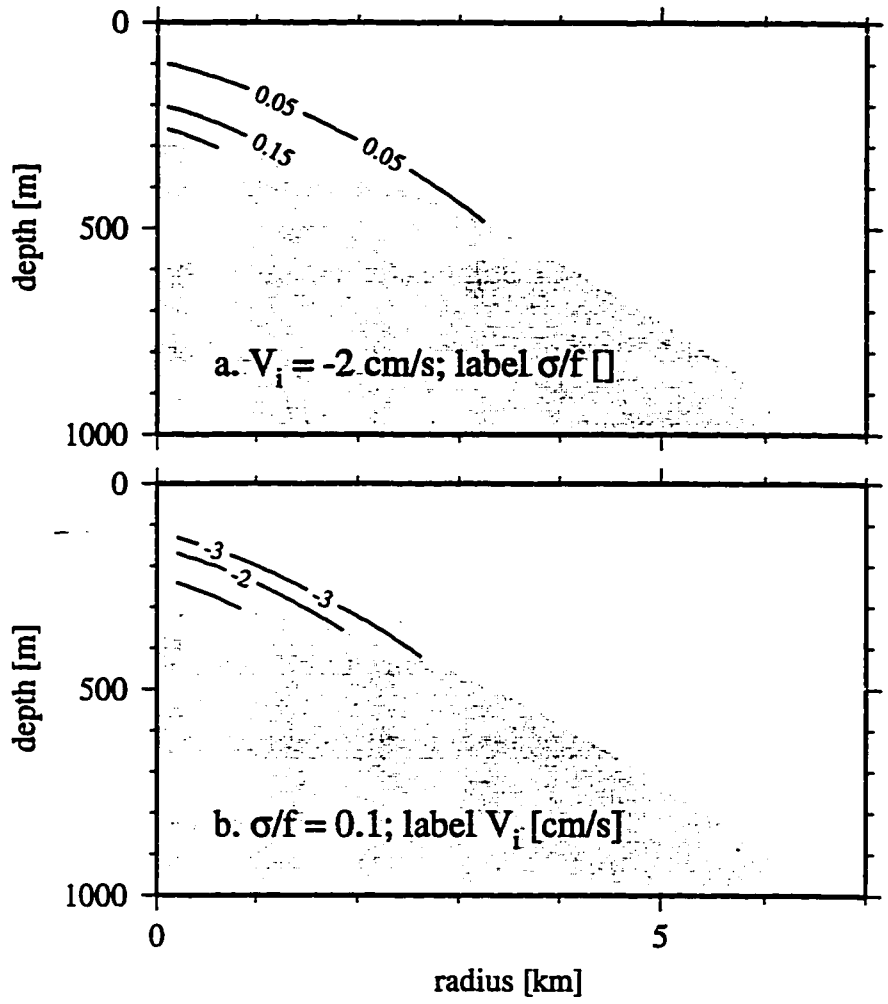

Figure 4.10. Stratified seamount-trapped wave critical surfaces for clockwise mean flow of shape as in Figure 4.1. (a) Mean current amplitude V_i = –2cm/s. Critical surfaces labelled with frequencies σ/f = 0.05, 0.15, 0.25. (b) Frequency σ/f = 0.1. Critical surfaces labelled with mean current amplitude V_i = –1, –2, –3 cm/s.

4.4.b. Superinertial cap and internal wave critical surfaces $\sigma_d = f_{\text{eff}}$

The effective Coriolis frequency f_{eff} (4.46) is the low-frequency bound for superinertial internal waves of form (4.10). For the clockwise mean flow of Figure 4.1 it is reduced relative to the planetary Coriolis frequency f near the

bottom above the seamount (Figure 4.11). For mean flow with vertical shear obeying ($(V_z)^2/\left(N^2+B_z\right) \ll 1$) and nearly in solid-body rotation ($V_r \sim V/r$), (4.46) reduces to $f_{eff} \approx f+\zeta$, the form found based on scaling of near-inertial waves in a solid-body current by Kunze (1985). Here, f_{eff} (4.46) includes effects of both horizontal and vertical mean shear and is not limited to near-inertial wave scaling; its form is also noted by Brink (1995). Dominant contributions to f_{eff} (4.46) of Figure 4.11 are from $(f+\zeta)$ and $(f+2V/r)$, as seen in Figure 4.4.

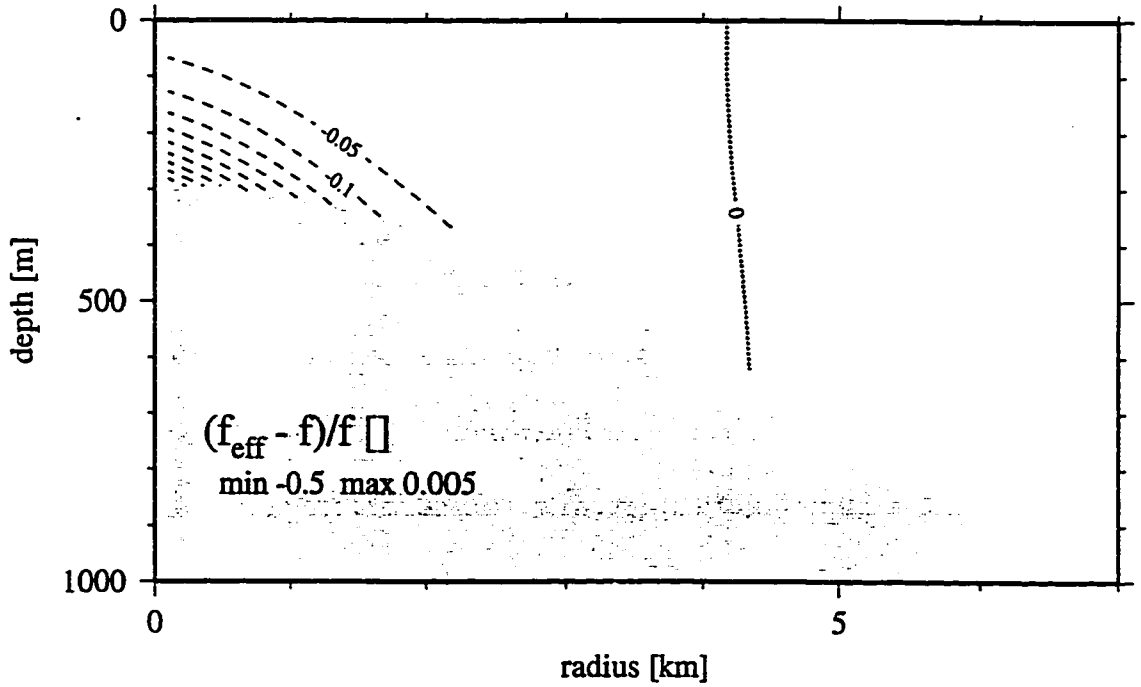

Figure 4.11. Normalized deviation from f of effective Coriolis frequency f_{eff} (4.46), the low frequency bound of superinertial internal waves, in clockwise current V_i = −1.5cm/s of shape in Figure 4.1.

An internal wave critical surface ($\sigma_d = f_{\text{eff}}$) is the boundary of a region inside (outside) of which the wave equation (C.9) is hyperbolic (elliptic) due to a positive (negative) discriminant (4.45). When formed by mean flow with structure shown in Figure 4.1 the internal wave critical surface curves upward and inward from the point where it intersects the seamount (Figure 4.12). The region it encloses is called a *superinertial cap* because within it a wave of subinertial frequency $\sigma < f$ that has $\sigma_d > f_{\text{eff}}$ need not be trapped to the seamount. Azimuthal propagation of such a wave may be accompanied by radial and/or vertical propagation as for a superinertial internal wave. For a given mean flow amplitude, the horizontal and vertical extent of the superinertial cap increases for waves of increasing frequency (Figure 4.12a). At a fixed frequency, as mean flow strength increases the superinertial cap grows in horizontal and vertical extent (Figure 4.12b).

The curving boundary of a superinertial cap is called an internal wave critical surface because it is a critical layer near its shallowest point. Energy excited within the hyperbolic domain with subinertial frequency obeying $\sigma_d > f_{\text{eff}}$ travels along internal wave rays outward until it reaches the boundary of the superinertial cap (Figure 4.13). For a clockwise current increasing in magnitude with radius, where the boundary is oriented dominantly vertically (horizontally) a wave encounters a turning point (critical layer); in the relevant one-dimensional limits, an internal wave ray propagating across

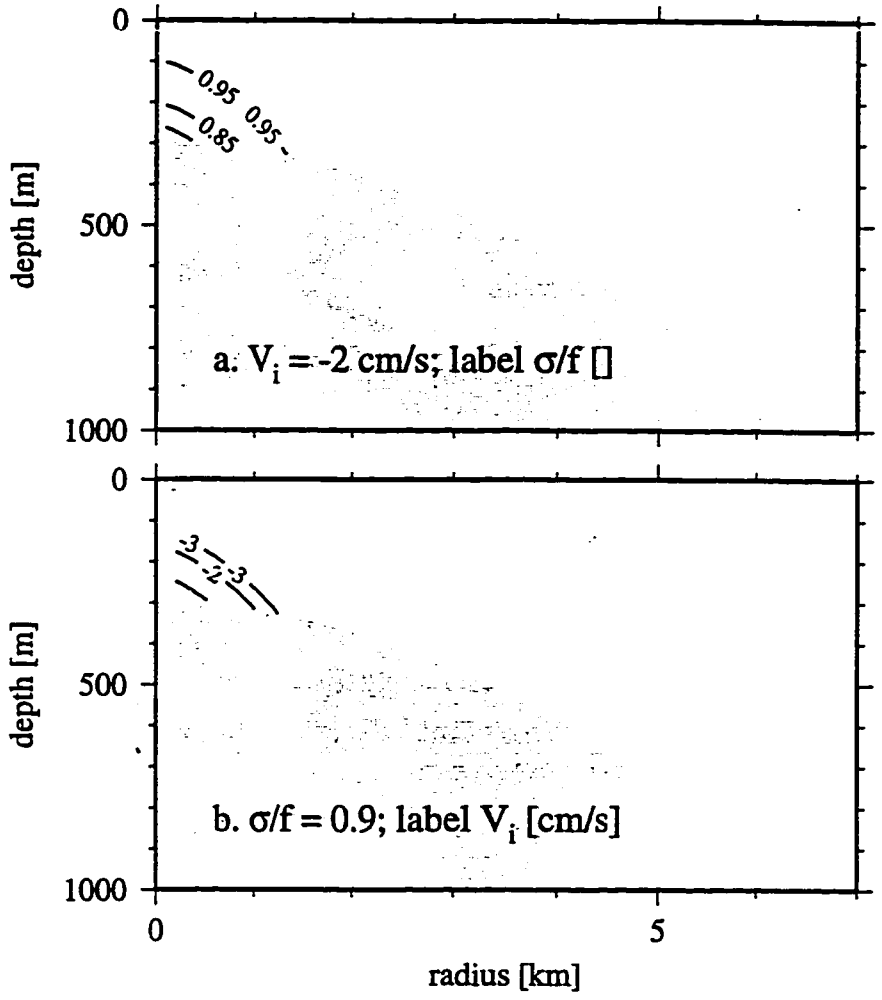

Figure 4.12. Internal wave critical surfaces for mean flow of radial-vertical structure in Figure 4.1. (a) Mean current amplitude $V_i = -2$cm/s , frequencies $\sigma/f = 0.75, 0.85, 0.95$. (b) Frequency $\sigma/f = 0.9$, mean current amplitude $V_i = -1, -2, -3$ cm/s .

mean flow sheared horizontally (vertically) reaches a vertical (horizontal) surface that is a turning point (critical layer) as the Doppler-shifted frequency approaches the lower bound of the internal-wave band (Gill 1982, Lighthill 1978). An upward ray in the superinertial cap is trapped laterally by turning-point reflections and eventually reaches the horizontally-oriented critical

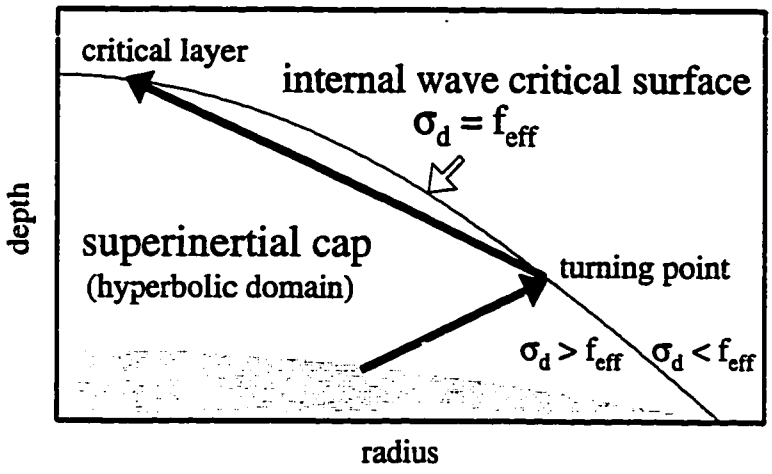

Figure 4.13. Schematic *superinertial cap* bounded by *internal wave critical surface* formed in mean clockwise current increasing with radius. Subinertial ($\sigma < f$) tidal currents excite waves at an effectively superinertial ($\sigma_d > f_{eff}$) frequency traveling on rays clockwise *and* away from the bottom. A critical layer occurs where the $\sigma_d = f_{eff}$ is nearly horizontal. A turning-point reflection off a more vertical section of this surface is also shown here.

layer. For clockwise current magnitude decreasing with radius, more vertical regions of the $\sigma_d = f_{eff}$ surface may act as critical levels, not turning points.

4.5. Internal wave critical surfaces at Fieberling Guyot

Extensive observations of currents at Fieberling Guyot, a tall seamount at 32.4° N in the eastern North Pacific, were collected during the Flow Over Abrupt Topography (TOPO) initiative of the Office of Naval Research (Eriksen 1991, Roden 1994, Brink 1995, Kunze and Toole 1996). Currents are dominated by mean clockwise azimuthal flow and amplified diurnal tides that are slightly subinertial at this latitude, $\sigma_{K_1} = 0.93f$. This section shows internal

wave critical surfaces, as defined and explained in the previous section, for the specific example of diurnal currents at Fieberling using mean flow and stratification based on measurements.

Measured mean flow at Fieberling is clockwise with maximum amplitude V_i, occurring near $7-8$km radius, that fluctuates between about -5 and -15cm/s. At smaller radii there is nearly solid body rotation, and at greater radii current appears to decay over a few km. The maximum is at 550 m deep, slightly below the seamount summit, above and below which strength falls off over $100-200$ m. A unit-normalized shape function (4.3) with these features is

$$G(r,z) = (4e)^{1/4}\frac{r}{R_i}\exp\left(-\left(\frac{r}{R_i}\right)^4\right)\exp\left(-\left(\frac{z+z_i}{Z_i}\right)^2\right), \qquad (4.48)$$

where $R_i = 10.25$km, $z_i = -550$ m, and $Z_i = 100$ m. For $V_i = -10$cm/s, cyclogeostrophic (4.1) vertical displacements (Figure 4.14) for stratification profile $N^2(z)$ (not shown) based on that measured (Roden and Fredericks 1992) are roughly consistent with observations. Mean vertical displacements at the center relative to radius $7-8$km, estimated from data shallower than 500 m, reach 4 m (Kunze and Toole 1996) or about 13 m (based on $0.11°C$ temperature anomaly, Brink 1995). These are smaller but agree reasonably with $10-15$ m in Figure 4.14 considering the difficulty of the measurement.

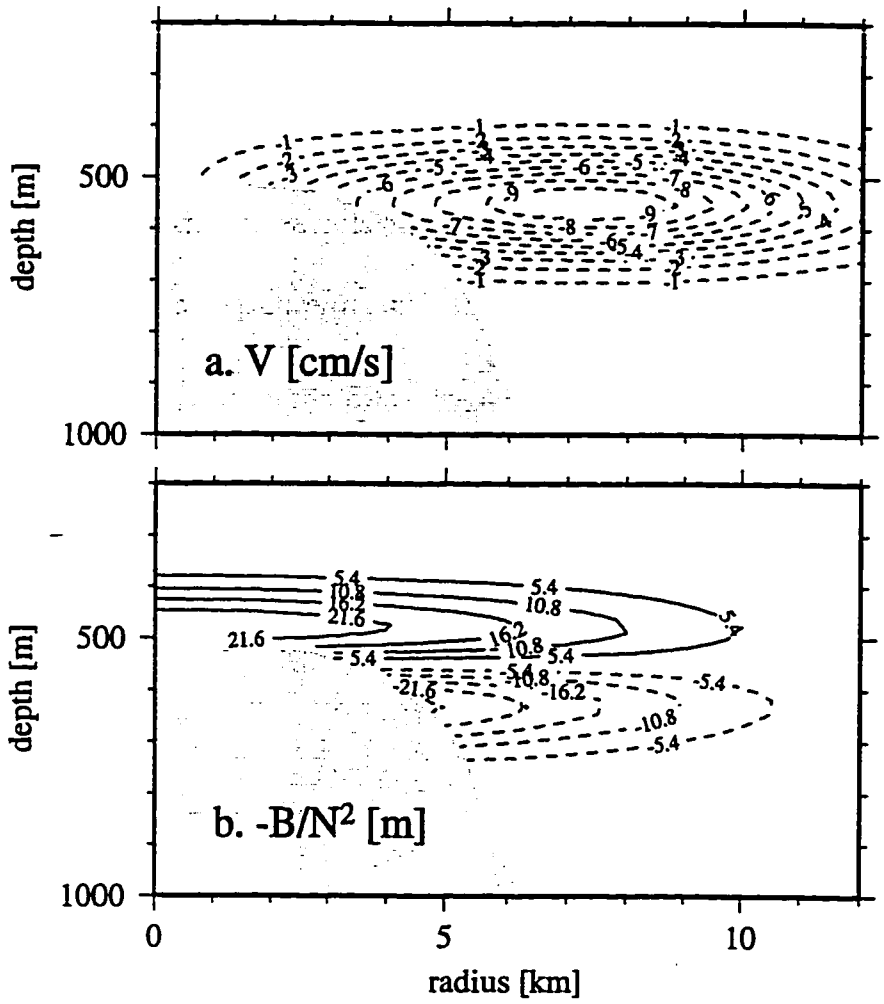

Figure 4.14. Mean azimuthal current based on measurements from Fieberling Guyot. (a) Analytic function (4.3) with shape (4.48) for $V_i = -10\text{cm/s}$, (b) Cyclogeostrophic (4.1) vertical displacements using $N^2(z)$ (not shown) based on data (Roden and Fredericks 1991).

For mean flow of Figure 4.14, the low-frequency bound f_{eff} (4.46) of superinertial internal waves is reduced by up to $0.43f$ relative to f (Figure 4.15). As in the example of Section 4.4.b, f_{eff} is dominantly controlled by $f+\zeta$ and $f+2V/r$. The vertical component of vorticity $\zeta = \frac{1}{r}(rV)_r$ (not shown)

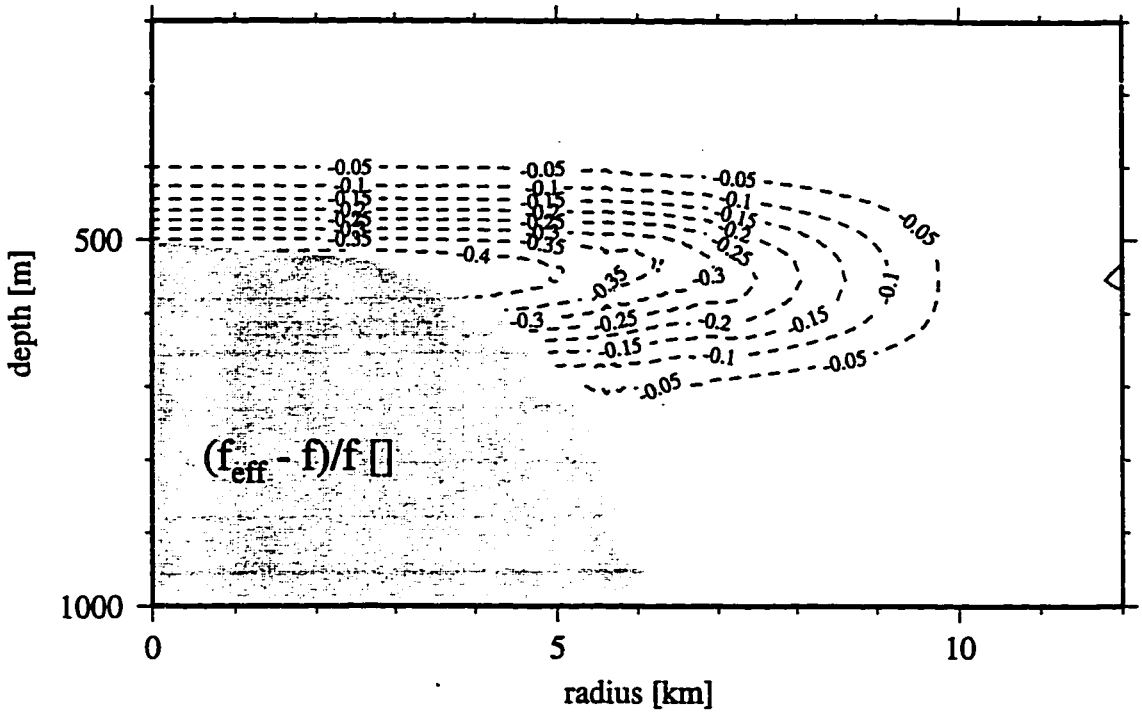

Figure 4.15. Normalized deviation from f of effective Coriolis frequency f_{eff} (4.46) for mean flow of Figure 4.14.

reaches $-0.42f$ at inner radii, and rises to $+0.2f$ due to the rapid decay with radius of (4.48) near radius 11km. As discussed in Section 4.2.a, conditions for baroclinic instability are met; such instabilities are not addressed here.

Clockwise mean flow stronger than V_i = 4cm/s causes an internal wave critical surface for diurnal ($\sigma_{K_1} = 0.93f$) currents (Figure 4.16). The critical surface occurs where the intrinsic frequency σ_d (4.44) reaches the lower bound f_{eff} (4.46) for superinertial internal waves. It extends laterally away from the seamount near the summit depth, encompassing a larger region for stronger mean flow (Figure 4.17). Within the region bounded by the critical

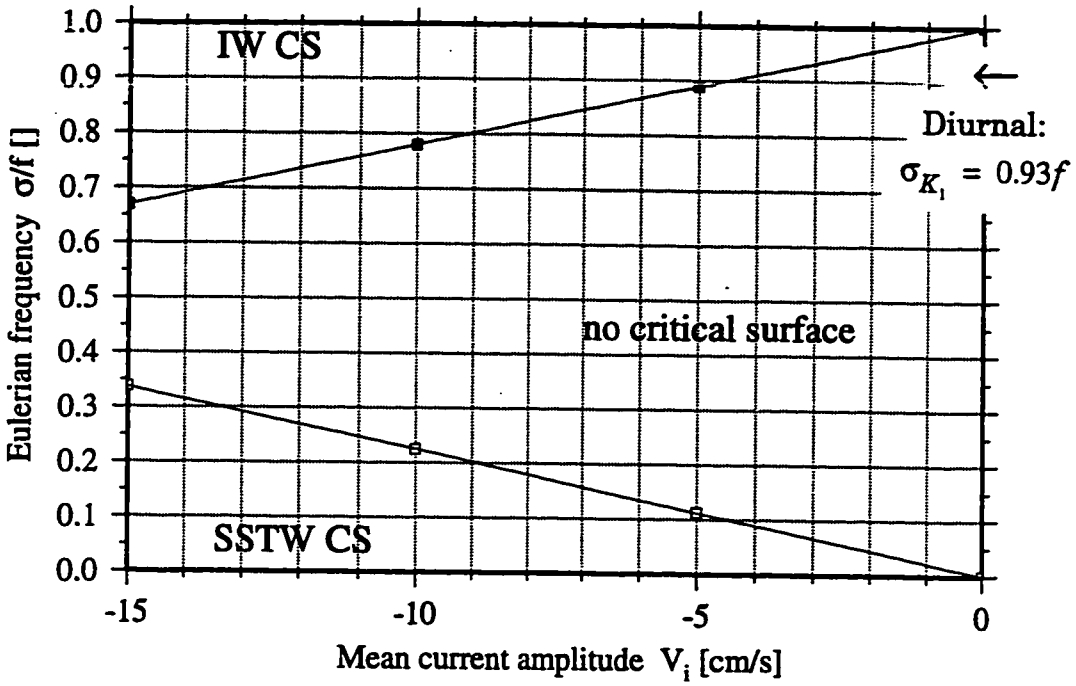

- $\sigma_d = f_{eff}$ Internal wave critical surface forms
- $\sigma_d = 0$ Stratified seamount-trapped wave critical surface forms

Figure 4.16. Critical surface formation (shown as Figure 4.9) for mean flow of shape in Figure 4.14. For diurnal ($\sigma_{K_1} = 0.93f$) currents, amplitudes $V_i > -4$cm/s cause an internal wave critical surface that bounds an effectively superinertial domain (Figure 4.17).

surface, diurnal motions are effectively superinertial and thus need not be trapped to the bottom. Internal wave rays excited at the diurnal frequency within the superinertial domain propagate outward from the bottom to the critical surface (Figure 4.13). As the $\sigma_d = f_{eff}$ surface is approached where it is horizontal, a critical level forms (Lighthill 1978): wave scales diminish, shear increases, and hence the Richardson number decreases and turbulent overturns may be triggered. Wave trapping and critical layer formation occurs

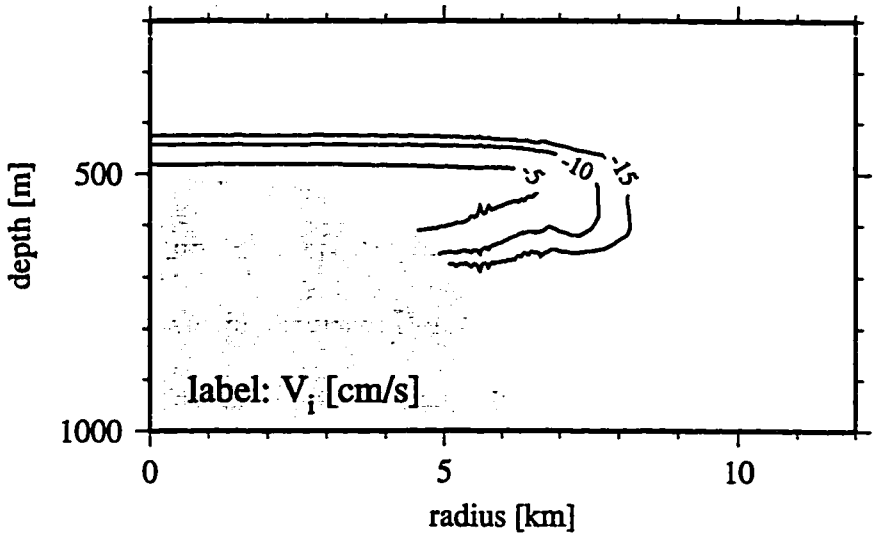

Figure 4.17. Internal wave critical surfaces, $\sigma_d = f_{eff}$, for diurnal currents ($\sigma_{K_1} = 0.93f$) at Fieberling Guyot in mean flow with $V_i = -5, -10, -15$cm/s and radial-vertical structure of Figure 4.14.

similarly in a Gulf Stream ring (Kunze et al. 1995). An internal wave critical surface is a consistent explanation for the low Richardson numbers and high turbulent dissipation observed to extend radially outward atop the summit plain (Kunze and Toole 1996).

4.6. Conclusions

This chapter demonstrates how radially and vertically sheared mean azimuthal flow (i) changes resonance frequencies and (ii) distorts spatial scales of trapped waves, and (iii) causes two types of critical surface.

The stratified seamount-trapped wave of Section 3.2 in mean flow of Figure 4.1, both idealizations of Cobb Seamount measurements (Chapter 2),

does not form critical surfaces. Even though mean vorticity reaches $|\zeta/f| = 0.5$ (Figure 4.2), effects on the wave are limited to a weak increase ($0.001f$) in resonance frequency (Figure 4.5) and weakly reduced spatial scales (Figure 4.6). Mean radial shear, not vertical, is dominantly responsible. The resonance frequency increase is smaller than Doppler shift estimates. To understand this the analogy is made between a stratified seamount-trapped wave in a mean azimuthal current, and a stratified slope-Kelvin wave (Figure 3.7) cross-slope mode (Figure 3.9) of fixed alongslope wavelength in mean flow along a cartesian waveguide. Quasigeostrophic theory is used in the cartesian waveguide (Section 4.3) to determine the senses of changes to resonance frequency and vertical trapping scale due to constant mean flow, uniform shear, and uniformly varying shear (Figure 4.7). Horizontal shear variations of the sense in Figure 4.1 cause a downslope potential vorticity gradient (Figure 4.3) opposite to the topographic potential vorticity gradient that supports waves. In the cartesian waveguide, a mean flow potential vorticity gradient of this sense acts both to decrease the frequency, in opposition to the Doppler shift, and to reduce the scales of the wave (Figure 4.7d). Thus we conclude modifications to the seamount-trapped wave are due to the potential vorticity gradient caused by variations in horizontal shear.

Mean flow causes singularities where the discriminant (4.45) of the governing equation (C.9) vanishes. If this occurs because the phase speed of the

wave is overcome by clockwise mean flow so the intrinsic frequency (4.44) vanishes ($\sigma_d = 0$) a *stratified seamount-trapped wave critical surface* forms (Figure 4.10). This may be understood in terms of a stratified slope-Kelvin wave approaching a critical layer in horizontally sheared mean flow (Figure 4.8), where both horizontal and vertical scales of the wave diminish. Clockwise mean flow reduces the low-frequency bound f_{eff} (4.46) for internal waves (Figure 4.11). Where the discriminant (4.45) vanishes because $\sigma_d = f_{eff}$, an *internal wave critical surface* forms (Figure 4.11). This surface bounds a region called a *superinertial cap* inside which subinertial currents are effectively superinertial (Figure 4.13). Stratified seamount-trapped wave critical surfaces (internal wave critical surfaces) form at relatively low (high) subinertial frequencies (Figure 4.9). For mean flow based on that measured at Fieberling Guyot (Figure 4.14), a superinertial cap forms at the diurnal frequency (Figure 4.16) and its internal wave critical surface boundary (Figure 4.17) occurs on the summit plain where amplified diurnal currents and turbulent dissipation are observed (Kunze and Toole 1996).

Chapter 5

Dissertation summary and conclusions

Observations reveal amplified subinertial tidal currents in stratification and mean shear at Cobb Seamount (Chapter 2). Diagnostics of tidally-forced stratified seamount-trapped waves under appropriate dissipative and mean flow influences (Chapter 3 and 4) compare favorably to the measurements. Among the reasons amplified subinertial tidal currents at a seamount are of interest (Chapter 1) are their similarity to continental-margin dynamics influenced by rotation, stratification, and sloping topography, and their role in the global mixing budget and highly productive biological communities.

Cobb Seamount (Figure 2.1) typifies many of tens of thousands of Pacific Ocean seamounts (Smith and Jordan 1988) in that it extends into thermocline stratification, has bottom slope angles of about $10°$, and is at a latitude where diurnal tidal currents are subinertial. At Cobb the scale fL/N is about $50 - 100$ m and spectra from a current meter 50 m above the bottom (Figure 2.2) show diurnal energy amplified more strongly than the dominantly semidiurnal tides in the surrounding ocean (Egbert et al. 1994). This prompted a October 1991 T. G. Thompson ADCP survey, used here to compare three-dimensional current structure to stratified seamount-trapped waves. Of the kinetic energy measured, 65-70% (Figure 2.4) lies in a least-squares fit to

a set (Table 2.1) of azimuthal harmonics (2.1) (Figure 2.3) of the first few azimuthal wavenumbers at zero, diurnal, inertial, and semidiurnal frequencies.

Main features of steady ADCP currents (Figure 2.6) are a bottom-intensified clockwise current reaching 4 – 5cm/s on the seamount terrace (Figure 2.7) and broad east-northeastward flow of about 7 – 8cm/s across the summit and past the flanks (Figure 2.8). Clockwise flow is not strong enough to isolate fluid from the current across the seamount as in models for Taylor cap formation by vortex stretching of flow incident on isolated topography (Hogg 1973, Chapman and Haidvogel 1992), unless this occurs in the deepest 40 – 50 m below ADCP coverage. CTD data show positive mean density anomaly, with isopycnal uplift of 2 – 4 m (Figure 2.10c), consistent with cyclogeostrophic balance (2.3) of the clockwise circulation (Figure 2.11). Models for incident flow vortex stretching, topographic form drag (Holloway 1987), and rectification of seamount-trapped waves (Section 3.5, Haidvogel et al. 1993) each cause clockwise bottom-intensified currents qualitatively consistent with that observed.

Measured diurnal currents (Figure 2.12a, $0.69f$) have energy in the first clockwise-propagating azimuthal wavenumber ($n = -1$, middle column Figure 2.3). Amplification reaches 5.3 times tidal currents in the surrounding ocean (Egbert et al. 1994) in a bottom-trapped region extending a few kilometers radially and about 100 m vertically away from the terrace. Amplified currents rotate clockwise in time, tracing out ellipses elongated azimuthally with

axes inclined to radial and azimuthal coordinate axes such that radial and azimuthal velocities are positively correlated, $\overline{uv} > 0$ (Figure 2.3d). Velocities at a fixed time turn anticlockwise with depth, and phase propagation is downward (Figure 2.12b). All observed diagnostics occur in a forced damped stratified seamount-trapped wave (Figure 2.16) that is resonant near the diurnal frequency, for measured bathymetry, stratification, and mean azimuthal flow.

Knowledge of stratified seamount-trapped waves (Brink 1989, 1990) is extended here in three ways. First, underlying physics are explained in terms of stratified topographic Rossby waves, giving intuition for wave structure and the effects of dissipation and mean flow. Second, observational diagnostics are described, particularly for a strongly damped wave. Decay timescales of a few days (Chapter 1) are implied by observed turbulence at Cobb Seamount that is strongest outside the bottom boundary layer (Mudge 1994), suggesting Rayleigh drag with Newtonian cooling and heating is a more appropriate dissipative parameterization than bottom stresses. Third, since observed mean flow (Figure 2.7) is similar in strength to amplified tidal currents (Figure 2.12), its effect is examined using wave solutions linearized about a mean current.

Stratified seamount-trapped waves are cross-slope (radial and vertical) modes of short topographic Rossby waves in stratification (Rhines 1970), or *stratified slope-Kelvin waves* (Figure 3.7). Stratified slope-Kelvin wave rays that constructively interfere with themselves (Figure 3.11) in the re-entrant waveguide formed by the sloping sides of a seamount form a resonance that is

a stratified seamount-trapped wave. Cross-slope structure is set by combined influences of (i) refraction by varying bottom slope (Figure 3.8), (ii) Airy-function behavior near turning points (3.29) (Figure 3.9), and (iii) geometric compression in cylindrical geometry (Figure 3.10). An inviscid stratified seamount-trapped wave carries energy and propagates phase purely azimuthally clockwise, since it is a superposition of equal-amplitude upgoing and downgoing stratified slope-Kelvin waves. In a forced damped wave, energy is dissipated most strongly near the summit and the upslope-energy wave dominates (Figure 3.18), so phase propagates radially outward and vertically downward (Figure 3.17) in addition to azimuthally clockwise.

Mean flow representative of the ADCP survey changes wave frequency and structure very weakly and is not strong enough to cause a critical surface. Even a mean current (Figure 4.1) with vorticity reaching $|\zeta/f| = 0.5$ (Figure 4.2) changes resonance frequency by just $0.001f$ (Figure 4.5) and weakly distorts wave scales (Figure 4.6). Mean radial shear, not vertical, is dominantly responsible. Quasigeostrophic theory is used to determine senses of changes to resonance frequency and vertical trapping scale due to constant mean flow, uniform shear, and uniformly varying shear (Figure 4.7). Mean flow changes the frequency weakly because its downslope potential vorticity gradient (Figure 4.3), opposite the potential vorticity gradient supporting the wave, counteracts Doppler shifting.

For bathymetry and stratification (Figure 2.1b,c) at Cobb Seamount the 3rd-highest-frequency radial-vertical mode stratified seamount-trapped wave without mean flow has frequency $0.70f$. Diagnostics of observed diurnal ($0.69f$) currents (Figure 2.12) do not agree with an inviscid wave (Figure 2.13), but are consistent with (Table 2.2) a forced and damped wave with 2-day decay timescale (Figure 2.14). Even though its vorticity reaches $-0.32f$, mean flow based on that measured (Figure 2.11) increases wave frequency by less than $0.01f$, and changes wave structure almost imperceptibly (Figure 2.16).

Stronger mean flow can (Figure 2.15) cause (i) a *stratified seamount-trapped wave critical surface* at low frequencies, or (ii) an *internal wave critical surface* bounding a *superinertial cap*, or region trapped to the seamount in which high-frequency subinertial motions become effectively superinertial. Stratified seamount-trapped wave critical surfaces (Figure 4.10) occur where the intrinsic, or Doppler-shifted, frequency vanishes; both horizontal and vertical wave scales diminish (Figure 4.8). A superinertial cap (Figure 4.12) is bounded by the surface where the intrinsic frequency reaches the effective Coriolis frequency f_{eff} (4.46) (Figure 4.11), the low-frequency bound for superinertial internal waves. At Fieberling Guyot, mean flow (Figure 4.14) reduces f_{eff} by $0.43f$ relative to f (Figure 4.15) and causes a superinertial cap (Figure 4.16) bounded by an internal wave critical surface (Figure 4.17) coincident with amplified diurnal currents and turbulence (Kunze and Toole 1996).

References

Andrews, D. G., J. R. Holton and C. B. Leovy, 1987: *Middle Atmosphere Dynamics (1st ed.)*. Orlando: Academic Press, 489 pp.

Baines, P. G., 1982: On internal tide generation models. *Deep-Sea Res.*, 29, 307-38.

Beckmann, A., 1995: Numerical modeling of time-mean flow at isolated seamounts. *Topographic effects in the Ocean, Proceedings 'Aha Huliko'a Hawaiian Winter Workshop*, P. Muller and D. Henderson, eds., Univ. of Hawaii, Honolulu, 57-66.

Boehlert G. W. and A. Genin, 1987: A review of the effects of seamounts on biological processes, in *Seamounts, Islands and Atolls, Geophys. Monogr. Ser.*, vol. 43, B. H. Keating et al. eds., AGU, Washington, D. C., 319-34.

Bowditch, N., 1977: *American Practical Navigator*. Defense Mapping Agency Hydrographic Center, 1386 pp.

Boyer, D. L., P. A. Davies, W. R. Holland, F. Biolley, and H. Honji, 1987: Stratified rotating flow over and around three-dimensional topography. *Phil. Trans. R. Soc. Lond. A*, 322, 213-41.

Budinger, T. F., and B. J. Enbysk, 1960: Cobb Seamount, a deep-sea feature off the Washington coast, *School of Oceanography Tech. Rep. 60*, University of Washington, 88 pp.

Brink, K. H., 1982: A comparison of long coastal trapped wave theory with observations off Peru. *J. Phys. Oceanogr.*, 12, 897-913.

Brink, K. H., 1989: The effect of stratification on seamount-trapped waves. *Deep-Sea Res.*, 36, 825-44.

Brink, K. H., 1990: On the generation of seamount-trapped waves. *Deep-Sea Res.*, 37, 1569-82.

Brink, K. H., 1995: Tidal and lower frequency currents above Fieberling Guyot. *J. Geophys. Res.*, 100, 10817-32.

Chapman, D. C., 1989: Enhanced subinertial diurnal tides over isolated topographic features. *Deep-Sea Res.*, 37, 1569-82.

Chapman, D. C. and D. B. Haidvogel, 1992: Formation of Taylor caps over a tall isolated seamount in a stratified ocean. *Geophys. Astrophys. Fluid. Dyn.*, 64, 31-65.

Charney, J. G., and Flierl, G. R., 1981: Oceanic analogues of large-scale atmospheric motions. In *Evolution of Physical Oceanography*, MIT Press, Cambridge, MA, 504-548.

Chereskin, T. K. and A. J. Harding, 1993: Modeling the performance of an acoustic Doppler current profiler. *J. Atmos. Oceanic. Technol.*, 10, 41-63.

Codiga, D. L., 1993: Laboratory realizations of stratified seamount-trapped waves. *J. Phys. Oceanogr.*, 23, 2053-71.

D'Asaro, E. A., 1984: Wind forced internal waves in the North Pacific and Sargasso Sea. *J. Phys. Oceanogr.*, 14, 781-94.

Dower, J., H. Freeland, and K. Juniper, 1992: A strong biological response to oceanic flow past Cobb Seamount. *Deep-Sea Res.*, 39, 1139-45.

Efron, B., and G. Gong, 1983: A leisurely look at the bootstrap, the jacknife, and cross-validation. *Amer. Stat.*, 37, 36-48.

Egbert, G. D., A. F. Bennett, and M. G. G. Foreman, 1994: TOPEX/POSEIDON tides estimated using a global inverse model. *J. Geophys. Res.*, 99(C12), 24821-52.

Eriksen, C. C., 1982: Observations of internal wave reflection off sloping bottoms. *J. Geophys. Res.*, 87, 525-38.

Eriksen, C. C., 1985: Implications of ocean bottom reflection for internal wave spectra and mixing. *J. Phys. Oceanogr.*, 15, 1145-56.

Eriksen, C. C., 1991: Observations of amplified flows atop a large seamount. *J. Geophys. Res.*, 96(C8), 15227-36.

Eriksen, C. C., 1995: Waves, mean flows and mixing at a seamount. *Topographic effects in the Ocean, Proceedings 'Aha Huliko'a Hawaiian Winter Workshop*, P. Muller and D. Henderson, eds., Univ. of Hawaii, Honolulu, 1-13.

Foster, M. R., P. A. Davies, and G. S. M. Spence, 1990: Rotating, nonlinearly stratified flow past an isolated obstacle. *Phys. Fluids A*, 2, 1975-82.

Freeland, H. J., 1994: Ocean circulation at and near Cobb Seamount. *Deep-Sea Res.*, 41, 1715-32.

Garrett, C. and D. Gilbert, 1988: Estimates of vertical mixing by internal waves reflected off a sloping bottom. In *Small-scale turbulence and mixing in the ocean, Proc. 19th Int. Liege Colloquium on Ocean Hydrodynamics*, J. C. J. Nihoul and B. M. Jamart, eds., Elsevier, New York, 405-24.

Genin, A., M. Noble, and P. Lonsdale, 1989: Tidal currents and anticyclonic motions on two North Pacific seamounts, *Deep-Sea Res.*, 36, 1803-16.

Gill, A. E., 1982: *Atmosphere-Ocean Dynamics*. Academic Press, 662 pp.

Gordon, H. B. and R. L. Hughes, 1981: A study of rotating baroclinic nonlinear flow around an island. *J. Phys. Oceanogr.*, 11, 1011-4.

Greenspan, H. P., 1969: The theory of rotating fluids. Cambridge Univ. Press, New York, 328 pp.

Gregg, M. C., 1989: Scaling turbulent dissipation in the thermocline. *J. Geophys. Res.*, 94, 9686-98.

Haidvogel, D. B., A. Beckmann, D. C. Chapman, and R.-Q. Lin, 1993: Numerical simulation of flow around a tall isolated seamount, Part II: Resonant generation of trapped waves. *J. Phys. Oceanogr.*, 23, 2373-91.

Hallberg, R., 1995: *Some aspects of the circulation in ocean basins with isopycnals intersecting the sloping boundaries*. Doctoral Dissertation, University of Washington, 244 pp.

Hendershott, M., 1981: Long waves and ocean tides. In *Evolution of Physical Oceanography*, MIT Press, Cambridge, MA, 292-341.

Hogg, N. G., 1973: On the stratified Taylor column. J. Fluid. Mech., 58, 517-37.

Hogg, N. G., 1980: Effects of bottom topography on ocean currents. In *Orographic Effects in Planetary Flows*, GARP Publication series, W. M. O., Geneva, 23, 167-205.

Holloway, G., 1987: Systematic forcing of large-scale geophysical flows by eddy-topography interaction. *J. Fluid Mech.*, 184, 463-76.

Hunkins, K., 1986: Anomalous diurnal tidal currents on the Yermak Plateau. *J. Mar. Res.*, 44, 51-69.

Huppert, H. E., 1975: Some remarks on the initiation of inertial Taylor columns. *J. Fluid Mech.*, 67, 397-412.

Huppert, H. E., and K. Bryan, 1976: Topographically generated eddies. *Deep-Sea Res.*, 23, 655-79.

Huthnance, J. M. 1978: On coastal trapped waves: analysis and numerical calculation by inverse iteration. *J. Phys. Oceanogr.*, 8, 74-92.

Joyce, T. M., 1989: On in situ "calibration" of shipboard ADCPs. *J. Atmos. Oceanogr. Technol.*, 6, 169-72.

Kunze, E., 1985: *Near-Inertial Wave Propagation in Geostrophic Shear*. Doctoral Dissertation, University of Washington, 90 pp.

Kunze, E., R. W. Schmitt, and J. M. Toole, 1995: The energy balance in a warm core ring's near-inertial critical layer. *J. Phys. Oceanogr.*, 25, 942-57.

Kunze, E. and J. M. Toole, 1996: Tidally-forced vorticity, diurnal shear and turbulence atop Fieberling Seamount. *J. Phys. Oceanogr.*, submitted.

Ledwell, J. R., A. J. Watson, and C. S. Law, 1993: Evidence of slow mixing across the pycnocline from an open-ocean tracer-release experiment. *Nature*, 364, 701-3.

Lee, C. M., 1995: *Observations and models of upper ocean response to atmospheric forcing: wind driven flow, surface heating and near-inertial wave interactions with mesoscale currents*. Doctoral Dissertation, University of Washington, 158 pp.

Levin, L. A., E. L. Leithold, T. F. Gross, C. L. Huggett and C. DiBacco, 1994: Contrasting effects of substrate mobility on infaunal assemblages inhabiting two high-energy settings on Fieberling Guyot. *J. Mar. Res.*, 52, 1-34.

Levine, M. D., J. D. Irish, T. E. Ewart, and S. R. Reynolds, 1986: Simultaneous spatial and temporal measurements of the internal wave field during MATE. *J. Geophys. Res.*, 91(C8), 9709-19.

Lighthill, J., 1978: *Waves in Fluids*. Cambridge University Press, New York, 504 pp.

Loder, J. H., 1980: Topographic rectification on the sides of Georges Bank. *J. Phys. Oceanogr.*, 10, 1399-416.

Lueck, R. G. and T. D. Mudge, 1996: Topographically induced mixing around a shallow seamount. *Science*, submitted.

Maas, L. R. M., and J. T. F. Zimmerman, 1989: Tide-topography interactions in a stratified shelf-sea II. Bottom trapped internal tides and baroclinic residual currents. *Geophys. Astrophys. Fluid Dyn.*, 45, 37-69.

McIntyre, M. E., 1980: An introduction to the Lagrangian-mean description of wave, mean-flow interaction, *Pure App. Geophys.*, 118, 152-76.

McNally, G. J., W. C. Patzert, A. P. Kirwan, and A. C. Vastano, 1983: The near surface circulation of the North Pacific using satellite-tracked drifting buoys. *J. Geophys. Res.*, 88, 7507-18.

Meincke, J., 1971: Observation of an anticyclonic vortex trapped above a seamount. *J. Geophys. Res.*, 76, 7432-518.

McPhaden, M. J., J. A. Proehl, and L. M. Rothstein, 1986: The interaction of equatorial Kelvin waves with realistically sheared zonal currents. *J. Phys. Oceanogr.*, 16, 1499-515.

Mudge, T. D., 1994: Mixing around a shallow seamount. M.S. Thesis, University of Victoria, 127 pp.

Muench, J. E., 1995: *Internal wave interactions with equatorial deep jets*. Doctoral Dissertation, University of Washington, 153 pp.

Muller, P., 1995: Ertel's potential vorticity theorem in physical oceanography. *Rev. Geophys.*, 33, 67-97.

Munk, W. H. 1966: Abyssal recipes. *Deep-Sea Res.*, 13, 707-30.

Munk, W. H. 1981: Internal waves and small scale processes. In *Evolution of Physical Oceanography*, MIT Press, Cambridge, MA, 292-341.

Noble, M., D. A. Cacchione, and W. C. Schwab, 1988: Observations of strong mid-Pacific internal tides above Horizon Guyot. *J. Phys. Oceanogr.*, 18, 1300-6.

Pedlosky, J., 1979: *Geophysical Fluid Dynamics*. Springer-Verlag, New York, 624 pp.

Pollard, R., and J. Read, 1989: A method for calibrating ship-mounted acoustic Doppler profilers and the limitations of gyro compasses. *J. Atmos. Oceanic. Technol.*, 6, 859-65.

Pratte, J. M., and J. E. Hart, 1991: Experiments on periodically forced flow over topography in a rotating fluid. *J. Fluid Mech.*, 229, 87-114.

Press, W. H., B. P. Flannery, S. A. Teukolsky and W. T. Vetterling, 1992: *Numerical Recipes in C*. (2 ed.). Cambridge: Cambridge University Press, 994 pp.

Proehl, J. A., 1988: *Equatorial wave-mean flow interaction: the long Rossby waves*. Doctoral Dissertation, University of Washington, 185 pp.

Rhines, P. B., 1969: Slow oscillations in an ocean of varying depth, Part II, Islands and seamounts. *J. Fluid Mech.*, 37, 191-205.

Rhines, P. B., 1970: Edge-, bottom-, and Rossby waves in a rotating stratified fluid. *Geophys. Fluid Dyn.*, 1, 273-302.

Rhines, P. B., 1977: The dynamics of unsteady currents, in *The Sea*, vol. 6, E. D. Goldberg et al., eds., Wiley Interscience, New York.

Roden, G. I., 1987: Effects of seamounts and seamount chains on ocean circulation and thermohaline structure, in *Seamounts, Islands and Atolls, Geophys. Monogr. Ser.*, vol. 43, B. H. Keating et al. eds., pp 335-54, AGU, Washington, D. C.

Roden, G. I., 1994: Effects of the Fieberling seamount group upon flow and thermohaline structure in the spring of 1991. *J. Geophys. Res.*, 99, 9941-61.

Roden, G. I. and W. J. Fredericks, 1992: North Pacific Ocean, Fieberling Seamount. CTD Data Report, University of Washington Contribution 1913.

RD Instruments, 1989: *Acoustic Doppler Current Profilers, Principles of Operation: A Practical Primer.* RD Instruments, San Diego, 39 pp.

Schar, C., and H. C. Davies, 1988: Quasi-geostrophic stratified flow over isolated finite-amplitude topography. *Dyn. Atmos. Ocean.*, 11, 287-306.

Smith, D. K., and T. H. Jordan, 1988: Seamount statistics in the Pacific Ocean. *J. Geophys. Res.*, 94, 2899-918.

Thompson, L., 1990: *Flow over finite isolated topography.* Doctoral Dissertation, MIT/WHOI Joint Program, 222 pp.

Toole, J. M., K. L. Polzin, and R. W. Schmitt, 1994: Estimates of diapycnal mixing in the abyssal ocean. *Science*, 264, 1120-3.

Uchida, R. N., and D. T. Tagami 1984: Groundfish fisheries and research in the vicinity of seamounts in the North Pacific Ocean. *Mar. Fish. Rev.*, 46, 1-17.

Wunsch, C., 1975: Internal tides in the ocean. *Rev. Geophys. Space. Phys.*, 13, 167-83.

Zhang, X., and D. L. Boyer, 1993: Laboratory study of rotating, stratified, oscillatory flow over a seamount. *J. Phys. Oceanogr.*, 23, 1122-41.

Appendix A. ADCP data reduction

a. Calculating absolute water velocity

Absolute velocity of water relative to the earth is the sum of Doppler velocity of water relative to the ship, measured by the ADCP, and navigation velocity of the ship relative to the earth, calculated using Global Positioning System (GPS). The hull-mounted 150 KHz RD Instruments ADCP has 4 Janus beams at 30 degrees from vertical. Data from half-overlapping depth bins with nominal vertical separation 8 m are collected using ping rate once per second and ensemble time one minute. Within 40-50 m of the bottom data are contaminated by bottom-reflected acoustic energy and excluded from the analysis. Sperry MK-37 ship gyrocompass headings are passed directly to the ADCP data collection software during each one-minute ensemble, where they are used to produce Doppler velocity in east and north coordinates. Heading data shows no significant Shuler oscillations (Bowditch 1964), indicating effective performance of gyrocompass damping circuitry.

The ADCP acoustically measures ship movement relative to the earth to calculate bottom-track velocity. Bottom-track velocity above the flanks of the seamount is not usable because over steep slopes all four acoustic beams do not reflect simultaneously from a single depth range. For this reason the navigation velocity, of comparable quality to the bottom-track velocity and with coverage for all portions of the survey, is used instead of bottom-track velocity to produce absolute water velocity.

Bias in Doppler velocities due to heading-dependent behavior of the ship gyrocompass is removed using simultaneous bottom-track and navigation velocities during transits across the seamount terrace. The survey was conducted at about 10 kts, at which speed transducer alignment bias of one degree from the axis of the ship hull introduces a spurious cross-ship velocity of 9 cm/s. Gyrocompass heading bias introduces spurious currents similarly. These biases appear in both Doppler and bottom-track velocities. Unbiased navigational (subscript GPS) and biased bottom-tracked (subscript BT) east and north ship velocities (u, v) are related by

$$\begin{aligned} u_{GPS} &= u_{BT}\cos\phi + v_{BT}\sin\phi \\ v_{GPS} &= -u_{BT}\sin\phi + v_{BT}\cos\phi \end{aligned} \tag{A.1}$$

where ϕ is a clockwise angle representing combined bias due to transducer alignment and the gyrocompass (Pollard and Read 1989, Joyce 1989). We find ϕ varies with heading predominantly as a first harmonic (Figure A1). A rotational transformation of form (A.1) with heading-dependent ϕ determined by least-squares fit is applied to the Doppler velocities with the result that they differ little before and after sharp turns made from various headings.

b. Estimating measurement error

Absolute water velocity is Doppler velocity plus the motion of the ADCP transducer relative to earth, in the form of the navigation velocity calculated

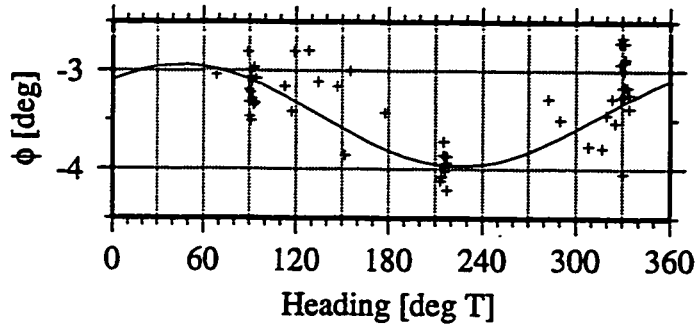

Figure A1. Combined ADCP transducer alignment angle and gyrocompass bias ϕ (A.1) as a function of heading. Variations are caused by the gyrocompass, as transducer alignment is fixed. Each cross is an estimate, using at least 20 one-minute ensembles, from simultaneous navigation and bottom-track velocities on a transect across the terrace. Values near 90, 210, and 330 degrees are from the pinwheel ADCP survey (Figure 2.1a), data at other headings are from the bathymetric survey. Smooth curve is least-squares fit.

by first-differencing GPS fixes. Surface waves introduce significant noise by causing motion of the GPS receiver, located on the mast at about 26 m above the center of mass of the ship, relative to the ADCP transducer. This exceeds that due to the random error of the GPS fixes themselves, determined to be 3 m while holding station during very calm seas. Typical random error in one-minute ship velocity was 10 cm/s. Random error of one-minute Doppler velocities is 3 cm/s (Chereskin and Harding 1993, RD Instruments 1989). Thus random error of one-minute absolute water velocity is $\sqrt{3^2 + 10^2} = 10.5$ cm/s. A 6-minute running mean reduces this by a factor $1/\sqrt{5}$, resulting in absolute water velocity random error of approximately 5 cm/s.

Appendix B. CTD data analysis

The Parizeau (AUG) and (OCT) Thompson surveys are treated independently but identically. AUG data are downward profiles of a Guildline CTD with 1-m sampling (Dower et al. 1992) and 63 (81) casts in inner (outer) regions divided at radius 5km; OCT data are SeaBird Mark IV CTD "tow-yos" with 2-dBar sampling and 55 (21) casts in inner (outer) regions.

Casts give potential density σ_θ at fixed negative values of the vertical coordinate z (positive upward, origin at the sea surface). Background potential density $\overline{\sigma_\theta}$ is an ensemble mean over all casts at fixed depth. We invert individual casts from σ_θ values at each z, to negative vertical coordinate Z values at each isopycnal level in the ensemble-mean profile, by linear interpolation. Vertical displacements are $\eta = Z - \overline{Z}$ (positive upward), with rms value $\eta_{rms} = \sqrt{\overline{\eta^2}}$, where $\overline{Z}$ is the ensemble mean over all casts.

Seamount-associated isopycnal displacement $\Delta Z = \langle Z \rangle_{inner} - \langle Z \rangle_{outer}$ is positive for upward displacement over the seamount, and has standard error

$$\sqrt{\left(\left(\frac{1}{n_{inner}} + \frac{1}{n_{outer}}\right) / (n_{inner} + n_{outer} - 2)\right)\left(s_{inner}^2 n_{inner}^2 + s_{outer}^2 n_{outer}^2\right)},$$

where s_{inner}, s_{outer} are standard errors of $\langle Z \rangle_{inner}$, $\langle Z \rangle_{outer}$ and n_{inner}, n_{outer} are numbers of samples (Press et. al. 1992); ΔZ of one (two) standard error(s) differs significantly from zero at the 67% (95%) level by the student's t test.

Appendix C. Wave solution technique

a. General governing equations

Hydrostatic and Boussinesq momentum, buoyancy and continuity equations for a uniformly rotating and continuously stratified ocean are (2.5)

$$
\begin{aligned}
u_t + \frac{V}{r}u_\theta - \left(f + \frac{2V}{r}\right)v &= -p_r + F^u - Ru && (a)\\
v_t + \frac{V}{r}v_\theta + wV_z + \left(f + \frac{1}{r}(rV)_r\right)u &= -\frac{1}{r}p_\theta + F^v - Rv && (b)\\
0 &= -p_z + b && (c)\\
b_t + \frac{V}{r}b_\theta + B_r u + \left(N^2 + B_z\right)w &= F^b - Rb && (d)\\
\frac{1}{r}(ru)_r + \frac{1}{r}v_\theta + w_z &= 0\,. && (e)
\end{aligned}
\qquad \text{(C.1)}
$$

Here (p, u, v, w, b) are reduced pressure (pressure/ρ_o, where ρ_o is a constant reference density), radial, azimuthal, and vertical velocity, and buoyancy perturbations as functions of (r, θ, z, t) in cylindrical coordinates, with Rayleigh drag and Newtonian cooling and heating of timescale R^{-1}. Linearization is about specified azimuthal mean flow $V(r, z)$ (4.3) and associated cyclogeostrophic (2.3) buoyancy and reduced pressure $B(r, z)$, and $P(r, z)$,

$$
\begin{aligned}
-\frac{V^2}{r} - fV &= -P_r\\
0 &= -P_z + B.
\end{aligned}
\qquad \text{(C.2)}
$$

As explained in Section 3.4, boundary conditions are (3.36)

$$\begin{aligned} (p,u,v,w,b) &= (0,u_F,v_F,0,0) \quad \text{as} \quad r\to\infty && (a)\\ (p,u,v,w,b) &\quad \text{bounded at} \quad r=0 && (b)\\ w+h_r u &= w_E(u,v) \quad \text{at} \quad z=-h && (c)\\ w &= 0 \quad \text{at} \quad z=0 && (d) \end{aligned} \tag{C.3}$$

where (u_F, v_F) are spatially uniform oscillatory far-field horizontal currents maintained by body forces $F^{u,v,b}$ (C.1), and w_E is the pumping of a bottom-stress parameterized time-dependent Ekman layer (Section d below). The arbitrary far-field current ellipse combines anticlockwise- and clockwise-rotating components of magnitudes and phases set by complex constants u^{ACW} and u^{CW}, and grows (decays) over time $T_{td} > 0$ (< 0); as a result (3.37),

$$\begin{aligned} u_F(r,\theta,z,t) &= u_F(\theta,t) = u_F^+(\theta,t) + u_F^-(\theta,t) = \\ &\exp\left(\frac{t}{T_{td}}\right)\Re\left[\tilde{u}_F^+\exp\left(i\varphi^+\right)+\tilde{u}_F^-\exp\left(i\varphi^-\right)\right] && (a)\\ v_F(r,\theta,z,t) &= v_F(\theta,t) = v_F^+(\theta,t) + v_F^-(\theta,t) = \\ &\exp\left(\frac{t}{T_{td}}\right)\Re\left[\tilde{v}_F^+\exp\left(i\varphi^+\right)+\tilde{v}_F^-\exp\left(i\varphi^-\right)\right] && (b) \end{aligned} \tag{C.4}$$

for '+' ('-') superscripts anticlockwise (clockwise) propagation $\left\{\begin{matrix}\varphi^+ = +\theta-\sigma t\\ \varphi^- = -\theta-\sigma t\end{matrix}\right\}$,

and complex constants defined

$$\tilde{u}_F^+ = u_F^{ACW} \qquad \tilde{u}_F^- = u_F^{CW}$$
$$\tilde{v}_F^+ = iu_F^{ACW} \qquad \tilde{v}_F^- = -iu_F^{CW}.$$

Waves are excited as a response to u_F through the condition (C.3)(c) of no flow perpendicular to the sloping bottom. Total variables are divided (p, u, v, w, b) $= (0, u_F, v_F, 0, 0) + (p, u_S, v_S, w, b)$ into far-field and seamount-trapped components. Far-field flow (C.4) is set by $\sigma, u^{ACW}, u^{CW}, R$, and T_{td}, and obeys

$$u_{F_t} + \frac{V}{r}u_{F_\theta} - \left(f + \frac{2V}{r}\right)v_F = F^u - Ru_F \qquad (a)$$
$$v_{F_t} + \frac{V}{r}v_{F_\theta} + \left(f + \frac{1}{r}(rV)_r\right)u_F = F^v - Rv_F \qquad (b) \qquad \text{(C.5)}$$
$$B_r u_F = F^b. \qquad (c)$$

Free waves are eigensolutions to (C.1) and (C.2) for $F^{u,v,b} = (u_F, v_F) = R =$ $w_E = 0$, resonances found in practice for $(u_F, v_F) \ll (u_S, v_S)$ and $u^{ACW} = 0$.

b. Waves on mean flow

Chapters 2 and 4 treat nonzero mean flow $(V, B, P \neq 0)$ with only clockwise-rotating steady amplitude far-field currents $(u^{ACW} = T_{td} = 0)$ and no bottom stress $(w_E = 0)$. Seamount-trapped variables take form (2.7), using p as an example and dropping the '-' superscripts that follow (C.4),

$$p(r,\theta,z,t) = \Re\{\tilde{p}(r,z)\exp[i(-\theta-\sigma t)]\} \qquad \text{(C.6)}$$

where $\tilde{p}(r,z)$ is the *modal structure function.* For $\sigma_d' \equiv \sigma + V/r + iR$,

$N_{tot}^2 \equiv N^2 + B_z$, $f_1 \equiv f + 2V/r$, $f_2 \equiv f + \frac{1}{r}(rV)_r$, and $f_3 \equiv f_2 - f_1\frac{V_z}{N_{tot}^2}$, (C.6) in ((C.1) less (C.5)) with $B_r = f_1 V_z$ (C.2) yields modal structure function relations

$$\begin{aligned}
-i\sigma_d'\tilde{u}_S - f_1\tilde{v}_S &= -\tilde{p}_r && (a)\\
-i\sigma_d'\tilde{v}_S + \tilde{w}V_z + f_2\tilde{u}_S &= \frac{i}{r}\tilde{p} && (b)\\
0 &= -\tilde{p}_z + \tilde{b} && (c)\\
-i\sigma_d'\tilde{b} + f_1 V_z\tilde{u}_S + N_{tot}^2\tilde{w} &= 0 && (d)\\
\frac{1}{r}(r\tilde{u}_S)_r - \frac{i}{r}\tilde{v}_S + \tilde{w}_z &= 0\,. && (e)
\end{aligned} \qquad \text{(C.7)}$$

For $M \equiv f_1 f_3 - (\sigma_d')^2$, manipulation of (C.7) gives $(\tilde{u},\tilde{v},\tilde{w},\tilde{b})$ functions of $\tilde{p}$,

$$\begin{aligned}
\tilde{u}_S &= \frac{1}{M}\left(i\sigma_d'\tilde{p}_r - \frac{i\sigma_d' f_1 V_z}{N_{tot}^2}\tilde{p}_z + \frac{if_1}{r}\tilde{p}\right) & \tilde{w} &= \frac{i\sigma_d'}{N_{tot}^2}\tilde{p}_z - \frac{f_1 V_z}{N_{tot}^2}\tilde{u}_S\\
\tilde{v}_S &= \frac{1}{M}\left(f_3\tilde{p}_r - \frac{\sigma_{d*}^2 V_z}{N_{tot}^2}\tilde{p}_z + \frac{\sigma_d'}{r}\tilde{p}\right) & \tilde{b} &= \tilde{p}_z.
\end{aligned} \qquad \text{(C.8)}$$

Complete solutions follow by numerically solving (Section e below), with boundary conditions in $\tilde{p}$ ((C.3) using (C.8)), the equation for $\tilde{p}$ from (C.7):

$$C_A\tilde{p}_{rr} + C_B\tilde{p}_{rz} + C_C\tilde{p}_{zz} + C_D\tilde{p}_r + C_E\tilde{p}_z + C_F\tilde{p} = C_G. \qquad \text{(C.9)}$$

Here $C_B^2 - 4C_AC_C$ is the discriminant (4.45), $C_G = 0$, and

$$C_A = \sigma_d' M$$

$$C_B = -2\sigma_d' M f_1 V_z / N_{tot}^2$$

$$C_C = \sigma_d' M^2 / N_{tot}^2 + \sigma_d' M f_1^2 (V_z)^2 / N_{tot}^4$$

$$C_D = -\frac{M}{r}(f_3 - f_1) + \sigma_d' M - r\sigma_d'\left(\frac{M}{r}\right)_r + \frac{\sigma_d' M_z f_1 V_z}{N_{tot}^2} - M\left(\frac{\sigma_d' f_1 V_z}{N_{tot}^2}\right)_z$$

$$C_E = -\frac{MV_z}{rN_{tot}^2}\left(f_1^2 - (\sigma_d')^2\right) + \frac{r\sigma_d' f_1 V_z}{N_{tot}^2}\left(\frac{M}{r}\right)_r - M\left(\frac{\sigma_d' f_1 V_z}{N_{tot}^2}\right)_r + M\left(\frac{\sigma_d'}{N_{tot}^2}\left(M + \frac{f_1^2 (V_z)^2}{N_{tot}^2}\right)\right)_z - \frac{\sigma_d' M_z}{N_{tot}^2}\left(M + \frac{f_1^2 (V_z)^2}{N_{tot}^2}\right)$$

$$C_F = -\frac{\sigma_d' M}{r^2} - f_1\left(\frac{M}{r}\right)_r + M\left(\frac{f_1}{r}\right)_r - \frac{M}{r}\left(\frac{f_1^2 V_z}{N_{tot}^2}\right)_z + \frac{M_z f_1^2 V_z}{rN_{tot}^2}.$$

c. Time-dependent or mixed clockwise and anticlockwise forcing

In Chapter 3 nonzero u^{ACW}, R, w_E, and T_{td} are each considered individually, with no mean flow ($V = B = P = 0$). For nonzero u^{ACW}, trapped flow components have form following (C.4), using p for example,

$$p(r, \theta, z, t) = \Re\left[\tilde{p}^+(r,z)\exp\left(i\varphi^+\right)\right] + \Re\left[\tilde{p}^-(r,z)\exp\left(i\varphi^-\right)\right].$$

In this case, $\tilde{p}^+$ and $\tilde{p}^-$ each obey (C.9) and are solved for independently, with +/- forms of (C.8) giving the complete flow field. Solutions for nonzero T_{td} are found by replacing R with T_{td}^{-1}, as explained in Section 3.4.

d. Ekman pumping due to bottom stress

Pumping velocity w_E (C.3)(c) (Section 3.4) is from Ekman convergence for bottom stress proportional to flow above the bottom boundary layer (3.38),

$$\left[\tau^r, \tau^\theta\right]\Big|_{z=-(h+\delta_E)} = \kappa_E \left[u, v\right]\Big|_{z=-h} , \qquad \text{(C.10)}$$

where δ_E is boundary layer thickness and κ_E is a constant resistance parameter (dimensions [length/time]). Flow in the boundary layer, above which stresses are zero, obeys (C.1) with additional stress divergence terms $\left(\tau_z^r, \tau_z^\theta\right)$ in (C.1)(a),(b); there is no stress divergence in the hydrostatic vertical momentum equation nor buoyancy mixing. Continuity (C.1)(e) is integrated vertically across the boundary layer, Liebnitz' rule is used, the kinematic condition $(w = -h_r u)\big|_{z=-(h+\delta_E)}$ is applied at the bottom, terms proportional to δ_E and its gradients are ignored, and (u, v) in the boundary layer are taken to be vertically uniform and equal to $(u, v)\big|_{z=-h}$. The result relates $\tilde{w}_E$ to $\left(\tilde{\tau}^r, \tilde{\tau}^\theta\right)$, modal structure functions (defined as in (C.6)) for pumping and stresses, as

$$\tilde{w}_E = \frac{1}{\tilde{M}}\left[\frac{1}{r}\left(r\left(-i\sigma\tilde{\tau}^r + f\tilde{\tau}^\theta\right)\right)_r - \frac{i}{r}\left(-f\tilde{\tau}^r - i\sigma\tilde{\tau}^\theta\right)\right]\Bigg|_{z=-(h+\delta_E)}.$$

With (C.10) and (C.8), this gives (C.3)(c) in terms of $\tilde{p}|_{z=-h}$ alone.

e. Numerical technique

The system has been reduced to an equation in $\tilde{p}\,(r,z)$ (C.9), with boundary conditions (using (C.8) in (C.3)) of form (C.9). It is solved numerically, following Brink (1989, 1990), on $-h<z<0$ and $0<r<R_o$ for maximum radius R_o. The outer boundary condition (C.3)(a) is applied as $(r\tilde{u}_S)_r = 0$ at $r = R_o$, as is appropriate (Brink 1982). The center boundary condition (C.3)(b) is equivalent to $\tilde{p} = 0$, as required for finite $\tilde{p}_r$ and $\tilde{p}_z$, using (C.8) in the condition $r\tilde{u}_S = 0$ as $r \to 0$ (boundedness of $\tilde{u}_S$). The grid is equispaced in *transformed* coordinates (r', z'), over $-H<z'<0$ and $0<r'<R_o$. The radial grid $r' = s^r R_o\,[1-\exp(-r/R_s)]$ telescopes, where R_s is fixed and $s^r \equiv (1-\exp(-R_o/R_s))^{-1}$. The vertical grid is stretched, $z' = zH/h$. Define

$$a = \left(s^r R_o - r'\right)/R_s \qquad c = H/h \qquad e = -Hh_{r'}/h^2$$
$$b = -h_{r'}z'/h \qquad d = z'\left(2\,(h_{r'})^2 - hh_{r'r'}\right)/h^2$$

and by chain rules, (C.9) (the equation and boundary conditions) transforms to

$$C'_A\,\tilde{p}_{r'r'} + C'_B\,\tilde{p}_{r'z'} + C'_C\,\tilde{p}_{z'z'} + C'_D\,\tilde{p}_{r'} + C'_E\,\tilde{p}_{z'} + C_F\,\tilde{p} = C_G\,,\ \text{where}$$

$$C'_A = a^2 C_A \qquad C'_D = -aC_A/R_s + aC_D$$

$$C'_B = 2a^2 bC_A + acC_B \qquad C'_E = \left(a^2 d - \frac{ab}{R_s}\right)C_A + aeC_B + abC_D + cC_E.$$

$$C'_C = a^2 b^2 C_A + abcC_B + c^2 C_C$$

This equation is discretized with centered first differences (e.g. Proehl 1988) and solved directly by matrix inversion using sparse matrices in MATLAB. Cobb Seamount solutions (Chapter 2) use R_o = 40km, R_s/R_o = 0.3, and H = 2750 m, and require I = 100 r values (equispaced in r') and J = 200 z values (equispaced in z') (Figure C1a) to resolve the bathymetric and stratifi-

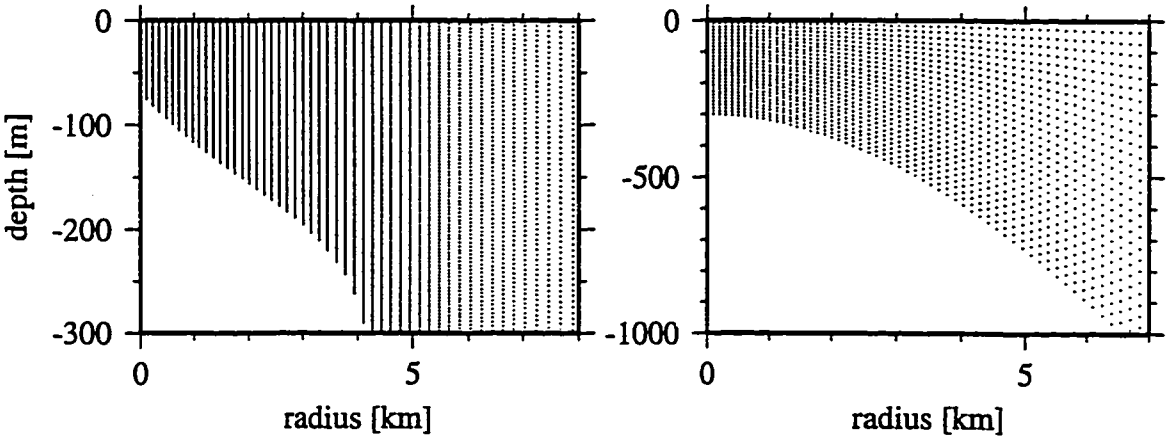

Figure C1. Summit numeric grid. (a) Chapter 2. (b) Chapter 3, 4.

cation profiles (Figure 2.1b,c). This is manageable on a workstation, with execution times no longer than a few hours, though memory requirements are rather large. Solutions for constant N and Gaussian h (r) (Chapter 3, 4) use R_o = 60km and R_s/R_o = 0.25 with I = 150 and J = 30 (Figure C1b).

Daniel L. Codiga

Personal:

Born October 7, 1965 in Mountain View, California.

Education:

1996 Ph.D. Oceanography, University of Washington.

1991 M.S. Oceanography, University of Washington.

1987 B.S. Applied Physics, highest honors, University of California Davis.

Awards:

Chateaubriand Postdoctoral Scholarship, France.

Office of Naval Research Graduate Fellowship.

Publications:

Codiga, D. L., and C. C. Eriksen, 1994. Spatial structure of flow at Cobb Seamount: an ADCP survey. *EOS Transactions*, 75(3): 164.

Codiga, D. L., 1993. Laboratory realizations of stratified seamount-trapped waves. *Journal of Physical Oceanography*, 23(9): 2053-71.

Codiga, D. L., P. B. Rhines, and C. C. Eriksen, 1992. Stratified seamount-trapped waves: a laboratory perspective. *EOS Transactions*, 72(51): 32.